Scaling Fixed Field Accelerators: Theory and Modelling of Horizontal- and Vertical-Excursion Accelerators

Max Emil Topp-Mugglestone
Wolfson College

Thesis submitted in fulfilment of the requirements for the degree of Doctor of Philosophy at the University of Oxford

Hilary Term, 2024

Acknowledgements

My thanks go first and foremost to my all-star team of supervisors: Suzie Sheehy and Brian Foster at Oxford, and Shinji Machida and J.-B. Lagrange at Rutherford Appleton Laboratory. Suzie, thank you for this opportunity and all of your insights - you never failed to offer a fresh perspective on my research when I needed it. Brian, thank you for the advice throughout the final years of my PhD – your feedback and support has been invaluable. Shinji, I am so thankful to have had your guidance throughout my research; I couldn't have asked for a more capable and perceptive hand to help me through completing the PhD. J-B., thank you for being there always as a source of advice, and for your meticulous attention-to-detail in helping me with my research (all the way from the start to the very last minute). I have cherished the time I spent working with all of you and hope for more opportunities to collaborate in the future.

I would like to thank Yoshihiro Ishi and Tomonori Uesugi at KURNS for their assistance and expertise in running experiments on the KURNS main ring FFA – it would not have been possible without them. Likewise, I owe a great deal to Emi Yamakawa and Carl Jolly for their help in carrying out the experiment and taking data – thank you for making my time in Japan such a fantastic experience. I also give my thanks to David Posthuma de Boer for volunteering his knowledge of signal-processing techniques to help me with my data analysis.

I must also thank the rest of the ISIS intense beams group, David Kelliher and Chris Rogers, whose feedback in Monday morning meetings always helped spark new directions in my research, and whose support I am incredibly grateful for. The opportunities I have

been able to take advantage of in working together with the Intense Beams Group have been instrumental in developing my PhD research, and moreover my skills as a physicist.

Attending the USPAS cyclotron school, run by Thomas Planche and Rick Baartman, helped advance my foundations in new areas of accelerator physics, and I am greatly thankful to both Thomas and Rick for the time and work they put into this course. Similarly, I extend my thanks to all of the lecturers at the John Adams Institute and at the CERN Accelerator School 2019 Introductory Course, whose introductions to accelerator physics concepts served as a starting point for almost everything I have done since. I have learnt so much, and I hope to continue doing so as my journey in accelerator physics continues.

This acknowledgements section would hardly be complete without mention of the Angels: Jake and Laurence, I am so grateful to have had you there throughout my PhD for support, company, and always being keen for a pint (or several). At this point in my acknowledgements, it's been a long time coming but, thank you also to Gemma. And finally, thank you to all of my other friends in Oxford, RAL, and beyond.

Last, I thank those to whom perhaps I owe the most. Mārtiņš, you have been one of the closest friends I could ever have hoped for; thank you for everything you have done for me. Molly, thank you for being there for me always. I would not be here without either one of you. I am immensely grateful to you, the staff at Oslo Universitetssykehus, and every one of my friends and family who supported me or reached out during my recovery.

Abstract

Fixed Field Accelerators, or FFAs, are accelerators that use time-independent magnetic fields, permitting the orbit to move as the beam is accelerated. Spatially-dependent magnetic fields allow for the control of orbit geometry during acceleration and the control of focussing strength along the orbit. Scaling FFAs represent the subset of fixed field accelerators in which the magnetic fields follow scaling laws that ensure geometric similarity between closed orbits of different energies and energy-independent focussing behaviour. Vertical-excursion FFAs (vFFAs) present a novel variant on the scaling FFA template where higher-energy orbits are vertically translated copies of lower energy ones, introducing complexities in optics and orbits due to coupled particle motion across the two transverse planes and non-planar orbit behaviour. Because of this, previous design and study of vFFA rings has depended entirely on numerical integration methods.

This study presents analytical methods for studying optics in both horizontal- and vertical-excursion FFAs, deriving for the first time an analytic model of the vFFA. A multipole decomposition approach, termed 'harmonic analysis,' is developed to study vFFA optics in cases where the analytic model has limitations. This technique is then further used in the study of nonlinear (higher-order) effects in conventional FFAs beyond the capabilities of the linear analytic modelling. The nonlinear effects studies are additionally benchmarked with experimental studies of amplitude-dependent tune shift, showing good agreement. To demonstrate the strength of the newly-developed analytic techniques, the vFFA as a muon accelerator stage for a muon collider is studied, where insights provided by the analytic model enable an optimisation that was not previously possible.

Contents

List of Figures

Chapter 1

Fixed Field Accelerators

Scaling Fixed Field Accelerators (FFAs) represent a class of circular accelerator in which magnetic fields are constant over time, and energy scaling of bending and focussing fields is achieved by allowing a spatial excursion of the orbit in a spatially-dependent field that obeys a mathematically-derived scaling law. This type of operation holds a number of advantages over other machine types, allowing rapid acceleration from injection to top energy without the need to ramp magnets and arbitrary pulse structures to be realised (which cannot be achieved in a synchrotron), whilst surpassing energy and focussing strength limits associated with machines such as classical isochronous cyclotrons.

In this chapter, we introduce a number of the formalisms and mathematical tools that will be used throughout the thesis in developing methods to study FFAs; with a mathematical basis established, we progress to a brief overview of the history of the FFA and its relation to other accelerator types. We then derive scaling laws for horizontal- and vertical-excursion machines, which set the conditions these machines must satisfy in order for focussing behaviour to remain independent of the energy. We motivate a number of reasons for the construction of these machines over other accelerator types, and explain the need for further study of their properties.

1.1 Theory of accelerating and focussing charged particles

A charged particle with charge q acts in a generalised electromagnetic field with electric component $\mathbf{E}$ and magnetic component $\mathbf{B}$ according to the Lorentz force [1]:

$$\frac{d\mathbf{p}}{dt} = q(\mathbf{E} + \mathbf{v} \times \mathbf{B}), \tag{1.1}$$

where $\mathbf{p}$ is the particle's momentum, $\mathbf{v}$ is its velocity, and t represents time. The electric component gives energy to the particle and therefore can be used to accelerate the particle. The electric force can also be used for controlling the particle's direction; however, as the particle's velocity grows, the term from the magnetic field, which is proportional to the magnitude of the particle's velocity, increases - implying that at high energy, magnetic fields, rather than electric fields, are the most efficient means of influencing a particle. However, the magnetic force always acts perpendicularly to the existing momentum of the particle; magnetic fields cannot increase the energy of a particle as the dot product of the force vector and the velocity vector will always be zero - they can only redirect its momentum. Most modern accelerators, then, use both electric and magnetic components; the former is used to accelerate the beam in accelerating structures known as radiofrequency (RF) cavities, whilst the latter is used to bend the beam along a desired trajectory - and to focus the beam on this trajectory, so that particles with deviations from the ideal trajectory can be transported without being lost.

Under a constant, spatially-invariant, time-independent dipole field, a charged particle experiences a constant force perpendicular to its motion. This can be considered as the centripetal force of circular motion; the required force to keep a particle travelling in a circular arc of radius ρ. This force is given by

$$|\mathbf{F}| = \frac{\gamma m |\mathbf{v}|^{\mathbf{2}}}{\rho}, \tag{1.2}$$

for an object of rest mass m and relativistic gamma factor $\gamma = 1/\sqrt{1 - v^2/c^2}$. Substituting in the magnitude of the Lorentz force and cancelling terms gives

$$\frac{\gamma m|\mathbf{v}|}{\rho} = \frac{|\mathbf{P}|}{\rho} = q|\mathbf{B}|, \tag{1.3}$$

in which $|\mathbf{P}|$ is the magnitude of the particle's momentum. This equation is by convention rearranged into the form

$$B\rho = P/q, \tag{1.4}$$

the value of which is a parameter referred to as magnetic rigidity. This parameter effectively quantifies the resistance of the beam to being redirected by a magnetic field, defining the expected radius of curvature for the beam when subject to a given magnetic field. Knowledge of this enables the choice of appropriate field strengths for bending and focussing elements to achieve the desired beam properties, and to direct it along our preferred trajectory.

1.1.1 Frenet-Serret Coordinates

To understand the behaviour of beams in accelerators where the trajectory curves, it is necessary to establish some frameworks in which we can analyse the dynamics. Whilst in principle the dynamics of the system are independent of our reference frame, the ability to derive and solve the equations of motion is aided by a sensible choice of coordinates. When analysing the focussing of a system, we need to understand the motion of particles with respect to some idealised 'reference' trajectory; it becomes useful to think about the system in terms of position along the reference trajectory, and displacements of individual particles with respect to the reference position that tracks along the trajectory. The approach commonly taken in accelerator physics is to use Frenet-Serret coordinates [2]. In this coordinate system, positions are specified in terms of a distance s along the reference trajectory $\mathbf{r_0}(\mathbf{s})$, and the transverse position orthogonal to the trajectory at the point s. The locally-defined unit vector $\hat{\mathbf{s}}$ is then tangential to the reference orbit, whilst x and

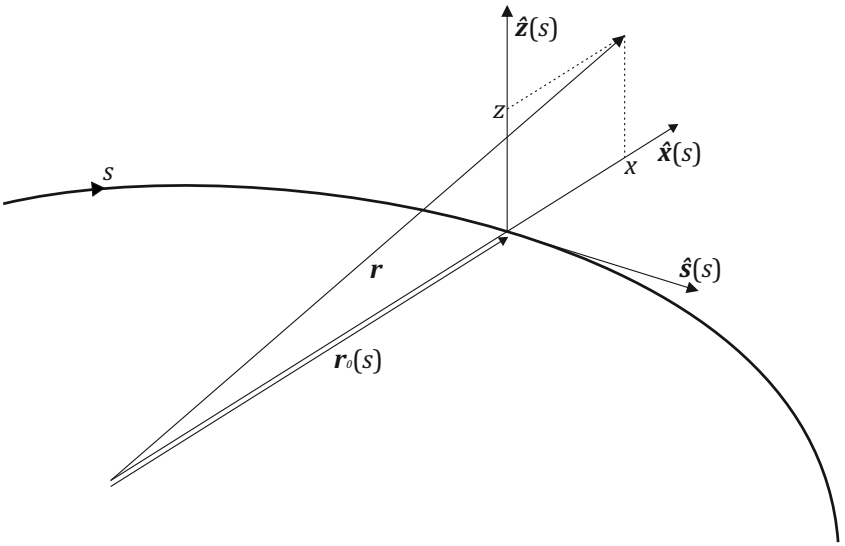

Figure 1.1: A torsionless Frenet-Serret coordinate system.

z represent a pair of transverse coordinates defined with orthogonal unit vectors such that $\hat{\mathbf{x}}(s) \times \hat{\mathbf{s}}(s) = -\hat{\mathbf{z}}(s)$. The Frenet-Serret formulae state that:

$$\frac{d\hat{\mathbf{s}}}{ds} = \frac{1}{\rho}\hat{\mathbf{x}} \tag{1.5}$$

$$\frac{d\hat{\mathbf{x}}}{ds} = -\frac{1}{\rho}\hat{\mathbf{s}} + \tau\hat{\mathbf{z}} \tag{1.6}$$

$$\frac{d\hat{\mathbf{z}}}{ds} = -\tau\hat{\mathbf{x}} \tag{1.7}$$

in which the scalar parameters $\rho(s)$ and $\tau(s)$ parametrise the reference orbit in terms of a radius of curvature and a torsion (the non-planar tendency of the curve). The dynamics of a system can be simplified in the case where we can assume the torsion to be zero, and the trajectory exists as a planar arc defined simply by its radius of curvature; in this case, Fig. 1.1 gives a diagrammatic representation of a Frenet-Serret coordinate system.

In such a Frenet-Serret frame, an arbitrary point represented with coordinates (s, x, z) corresponds to a Cartesian vector $\mathbf{r}$ as:

$$\mathbf{r}(s) = \mathbf{r}_0(s) + x\hat{\mathbf{x}} + z\hat{\mathbf{z}}. \tag{1.8}$$

The relationship between the Cartesian coordinates (X, Y, Z) and the Frenet-Serret coordinates (x, s, z), in the case that $\mathbf{r}_0(s)$ describes a circular arc of constant radius ρ centred on the origin, is then given by

$$\begin{aligned} X &= (x + \rho)\cos\left(\frac{s}{\rho}\right) - \rho \\ Y &= (x + \rho)\sin\left(\frac{s}{\rho}\right) \\ Z &= z \end{aligned} \tag{1.9}$$

assuming the vector $\hat{\mathbf{x}}$ is collinear with $\mathbf{X}$ at $s = 0$.

The Frenet-Serret system gives a useful framework for parameterising motion of the beam, and its response to focussing and defocussing forces induced by magnets.

1.1.2 Hamiltonian Dynamics

One of the most ubiquitous tools used in accelerator physics is Hamiltonian dynamics. The Hamiltonian approach allows us to construct a system of coupled $2n$ first order differential equations for $2n$ variables, given the kinetic and potential energy. A key advantage of the Hamiltonian method is the ability to use canonical transformations to express the system in the best possible phase space coordinate system, whilst preserving the invariants of the system.

The Hamiltonian is defined as the Legendre transformation of the Lagrangian L,

$$H(p_i, x_i, t) = \sum [\dot{x}_i p_i - L(x_i, \dot{x}_i, t)], \tag{1.10}$$

in which x_i and $\dot{x}_i$ are the position and velocity coordinates of the particle (dot notation denoting the derivative with respect to the independent variable of the system, in this case

t), and p_i is the canonical momentum - itself defined as follows:

$$p_i \equiv \frac{\partial L}{\partial \dot{q}_i}. \tag{1.11}$$

The Lagrangian is expressed in terms of the kinetic energy T and the potential energy V as

$$L = T - V, \tag{1.12}$$

which, for a charged particle in a generalised electromagnetic field specified with a vector potential $\mathbf{A}$ and a scalar potential ϕ is given as

$$L = -mc^2\sqrt{1-\beta^2} - q\phi + q\mathbf{v}\cdot\mathbf{A}, \tag{1.13}$$

with m representing the mass of the particle, c the speed of light, e the charge of the particle, and v its velocity, with $\beta = v/c$. The scalar and vector potentials are related to the magnetic and electric fields via the following expressions:

$$\mathbf{B} = \nabla \times \mathbf{A}, \tag{1.14}$$

$$\mathbf{E} = -\nabla\phi - \frac{\partial \mathbf{A}}{\partial t}. \tag{1.15}$$

The Hamiltonian for a charged particle in an electromagnetic field is then given as

$$H = q\phi + \sqrt{(\mathbf{p} - q\mathbf{A})^2c^2 + m^2c^4}. \tag{1.16}$$

Via the principle of least action, which acts to minimise the action of the system

$$W = \int_{t_1}^{t_2} [L(x_i, \dot{x}_i, t)]dt, \tag{1.17}$$

we obtain Hamilton's equations

$$\dot{x}_i = \frac{\partial H}{\partial p_i}, \dot{p}_i = -\frac{\partial H}{\partial x_i}, \tag{1.18}$$

which characterise the equations of motion of the system.

Deriving practical equations of motion directly from Eq. (1.16) for non-trivial cases is challenging, and making approximations to simplify this Hamiltonian is often convenient.

For example, under the assumption that $(\mathbf{p}-q\mathbf{A})^2$ is small in comparison to m^2c^2, a Taylor expansion [3] enables us to reduce the Hamiltonian to the form

$$H \simeq q\phi + \frac{1}{2m}\left(\mathbf{p}-q\mathbf{A}\right)^2. \tag{1.19}$$

Applying Hamilton's equations (Eq. (1.18)) gives firstly

$$\frac{dx_i}{dt} = \frac{\partial H}{\partial p_i} = p_i/m + q\frac{A_i}{m}, \tag{1.20}$$

and recalling that p_i represents the canonical momenta of the system (in this case $p_i = mv_i + \frac{q}{c}A_i$), this can be recognised as simply $\dot{x}_i = v_i$. Secondly, using $\dot{p}_i = -\frac{\partial H}{\partial q_i}$,

$$\begin{aligned}\dot{p}_i = m\ddot{x}_i + \frac{q}{c}\dot{A}_i =& \frac{(\mathbf{p}-q\mathbf{A}/c)}{m}q\frac{\partial \mathbf{A}}{\partial x_i} - q\frac{\partial \phi}{\partial x_i} \\ =& qv_j\nabla_i A_j - q\nabla_i\phi,\end{aligned} \tag{1.21}$$

then explicitly writing out the time-derivative of the vector potential

$$\dot{A}_i = \frac{\partial A_i}{\partial t} + v_j\nabla_j A_i, \tag{1.22}$$

to rewrite Eq. (1.21) as

$$m\ddot{x}_i = -q\left(\frac{\partial A_i}{\partial t} + v_j\nabla_j A_i\right) + qv_j\nabla_i A_j - e\nabla_i\phi, \tag{1.23}$$

the identity $\mathbf{v}\times(\nabla\times\mathbf{A}) = \nabla(\mathbf{v}\cdot\mathbf{A}) - (\mathbf{v}\cdot\nabla)\mathbf{A}$ can be used together with the definitions of the scalar and vector potentials (Eq. (1.14) and Eq. (1.15)) to obtain the familiar Lorentz force law:

$$m\ddot{\mathbf{x}} = q\left(\mathbf{E} + \mathbf{v}\times\mathbf{B}\right). \tag{1.24}$$

This result demonstrates the utility of the charged particle Hamiltonian to obtain useful results, and the use of approximations to facilitate this. To employ such an approach, a choice of coordinates must be made such that the dynamical variables remain small, and thus that the Hamiltonian can be Taylor-expanded into a manageable form. For circular accelerators, use of the Frenet-Serret coordinate system with an appropriate choice of reference trajectory is what enables this. However, a series of canonical transformations must

first be employed to rewrite the relativistic charged particle Hamiltonian in the new basis. A generating function of the third kind [4] can be used to define the transformation between the Cartesian coordinates and the Frenet-Serret coordinates: the equations relating the Cartesian coordinates X_i and momenta P_i to the new Frenet-Serret variables (x_i, p_i) are then

$$\begin{aligned} X_i &= -\frac{\partial F_3}{\partial P_i}, \\ p_i &= -\frac{\partial F_3}{\partial x_i}. \end{aligned} \tag{1.25}$$

The transformation of the position variables is already known, as in Eq. (1.9), and this enables us to derive an appropriate generating function F_3:

$$F_3 = -\left((x+\rho)\cos\left(\frac{s}{\rho}\right) - \rho\right) P_X - (x+\rho)\sin\left(\frac{s}{\rho}\right) - zP_Z. \tag{1.26}$$

The new momenta can then be computed as

$$\begin{aligned} p_x =& P_X \cos\left(\frac{s}{\rho}\right) - P_Y \sin\left(\frac{s}{\rho}\right), \\ p_s =& P_Y \cos\left(\frac{s}{\rho}\right) + P_Z \sin\left(\frac{s}{\rho}\right). \\ p_z =& P_Z, \end{aligned} \tag{1.27}$$

A Hamiltonian transformed under a generating function of the third kind follows

$$H_1 = H_0 + \frac{\partial F_3}{\partial t}, \tag{1.28}$$

though F_3 has no explicit time-dependence in the case described here. Writing the new Hamiltonian, then, merely requires substitution of the new variables, and re-expressing the Cartesian vector potential from the X, Y, Z-frame to the Frenet-Serret frame:

$$\begin{aligned} A_x =& A_X \cos\left(\frac{s}{\rho}\right) - A_Y \sin\left(\frac{s}{\rho}\right), \\ A_s =& A_Y \cos\left(\frac{s}{\rho}\right) + A_X \sin\left(\frac{s}{\rho}\right), \\ A_z =& A_Z. \end{aligned} \tag{1.29}$$

This gives

$$H_1 = c\sqrt{\left(\frac{p_s}{1+x/\rho} - qA_s\right)^2 + (p_x - qA_x)^2 + (p_z - qA_z)^2 + m^2c^2} + q\phi \tag{1.30}$$

The Hamiltonian above describes the motion in terms of time t as the independent variable, but the accelerator system is typically defined in terms of the positions of elements along the reference trajectory; it is therefore convenient to make a switch of the independent variable t to path length s instead, using a further canonical transformation. Using Eq. (1.10) with the definition of the action (Eq. (1.17)), the action for 3-dimensional particle motion in the Frenet-Serret coordinate system can be written as

$$W = \int_{t_0}^{t_1} [p_x\dot{x} + p_s\dot{s} + p_z\dot{z} - H]dt. \tag{1.31}$$

The action can be written instead as

$$W = \int_{s_0}^{s_1} [p_x x' + p_z z' + p_s - Ht']ds, \tag{1.32}$$

where $q' = \frac{dq}{ds}$. In the former definition, the conjugate variables are

$$(x, p_x), (z, p_z), (s, p_s) \tag{1.33}$$

and by analogy, the conjugate variables for the latter can be recognised as:

$$(x, p_x), (z, p_z), (H, t). \tag{1.34}$$

In this case, p_s becomes an invariant of the motion, and takes the place of the Hamiltonian in the transformed system (i.e. $H_s = p_s$). Expanding the Hamiltonian for relativistic particle motion, Eq. (1.30), and rearranging for the new Hamiltonian p_z, the following Hamiltonian is derived:

$$H_s = p_s = -\left(1 + \frac{x}{\rho}\right)\sqrt{\frac{(E - q\phi)^2}{c^2} - \frac{m^2c^2}{P_0} - (p_x - qA_x)^2 - (p_z - qA_z)^2} - q\left(1 + \frac{x}{\rho}\right)A_s, \tag{1.35}$$

in which we have used the fact that $H_t = T + V = E$. By convention, we normalise the Hamiltonian and momenta by a reference momentum P_0 as follows:

$$\tilde{H} = \frac{H}{P_0}, \tilde{p_i} = \frac{p}{P_0}, \tag{1.36}$$

giving

$$\tilde{H} = \tilde{p_s} = -\left(1 + \frac{x}{\rho}\right)\sqrt{\frac{(E - q\phi)^2}{P_0^2 c^2} - m^2c^2 - (\tilde{p_x} - \frac{q}{P_0}A_x)^2 - (\tilde{p_z} - \frac{q}{P_0}A_z)^2} - \frac{q}{P_0}\left(1 + \frac{x}{\rho}\right)A_s \tag{1.37}$$

as the final form of the accelerator Hamiltonian.

Additionally, this thesis concerns transverse dynamics only, and the longitudinal components of this Hamiltonian are assumed to be constants, which can therefore be ignored. However, a complete description of accelerator dynamics requires full consideration of longitudinal motion in addition to transverse motion; whilst this thesis focusses on the transverse stability and behaviour of the accelerator, understanding longitudinal motion and coupling between transverse and longitudinal planes is vital to the development of accelerators, and future studies may use the full 6D Hamiltonian.

1.1.3 Transfer Maps

A transfer map relates the dynamical variables of the accelerator at an arbitrary point s_0 to the dynamical variables at a second point s_1:

$$\mathbf{x}(s_1) = \mathbf{M}(\mathbf{x}(s_0)), \tag{1.38}$$

where the 4-dimensional vector $\mathbf{x} = (x, \tilde{p_x}, z, \tilde{p_z})$ denotes the transverse dynamical variables of the system, and $\mathbf{M}$ is some 4-dimensional vector with components that are functions of these dynamical variables. In the case that the output variables can be said to linearly depend on the input variables - which is sufficient to describe the behaviour associated with small displacements from the reference trajectory, in many cases - then $\mathbf{M}$ can

be expressed as a matrix product:

$$\mathbf{x}(s_1) = \mathbf{M}(\mathbf{x}(s_0)) = \mathcal{M}\mathbf{x}(s_0). \tag{1.39}$$

Transfer maps must be derived by solving the equations of motion for the region of space between s_0 and s_1, and computing the integral over this distance. The simplest example of a linear transfer map, or transfer matrix, is that of a drift space - i.e. a region of free space where a particle is not affected by any external magnetic or electric fields. Beginning from the Frenet-Serret Hamiltonian (Eq. (1.37)), we substitute in the corresponding vector and scalar potentials (in this case, all components are zero) and take the limit $\rho \to \infty$ to obtain

$$H_s = -\sqrt{\frac{(E - q\phi)^2}{c^2} - m^2c^2 - \tilde{p_x}^2 - \tilde{p_z}^2}. \tag{1.40}$$

In order to find a set of linear equations of motion, we must expand this in terms of the dynamical variables. Doing so we find

$$H_{\text{drift}} \simeq \frac{\tilde{p_x}^2}{2} + \frac{\tilde{p_z}^2}{2}, \tag{1.41}$$

when we neglect constant terms (as the equations of motion depend only on the derivatives of H). Applying Hamilton's equations, we find for the horizontal coordinate

$$\begin{aligned} \frac{dx}{ds} &= \frac{\partial H}{\partial \tilde{p_x}} = \tilde{p_x} \\ \frac{d\tilde{p_x}}{ds} &= -\frac{\partial H}{\partial x} = 0. \end{aligned} \tag{1.42}$$

The vertical equations of motion are identical in form (exchanging x for z). The above equations are solved by solutions of the form

$$\begin{aligned} x(s) &= s\tilde{p_x}(s_0) + C \\ \tilde{p_x}(s) &= 0 + D, \end{aligned} \tag{1.43}$$

where C and D are constants to be found. Applying the boundary conditions that at $s = s_0$, $x = x(s_0)$ and $\tilde{p_x} = \tilde{p_x}(s_0)$ gives the exact solution to the equations of motion

$$\begin{aligned} x(s) &= s\tilde{p_x}(s_0) + x(s_0) \\ \tilde{p_x}(s) &= 0 + \tilde{p_x}(s_0), \end{aligned} \tag{1.44}$$

and doing the same for the z, p_z plane enables us to write the full system as the 4D transfer matrix for a drift of length L

$$\mathcal{M}_{\text{drift}} = \begin{pmatrix} 1 & L & 0 & 0 \\ 0 & 1 & 0 & 0 \\ 0 & 0 & 1 & L \\ 0 & 0 & 0 & 1 \end{pmatrix}. \tag{1.45}$$

One consequence of deriving the map from the Hamiltonian in this manner is that it guarantees symplecticity [4]. A symplectic matrix $\mathcal{M}$ with dimensions $2n \times 2n$ is one that satisfies the condition

$$\mathcal{M}^T \mathcal{S} \mathcal{M} = \mathcal{S}, \tag{1.46}$$

in which $\mathcal{M}^T$ denotes the transpose of $\mathcal{M}$, and $\mathcal{S}$ is a $2n \times 2n$ block diagonal square matrix whose diagonals are $\mathcal{S}_2$:

$$\mathcal{S}_2 \begin{pmatrix} 0 & 1 \\ -1 & 0 \end{pmatrix}. \tag{1.47}$$

A symplectic matrix always has a determinant of 1, and the product of any two symplectic matrices is itself symplectic. A symplectic transformation has an associated conserved quantity that is always preserved; this gives rise to important results used in accelerator physics, such as Liouville's theorem, which states that the density of particles in phase space is conserved for a Hamiltonian system [5].

1.1.4 Beam Optics in Periodic Systems

For a particle travelling multiple turns in an accelerator, the fields as seen by the reference particle will necessarily be periodic on the scale of one turn: after one full revolution any particle will once again see the same sequence of focussing elements in the same order. However, circular accelerators (and even single-pass machines) are often periodic on a smaller scale as well, being constructed from sequences of identical magnetic structures termed 'cells'. A cell refers to the smallest unit of periodicity of a lattice. By deriving transfer matrices for each element of a cell, a first-order transfer map for the full period can

be assembled by multiplying together each individual matrix:

$$\mathcal{M}_{\text{Cell}} = \prod_{i=0}^{n-1} \mathcal{M}_i, \tag{1.48}$$

in which $\mathcal{M}_i$ represents the transfer matrix for the i-th element of the cell, and n is the number of elements in the cell. Whilst this approach can be used to track individual particles, exploiting the property of periodicity in this map enables us to derive a description of the dynamics of an entire beam - a more useful approach, when we consider the laborious task of tracking every particle when real beams can comprise 10^{13} particles [6] or more. If we assume decoupled motion (that the horizontal and vertical planes do not interact, and the transfer matrix of the cell is a block diagonal), then we can consider the horizontal and vertical motion separately using two separate 2×2 transfer matrices. Assuming periodic motion, a horizontal 2×2 transfer matrix of the cell, $\mathcal{M}_x$, can be written in terms of the periodic functions $\sin$ and $\cos$ and some phase advance μ_x that is a property of the focussing structure, to give the matrix

$$\mathcal{M}_x = \mathcal{I}_2 \cos \mu_x + \mathcal{S}_2 \mathcal{A} \sin \mu_x. \tag{1.49}$$

In this, $\mathcal{I}_N$ is the $N \times N$ identity matrix, and $\mathcal{A}$ is some matrix to be found. We can place constraints on the elements of $\mathcal{A}$ from the requirement that $\mathcal{M}_x$ is symplectic. By substituting Eq. (1.49) into Eq. (1.46), one finds that the off-diagonal elements of $\mathcal{A}$ must be equal, enabling $\mathcal{A}$ to be written as

$$\mathcal{A} = \begin{pmatrix} \gamma_x & \alpha_x \\ \alpha_x & \beta_x \end{pmatrix}, \tag{1.50}$$

where α, β, and γ are known as the Courant-Snyder parameters [7]. The same substitution also gives the constraint that $\beta_x \gamma_x - \alpha_x^2 = 1$. A consequence of the fact that this derivation is independent of where in the cell we started our cell transfer matrix is that these parameters can be calculated independently for any point in the cell, and can therefore be written as functions of position s. $\beta_x(s)$ is often referred to as the beta-function. The horizontal cell

transfer matrix can be expressed in terms of the Courant-Snyder parameters as

$$\mathcal{M}_x = \begin{pmatrix} \cos\mu_x + \alpha_x \sin\mu_x & \beta_x \sin\mu_x \\ -\gamma_x \sin\mu_x & \cos\mu_x - \alpha_x \sin\mu_x, \end{pmatrix} \tag{1.51}$$

a description that can be used to gain a number of insights into the behaviour of the beam. The eigenvalues of this transfer matrix, λ_i are a conjugate pair given by

$$\begin{aligned} \lambda_{1,2} &= \cos\mu_x \mp \sin\mu_x \sqrt{\alpha^2 - \beta\gamma} \\ &= \cos\mu_x \mp i \sin\mu_x = e^{\mp i\mu} \\ &= \frac{\mathcal{M}_{11} + \mathcal{M}_{22} \mp \sqrt{\mathcal{M}_{11}^2 + 4\mathcal{M}_{12}\mathcal{M}_{21} - 2\mathcal{M}_{11}\mathcal{M}_{22} + \mathcal{M}_{22}^2}}{2}, \end{aligned} \tag{1.52}$$

enabling the phase advance per cell to be calculated as

$$\mu_x = \left| \arctan\left[\frac{\mathrm{Im}(\lambda_i)}{\mathrm{Re}(\lambda_i)} \right] \right|. \tag{1.53}$$

For stability, the phase advance μ_x must be real, and $|\lambda_i|$ must be 1.

Normalising the phase advance μ_x by 2π gives a parameter which takes a value between 0 and $1/2$. This can be related to a property known as the (horizontal) tune, q_x, which refers to the number of complete transverse oscillations made by a particle over one period; cell tune refers to the number of oscillations over a cell, whilst ring tune (usually written with a capital Q_i) maps this over an entire revolution of the machine's circumference. μ_x is related to the fractional part of the tune by $q_x = \mu_x/2\pi$ or $q_x = 1 - \mu_x/2\pi$ depending on whether the fractional tune is above or below 0.5.

When λ_i is real, the tune reaches zero; stable optics cannot be achieved in this case, as this implies each particle returns exactly to the same position after one period (meaning that any imperfections in the fields seen by the beam will add over the course of many turns). For the opposite limiting case, where λ_i is entirely imaginary, we must take the limit

$$\lim_{\lambda \to 1} \left| \arctan\left[\frac{\mathrm{Im}(\lambda)}{\mathrm{Re}(\lambda)} \right] \right| / 2\pi = \frac{1}{2}. \tag{1.54}$$

This tells us that a particle will return to its original position after 2 periods. As a result, a particle receiving a transverse kick will receive the same transverse kick after 2 turns, and

the effect of any perturbations will again grow over time. The same logic in fact applies in general for any case where

$$nQ = m, \tag{1.55}$$

for integer n and m. This condition is known as a resonance, and the order of the resonance is given by the value of $|n|$.

The tune can alternately be computed from the beta-function of a cell by integrating the phase advance over one cell as

$$Q_\beta = \frac{1}{2\pi}\int_0^C \frac{1}{\beta(s)}ds, \tag{1.56}$$

for a period of length C, and the fractional part can be taken by subtracting the integer part of the tune to give $0 < q_\beta < 1$. This is equivalent to the value of the fractional tune calculated from normalising Eq. (1.53) by 2π for $q_\beta < 1/2$, but equivalent to $1 - \mu_x/2\pi$ for $q_\beta > 0.5$. The fractional tune is computed using Eq. (1.53) throughout this thesis unless otherwise noted.

If we record the position x and transverse velocity $x' = dx/ds$ of a particle at the same point every cell as the particle travels through a periodic beamline, we find that (for a non-integer tune) the particle traces an ellipse on the transverse x, x' phase space plane (Fig. 1.2). The parameters of this ellipse are determined by the Courant-Snyder parameters at the chosen point in the cell, as well as the amplitude of the individual particle, J_x (also known as its action). The area of the ellipse, however, is a constant throughout the cell, and is determined solely by the particle's amplitude. We term the area of this ellipse the single-particle emittance, ϵ_x (though it is also known as the Courant-Snyder invariant). The emittance may be calculated as

$$\frac{\epsilon_x}{\pi} = \gamma x^2 + 2\alpha x x' + \beta x'^2 = 2J_x. \tag{1.57}$$

An emittance for a beam as an ensemble is then commonly defined by either taking the root-mean-square single-particle emittance for all particles in the beam (called the r.m.s.

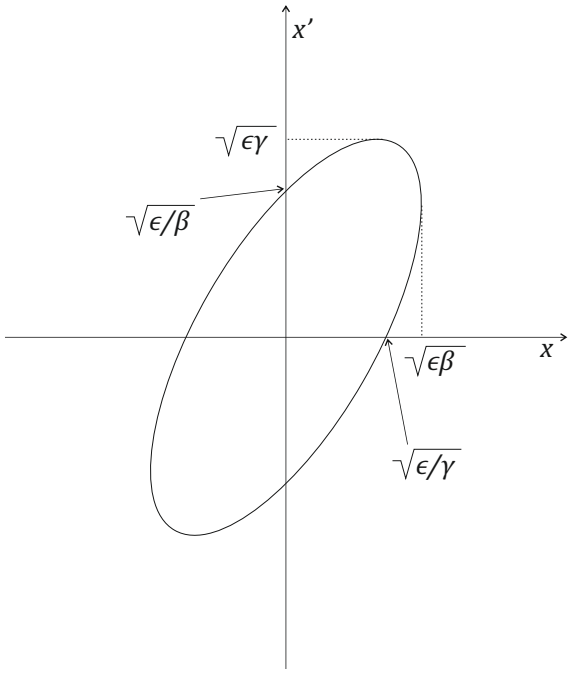

Figure 1.2: Phase space ellipse for a single particle progressing through a linear, periodic lattice. The geometry of the ellipse is given in terms of the Courant-Snyder parameters and the emittance ϵ.

emittance) or taking the area of a fixed ellipse in phase space that contains a specified fraction of the particles in the beam (termed the geometric emittance).

Under symplectic transformations, the area of the phase space ellipse is preserved, and emittance is an invariant of the system.

1.2 History of Fixed Field Accelerators

Fixed-field accelerators – i.e. the class of machines whose magnetic fields are time-independent – have a long history in accelerator physics, beginning with the development of the cyclotron in the 1930s.

Early cyclotrons were constructed of a pair of hollow D-shaped electrodes (termed 'dees'), placed between the poles of an iron magnet [8] – an arrangement depicted in Fig. 1.3. With electrodes charged to opposite potentials, a charged particle with charge q crossing the gap between them could gain energy proportional to the voltage difference between

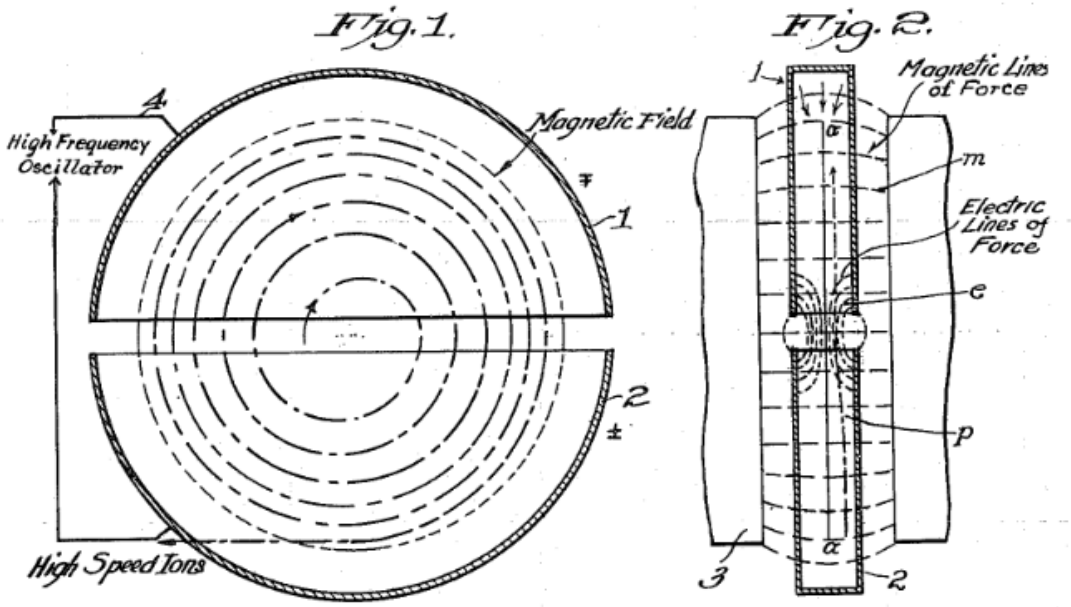

Figure 1.3: Diagram of an early cyclotron. [8]

the two 'dees' (which creates a corresponding electric field $\mathbf{E}$). After crossing the gap, the particle's trajectory within the electrode would be bent in a circular fashion by the vertically directed magnetic field $\mathbf{B}$, according to the Lorentz force (Eq. (1.1)). After bending through 180 degrees, a particle would once again encounter the gap. By engineering the power supply such that the potential on the 'dees' would alternate with an RF frequency that corresponded to the particle's motion, it would then be possible to ensure that every time the particle crossed the gap it would see an accelerating potential difference.

In the nonrelativistic case, the circular motion of a particle in a uniform magnetic field is governed by the following relation:

$$m\omega = q|\mathbf{B}|, \tag{1.58}$$

where ω is the angular frequency of the motion, and m and q are the mass and charge of the particle respectively. This shows that for a nonrelativistic particle in a uniform magnetic

field, the frequency of revolution is constant and independent of the energy; i.e. the machine is isochronous. Hence, the electrodes can be excited by a radiofrequency wave of constant frequency.

These properties – a time-independent magnetic field, and constant RF frequency – mean that the cyclotron is able to achieve incredibly energy-efficient operation (with beam power in certain modern cyclotrons able to reach up to around 18% of the wall-plug power [9]) and high beam current due to its ability to deliver a continuous beam. This mode of operation is referred to as continuous wave (CW) operation. However, the isochronous cyclotron as described above has a number of limitations. Firstly, when relativistic effects can no longer be neglected, we must include a correction factor in the above relation (Eq. (1.58)):

$$\gamma m\omega = q|\mathbf{B}|, \tag{1.59}$$

where γ is the Lorentz factor. This implies that for isochronicity to be maintained (i.e. for ω to remain constant) the B field must scale proportionally to γ. Hence, the B-field must increase radially as the particle's energy increases. Given that ω is constant, and ω is defined as v/R, (v being the velocity of the particle and R the radius of its orbit), R must be proportional to v. We can thus write

$$B(R) = \gamma B_c = \frac{B_c}{\sqrt{1-\beta^2}} = \frac{B_c}{\sqrt{1-(R/R_\infty)^2}}, \tag{1.60}$$

in which two new quantities are defined: B_c (the [theoretical] magnetic field at the centre of the machine, equal to $m\omega/q$), and $R_\infty = c/\omega$, the orbit radius for $v = c$.

However, vertical focussing must also be considered. To satisfy the requirement for vertical focussing in an azimuthally-symmetric field, we find that there must be a radial field component B_r with magnitude proportional to the vertical displacement z from the midplane, i.e.

$$B_r = gz, \tag{1.61}$$

in which g is a scalar representing the gradient of the radial field. Consequently, from the Lorentz force, we have

$$F_z = qvB_r = qvgz, \tag{1.62}$$

and we require the sign of g to be negative for stability in the vertical plane. From Maxwell's equations we have $\nabla \times \mathbf{B} = 0$, and therefore we find that

$$\frac{\partial B_z}{\partial r} = \frac{\partial B_r}{\partial z} = g. \tag{1.63}$$

The implication of this is that for g to be negative, and for vertical stability to be maintained, B_z must too decrease with radius - a condition that is incompatible with the isochronicity criterion, Eq. (1.60).

For this reason, isochronous cyclotrons with azimuthally-invariant field distributions were limited in energy reach by relativistic effects; going to higher energies with such machines would require breaking the isochronicity condition. This was initially seen as a fundamental limitation of the cyclotron, with contemporary scientists predicting a maximum energy achievable with proton cyclotrons of the order of 12 MeV [10].

However, L. H. Thomas [11] proposed a solution: cyclotrons with azimuthally varying fields (AVF cyclotrons) could be constructed. This configuration distorted the orbits from being completely circular, and introduced azimuthal components into the magnetic field; the interaction of radial components of the particle momenta with the azimuthal components of the fields created an effect analogous to the edge focussing [7] discussed elsewhere in accelerator physics. In many modern cases this azimuthal variation comes in the form of dividing the cyclotron into a number of separated magnets, i.e. a so-called sector cyclotron, in which case the vertical focussing can be considered directly as edge focussing. These concepts are discussed in more detail in [12], and a discussion of isochronicity in these machines may be found in [13].

Even so, isochronous cyclotrons are not without limitations. Looking at the isochronicity condition, Eq. (1.60), as v approaches c, the required magnetic field grows asymptotically. This places obvious practical constraints on the energy reach of the machine; for

instance, the radial field gradient results in very small turn separation at the high energy extreme, rendering extraction impractical. Even modern isochronous cyclotrons such as those built at PSI [14] and TRIUMF [15] are designed for a maximum energy of only 500-600 MeV.

The only way to circumvent this limitation is to relax the isochronicity condition, meaning that the angular frequency is no longer constant over the acceleration cycle. As a result, the RF frequency must be ramped synchronously with the changing revolution frequency as the particle is accelerated; this class of machine is known as a synchrocyclotron [16]. This removes the limit on the machine energy faced by the conventional isochronous cyclotron. However, it forces the machine into pulsed operation and, as a result, the maximum achievable beam current is drastically reduced. A more in-depth discussion of types of cyclotrons and their associated dynamics may be found in [13]. Beam current and energy efficiency were some of the key advantages of the cyclotron, but these could not be maintained at higher energies. Because of this, synchrocyclotron-type designs became unfavourable compared to synchrotron alternatives – machines in which magnetic fields are also increased in proportion to the beam energy. In synchrotrons, the beam can be confined to a single closed orbit for all energies, reducing not only the footprint but also the complexity and cost of the magnets. This would also simplify the optics of the machine substantially, with tunes now able to be fixed such that they remain approximately constant over the acceleration cycle, reducing any risks associated with resonance crossing.

Cyclotrons and early synchrotrons also faced limits associated with the focusing strength of the optical systems, leading to large beam apertures and limiting the maximum energy reach of machines.

In the early 1950s, physicists at Brookhaven National Laboratory recognised that an array of magnetic quadrupoles with alternating polarities could be used to achieve stronger focussing in both planes [17] - a principle that is now known as alternating gradient focussing. A quadrupole that is able to focus the beam in the horizontal plane induces a

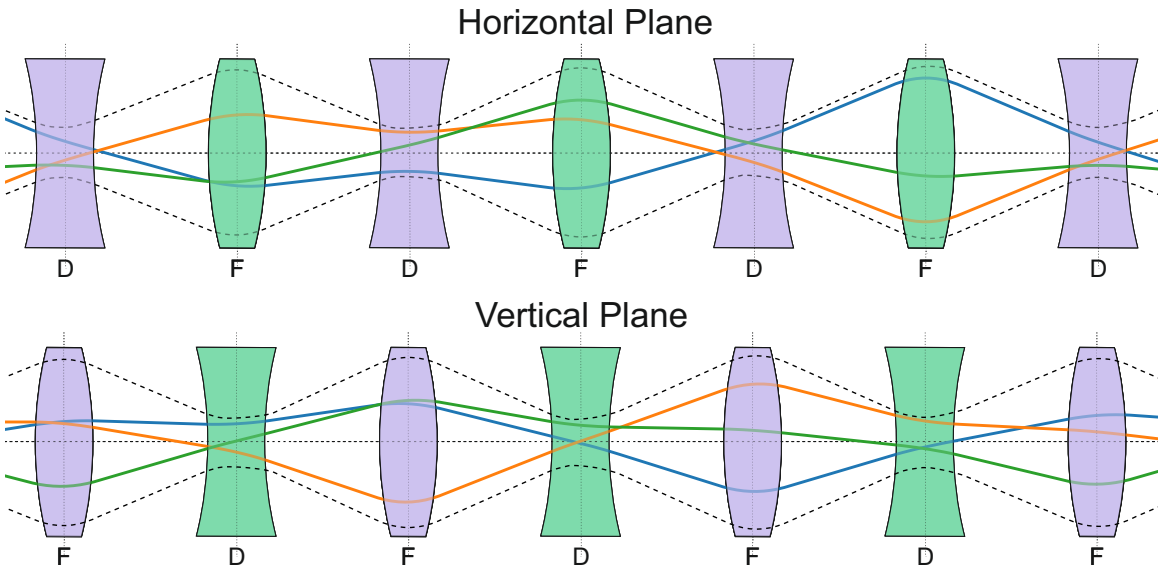

Figure 1.4: Diagram of the FODO structure in the horizontal and vertical planes: the lenses labelled F represent the focussing magnets, whilst those with the label D represent the defocussing magnets in the respective planes. The blue, green, and orange solid lines show example trajectories through the FODO lattice, as projected onto the horizontal and vertical planes, whilst the dotted black curve shows the overall envelope of the beam.

horizontal deflection towards the axis proportional to a particle's horizontal displacement from the axis; but simultaneously acts to defocus the beam in the vertical plane by inducing a vertical deflection away from the axis proportional to the particle's vertical displacement from the axis; likewise, a vertically focussing quadrupole behaves as a horizontally defocussing quadrupole.

These properties could be exploited by installing a horizontally focussing (F) quadrupole to focus the profile of the beam to a minimum in the horizontal plane, and then installing a vertically focussing (horizontally defocussing, or D) quadrupole at this beam 'waist'. In this manner, the defocussing effect of the vertical focussing quadrupole is minimised due to the small displacement of particles from the axis at this point. A further horizontally focussing (F) quadrupole is installed as the beam grows again, and by these means a periodic 'lattice' of alternating gradient magnets is constructed (see Fig. 1.4).

This simple form of lattice, consisting of alternating F and D magnets with equal drift

spaces between them, is known as a FODO lattice. This manner of focussing could easily be introduced into synchrotrons, where the beam could pass directly through the middle of the quadrupole magnets and the orbit would remain at a fixed position for all energies. This led to synchrotron-type machines becoming the dominant solution for most high-energy applications.

However, implementing alternating gradient focussing to cyclotron-type machines with a nonzero beam excursion over the accelerating cycle was more complicated. This is because a beam passing through a quadrupole off-axis will experience a dipole (bending) effect proportional to the displacement from the axis; this means that for a machine constructed of alternating quadrupoles, the direction of the bend will also alternate in sign. As a consequence, the machine has to contain an element of reverse bending magnets within the cell to achieve strong focussing.

Moreover, as machines reach progressively higher energies, emittance growth due to resonance behaviour becomes an issue of increasing concern – especially in hadron machines (as in electron machines, radiation damping [18] is able to mitigate the beam growth caused by resonance crossing). Previously, this had been a less critical issue, as the loss of efficiency due to the resultant beam losses could easily be compensated by the CW operation of the machine, and at lower energies the impact of particles colliding with accelerator components is much less damaging. In the synchrotron, focusing fields could be ramped synchronously with beam energy to maintain constant tune and choose the working point to avoid resonances, hence avoiding these effects at any energy. The idea to replicate this property in a fixed-field machine led to the development of the scaling fixed field accelerator (FFA) at MURA in the 1960s [19] (an idea also independently created by Ohkawa in Japan [20], and Kolomensky in Russia [21]).

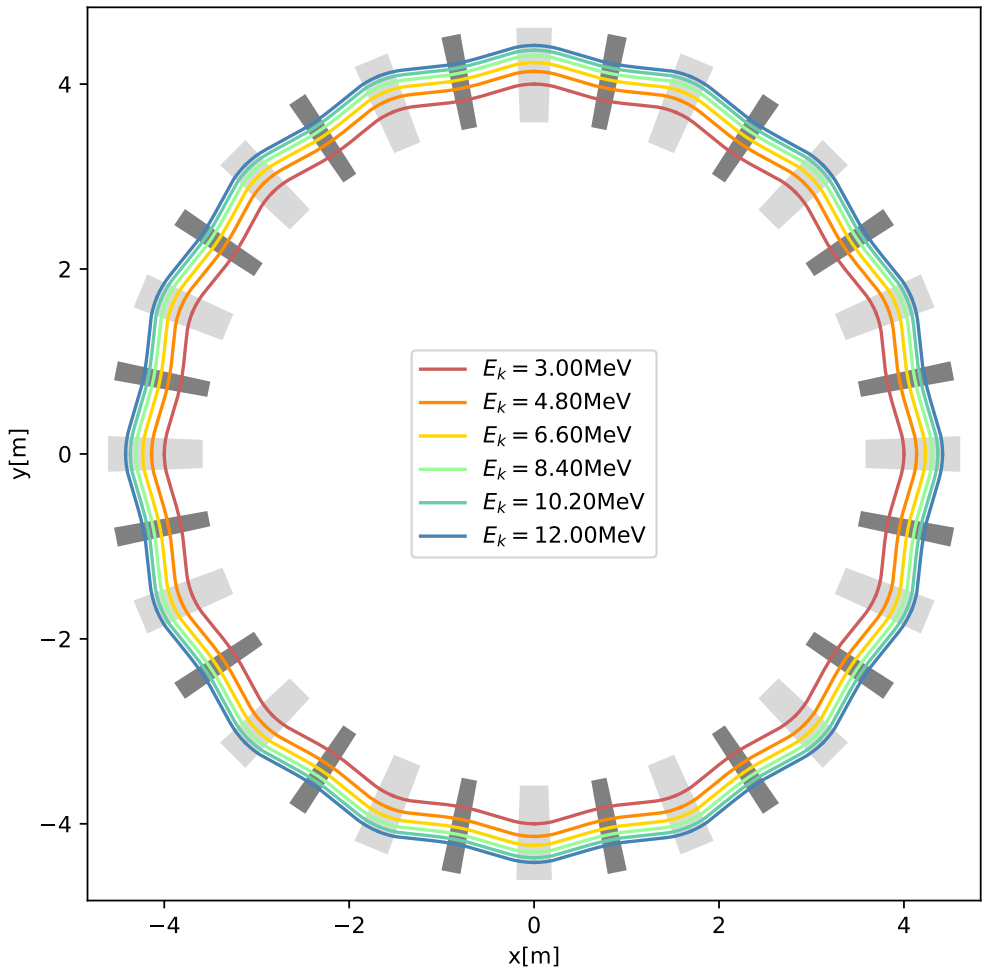

Figure 1.5: Plan view of an example scaling FFA ring. Shaded regions show the magnet positions, with the darker grey shade representing the reverse bend magnets.

1.3 Scaling Horizontal-Excursion Fixed-Field Accelerators

It was realised that careful engineering of spatially-dependent magnetic fields could yield the same constant-tune result in a fixed-field machine as achieved by scaling elements in time in a synchrotron. This required two criteria to be satisfied. Firstly, an orbit for a given energy would have to be geometrically similar to an orbit for any other given energy – i.e. orbits could expand radially with increasing momentum p, but could not change shape (as depicted in Fig. 1.5. This criterion is stated by Kolomensky as

$$\frac{\partial}{\partial p}\frac{\rho(p)}{\rho_0(p)} = 0, \tag{1.64}$$

in which ρ is the local radius of curvature of the orbit, and $\rho_0(p)$ is the mean radius of curvature of the orbit at a given momentum. Simultaneously, the gradient must increase radially such that each orbit sees the same focussing effect. The geometrical field index k is defined as follows:

$$k = -\frac{r}{B_z}\frac{\partial B_z}{\partial r}, \tag{1.65}$$

using B_z to denote the vertical magnetic field.

Since the field index must be a constant of the acceleration cycle, this leads to the second requirement:

$$\frac{\partial k}{\partial p} = 0 \tag{1.66}$$

These criteria can be fulfilled by fields that follow the scaling law given below:

$$B_z(r) = B_0\left(\frac{r}{r_0}\right)^k \tag{1.67}$$

The local field gradient at some point (θ, r) is then given by $kB_0(\theta)\left(\frac{r}{r_0}\right)^{k-1}$. The k-value is fixed, and r is always positive, so, to achieve alternating gradient focussing around a ring, the sign of B_0 must change with azimuthal position θ. Alternating the sign of B_0 causes not only an alternating gradient, however, but also an alternating dipole field, meaning that an FFA requires reverse bends to realise alternating gradient focussing.

A machine constructed to these specifications has the advantages of synchrotron-like fixed tune and strong focusing, whilst maintaining the cyclotron's advantages of time-independent magnetic fields. The need to ramp the magnetic fields for the synchrotron severely limits the synchrotron in a number of aspects: firstly, the repetition rate of the machine is restricted by the rate at which the magnets can be ramped (many times slower than for instance the ramping of the RF frequency), and, secondly, the ramping magnets are much less energy-efficient than time-independent counterparts. DC magnets are additionally much more suited to the application of superconducting technologies, which would increase the energy efficiency of a machine. Pulsed operation of magnets, additionally, is a common cause of failure in synchrotron machines: 17% of downtime of the ISIS synchrotron between 2013 and 2017 could be attributed to failures of AC magnets and their power supplies [22], compared to just 2% of downtime hours being ascribed to issues with DC magnets and their power supplies. A fixed-field machine is thus able to eliminate one of the principal sources of machine failure, leading to comparatively more reliable operation.

Moreover, the removal of the need for synchronously pulsed magnets relaxes the constraints on achievable pulse structures, enabling schemes such as beam stacking [23] to be implemented. Beam stacking is a mode of operation in which a first beam is injected, accelerated to some extraction energy E, and then allowed to debunch and coast while a second beam is injected, accelerated to an energy $E-dE$ and debunched [24]. This process may be repeated indefinitely to accumulate coasting beams at close to top energy, where they can all be captured and rebunched before extraction to form a single high-intensity beam. By doing this, it becomes possible to increase the intensity of an extracted beam in a machine where the intensity at injection is already restricted by space-charge forces (which are more predominantly repulsive at lower energies [25]).

However, the FFA as described above is still limited in certain aspects. The scaling law not only dictates that multipoles at all orders must be present, but also fixes their values as a function of the k-value. This has implications for higher-order properties of the machine

optics such as amplitude-dependent tune shifts, limiting the dynamic aperture (the area of transverse phase space in which a particle can survive for a large number of turns). Additionally, reverse bending cannot be eliminated (leading to an increased ring size over what could be achieved without the need for reverse bending for the same energy), and the need for synchronous RF means that CW operation is impossible.

To address the matter of the reverse bending requirement, which increases the minimum footprint required for an FFA machine, the spiral-sector magnet was proposed [26]. These magnets take advantage of edge focussing effects [7] in order to focus beams in the vertical plane, eliminating the need for reverse-bend magnets. A requirement of maintaining the scaling is that the edge angle (the angle of the magnet end plane with respect to the direction of the beam) must remain constant as a function of the momentum – and therefore must remain constant as a function of the radius. This constraint forces a modification of the scaling law to include a term that accounts for the relationship between the radial coordinate and the azimuthal dependence needed to maintain this property:

$$B_z(r,\theta) = B_0 \left(\frac{r}{r_0}\right)^k \left[1 + \sin\left(N\theta - N\tan\zeta \log\frac{r}{r_0}\right)\right]. \tag{1.68}$$

Here, N is the periodicity of the ring (i.e. the number of cells), θ is the azimuthal coordinate, and ζ is a parameter defining the spiral angle. This idea was later generalised with the development of the FD or DF spiral concepts [27], which proposed lattices incorporating some element of spiral angle as well as a reverse bend, occupying a middle ground between the original radial-sector designs and the full spiral-sector reverse-bend-free machines. Figure 1.6 shows an example of a spiral-sector FFA lattice based on the FD-spiral concept, and how altering the spiral angle affects its geometry. Due to the scaling law, introducing a spiral angle affects not only the focussing strength at linear order, but also the strength of higher-order multipole effects. This can negatively impact the machine's dynamic aperture, and understanding of these effects is therefore critical to choosing the design parameters of any new ring.

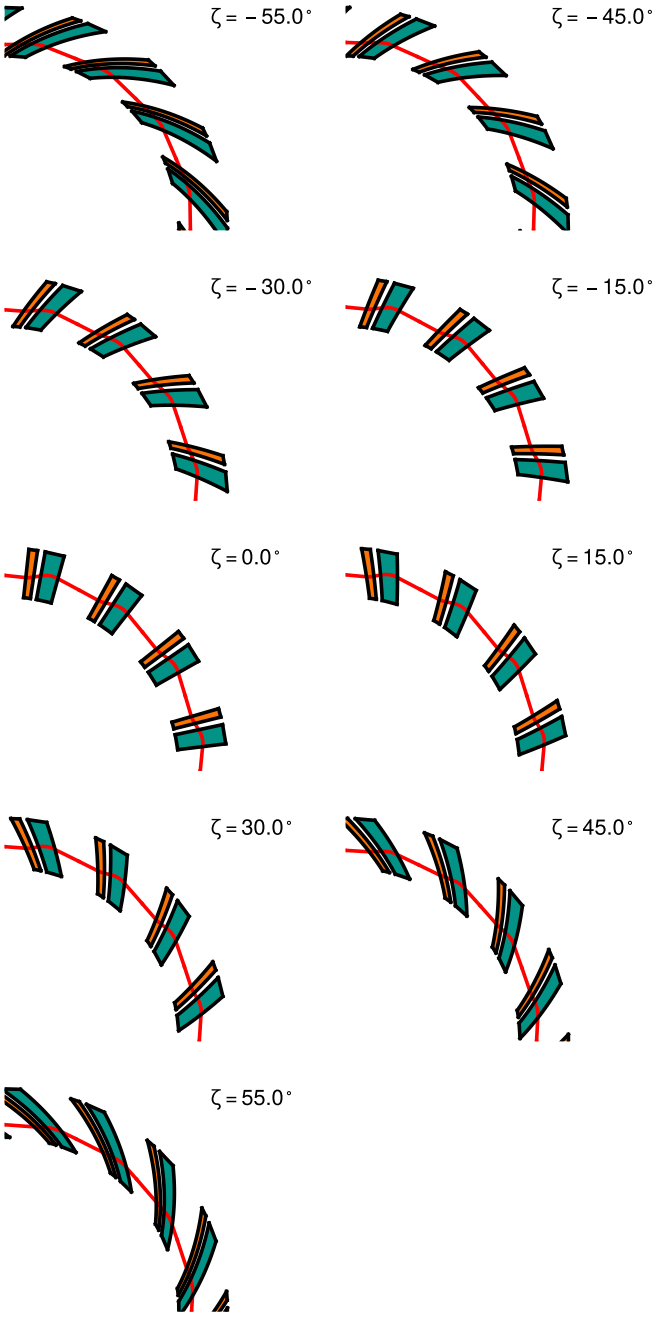

Figure 1.6: Plan view of FD-spiral FFA rings for different values of ζ.

1.4 The Vertical-Excursion Fixed Field Accelerator

It is not in fact a requirement for an FFA that higher energy orbits must expand radially; for instance fields could be constructed such that stable orbits for all energies could exist as vertically translated copies of each other, and an accelerated particle could adiabatically track between these orbits as its energy increases – a concept now known as the Vertical-Excursion Fixed Field Alternating Gradient Accelerator (vFFA). This concept was originally proposed by Ohkawa [28] , who referred to it as the electron cyclotron, and was further studied by Leleux [29] and Teichman [30]. In recent years, the concept was independently rediscovered by Brooks [31], and studied using modern numerical techniques and tracking codes by a number of groups [32, 33, 34].

The vertical translation of successive orbits satisfies Eq. (1.64) by default, but a new relation is required to describe the vertical scaling of the fields. As an equivalent to the field index for the horizontal excursion FFA (henceforth referred to as an hFFA), a vFFA normalised field gradient m can be defined as:

$$m = \frac{1}{B_z(z)} \frac{\partial B_z}{\partial z} \tag{1.69}$$

To ensure scaling (i.e. constant focusing strength as a function of energy), this m must not depend on the momentum of the orbit – i.e.:

$$\frac{\partial m}{\partial p} = 0, \tag{1.70}$$

and hence

$$\frac{\partial}{\partial z}\left(\frac{1}{B_z}\frac{\partial B_z}{\partial z}\right) = 0, \tag{1.71}$$

implying

$$\left(\frac{\partial B_z}{\partial z}\right)^2 - B_z \frac{\partial^2 B_z}{\partial z^2} = 0, \tag{1.72}$$

which can only be satisfied by

$$B_z(z) = B_0 e^{mz}. \tag{1.73}$$

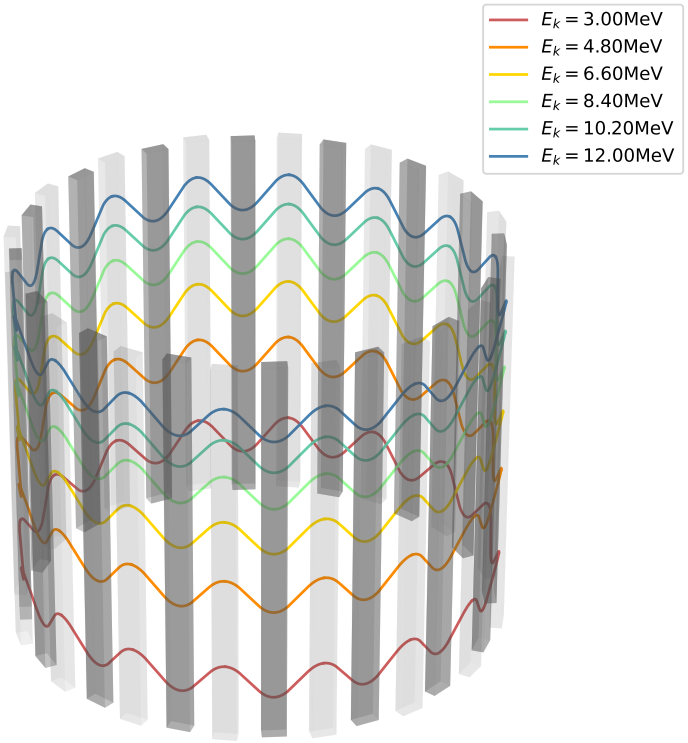

Figure 1.7: 3D view of an example scaling vFFA ring. Shaded volumes show the magnet geometry, with the darker grey shade representing the reverse bend magnets.

By adhering to this scaling law, it becomes possible to construct a machine with constant tunes over the acceleration cycle where higher energy orbits are vertically stacked above lower energy orbits (illustrated in Fig. 1.7). In this configuration, the advantages of the scaling hFFA are maintained, but all orbits share the same path length. This fact means that, for a relativistic particle ($v \simeq c$), the machine can be operated isochronously.

The vFFA represents a machine that is, in principle, capable of cyclotron-level power efficiency and reliability, synchrotron focussing strength and energy reach, and arbitrary repetition rates and pulse structures. This renders it an ideal candidate for machines on the intensity frontier (e.g. spallation source proton drivers), or machines where rapid acceleration from injection to top energy is a priority (e.g. muon accelerator rings). Its dynamics and behaviour, and the process of optimising vFFA lattices, however, have seen little study, and current understanding relies purely on extensive numerical simulation. In order to refine the understanding of the machine, and to develop efficient lattice design processes, new formalism and investigative techniques must be developed.

1.5 Acceleration in FFAs

As discussed in Section 1.1, magnetic fields alone cannot induce an energy gain in a particle. The beam's energy may only be increased by passing through an electric field component aligned with the momentum of the beam. In multi-pass machines, this requires an alternating electric potential.

In the case of the classical cyclotron, this was achieved using electrodes (dees) charged using an alternating radiofrequency (RF) voltage. However, this approach became limited at higher frequencies, where the wavelength of the RF is similar to the dimensions of the resonant circuit that creates the alternating field [35]; in this case, the power radiated from the system begins to become significant and efficient acceleration is no longer possible. It is this factor that led to the development of the cavity resonator for accelerators.

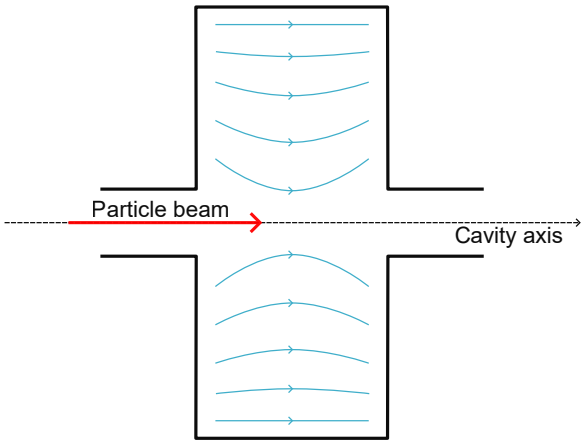

Figure 1.8: Schematic representation of an RF cavity. The electric field lines are depicted as blue lines between the cavity walls (solid black lines).

A cavity resonator (usually referred to as an RF cavity in accelerator physics, due to the frequencies used) is a hollow structure comprised of a thin conducting shell. A source of electromagnetic waves with frequency corresponding to a resonant frequency of the cavity is able to induce standing wave modes within the cavity, as illustrated in Figure 1.8. By engineering the geometry of a cavity such that it resonates in a mode with longitudinal electric field components along the axis (oscillating at a frequency that is an integer multiple of a beam's revolution frequency), the cavity can be used to accelerate a beam. The ability of a cavity to accelerate a beam is often expressed in terms of its gradient, written in units of voltage per metre, which is the accelerating voltage seen by the beam divided by the longitudinal dimension of the cavity.

In FFAs, due to the excursion of the beam during the acceleration cycle, it is necessary to construct cavities with wide transverse apertures and wide 'good field regions' - i.e. minimising transverse field components across the width of the region occupied by the beam during acceleration. Depending on the properties of the machine, and the energy ranges in which it operates, it may also be necessary to adjust the frequency of the accelerating field during the acceleration. An example of an FFA cavity with tunable resonant frequency is discussed in [36].

These accelerating cavities are inserted in drifts between the magnets (Fig. 1.9 shows

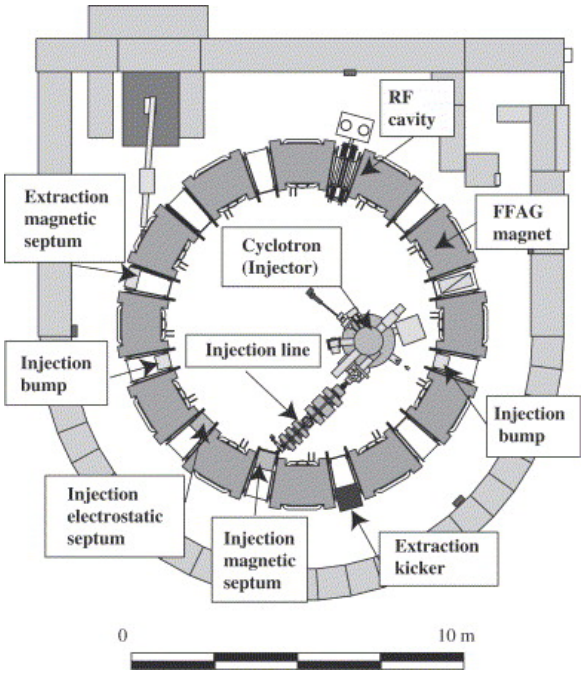

Figure 1.9: Layout of the KEK 150 MeV facility, showing the position of the RF cavity in the ring. Reproduced from [36].

the layout of an FFA including an accelerating cavity) at one or more locations around the ring. When a cavity imparts energy to the beam, this results in an effective translation of the equilibrium orbit for the beam, and this is what causes the excursion of the beam from injection to extraction.

1.6 Applications of FFAs

Fixed Field Accelerator technology is well-suited to a wide range of different use-cases, of which some examples are listed below.

The capacity for robust, reliable, and efficient operation combined with high repetition rate acceleration profiles makes FFAs a good candidate as a driver accelerator for Accelerator Driven Subcritical Reactors (ADSR) [37]. ADSR machines are a class of nuclear reactor which is operated below the critical limit for a self-sustaining nuclear chain reaction; the reaction is instead sustained by externally-produced neutrons originating from the impingement of a proton beam on a target. The most immediately obvious advantage

of such a machine would be superior safety characteristics in comparison to conventional reactor types, as failures would not be able to result in uncontrolled criticality incidents. However, this is not the only application of the ADS technology: ADSR reactors would be capable of transmuting (and use as fuel) minor actinide and long-lived fission products found in nuclear waste from conventional reactors, giving a safe and effective way to reduce the negative impacts associated with nuclear power.

An accelerator designed for the operation of this type of reactor needs to be able to continuously provide a beam with minimal downtime and maximum power efficiency (in order to optimise the facility's power output), rendering an FFA an ideal choice as a candidate proton driver for ADSR facilities. This synergy was tested with experiments at the Kyoto University Critical Assembly [38], a research reactor which was driven by the KURNS main ring FFA [39].

The ability for high repetition rate operation, in combination with the delivery of arbitrary pulse structures, would also be a key advantage for a future neutron spallation source such as ISIS 2 [40]. Spallation sources accelerate a high-intensity proton beam to an energy on the GeV scale before colliding the beam with a target. This causes the excitation of nuclei in the target, promoting the ejection of neutrons, which are directed towards experiment stations. Here, the neutron pulses are used in techniques such as neutron diffraction for imaging atomic and magnetic structure (which has applications across a variety of fields, from materials science to biomedical research). The ISIS facility [41] additionally has the ability to produce muon beams (via the impact of the proton beam on a graphite target, causing the production of pions which decay to muons).

An FFA in this context gives the potential for operation at a similar repetition rate to the Rapid Cycling Synchrotron (RCS) spallation facilities currently in operation [41, 42], but with enhanced power efficiency (due to reduction in eddy current losses during ramping of magnets, and the possibility to operate entirely with superconducting magnets). At the same time, intensity limits that affect synchrotrons of comparable injection energies can be

surpassed via the use of the beam stacking technique discussed previously. Additionally, flexibility in pulse structure would grant increased versatility in meeting the demand of users at the facility.

Removing the constraint of keeping acceleration in line with the ramp rates of magnets also enables more rapid acceleration to high energies than might be achieved with conventional synchrotrons. Acceleration to top energy within a minimal time interval is a critical requirement for the acceleration of short-lived particles, such as muons, which have a lifetime of 2.2μs [43] in their rest frame. The ability to rapidly accelerate muons would render feasible the construction of a muon collider for high energy physics. The choice to accelerate muons over electrons gives a means to circumvent the energy limits faced by circular electron colliders (imposed by synchrotron radiation [44]), whilst avoiding the disadvantages associated with colliding hadrons (which are compound particles, leading to a smaller fraction of the total energy being available to each parton in a collision, and introducing additional uncertainties into collisions due to the momentum distribution of partons within the proton). As such, a muon collider is a promising candidate for a future energy-frontier physics experiment, and the application of FFA technology in this context would serve to facilitate rapid muon acceleration with a high survival rate to collision energy. The potential power savings of an FFA over an equivalent pulsed-magnet design are also a key advantage for this application.

An additional potential application for FFA technology is in the medical field, where accelerators (often cyclotrons) are used for the treatment of tumours in hadron therapy [45]. Here, cheap operating costs and high reliability are critical to maximising patient throughput and positive treatment outcomes. FFAs have the potential to deliver this type of performance for proton and ion therapy in applications currently served by synchrotrons [46] where a range of different treatment energies are desired (without the use of the energy degraders typically required to vary the energy of the output beam in cyclotrons [47]).

The application of FFA technology to this use case has been explored in design studies

including the RACCAM project [48], which proposed a spiral-sector scaling FFA with variable extraction energy for proton therapy, and the PAMELA collaboration [49], which explored the use of a non-scaling FFA ring for charged particle therapy. Recent studies have also revealed the prospect of more effective cancer treatment with high-intensity dose delivery, which has been named FLASH therapy [50]. FFAs would be able to access these intensity regimes, enabling further clinical testing of this effect and, ultimately, treatments using FLASH dose rates, pending positive results from clinical trials.

Moreover, FFA principles may be applied to beam transport and delivery systems to facilitate transport of multiple energies without alteration of magnet settings, enabling rapid energy switching and thereby facilitating more advanced treatment and increasing patient throughput [47].

1.7 Thesis Outline

The structure of this thesis is as follows.

Chapter 2 discusses methods of determining analytically appropriate reference orbits for both hFFAs and, for the first time, vFFAs, together with the limitations of these methods. In Chapter 3, the Hamiltonian formalism is used to derive linear transfer maps for accelerator elements in both types of machines. These are then used in combination with the orbit models from Chapter 2 to develop complete optical models of h- and vFFAs. Lastly, Chapter 3 also contains a short discussion of the regions in which the assumptions used to derive the analytic models break down, and introduces a numerical method, 'Harmonic Analysis' for studying the optics of vFFAs in these cases.

Chapter 4 is concerned primarily with nonlinear effects in hFFAs, examining the sources of tune shift using the harmonic analysis methodology, and employing simulations to check this work. This chapter additionally contains experimental methods and data analysis for an experiment used to achieve the first measurements of amplitude-dependent tune shifts in a radial-sector DFD triplet hFFA, which confirms the findings of the harmonic analysis and

computational studies. The harmonic analysis technique is then applied to a novel lattice and used to probe the effects of spiral angle on amplitude-dependent tune shift in hFFAs.

Lastly, Chapter 5 uses the analytic model of the vFFA to examine in detail one possible use-case for the vFFA technology in the context of a muon collider complex. The analytic model is first used to give insight into optimisational procedures given an existing lattice as a starting point, and then employed to design new lattices to target different sets of parameters.

Conclusions and recommendations for further work are summarised in Chapter 6.

Chapter 2

Closed Orbits in Fixed Field Accelerators

The development of new particle accelerators depends on our ability to predict their behaviour prior to construction. Resources may only be invested into the construction of a machine given that we are able to predict its eventual performance, and that we are certain that it will behave as expected and produce results for the end user. To this end, a number of tools are employed, from the linear optics formalisms developed by Courant and Snyder [51] to modern numerical optimisation routines and particle tracking codes. Whilst the latter may offer the most complete picture of the behaviour of a beam given a specified arrangement of magnets, each configuration must be evaluated separately, which is computationally intensive and time-consuming, ultimately offering limited understanding of the effect of varying any individual parameter on the machine's behaviour. This point is once again critical when it comes to the operation of a machine following its construction: an operator must understand the effect of each input on the beam, and which to change to achieve the desired effect. The existence of a refined model and a detailed understanding therefrom, then, is crucial to the implementation and operation of any accelerator type. These models are especially important for scaling FFAs, where all orders of the magnetic field are dictated by scaling laws, causing an complex interdependence of orbit and optics parameters. Of particular importance is the development of modelling techniques for the vFFA.

Modelling of particle accelerators first requires the determination of an appropriate reference orbit. In synchrotrons and linear accelerators (linacs), typically a desired trajectory is determined, dipole elements are placed to achieve this trajectory, and focussing elements (quadrupoles and higher order correctors) are then positioned about this specified orbit. For periodic lattices, it is a requirement that this trajectory be a closed orbit - i.e. that the trajectory returns to an identical position in terms of the local coordinate system after one cell. In contrast to synchrotrons and linacs, modelling of an FFA is complicated by the requirement that the accelerator must support a continuum of closed orbits as a function of energy, and that each closed orbit must be determined by the configuration of the lattice - the closed orbit cannot be set a priori. This chapter explores methods of determining closed orbits in FFA-type machines, deriving analytic results for a number of different lattice geometries, and benchmarking these against results from numerical simulations.

These models offer insight into the behaviour of the FFA system, compared to the more 'black-box' approaches of numerical simulation; an analytic solution for the closed orbit system reveals precisely how a desired variable (e.g. on-beam magnetic field strength) may be affected by changing a given set of input parameters. Moreover, establishing a lattice with a closed orbit at a new point in parameter space can be challenging in a pure numerical approach, particularly with a complicated multidimensional parameter space such as that required for the vFFA; the derivation of an analytic model solves this issue, and can be used to inform numerical simulations when more detail is required than the analytic model can provide in itself. Numerical simulations are also computationally intensive, and require many CPU-hours to completely explore a parameter space. By contrast, the analytic models developed here provide solutions for a given input effectively instantaneously, and are well-suited to the exploration of multidimensional parameter spaces. However, analytic models of closed orbits need to rely on a number of approximations to allow for exact solutions, and to verify the models' accuracy it is necessary to test their predictions against numerical tracking models in which these approximations have been relaxed.

This chapter reviews approaches to determining closed orbits in hFFA FODO and triplet rings, and derives for the first time equivalent solutions for vFFA lattices based on a straight-line FODO geometry as well as triplet and FODO ring geometries. Results from each model are then tested for a range of inputs, and compared with equivalent numerical simulations, to understand the behaviour and limitations of these closed orbit models. The effect of fringe fields on closed orbits in vFFA lattices is then discussed in more detail at the end of the chapter.

2.1 Closed orbits in hFFA FODO Lattices

A FODO lattice is here defined as a lattice with two elements per cell - one horizontal focussing (normal bend) element and one horizontal defocussing (reverse bend) element. The midpoints of these are spaced evenly (such that, if the cell is defined from the midpoint of the F-magnet, the centre of the cell is the midpoint of the D-magnet, and the cell is symmetric about this point). A half cell (i.e. from the midpoint of the F-magnet to the midpoint of the D-magnet) of an hFFA FODO lattice is shown in Fig. 2.1.

2.1.1 Analytic model

As a first step towards the lattice design of an hFFA, we begin by developing an analytic model for a closed orbit based on a number of assumptions: firstly, that the field is zero outside of the magnets (i.e. fringe fields can be neglected); secondly that the field is constant along the closed orbit trajectory within the magnets; and lastly that the closed orbit lies on the horizontal magnet midplane (given that there is zero horizontal field on the midplane). Under these approximations, a 2D closed orbit model can be constructed from circular arcs of constant radius and straight lines joining these arcs (Fig. 2.1) [52].

The geometry of the system is then parameterised in terms of the number of cells in the ring (N), the opening angle of the F and D magnets from the machine centre (respectively β_F and β_D), the radius of the orbit at the centre of the F-magnet (r_0), and the bending

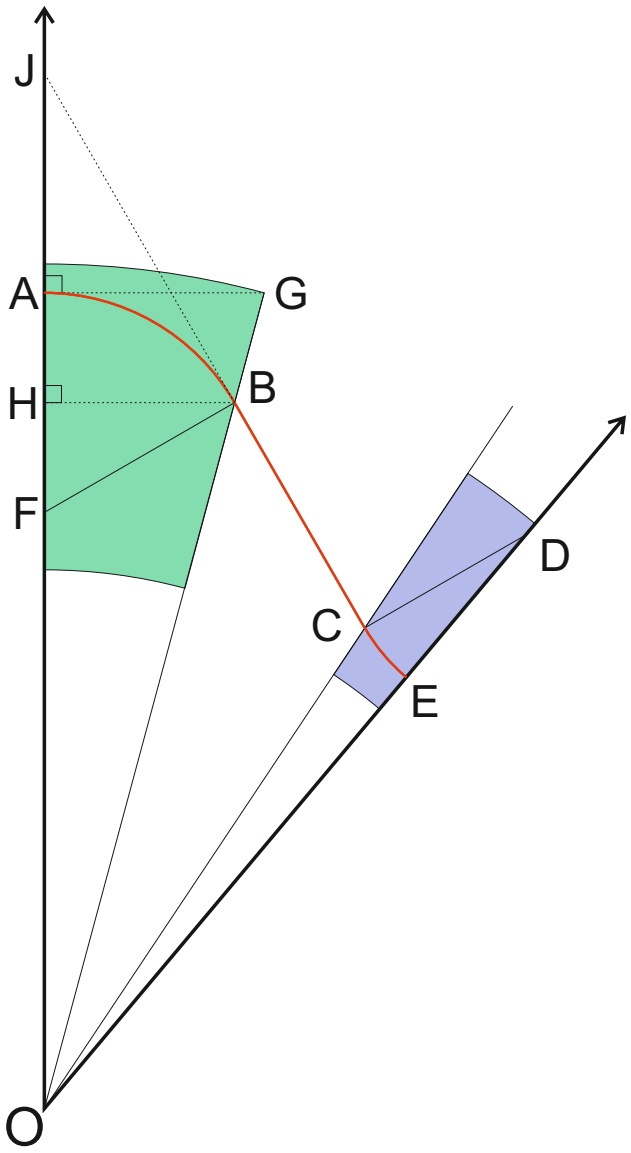

Figure 2.1: 2D geometry of a closed orbit (red) through a half-cell of an hFFA FODO lattice, beginning at the midpoint of the F-magnet and finishing at the midpoint of the D-magnet. The diagram shows the projection on the horizontal plane, with O denoting the machine centre, and the green and blue shaded regions depicting the horizontal F and D magnets respectively. The geometry is symmetric about the centre of the F and D magnets, so the properties of the half-cell completely determine the geometry of the whole cell.

Parameter	Definition
β_F	$\angle AOB$
β_D	$\angle COE$
$\frac{\pi}{N}$	$\angle AOE$
r_0	$\overline{OA}$
θ_F	$\angle AFB$
Variable	**Definition**
θ_D	$\angle CDE$
ρ_F	$\overline{AF} = \overline{BF}$
ρ_D	$\overline{CD} = \overline{ED}$
r_1	$\overline{OB}$
r_2	$\overline{OC}$
r_3	$\overline{OE}$
L_s	$\overline{BC}$

Table 2.1: Definitions of all input parameters and output variables that completely specify the geometry of an hFFA FODO closed orbit in terms of Fig. 2.1. Note that whilst the figure depicts radial sector magnets, the properties of the closed orbit geometry, and the definitions above are identical for spiral sector magnets.

angle in the F-magnet (θ_F). These parameters uniquely determine the geometry of the closed orbit. There are a number of remaining variables in the geometry that set important lattice properties, and these can be evaluated as a function of the input parameters: the bending angle in the D-magnet (θ_D); the radii of curvature in F and D magnets (ρ_F and ρ_D respectively); the radii of the orbit with respect to machine centre at the edge of the F magnet (r_1), edge of the D-magnet (r_2), and centre of the D-magnet (r_3); and the length of the path travelled between the two magnets, L_s. The parameters and variables listed here are defined geometrically in Fig. 2.1 and Table 2.1.

First, ρ_F can be set using the relationship

$$\rho_F \left(\sin\theta_F + [1-\cos\theta_F]\tan\beta_F\right) = \frac{r_0 \sin\beta_F}{\sin\theta_F}, \tag{2.1}$$

which is derived from computing the length $\overline{AG}$. r_1 is then determined from evaluating the length $\overline{HB}$:

$$\rho_F \sin\theta_F = r_1 \sin\beta_F. \tag{2.2}$$

r_2 can be computed by considering the length $\overline{OJ}$, leading to the relation

$$r_2 \left(\cos\left[\pi/N - \beta_D\right] + \sin\left[\pi/N - \beta_D\right]\tan\theta_F\right) = r_1 \left(\cos\beta_F + \sin\beta_F \tan\theta_F\right). \tag{2.3}$$

The normal bend of the F magnet and the reverse bend of the D magnet must sum to the total bending angle of the cell, and as a result we find

$$\theta_F - \theta_D = \frac{\pi}{N}. \tag{2.4}$$

ρ_D may then be determined from r_2, $\beta_F$and θ_D using

$$r_2 \sin\beta_D = \rho_D \sin\theta_D, \tag{2.5}$$

by analogy to Eq. (2.2). r_3 can be computed with

$$r_3 = r_2 \cos\beta_D - \rho_D(1-\cos\theta_D), \tag{2.6}$$

and finally the drift length L_s may be calculated using the equation

$$L_s = r_2 \sin(\pi/Nc - \beta_F - \beta_D)/\cos(\theta_F - \beta_F). \tag{2.7}$$

The equations above give a complete set of geometrical parameters needed to evaluate an hFFA FODO lattice.

2.1.2 Numerical Benchmarking

The analytic model relies on the set of approximations described at the beginning of the previous section, and does not fully account for every aspect of the machine that may affect the closed orbit (e.g. soft edges of magnetic fields, fringe field effects, and transverse field gradients). To check its performance, an alternative approach is needed, making use of a more complete description of the magnetic fields. This is done using the numerical integration code FIXFIELD [53], discussed in Appendix A. FIXFIELD uses a 4th order Runge-Kutta method [54, 55, 56] to track a charged particle with given momentum numerically through an arbitrary superposition of magnetic fields using a fixed step size (in this case 0.01m). To find a closed orbit for a given cell, the particle is initiated on the azimuthal cell boundary with a given set of 4D transverse coordinates (radial position, vertical position, and the corresponding momenta). Tracking is then applied until the particle encounters the opposite cell boundary, and the transverse coordinates at this point are recorded using an interpolative method. The 4D transverse displacement between initial and final coordinates is computed, and a numerical optimisation method (e.g. the Nelder-Mead simplex [57]) is used to pick a new set of initial coordinates. The process is then iterated until the displacement between initial and final coordinates is smaller than a chosen threshold value.

A model of an hFFA FODO cell is assembled in FIXFIELD according to the parameters shown in Table 2.2, which are based on the parameters of the FETS-FFA demonstrator ring [58] - in this case the azimuthal spacing of the magnets has been adjusted to match the FODO geometry (i.e. evenly spaced F- and D- magnets). The magnets are modelled with a field falloff governed by an Enge function [59], with the c_1 coefficient given in the table as

Parameter	Value
N	16
β_F	2.25°
β_D	1.15°
r_0	4m
θ_F	19°
k	8.0095
c_1	0.07m

Table 2.2: Default parameters of the example hFFA FODO lattice used to generate Fig. 2.2. The field index k and the Enge c_1 coefficient are used to inform the numerical model, and do not affect the analytic model.

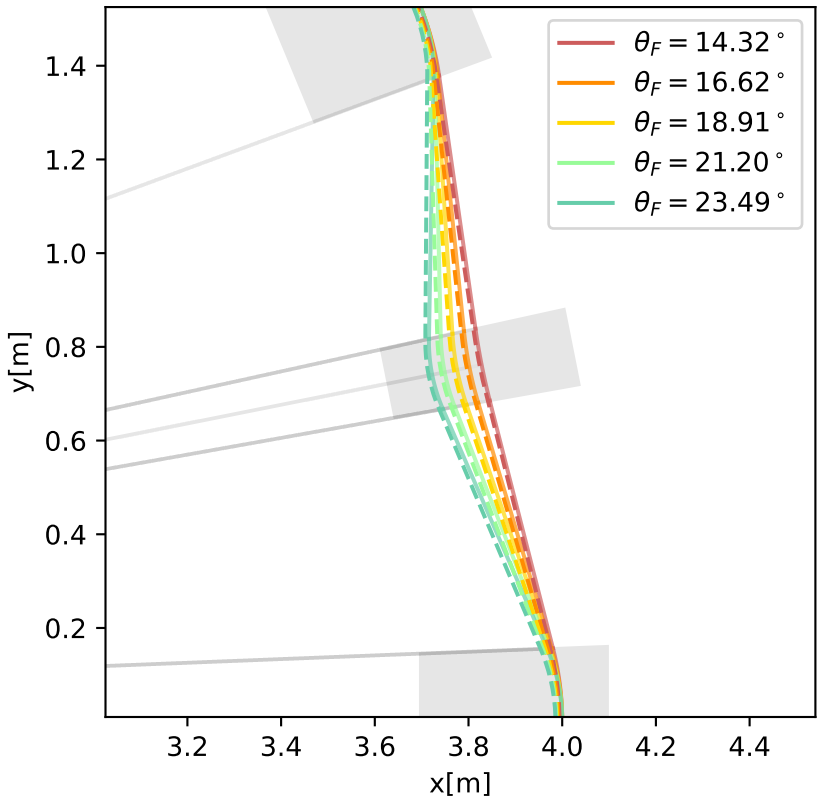

Figure 2.2: Closed orbit for a range of different θ_F values in an example hFFA FODO lattice; solid lines show the analytic prediction of the closed orbit, whilst the dashed lines represent the closed orbit from the numerical evaluation. The grey shaded regions show the positions of the F and D magnets, and the grey lines indicate the position of the origin. θ_F is varied whilst all other parameters are kept at the nominal values described in Table 2.2.

an effective fringe field length. The fields of the two magnets in FIXFIELD are computed from the bending radii of the F and D magnets, accounting for the magnetic rigidity of the test particle (see Eq. (1.4)). Figure 2.2 shows the effect of changing the bending angle of the F-magnet on the closed orbit in both analytic and numerical models. As θ_F increases, the difference between r_0 and r_1 increases. Consequently, the field gradient of the magnet begins to have a greater effect, weakening the approximation of a constant radius arc of circle. Figure 2.3 shows a comparison between the vertical dipole field in the analytic model and the numerical simulation, showing an increased azimuthal variation in field strength over the length of the magnet as θ_F is increased. This causes a discrepancy between the dipole components of the two models that grows with θ_F, leading to a proportional increase in the difference between the analytic and numerically simulated closed orbits (Fig. 2.4). Nonetheless, for the range of values tested, the difference between the analytic prediction and the numerical simulation remains small, with a maximum radial difference between the two models of 0.02% (recorded at the centre of the D-magnet).

2.2 Closed orbits in hFFA triplet Lattices

A triplet lattice is defined as a lattice with three magnets per cell - two identical magnets symmetrically positioned about a magnet of opposite polarity (Fig. 2.5). As such, the cell can be configured as either an DFD or FDF triplet, depending on whether the central magnet is a normal or reverse bend magnet; whilst the diagram and the equations that follow are defined in terms of a DFD configuration, exchanging the sign of θ_F and making some corresponding sign changes in the following equations makes it possible to switch to an FDF configuration. This chapter considers only the case where the internal drift length between the external magnets and the central magnet is small compared to the lengths of the magnets and the external drift.

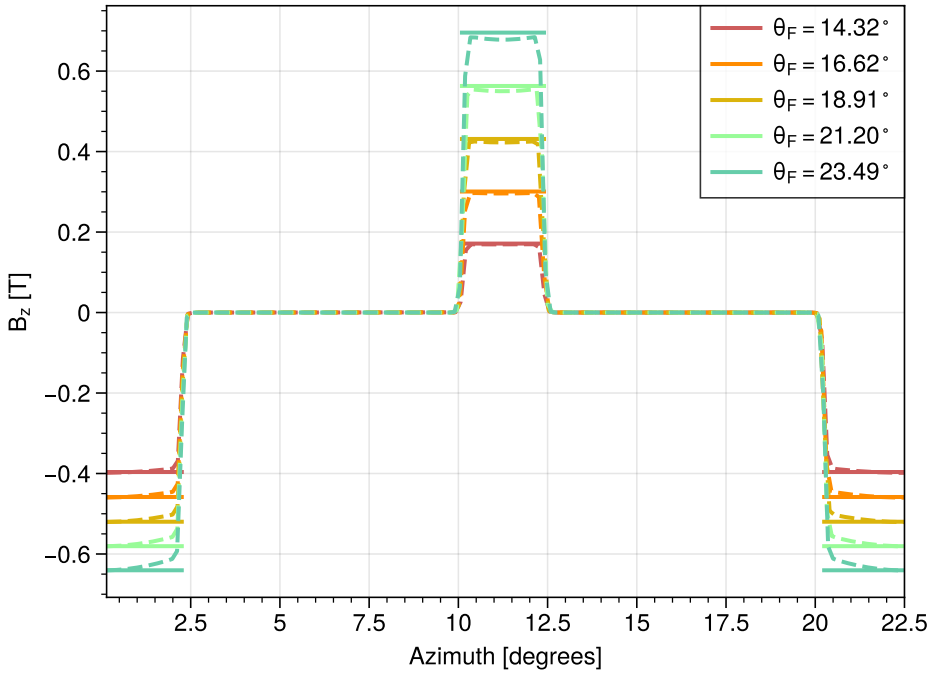

Figure 2.3: Vertical magnetic field B_z on the closed orbit for the example hFFA FODO lattice; solid lines show the analytic value, whilst the dashed lines represent the field measured in the numerical simulation.

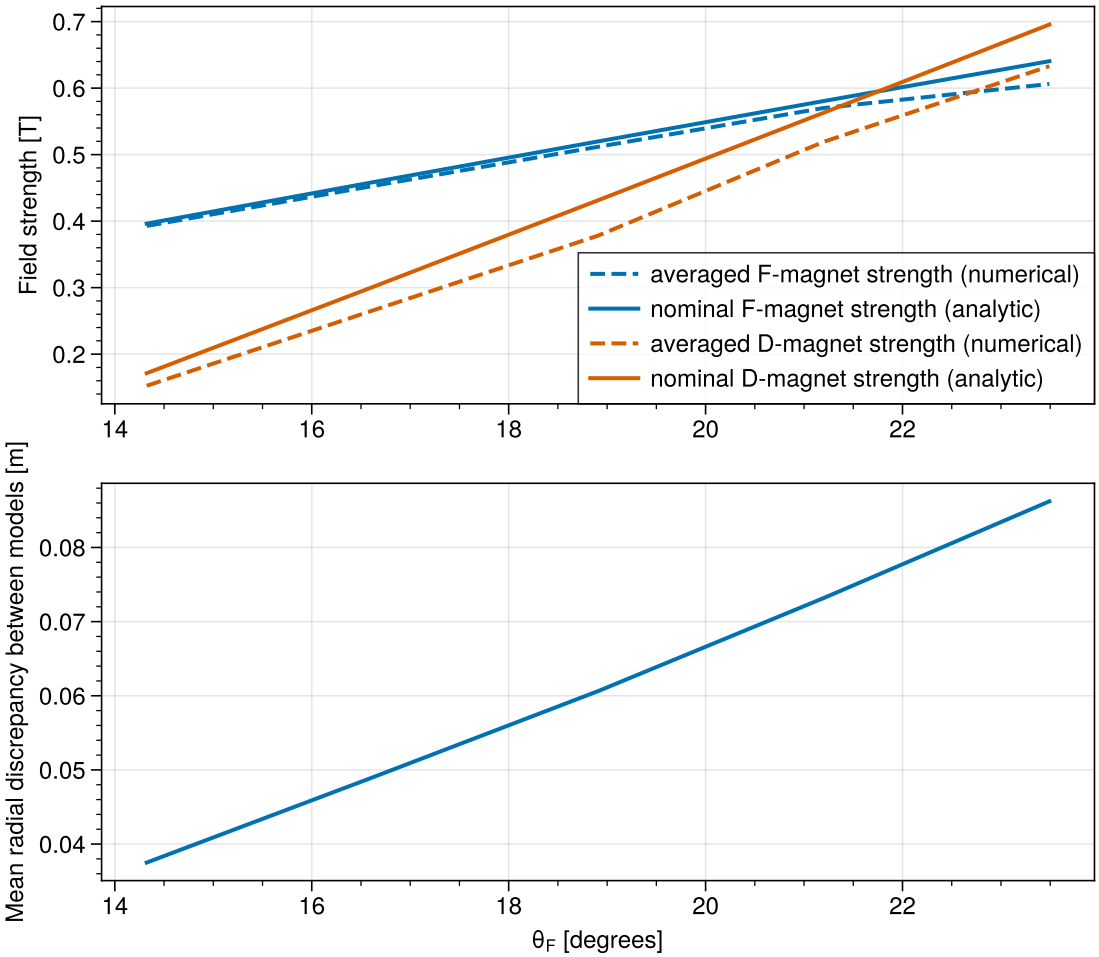

Figure 2.4: The first subplot displays the vertical B field in the F- and D-magnets of the example hFFA FODO lattice as θ_F is varied, with the solid lines displaying the value predicted by the analytic model, and the dotted line corresponding to a value measured from the numerical simulation averaged over the length of the magnet (to account for the azimuthal variation. The lower subplot displays the mean displacement of the analytic closed orbit from the numerical closed orbit as a function of θ_F.

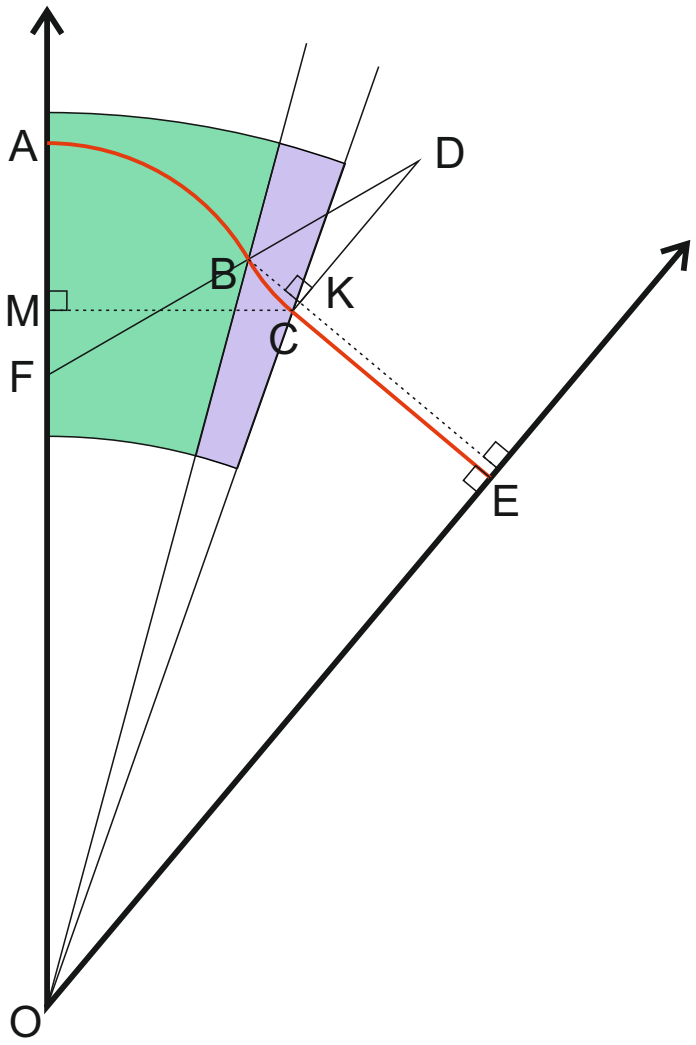

Figure 2.5: 2D geometry of a closed orbit (red) through a half-cell of an hFFA triplet lattice, beginning at the midpoint of the F-magnet and finishing at the midpoint of the drift. The diagram shows the projection on the horizontal plane, with O denoting the machine centre, and the green and blue shaded regions depicting the horizontal F and D magnets respectively. The geometry is symmetric about the centre of the F magnet and about the centre of the drift, so the properties of the half-cell completely determine the geometry of the whole cell.

Parameter	Definition
β_F	$\angle AOB$
β_D	$\angle BOC$
$\frac{\pi}{N}$	$\angle AOE$
r_0	$\overline{OA}$
θ_F	$\angle AFB$
Variable	**Definition**
θ_D	$\angle BDC$
ρ_F	$\overline{AF} = \overline{BF}$
ρ_D	$\overline{BD} = \overline{CD}$
r_1	$\overline{OB}$
r_2	$\overline{OC}$
r_3	$\overline{OE}$
L_s	$\overline{CE}$

Table 2.3: Definitions of all input parameters and output variables that completely specify the geometry of an hFFA triplet closed orbit in terms of Fig. 2.5. As in the previous section the figure depicts radial sector magnets, though the properties of the closed orbit geometry, and the definitions above are identical for spiral sector magnets.

2.2.1 Analytic model

Applying the same approximations used in Section 2.1.1, it is possible to construct a model of the geometry of the closed orbit through an hFFA triplet lattice. The input parameters and output variables are defined in Table 2.3. Many of the constraints in Section 2.1.1 remain the same: Eq. (2.1-2.4) can be used to determine ρ_F, r_1, and θ_D respectively. Then, ρ_D can be computed from known parameters by evaluating the length $\overline{BK}$ (Fig. 2.5):

$$\begin{aligned}\rho_D \left(\sin\left(\theta_F - \pi/N\right) - \left(1 - \cos(\theta_D)\right)\tan\left(\pi/N - \beta_F - \beta_D\right)\right) = \\ r_1 \left(\sin(\pi/N - \beta_F) - \cos(\pi/N - \beta_F)\tan(\pi/N - \beta_F - \beta_D)\right).\end{aligned} \tag{2.8}$$

Next, deriving an expression for the length $\overline{OM}$ enables r_2 to be calculated:

$$r_2\cos(\beta_F + \beta_D) = (r_1\cos(\beta_F) - \rho_D\sin(\theta_D)\sin(\pi/N) - \rho_D(1 - \cos(\theta_D))\cos(\pi/N)), \tag{2.9}$$

and r_3 can then be found through simple trigonometry as

$$r_3 = r_2\cos(\pi/N - \beta_F - \beta_D). \tag{2.10}$$

Lastly, the drift length is simply given by

$$L_s = r_2\sin(\pi/N - \beta_F - \beta_D). \tag{2.11}$$

2.2.2 Numerical Benchmarking

A simulated model of a triplet lattice is generated based on magnet positions and magnetic fields computed from the results of the analytic model (with input parameters listed in Table 2.4).

Figure 2.6 shows closed orbits through a number of different triplet lattices with different θ_F. It is evident here that the error is more sensitive to the value of θ_F than in the previously simulated FODO case. This is due to the short length of the D-magnet for this lattice causing fringe-field effects to become more dominant - as the D-magnet is 32cm in length at the reference radius r_0, and the characteristic length of the fringe fields on each

Parameter	Value
N	12
β_F	5.40°
β_D	3.43°
r_0	5.4m
θ_F	45°
k	7.6
c_1	0.07m

Table 2.4: Default parameters of the example hFFA triplet lattice used to generate Fig. 2.6. These parameters are based on the DFD triplet lattice operated at the Institute for Integrated Radiation and Nuclear Science (KURNS) [39]. The field index k and the Enge c_1 coefficient are used to inform the numerical model, and do not affect the analytic model.

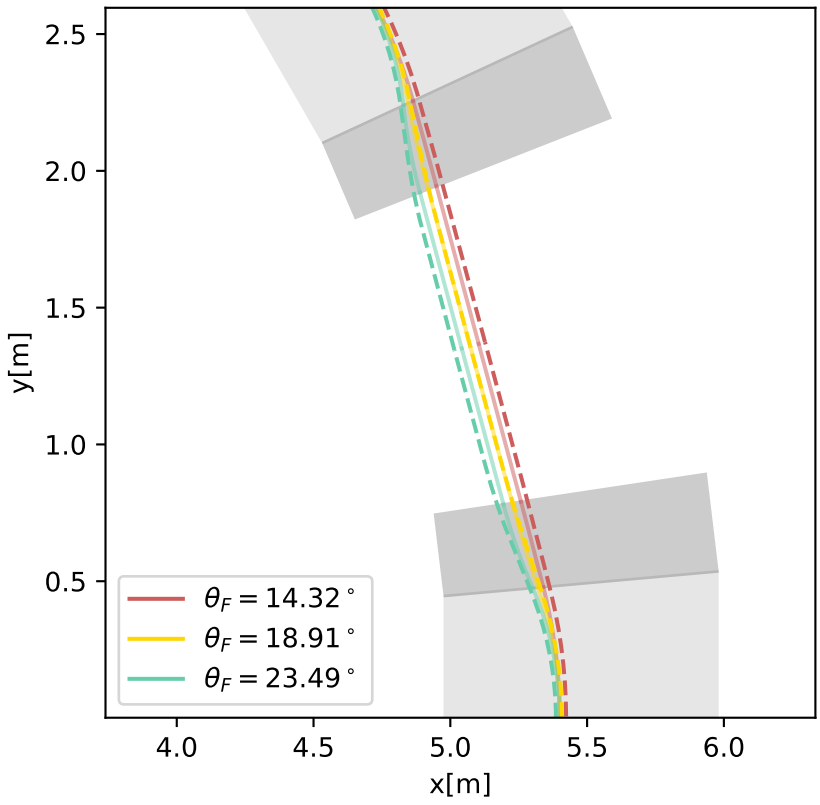

Figure 2.6: Closed orbit for a range of different θ_F values in an example triplet lattice based on the parameters of the KURNS FFA ring; solid lines show the analytic prediction of the closed orbit, whilst the dashed lines represent the closed orbit from the numerical evaluation. The light grey shaded region shows the position of the F magnet, whilst the D magnet is shown in dark grey. θ_F is varied whilst all other parameters are kept at the nominal values described in Table 2.4.

end is 7cm, this means that there is a large degree of variation from the nominal constant dipole field over the length of the magnet.

In this section we have shown that, for the hFFA, the use of an analytic model based on the geometry of the accelerator enables the determination of the closed orbit from input parameters; the same input parameters can be used in numerical simulations to obtain closed orbits that closely follow the predictions of the analytic model, even when factors such as fringe field effects and magnet gradients are considered.

2.3 Closed orbits in vFFA FODO Lattices

Whilst analytic models for hFFA design and operation have existed for a number of years, modelling of the vFFA closed orbit so far has relied entirely on computational studies using tracking codes. The practicality of the vFFA as a feasible machine for real-world applications depends on the ability to make ready estimates of beam behaviour. Operation of a machine requires knowledge of its response to changes in input, and having an online model available for use in a control room can be of vital importance in achieving operational goals. An analytical model also gives a sense of intuitive understanding of the behaviour of such a machine, which at present is a disadvantage of the concept compared to existing synchrotrons, cyclotrons or even hFFAs - despite the potential advantages (as discussed in Chapter 1).

As for the hFFA, a FODO cell is defined as a two element cell with evenly spaced normal bend and reverse bend magnets. Figure 2.8 illustrates the geometry of an example vFFA FODO half cell. Importantly, the closed orbit here can exhibit curvature both horizontally and vertically, a phenomenon first studied using numerical integration codes [32]. Understanding the properties of this nonplanar orbit is critical to correctly modelling the dynamics of the vFFA machine.

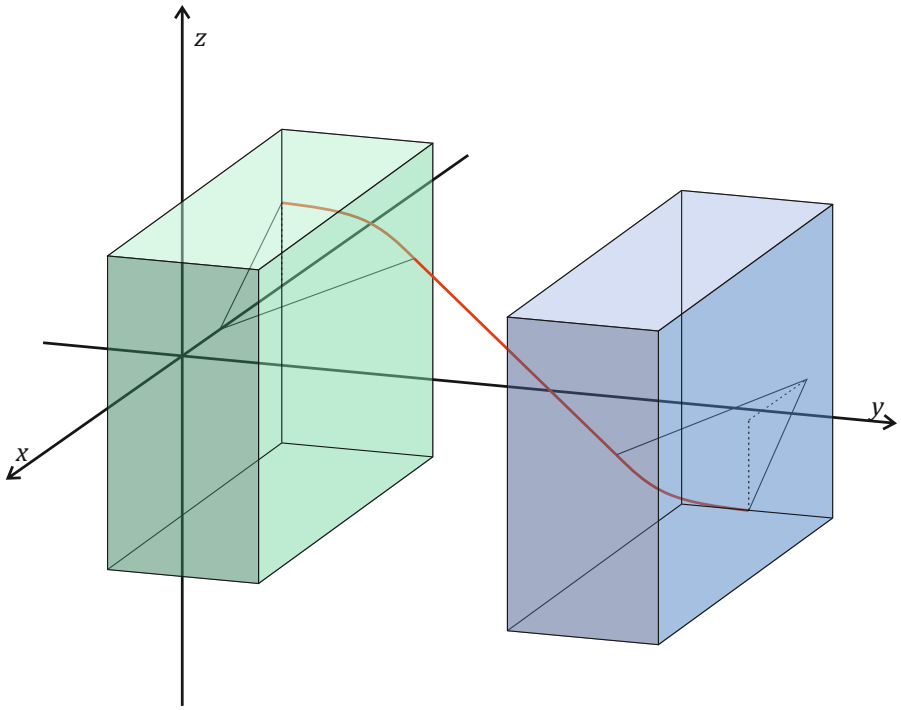

Figure 2.7: Closed orbit of a straight vFFA FODO half cell (i.e. zero net bending angle). The closed orbit is shown in red, whilst the F-magnet and D-magnet are drawn in green and blue respectively. z denotes the vertical axis, x the horizontal, and y the longitudinal.

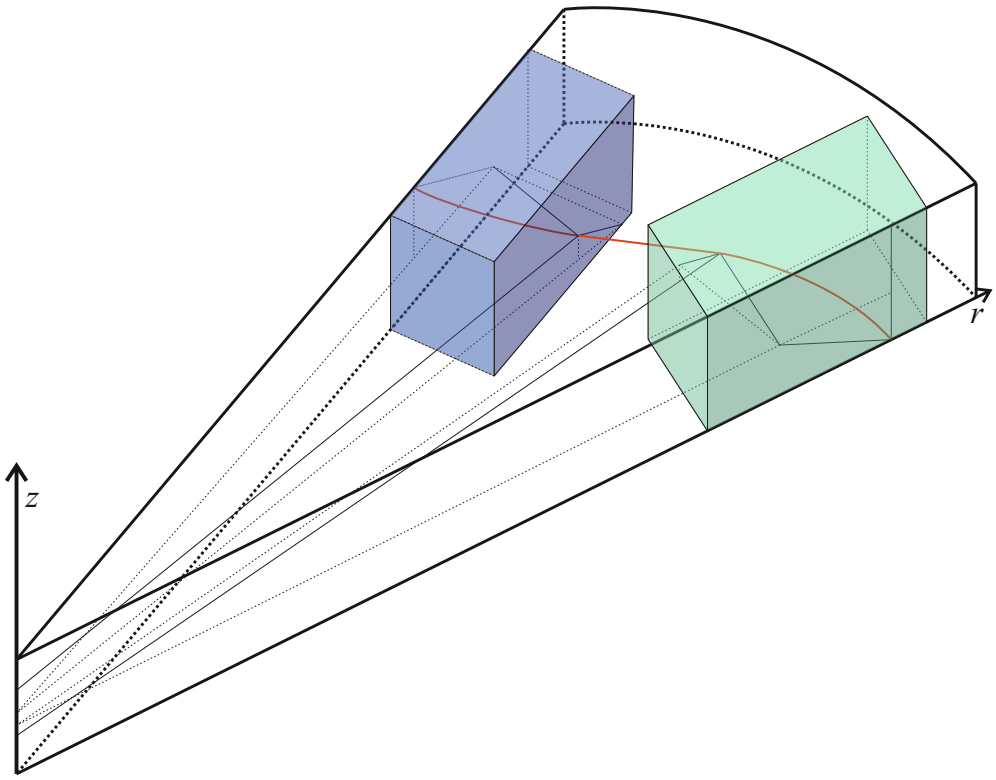

Figure 2.8: Closed orbit of a vFFA FODO half-cell with a nonzero net bending angle. The closed orbit is shown in red, whilst the F-magnet and D-magnet are drawn in green and blue respectively. The z-axis is positioned at the machine centre, and r is the radial direction.

2.3.1 Analytic model

To develop a model of closed orbit behaviour in the vFFA, it is first necessary to come up with a set of approximations that simplify the system, and a set of constraints that, together with the approximations, enable a complete description of the system. For the hFFA it was seen that the geometry could be parameterised in terms of circular arcs and straight line segments under a small set of specific approximations. As a first-pass analytic approach to the vFFA, the same approach is possible, beginning from a similar set of assumptions. First, it is assumed that outside of the magnet boundaries the field is zero, and the closed orbit is straight. Second, it is assumed that the magnetic field is constant along the orbit inside the magnets; hence, the orbit follows a plane circular arc within the magnet. In contrast to the hFFA, tracking studies [32] have shown that the orbit cannot be assumed to lie in the horizontal plane; instead, different constraints must be imposed.

From symmetry, the orbit must be perpendicular to the boundaries of the half-cell (Figs. 2.7 and 2.8) when it crosses these points. The boundaries exist within the magnets, and hence the orbit at the boundary must exist as a section of a plane circular arc. To achieve a vertical deviation of the orbit that matches the behaviour observed in tracking, the planes of curvature must be transformed such that they are no longer purely coplanar with the horizontal plane. The only valid transformations that preserve the perpendicularity constraint at the boundary are rotations of the plane of curvature about an axis perpendicular to the cell boundary; the angle of this transformation, or the *inclination*, is denoted γ. This can be seen in its simplest case in Fig. 2.9, which illustrates a cell of a straight-line vFFA FODO lattice: in this case, the inclination angles for each magnet are defined as $\angle AFB$ and $\angle HDE$ respectively. Inclination is specific to each magnet, and may not necessarily be the same between different magnets in the same lattice.

It is important to relate this geometry to the magnetic fields of the vFFA, and thereby to justify the approach of approximating the orbit as an inclined planar arc. Maintaining the assumption that the field is constant over the length of the magnet, and using a set

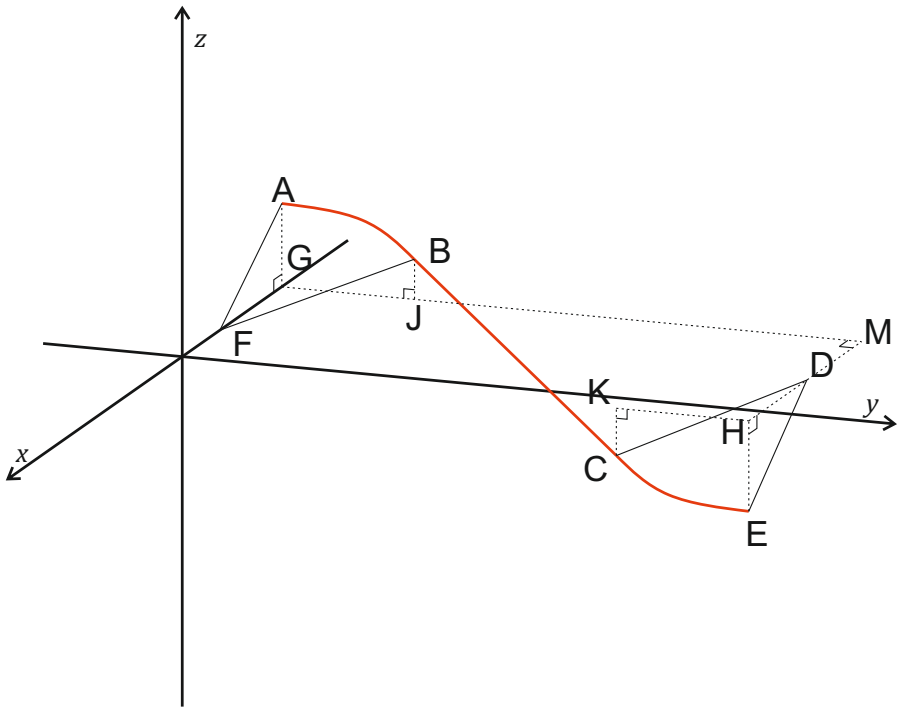

Figure 2.9: 3D geometry of a closed orbit through a half-cell of a vFFA FODO lattice with zero net bending, beginning at the midpoint of the F-magnet and finishing at the midpoint of the D-magnet.

Parameter	Definition	Variable	Definition
L_F	$\overline{GJ}$	θ_D	$\angle CDE$
L_D	$\overline{KH}$	ρ_F	$\overline{AF} = \overline{BF}$
L_c	$\overline{GM}$	ρ_D	$\overline{CD} = \overline{ED}$
θ_F	$\angle AFB$	L_s	$\overline{BC}$
γ_F	$\angle AFG$	γ_D	$\angle HDE$

Table 2.5: Definitions of all input parameters and output variables that completely specify the geometry of closed orbit through a vFFA FODO lattice with zero bending angle per cell. Definitions are given in terms of Fig. 2.9.

of Cartesian coordinates X, Y, Z to describe position relative to the axis of the magnet (Y representing the longitudinal coordinate, X representing horizontal with the midplane positioned at $X = 0$, and Z being the vertical axis), we express the fields within the magnet as follows:

$$\begin{aligned} B_X &= B_0 e^{mZ} f(X), \\ B_Y &= B_0 e^{mZ} g(X), \\ B_Z &= B_0 e^{mZ} h(X), \end{aligned} \tag{2.12}$$

where $f(X), g(X)$, and $h(X)$ are functions to be determined. Note that within the magnet body, the assumption is made that the field does not depend on the longitudinal coordinate Y.

Writing Maxwell's equation $\nabla \times \mathbf{B} = \mathbf{0}$ out in terms of its Cartesian components, we obtain

$$\begin{aligned} \frac{\partial B_Z}{\partial Y} - \frac{\partial B_Y}{\partial Z} &= 0, \\ \frac{\partial B_X}{\partial Z} - \frac{\partial B_Z}{\partial X} &= 0, \\ \frac{\partial B_Y}{\partial X} - \frac{\partial B_X}{\partial Y} &= 0, \end{aligned} \tag{2.13}$$

into which we substitute our ansatz for the fields (Eq. (2.12)) to give

$$\begin{aligned} 0 - \frac{\partial B_Y}{\partial Z} &= 0, \\ m e^{mZ} f(X) - e^{mZ} \frac{dh(X)}{dX} &= 0, \\ \frac{\partial B_Y}{\partial X} - 0 &= 0. \end{aligned} \tag{2.14}$$

It can be seen here that B_Y must be zero as a consequence of the field being constant with respect to the longitudinal coordinate. Equation (2.14) requires that

$$\frac{dh(X)}{dX} = m f(X) \tag{2.15}$$

Taking Maxwell's equation for the divergence of the magnetic field $\nabla \cdot B = 0$, and writing it once again in terms of its Cartesian components,

$$\frac{\partial B_X}{\partial X} + \frac{\partial B_Y}{\partial Y} + \frac{\partial B_Z}{\partial Z} = 0 \tag{2.16}$$

gives the constraint

$$\frac{df\left(X\right)}{dX} = -mh\left(X\right) \tag{2.17}$$

Combining Eq. (2.15) and Eq. (2.17), we find that $h\left(X\right)$ must take the form $C\cos mX + D\sin mX$, where C and D are constants to be found from boundary conditions (likewise, $f\left(X\right)$ is expressed as $C\sin mX + D\cos mX$). Defining the vFFA magnet midplane at $X = 0$ as the plane in which the horizontal field is zero and the vertical field is at its maximum, C and D are fixed at 1 and 0 respectively, and therefore the fields within the magnet body can be written as follows:

$$\begin{aligned} B_X &= -B_0 e^{mZ}\sin mX, \\ B_Y &= 0, \\ B_Z &= B_0 e^{mZ}\cos mX. \end{aligned} \tag{2.18}$$

From the Lorentz force (Eq. (1.1)), the plane of curvature of the orbit must be perpendicular to the magnetic field. This means that the inclination angle γ of the plane of curvature with respect to the horizontal plane is equal to the angle between the total magnetic field and the vertical unit vector $\hat{\mathbf{Z}}$:

$$\frac{\mathbf{B}\cdot\hat{\mathbf{Z}}}{|\mathbf{B}|} = \cos\gamma. \tag{2.19}$$

Substitution of Eq. (2.18) gives

$$\cos\gamma = \cos mX, \tag{2.20}$$

and hence the inclination can be equated to the horizontal offset of the closed orbit from the vertical magnet midplane multiplied by the normalised field gradient m.

The simultaneous horizontal and vertical variation of orbit position in the vFFA can seem non-intuitive at first, but with a simple assumption (a constant dipole field within the magnet) and the constraint of perpendicularity to the boundary of the half-cell, we have now shown how it can be explained as a consequence of the horizontal displacement of the closed orbit from the magnet midplane. This displacement results in a rotation of the plane of curvature through an angle proportional to the value of the displacement and the

normalised field gradient m. With this knowledge in place, the closed orbit for a vFFA FODO lattice can be constructed.

2.3.1.1 Straight line solution

As a simple first exercise, a model of a vFFA lattice is constructed with a total bending angle per cell of zero (Fig. 2.9, Table 2.5) - i.e. a 'straight' vFFA beamline. The lattice is specified in terms of the length of the cell L_c, the length of each magnet, L_F and L_D, the bending angle in the F-magnet, θ_F, and the inclination angle in the F-magnet γ_F. The bending radii in each magnet (ρ_F, ρ_D), the bending and inclination angles in the D-magnet (θ_D, γ_D), and the length of the drift (L_S) must then be determined from geometric constraints. For the horizontal and vertical components of the bending in each magnet to cancel each other, this implies that

$$\gamma_F = \gamma_D. \tag{2.21}$$

This means that the closed orbit can be expressed in a single plane, and therefore we also find that

$$\theta_F = \theta_D. \tag{2.22}$$

Radii of curvature are then expressed in terms of the lengths of the magnets:

$$L_F = \rho_F \sin\theta_F, \tag{2.23}$$

$$L_D = \rho_D \sin\theta_D, \tag{2.24}$$

and then the length of the drift is simply given by

$$L_S = \frac{(L_c - L_F - L_D)}{\cos\theta_F}. \tag{2.25}$$

This completely parametrises the geometry of the simplest possible vFFA configuration. As Eq. (2.21) shows that the inclination in each magnet is equal, the orbit solution here describes planar motion in a plane rotated at angle γ_F with respect to the horizontal. In the limiting case that $\gamma_F = 90°$, the motion is purely vertical. Comparing this limit to

Parameter	Definition
β_F	$\angle SO_3P$
β_D	$\angle DO_2F$
$\frac{\pi}{N}$	$\angle AO_0B$
r_0	$\overline{O_5K}$
θ_F	$\angle HJK$
γ_F	$\angle SJK$

Variable	Definition
θ_D	$\angle CDE$
ρ_F	$\overline{HJ} = \overline{JK}$
ρ_D	$\overline{CD} = \overline{ED}$
r_1	$\overline{O_4H}$
r_2	$\overline{O_1E}$
r_3	$\overline{O_0C}$
L_s	$\overline{EH}$
γ_D	$\angle CDM$

Table 2.6: Definitions of all input parameters and output variables that completely specify the geometry of a vFFA FODO closed orbit in terms of Fig. 2.10.

the straight-line hFFA closed orbit solution [60], which describes purely horizontal motion with an associated exponential scaling law for the horizontal plane ($B(X) = B_0e^{mx}$), we can recognise that these systems are identical aside from a 90° rotation of the coordinate system. That is to say, the closed orbit behaviour of a straight vFFA beamline with an inclination of 90° is equivalent to that of a straight hFFA beamline rotated about its longitudinal axis.

2.3.1.2 Ring solution

A ring geometry, consisting of plane circular arcs joined by straight lines, is defined with a number of input parameters: the number of cells in the ring (N), the opening angle of the F and D magnets from the machine centre (respectively β_F and β_D – defined in terms of the intersection of the closed orbit with the magnet end planes), the radius of the orbit at the centre of the F-magnet (r_0), and the bending angle in the F-magnet (θ_F), as well as the inclination angle for the F-magnet, γ_F. Figure 2.10 and Table 2.6 show the definition of each input parameter, as well as the remaining variables that characterise the lattice – the bending and inclination angles of the D-magnet θ_D and γ_D, the radii of curvature ρ_F and ρ_D for each respective magnet, and the radii of the orbit with respect to machine centre at the edge of the F magnet (r_1), edge of the D-magnet (r_2), and centre of the D-magnet (r_3).

As for the hFFA FODO or straight line vFFA FODO examples, the geometry of the

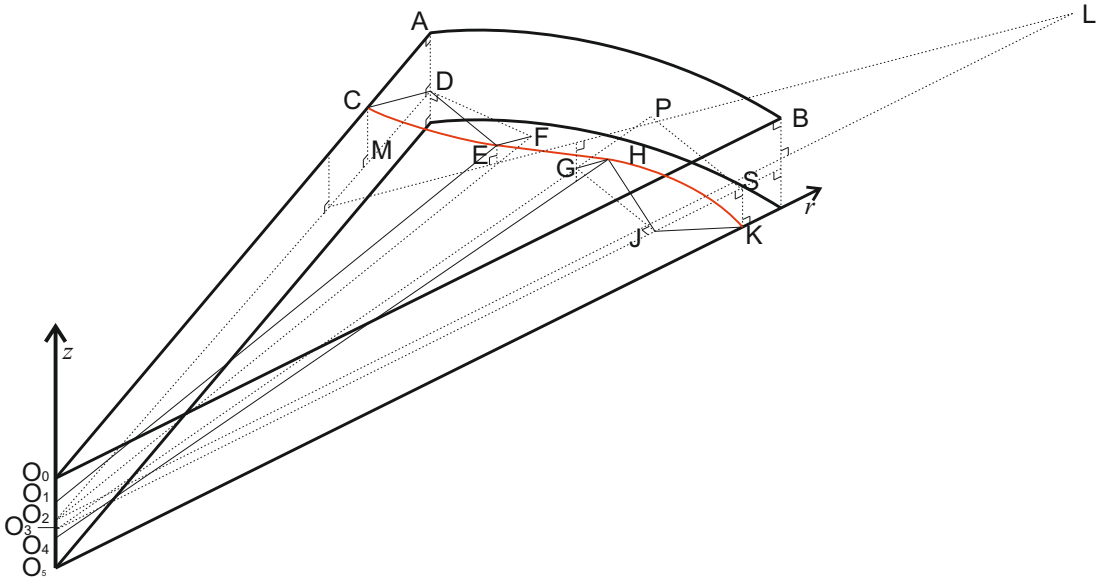

Figure 2.10: 3D geometry of a closed orbit through a half-cell of a vFFA FODO lattice, beginning at the midpoint of the F-magnet and finishing at the midpoint of the D-magnet. The O_i points all lie on the central axis of the machine, and the geometry is symmetric about the radial axes passing through the centre of the F and D magnets.

system (Fig. 2.10) can be used to derive a number of relations that determine all the unresolved lattice variables (Table 2.6). In analogy to Eq. (2.4) we find that the angles made by projecting $\angle HJK$ (θ_F) and $\angle CDE$ (θ_D) onto the horizontal plane must satisfy

$$(\angle HJK)_h - (\angle CDE)_h = \frac{\pi}{N}, \tag{2.26}$$

in which the subscript h denotes the projection onto the horizontal plane.

Consider a right angle triangle defined with angle θ and a hypotenuse of unit length. This triangle is rotated through an angle γ to the horizontal about the adjacent side (Fig. 2.11). Its projection onto the horizontal plane is also a right angle triangle, with angle θ_h between adjacent and hypotenuse, and hypotenuse length l. The adjacent side is common to both triangles, and has length $\cos\theta = l\cos\theta_h$, whilst the opposite side length of the projected triangle is given by $\sin\theta\cos\gamma = l\sin\theta_h$. Taking the ratio of these two equations gives the relation $\tan\theta_h = \tan\theta\cos\gamma$. Using this result along with trigonometric addition

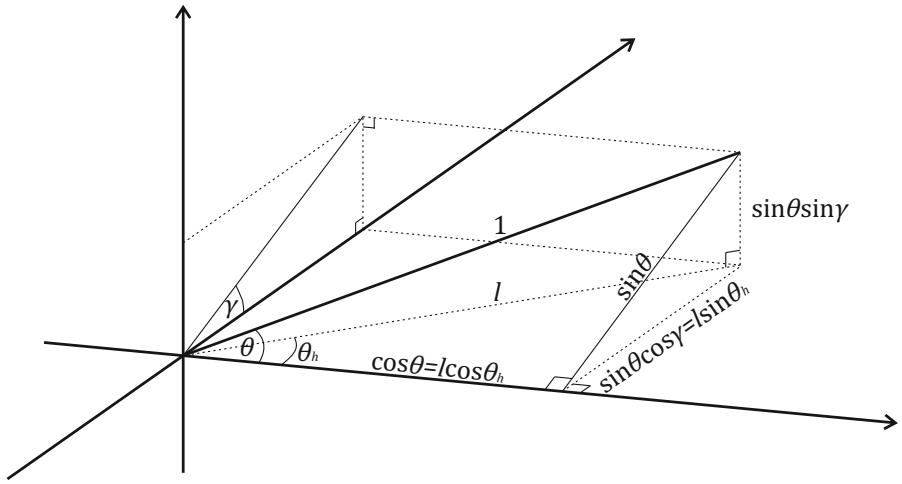

Figure 2.11: Diagram showing the projection of an inclined triangle onto the horizontal plane.

formulae to take the tangent of both sides of Eq. (2.26) we obtain

$$\frac{\tan\theta_F\cos\gamma_F - \tan\theta_D\cos\gamma_D}{1+\tan\theta_F\cos\gamma_F\tan\theta_D\cos\gamma_D} = \tan\left(\frac{\pi}{N}\right). \tag{2.27}$$

As this equation contains two unknown variables, an additional constraint is needed for a unique solution. This is found by expressing the vertical displacement travelled across the drift length in terms of the bending and inclination angles for each magnet:

$$\sin\theta_F\sin\gamma_F = \sin\theta_D\sin\gamma_D. \tag{2.28}$$

Solving Eqs. (2.27) and (2.28) simultaneously gives the following equation for θ_D:

$$\theta_D = \arctan\left(\frac{i\sqrt{(\tan\frac{\pi}{N} - \cos\gamma_F\tan\theta_F)^2 + \sin^2\gamma_F\sin^2\theta_F(\tan\frac{\pi}{N}\cos\gamma_F\tan\theta_F+1)^2}}{\sqrt{\sin^2\gamma_F\sin^2\theta_F - 1}(\tan\frac{\pi}{N}\cos\gamma_F\tan\theta_F+1)}\right), \tag{2.29}$$

from which the result can be substituted into Eq. (2.28) to set γ_D. An equation to set ρ_F can be found from computing the length $\overline{PS}$ as

$$\rho_F[\sin\theta_F + (1-\cos\theta_F)\cos\gamma_F\tan\beta_F] = r_0\tan\beta_F, \tag{2.30}$$

and computing the length $\overline{GJ}$ gives

$$r_1 \sin\beta_F = \rho_F \sin\theta_F. \tag{2.31}$$

Generating an expression for the length $\overline{O_2L}$ gives

$$r_1[\cos\beta_F + \tan\theta_F \cos\gamma_F \sin\beta_F] = r_2[\cos\left(\frac{\pi}{N} - \beta_D\right) + \tan\theta_F \cos\gamma_F \sin\left(\frac{\pi}{N} - \beta_D\right)], \tag{2.32}$$

with which r_2 can be determined. Finally, r_2 can be related to ρ_D by deriving an expression for the length $\overline{DF}$ as follows

$$r_2 \sin\beta_D = \rho_D \sin\theta_D, \tag{2.33}$$

and r_3 is computed as

$$r_3 = r_2 \cos\beta_D - \rho_D(1 - \cos\theta_D \cos\gamma_D). \tag{2.34}$$

Equations (2.27–2.34) then completely specify the geometry of the vFFA FODO lattice (under the approximations outlined at the beginning of the section). When γ_F is set to 0, γ_D becomes 0, and the system reduces to a planar solution identical to the hFFA FODO case.

2.3.2 Numerical Benchmarking

As with the hFFA, we wish to compare the results of the analytic model to those produced by a more detailed and computationally intensive simulation software, FIXFIELD. A lattice model was constructed using the analytic formulae above according to the parameters shown in Table 2.7. An equivalent lattice model was then simulated in the FIXFIELD code, using rectangular magnets with midplanes positioned according to the γ_F and γ_D values used in the analytic model (see Eq. 2.20). The strengths of these magnets were computed from the bending radii used in the analytic model, compensated for the change in the orbit's altitude between magnets (according to the scaling law). Initially, the FIXFIELD model used hard-edge magnets (i.e. fringe fields were not considered, and the field

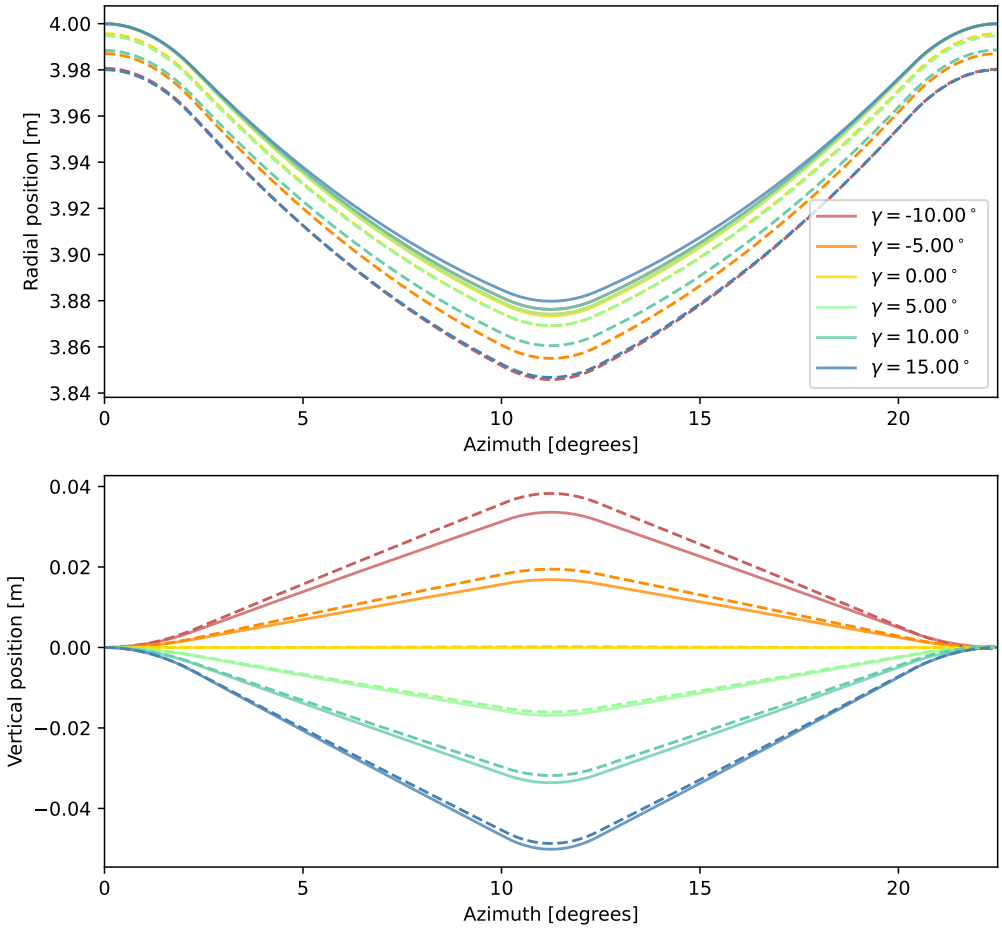

Figure 2.12: Radial and vertical positions of the closed orbits through an example vFFA FODO lattice as a function of different input γ_F. The solid lines denote the analytic predictions, whilst the dashed lines represent results from numerical simulation. Note that the radial position of the orbit in the analytic model is independent of the sign of γ_F, so the horizontal projections for both positive and negative γ_F are directly overlaid on top of each other.

Parameter	Value
N	16
β_F	$2.25°$
β_D	$1.15°$
r_0	4m
θ_F	$45°$
m	1m^{-1}
c_1	0.05m

Table 2.7: Default parameters of the example vFFA FODO lattice used to generate Figs. 2.12 (in which the fringe length L_f is not used) and 2.16. These parameters are based on those used in the previous section for the hFFA FODO studies. The normalised field gradient m and the Enge c_1 coefficient are used to inform the numerical model, and do not affect the analytic model; the value of c_1 is chosen based on the fringe model used in the FETS VFFA design study [32].

changes instantaneously from zero to the nominal value at the edge of the magnet); Figure 2.12 shows the agreement between numerical and analytic predictions for the closed orbit as γ_F is varied in the input. It can be seen that for the values of $\gamma_F \geq 0$ that were tested, the radial agreement remains close - within 1.5% - and the vertical discrepancy remains below 3%. This represents a comparable level of performance to the established analytic model for the hFFA described in an earlier section.

The displacement between the analytic and numerical predictions grows as a function of $|\gamma_F|$. The reason for the divergence of the analytic and numerical results is that the radius of curvature in the D-magnet ρ_D becomes smaller with increasing $|\gamma_F|$, and therefore there is a greater variation in the transverse position of the orbit with respect to the D-magnet midplane within the magnet. Due to the transverse gradient of the fields, this weakens the assumption of a constant radius of curvature within the magnet.

We find additionally a faster divergence between numerical and analytic results for the case of negative γ_F - this is theorised to be explained by the fact that the numerical modelling shows a smaller average radius for the closed orbit across all cases than that predicted by the analytic model. Negative γ_F implies a positive radial displacement of the magnet midplane, whilst positive γ_F implies a negative radial displacement of the magnet

midplane. This means that when simulating a lattice with a negative value of γ_F, the magnitude of displacement of the closed orbit from the magnet midplane is greater than for an equivalent positive value of γ_F. FIXFIELD uses a finite-order expansion of off-midplane fields, and hence a greater magnitude of displacement from the midplane introduces an increased discrepancy between the analytic model and the numerical model. A priority of future study should be cross-referencing this behaviour against predictions from other codes.

2.4 vFFA Triplet Lattices

A triplet lattice comprises three magnets per cell. These may be in an FDF configuration (as illustrated in the half-cell diagram shown in Fig. 2.13) - i.e. a reverse bend magnet sandwiched between two normal bend magnets - or a DFD configuration (i.e. two reverse bend magnets surrounding a normal bend).

2.4.1 Analytic model

Using the same approximations as Section 2.3.1, a simplified model of the geometry for a vFFA triplet lattice was constructed (presented in Fig. 2.10). The inclination of the plane of curvature in the D-magnet, γ_D, is defined as a rotation about an axis perpendicular to the cell boundary. The geometry is approximated with zero drift length within the triplet (i.e. the cell, if defined between midpoints of the central magnets of successive triplets, contains only one drift length) to simplify the model.

Beginning from the same approach of projecting the bending angles in F and D magnets onto the horizontal plane detailed in Section 2.3.1, an expression for the projection of the angle θ_F onto the horizontal can be found as

$$\angle HMJ = \arctan\left(\tan\theta_F \cos\gamma_F\right). \tag{2.35}$$

The projection of θ_D onto the horizontal plane, $\angle KGH$, can be expressed using

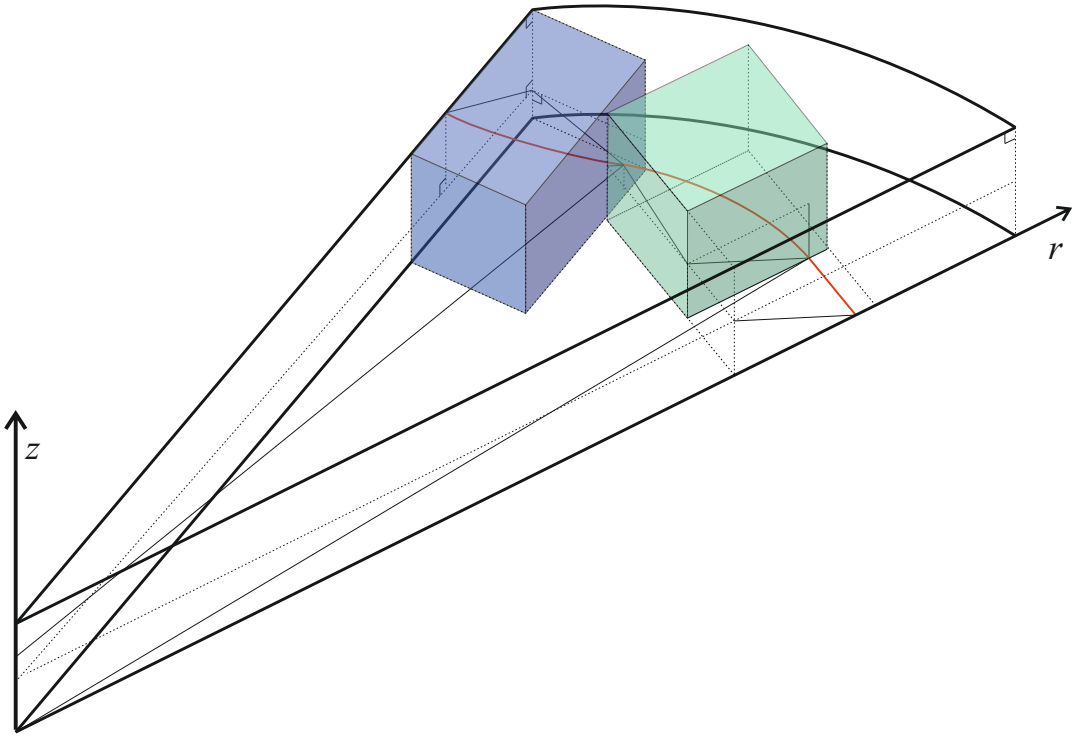

Figure 2.13: Closed orbit of a vFFA triplet half cell in an FDF configuration. The closed orbit is shown in red, whilst the F-magnet and D-magnet are drawn in green and blue respectively. The z-axis is positioned at the machine centre, and r is the radial direction.

Parameter	Definition
β_F	$\angle COD$
β_D	$\angle AOB$
$\frac{\pi}{N}$	$\angle AOD$
r_0	$\overline{OL}$
θ_F	$\angle HML$
γ_F	$\angle JML$

Variable	Definition
θ_D	$\angle FGH$
ρ_D	$\overline{FG} = \overline{GH}$
ρ_F	$\overline{HM} = \overline{ML}$
r_1	$\overline{OH}$
r_2	$\overline{OF}$
r_3	$\overline{OE}$
L_s	$\overline{EF}$
γ_D	$\angle FGK$

Table 2.8: Definitions of all input parameters and output variables that completely specify the geometry of a vFFA triplet closed orbit in terms of Fig. 2.14.

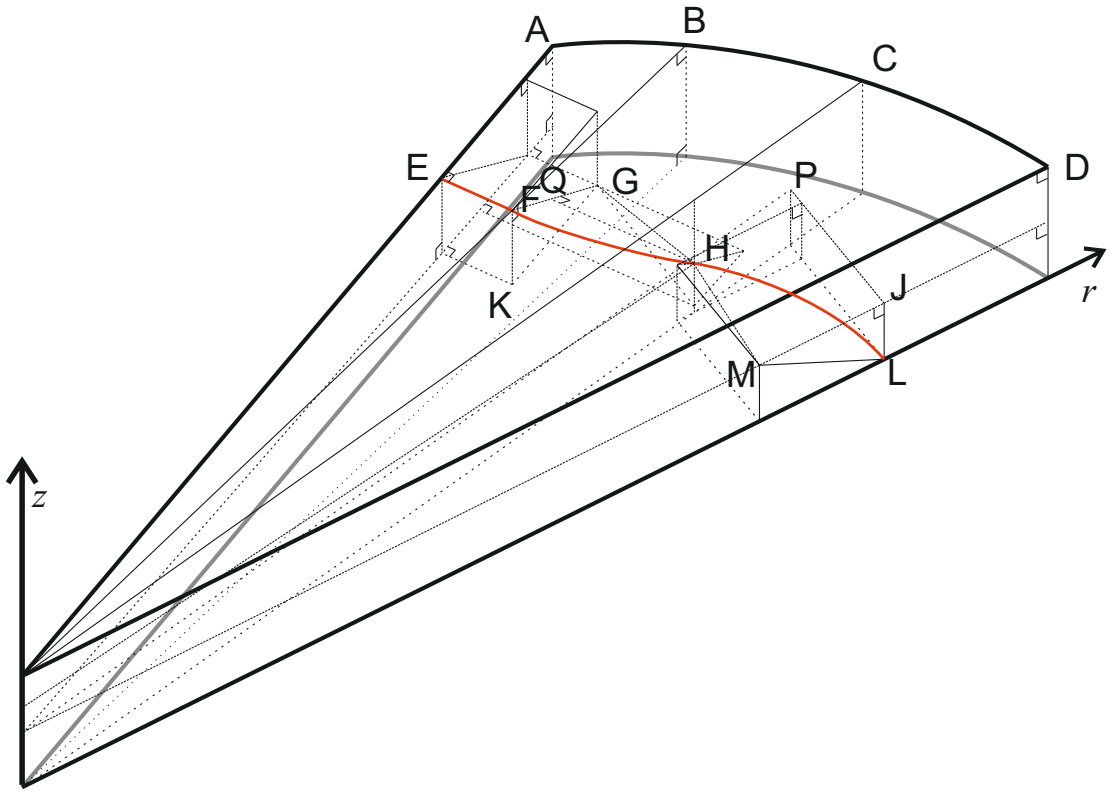

Figure 2.14: 3D geometry of a closed orbit through a half-cell of a vFFA triplet lattice, beginning at the midpoint of the drift and finishing at the midpoint of the F-magnet. The O_i points all lie on the central axis of the machine. This diagram shows a DFD triplet.

$$\tan\left(\angle KGH + (\pi/N - \beta_F - \beta_D)\right) = \tan\left(\theta_D + \arctan\left(\frac{\tan\pi/N - \beta_F - \beta_D}{\cos\gamma_D}\right)\right)\cos\gamma_D, \tag{2.36}$$

$$\tan\left(\angle KGH\right) = \frac{\tan^2\left(\pi/N - \beta_F - \beta_D\right) + \cos^2\gamma_D}{\sec^2\left(\pi/N - \beta_F - \beta_D\right)\cos\gamma_D\cot\theta_D - \tan\left(\pi/N - \beta_F - \beta_D\right)\sin^2\gamma_D}. \tag{2.37}$$

The equivalent of Eq. (2.27) for the vFFA triplet then becomes

$$\frac{\tan\theta_F\cos\gamma_F + \tan\left(\angle KGH\right)}{1 - \tan\theta_F\tan\left(\angle KGH\right)\cos\gamma_F} = \pi/N. \tag{2.38}$$

With this relation and Eq. (2.28), it becomes possible to solve the system for θ_D and γ_D.

Under the assumption that the value of $\arctan\left(\frac{\tan\pi/N - \beta_F - \beta_D}{\cos\gamma_D}\right)$ is small compared to θ_D, the result from the previous section (Eq. (2.29)) can be used to evaluate θ_D. As before, γ_D is then computed from Eq. (2.28).

Computing length $\overline{JP}$ gives the following relation

$$\rho_F[\sin\theta_F + (1 - \cos\theta_F)\cos\gamma_F\tan\beta_F] = r_0\tan\beta_F, \tag{2.39}$$

which can be used to determine ρ_F. r_1 is then calculated using Eq. (2.30).

ρ_D must be computed by considering the length $\overline{HQ}$, giving the expression

$$\rho_D = \frac{r_1\left(\sin\left[\pi/N - \beta_F\right] - \cos\left[\pi/N - \beta_F\right]\tan\left[\pi/N - \beta_F - \beta_D\right]\right)}{\sin\theta_D - (1 - \cos(\theta_D))\cos\gamma_D\tan\left[\pi/N - \beta_F - \beta_D\right]}. \tag{2.40}$$

Deriving a relation for the length $\overline{OS}$ we obtain

$$r_2\cos\left[\beta_F + \beta_D\right] = r_1\cos\beta_F - \rho_D\left(\sin\theta_D\sin\frac{\pi}{N} + (1 - \cos\theta_D)\cos\gamma_D\cos\frac{\pi}{N}\right), \tag{2.41}$$

giving r_2, from which r_3 can be computed via projection onto the radial axis at the centre of the drift:

$$r_3 = r_2\cos\left[\frac{\pi}{N} - \beta_F - \beta_D\right]. \tag{2.42}$$

Following this procedure, all variables associated with the vFFA triplet geometry depicted in Fig. 2.14 can be evaluated from the input parameters listed in Table 2.8. Once again, setting γ_F to 0 forces a planar solution, in which case we retrieve the hFFA triplet result shown in [52]. An additional note is that the definitions used and the equations derived above are given in terms of a DFD triplet; exchanging the sign of θ_F and making appropriate sign changes in Eqs. (2.39–2.42) we find the corresponding solution for the FDF triplet configuration.

2.4.2 Numerical Benchmarking

As in Section 2.3.2, model lattices were constructed in the FIXFIELD code using parameters derived from the analytic model based on Table 2.7. Magnets were simulated in FIXFIELD using a hard-edge model. The predictions for the closed orbit from the analytic model were then compared to the results from numerical simulation. The results shown in Fig. 2.15 show a maximum radial discrepancy of 1.0% between analytic and simulated orbits, whilst the vertical displacement between the predicted analytic closed orbit and simulated numerical closed orbit reaches a maximum of 0.3mm. Once again, this is consistent with the precision of the established model for hFFAs.

This demonstrates the successful development of analytic modelling techniques for the vFFA in a number of different configurations, showing how the non-planar nature of the closed orbits arises from the off-midplane fields of the vFFA magnet bodies, and how this effect can be modelled via the introduction of new parameters to describe the rotation of the planes of curvature. The results were found to agree with numerical simulations in the absence of fringe fields, and the closed orbit models can now be employed in developing an understanding of the optics of vFFA designs.

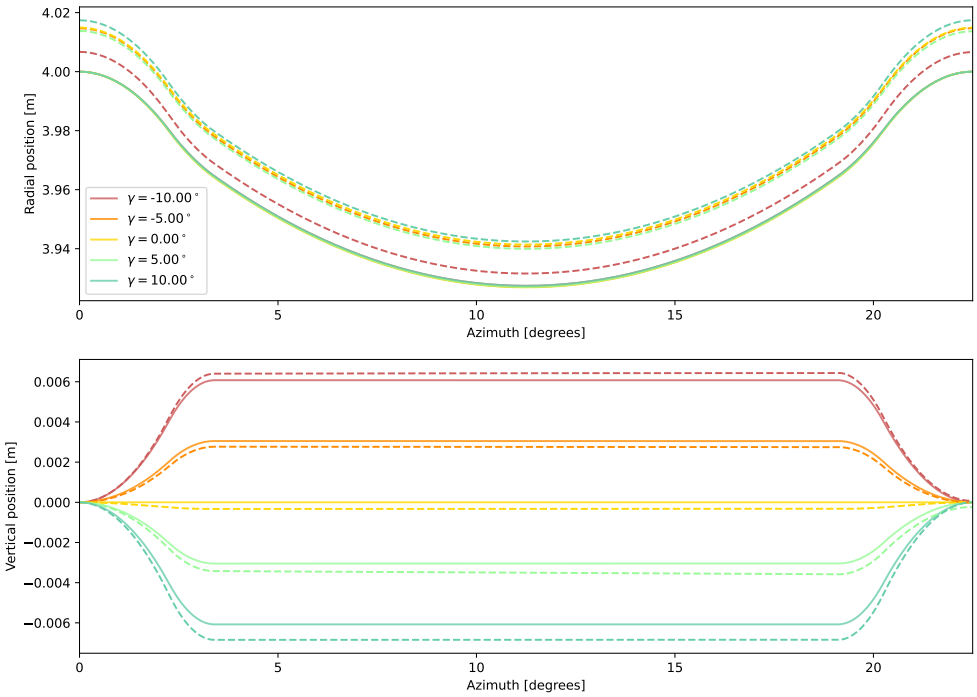

Figure 2.15: Radial and vertical coordinates of the closed orbits through example vFFA triplet latticeas a function of different input γ_F. The solid lines denote the analytic predictions, whilst the dashed lines represent results from numerical simulation. Note that the horizontal position of the orbit in the analytic model is independent of the sign of γ_F, so the horizontal projections for both positive and negative γ_F are directly overlaid on top of each other.

2.5 Effect of fringe fields in the vFFA

In contrast to the hFFA, the introduction of fringe fields has a much greater effect on the closed orbits due to the presence of longitudinal magnetic field components. When the beam crosses this longitudinal field at an angle, a dipole effect is induced. The dipole order effects of longitudinal fringe fields are not accounted for in this analytic model, and therefore the use of this approach may be more limited in smaller rings, especially those with rectangular magnets, (i.e. large edge angles) and for rings with low values of m. To assess the magnitude of the longitudinal field effect on closed orbits quantitatively, it is necessary to evaluate the integrated contribution of the longitudinal field at dipole order in comparison to the main dipole field of the magnet body. Maxwell's equation $\nabla \times \mathbf{B} = \mathbf{0}$ allows us to write

$$\frac{\partial B_Z}{\partial Y} = \frac{\partial B_Y}{\partial Z}, \tag{2.43}$$

which we integrate along the longitudinal axis to find

$$[B_Z]_b^a = \int_b^a \frac{\partial B_Y}{\partial Z} dY. \tag{2.44}$$

in which a and b denote arbitrary points along the longitudinal axis of the magnet. From the scaling law, we have

$$\frac{\partial B_Y}{\partial Z} = m B_Y, \tag{2.45}$$

and hence

$$[B_Z]_b^a = m \int_b^a B_Y dY. \tag{2.46}$$

Therefore, considering the integration over the length of the fringe field from the point at which $B_Z = 0$ to the point at which B_Z achieves its nominal value in the magnet body, we can see that the integral of the longitudinal field is proportional to the magnet body field strength B_{Z0} divided by the m-value. A beam crossing through this field at angle α will then see a dipole kick proportional to the longitudinal field integral multiplied by $\sin\alpha$.

Parameter	Value
N	771
β_F	$0.07782°$
β_D	$0.07782°$
r_0	4297m
θ_F	$0.3502°$
m	1m^{-1}
c_1	0.05m

Table 2.9: Default parameters of a large-ring vFFA FODO lattice, used to generate data for Fig. 2.16. These parameters are loosely based on preliminary designs for a muon accelerator ring for the LHC tunnel [61].

In the simplest-case of a FODO lattice with rectangular magnets, this crossing angle α is equal to the bending angle within the magnet θ.

The dipole contribution from the fringe field can then be compared to the integrated dipole field within the magnet body, which is given by the magnet length L multiplied by the nominal field value. The ratio of these contributions can be taken to be a dimensionless parameter that approximately quantifies the effect of fringe fields on the closed orbits:

$$\text{Dipole contribution ratio} \simeq \frac{\sin\theta_F}{mL}. \tag{2.47}$$

This definition can be used assuming a FODO lattice with a similar D-magnet and F-magnet length (relations for other types of lattices could be derived and would be expected to follow similar forms) to express the expected order of discrepancy between the analytic model and a more complete numerical simulation for a given set of input parameters. It does not completely quantify all factors involved, however, as it does not account for transverse field gradients or the fact that a small dipole order effect from longitudinal fringe components is ultimately unavoidable in the vFFA. The latter is a consequence of the fringe field containing some nonzero transverse dipole components, meaning that it is impossible for a trajectory to remain collinear with the longitudinal fields even if its initial crossing angle is zero.

To test this computationally, a numerical model was generated following the same steps

as the previous sections on the vFFA; however, fringe fields are now included in the model. The fringe falloff function used here is the same as in [32] - i.e. an arctangent function. Two FODO accelerator geometries were then simulated: one, a small ring based on the parameters listed in Table 2.7, in which the fringe field length is similar to the magnet length; the other a large ring based on a proposal for a vFFA-based muon accelerator ring for the Large Hadron Collider tunnel, with parameters listed in Table 2.9 – in which case the fringe field length is much smaller than the magnet length. A number of lattices based on each geometry are generated for a range of m-values to test the impact of fringe fields on the accuracy of the analytic model; Figure 2.16 shows the maximum 2-d transverse displacement between the analytic and numerical closed orbit models for two different lattices as a function of the dipole ratio. This shows that as the fringe fields become more significant and the dipole ratio increases, the discrepancy between the models increases; however, at low values of the dipole ratio the curves for each lattice flatten, implying that the longitudinal fields in the fringe field are no longer the dominant sources of error at higher m-values. Below $m = 12$ for the small ring case, closed orbits were not found in numerical simulation; the closed orbit deviates significantly from the magnet midplane at the ends of the magnets, at which point the field expansion used to compute the fringe fields in simulation displays asymptotic behaviour. Physically, in a machine built with rectangular magnets of the type designed in e.g. [62] the orbit would be crossing outside of the good field region. Similarly, the numerical optimiser routine used to find the closed orbit fails to converge for the large ring model at $m < 0.06$. All results were simulated at $\gamma_F = 0$ such that the magnet position is independent of m.

The results of this study demonstrate that the analytic model is most immediately applicable to the study of large-ring vFFA lattices with a low value of the dipole contribution ratio, with the model's predictions becoming more limited as the scale of the lattice decreases (increasing the value of θ_F and decreasing the value of L, thereby increasing the value of the dipole contribution ratio).

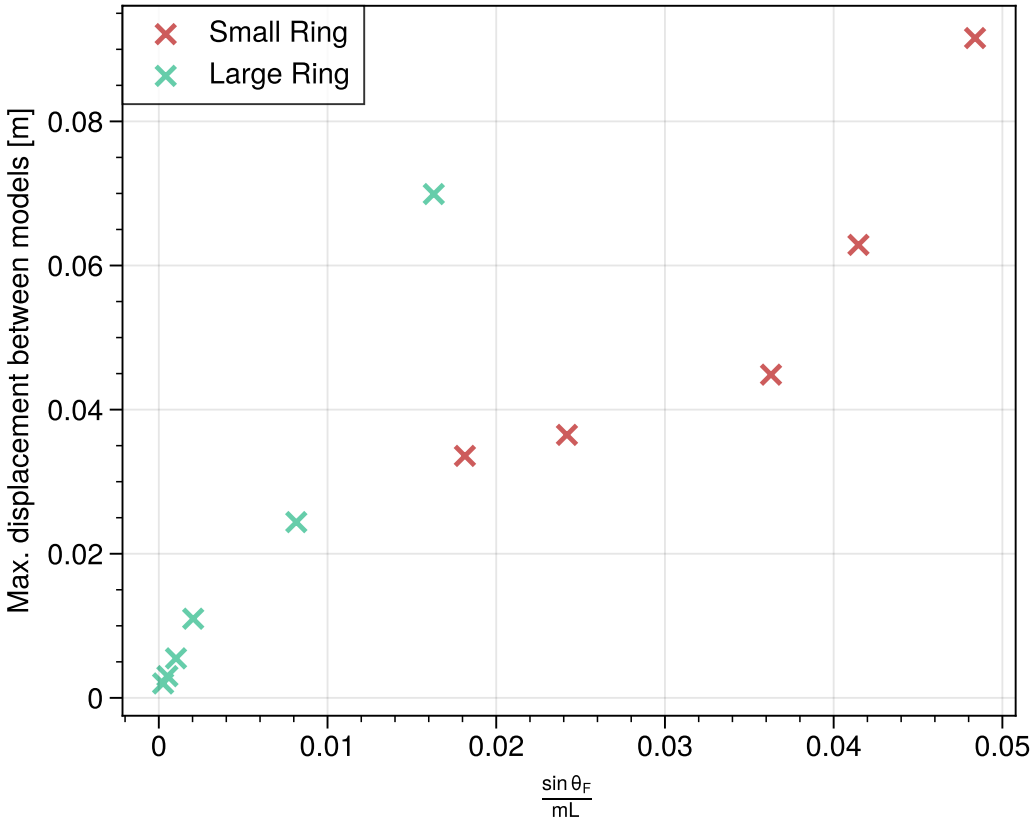

Figure 2.16: Maximum 2-d displacement between numerical and analytic models as a function of the dipole ratio. The small ring model follows the parameters shown in Table 2.7, whilst the large ring model is based on a vFFA muon accelerator ring for the Large Hadron Collider tunnel, and its parameters are displayed in Table 2.9. The fringe lengths in either case are equivalent.

2.6 Chapter summary

In this chapter, methods of defining analytic closed orbits were derived, reviewing both existing solutions for hFFAs as well as developing novel solutions for vFFAs by introducing the inclination parameter γ. hFFA solutions may be retrieved from the vFFA solutions by choosing $\gamma = 0$. Analytic models of hFFA and vFFA rings were then benchmarked against more complete numerical solutions, showing high levels of agreement. For the cases in which fringe fields could be ignored, it was shown that the new models of the vFFA closed orbits showed equivalent levels of performance to the established hFFA models across a range of parameters. However, when lattices with significant fringe fields are studied, or in cases where the radius of curvature is small compared to the radius of the machine, the predictive accuracy of the vFFA closed orbit model is limited. This means that studies in these regimes will need to rely more heavily on approaches based upon numerical simulations. A metric termed the 'dipole ratio' was derived to help quantify the domain in which the closed orbit models derived in this chapter are applicable.

Chapter 3

Linear Optics of Fixed Field Accelerators

Once the closed orbit for the system has been found using the techniques in Chapter 2, the linear beam dynamics may be understood in terms of optics expanded locally about this closed orbit.

In this chapter, we use the Frenet-Serret Hamiltonian and the hFFA scaling law explored in Chapter 1 to derive a complete set of transfer matrices for the hFFA, which can then be combined with the closed orbit modelling of Chapter 2 to obtain a complete optical model for the scaling hFFA. The predictions of this model for tune and lattice stability are then benchmarked against numerical simulation to demonstrate the validity of this approach.

This lays the groundwork for exploration of the optical properties of the vFFA using similar techniques, and this chapter derives transfer matrices for the magnet bodies and fringe fields of vFFA lattices. These are once again integrated with a closed orbit model to explore the optics of the vFFA as a function of input parameters, testing the accuracy of the analytic tune against computations based on numerical tracking studies. The limitations of the vFFA model are then discussed, showing regimes where the approximations used in developing the vFFA model begin to fail. For these cases, a new numerical methodology termed harmonic analysis is implemented for the purpose of gaining additional insight into the focussing behaviour where the applicability of the analytic model is limited.

3.1 Linear Optics in hFFAs

3.1.1 Linear Transfer Map for a Scaling hFFA Magnet Body Element

Within the body of a magnet for a scaling hFFA, we assume that the radius of curvature remains constant (as in Chapter 2), and that the magnetic field is constant along the trajectory (i.e. that the magnetic fields are constant as a function of the independent variable). The field in this region is then governed solely by the scaling law, Eq. (1.67). The scaling law can be locally expanded in terms of a horizontal coordinate x (defined as $x = (r - r_0)$ in which r_0 is the reference orbit position) to give the following:

$$B_z(x) = B_0 \left[1 + \frac{kx}{r_0} + \mathcal{O}\left(x^2\right)\right] \tag{3.1}$$

Where B_0 is the reference magnetic field at $r = r_0$. For off-midplane fields, we use Maxwell's equation for the curl of the magnetic field in free space $\nabla \times B = 0$ to obtain

$$\frac{\partial B_x}{\partial z} = \frac{k}{r_0} B_0 + \mathcal{O}\left(x^3\right), \tag{3.2}$$

and hence

$$B_x(z) = B_0 \left[\frac{kz}{r_0} + \mathcal{O}\left(z^2\right)\right], \tag{3.3}$$

using the fact that there is zero horizontal field at $z = 0$. At linear order, the magnetic fields in this case can be interpreted as behaving (locally) as a superimposed dipole and quadrupole field of strengths B_0 and $\frac{k}{r_0} B_0$ respectively. An appropriate vector potential that satisfies $\nabla \times A = B$ can be found as [7]:

$$\begin{aligned} A_x &= 0, \\ A_z &= 0, \\ A_s &= -B_0 \left[\left(x - \frac{x^2}{2\rho + x}\right) + \frac{k}{r_0}\left(\frac{1}{2}\left(x^2 - z^2\right)\right)\right], \end{aligned} \tag{3.4}$$

in which ρ is the radius of curvature of the coordinate system. This vector potential can then be substituted into the Frenet-Serret Hamiltonian (Eq. (1.37)) and expanded, discarding all

terms at greater than second order (such that the equations of motion are linear in the dynamical variables), to obtain the following Hamiltonian:

$$\mathcal{H} \;=\; \frac{1}{2}\tilde{p_x}^2 + \frac{1}{2}\tilde{p_z}^2 + \left[\frac{q}{P_0}B_0 - \frac{1}{\rho}\right] x + \frac{1}{2}\frac{q}{P_0}B_0\left(\frac{1}{\rho} + \frac{k}{r_0}\right)x^2 - \frac{k}{2r_0}\frac{q}{P_0}B_0 z^2. \quad (3.5)$$

In order for the map described by this Hamiltonian to be a *linear map*, it must map the zero vector to itself. This implies that we must choose a Frenet-Serret reference trajectory such that

$$\rho = \frac{P_0}{qB_0} \quad (3.6)$$

so that there exist no constant terms in the equations of motion. This leads to the linearised Frenet-Serret Hamiltonian

$$\mathcal{H} = \frac{1}{2}\tilde{p_x}^2 + \frac{1}{2}\tilde{p_z}^2 + \frac{1}{2\rho}\left(\frac{1}{\rho} + \frac{k}{r_0}\right)x^2 - \frac{k}{2\rho r_0}z^2, \quad (3.7)$$

from which equations of motion can be derived using Hamilton's equations:

$$\begin{aligned}
\frac{dx}{ds} &= \tilde{p_x}, \\
\frac{d\tilde{p_x}}{ds} &= -\frac{1}{\rho}\left(\frac{1}{\rho} + \frac{k}{r_0}\right)x, \\
\frac{dz}{ds} &= \tilde{p_z}, \\
\frac{d\tilde{p_z}}{ds} &= \frac{1}{\rho}\frac{k}{r_0}z.
\end{aligned} \quad (3.8)$$

These equations of motion can be solved separately for the uncoupled $x, \tilde{p_x}$ and $z, \tilde{p_z}$ phase space planes. In the horizontal plane the equations of motion can be expressed as the homogeneous second order linear differential equation

$$\frac{d^2x}{ds^2} = -\frac{1}{\rho}\left(\frac{1}{\rho} + \frac{k}{r_0}\right)x = -\omega_x^2 x, \quad (3.9)$$

which has a general solution of the form

$$x\,(s) = C_x e^{i\omega_x s} + D_x e^{-i\omega_x s}, \quad (3.10)$$

where C_x and D_x are constants to be found. Applying Eq. (3.8), we find

$$\tilde{p_x}\,(s) = i\omega_x C_x e^{\omega_x s} - i\omega_x D_x e^{-\omega_x s}. \quad (3.11)$$

Likewise, the motion in the vertical plane can be written as

$$\frac{d^2z}{ds^2} = \frac{1}{\rho}\frac{k}{r_0}z = -\omega_z^2 z, \tag{3.12}$$

noting that ω_z^2 is defined with the opposite sign. Solutions for $z\,(s)$ once again take the form of Eq. (3.10), whilst $\tilde{p_z}\,(s)$ is once again found by differentiation. To find the exact solution to the equations of motion, and hence a transfer map for the element, it is necessary to implement boundary conditions. At $s = 0$, the map must be equal to the identity: this means that $x\,(s=0) = x_0$ and $\tilde{p_x}\,(s=0) = \tilde{p}_{x0}$ (where the subscript 0 denotes the starting coordinate). Immediately, Eq. (3.10) then gives the constraint that $C + D = x_0$; Eq. (3.11) requires that $\omega\,(C_x - D_x) = \tilde{p}_{x0}$. We can therefore deduce that $C_x = \left(x_0 + i\frac{\tilde{p}_{x0}}{\omega}\right)/2, D_x = \left(x_0 - i\frac{\tilde{p}_{x0}}{\omega}\right)/2$. The same logic can be applied in the vertical plane, and the 4×4 transfer matrix for transport through an element of length L obtained:

$$\begin{pmatrix} x \\ \tilde{p_x} \\ z \\ \tilde{p_z} \end{pmatrix} = \mathcal{M} \begin{pmatrix} x_0 \\ \tilde{p}_{x0} \\ z_0 \\ \tilde{p}_{z0} \end{pmatrix}, \tag{3.13}$$

$$\mathcal{M} = \begin{pmatrix} \cos\omega_x L & \frac{\sin\omega_x L}{\omega_x} & 0 & 0 \\ -\omega_x \sin\omega_x L & \cos\omega_x L & 0 & 0 \\ 0 & 0 & \cos\omega_z L & -\frac{\sin\omega_z L}{\omega_z} \\ 0 & 0 & \omega_z \sin\omega_z L & \cos\omega_z L \end{pmatrix}, \tag{3.14}$$

$$\omega_x = \sqrt{\frac{1}{\rho}\left(\frac{1}{\rho} + \frac{k}{r_0}\right)}, \omega_z = \sqrt{-\frac{1}{\rho}\frac{k}{r_0}}. \tag{3.15}$$

This transfer matrix can be interpreted as a quadrupole with extra focussing strength in the horizontal plane coming from the geometric properties of the curved orbit. In the normal bend (F-magnet) ρ takes a positive sign and the matrix represents focussing in the horizontal plane, with defocussing occurring in the vertical plane; conversely, in the reverse bend (D-magnet) ρ is given a negative sign and the vertical plane gains focussing behaviour. A defocussing contribution of order $1/\rho$ is seen for negative ρ from the quadrupole-like $\frac{k}{r_0\rho}$ term of the expansion, but the geometric effect still acts as a focussing contribution (of order $1/\rho^2$).

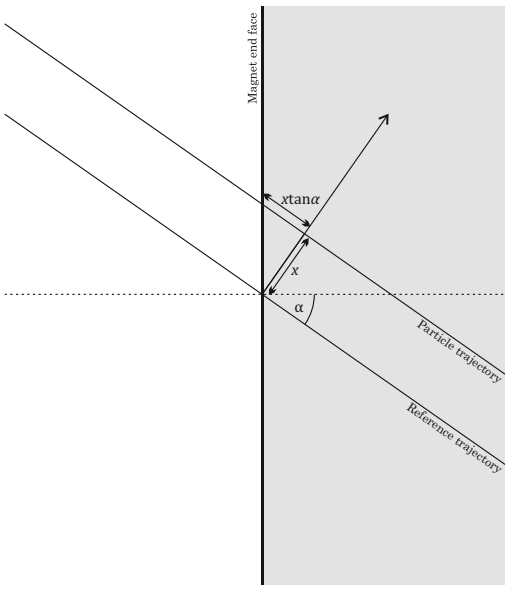

(a) Effect of crossing magnet boundary at an angle: a particle at displacement x travels an extra length within the magnet of $x \tan \alpha$.

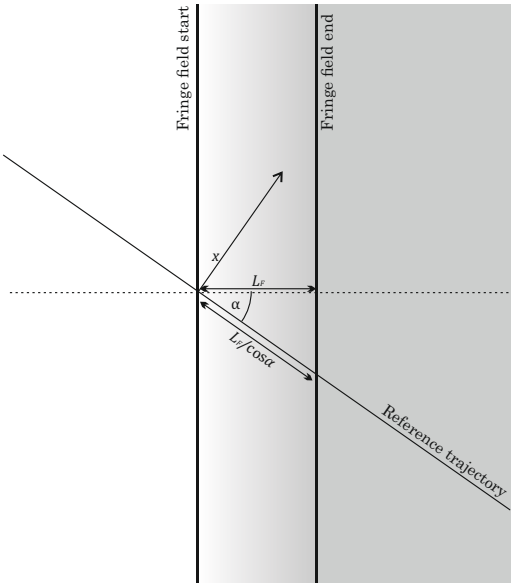

(b) Effective length of fringe field as a function of crossing angle α

Figure 3.1: Illustration of edge and fringe effects relating to the crossing angle α.

3.1.2 Linear Transfer Map for the Edge of a Scaling hFFA magnet

An additional focussing effect is seen by the beam when it crosses the end plane of a magnet at an angle α; this can be understood in terms of a particle travelling extra distance within the element as a function of the particle's transverse horizontal displacement from the reference trajectory (illustrated in Fig. 3.1a). This effect is not unique to hFFA magnets, and is seen also in dipoles; in many cases, it is discussed as a compound effect together with the effect of the fringe field (derived here in the following subsection) and both effects are referred to collectively as edge focussing. In this case, we treat them separately, as they arise from different sources, and this treatment leads to two separate thin lens transfer matrices with a smaller number of terms. When this approach is later paralleled for the vFFA, this enables the resulting 4D transfer matrices to be written in a more simplified form than would otherwise be possible.

The extra distance travelled by a particle can be expressed as

$$\delta L = x \tan \alpha, \tag{3.16}$$

and from the Lorentz force (Eq. (1.1)) we can consider this to apply a thin lens focussing kick such that

$$\begin{aligned} \delta x &= 0, \\ \delta \tilde{p_x} &= \delta L B_z \frac{q}{P_0} = x B_z \frac{q}{P_0} \tan \alpha, \\ \delta z &= 0, \\ \delta \tilde{p_z} &= -\delta L B_x \frac{q}{P_0} = -x B_x \frac{q}{P_0} \tan \alpha. \end{aligned} \tag{3.17}$$

Substituting in Eqs. (3.1) and (3.3) and the definition of ρ (Eq. (3.6)) leaves

$$\begin{aligned} \delta x &= 0, \\ \delta \tilde{p_x} &= \frac{1}{\rho} \left[x + \mathcal{O}\left(x^2\right) \right] \tan \alpha, \\ \delta z &= 0, \\ \delta \tilde{p_z} &= \frac{1}{\rho} \left[\mathcal{O}\left(zx\right) \right] \tan \alpha, \end{aligned} \tag{3.18}$$

rewritten in transfer matrix form as:

$$\mathcal{M}_{\text{edge}} = \begin{pmatrix} 1 & 0 & 0 & 0 \\ \frac{\tan \alpha}{\rho} & 1 & 0 & 0 \\ 0 & 0 & 1 & 0 \\ 0 & 0 & 0 & 1 \end{pmatrix}. \tag{3.19}$$

We find that the reference trajectory crossing the end plane of a magnet at an angle α, then, produces a defocussing effect in the horizontal plane.

3.1.3 Linear Transfer Map for the Fringe of a Scaling hFFA magnet

At the boundary of a magnet, the field cannot instantaneously transition from zero to the nominal strength within the magnet body – it must continuously change over a defined distance L_f. We therefore define the vertical and horizontal magnetic fields in the fringe

region according to

$$B_x(s) = \frac{f(s)}{\rho}\frac{kz}{r_0}, \tag{3.20}$$

$$B_z(s) = \frac{f(s)}{\rho}\left[1 + \frac{kx}{r_0} + \mathcal{O}\left(x^2\right)\right], \tag{3.21}$$

in which ρ denotes the radius of curvature within the magnet (and therefore in the above characterises the nominal dipole strength), and $f(s)$ is an arbitrary field falloff function that satisfies

$$f(0) = 0, f(L_f) = 1, \tag{3.22}$$

with the magnet entrance face situated at $s = L_f$. Whilst $f(s)$ should ultimately reflect the parameters of the chosen magnet design, as a first approximation a linear function is assumed:

$$f(s) = \begin{cases} 0 & s \leq 0, \\ s/L_f & 0 < s \leq L_f, \\ 1 & s > L_f. \end{cases} \tag{3.23}$$

To satisfy Maxwell's equation $\nabla \times B = 0$, we find that Eqs. (3.20) and (3.21) require a longitudinal field component:

$$B_y(s) = \frac{1}{L_f \rho}\left(z + \frac{kzx}{r_0}\right), \tag{3.24}$$

noting that the latter term inside the parentheses is second order and can be ignored for the purpose of the linear dynamics.

Introducing once again a crossing angle α with respect to the normal of the magnet end plane (Fig. 3.1b), two effects become apparent. The extent of the fringe field along the reference trajectory is modified by a factor $1/\cos\alpha$; we redefine the element length L in the rotated reference frame as $L = L_f/\cos\alpha$. Simultaneously, the fields defined by Eqs. (3.20) and (3.24) must be transformed to reflect the crossing angle (note that, as the rotation

is about the z-axis, B_z is independent of the crossing angle). This gives (at first order)

$$B_x(s) = \frac{skz}{\rho r_0 L_f}\cos\alpha - \frac{sz}{L_f\rho}\sin\alpha \qquad = \frac{skz}{\rho r_0 L} - \frac{sz}{L\rho}\tan\alpha, \tag{3.25}$$

$$B_y(s) = \frac{sz}{L_f\rho}\cos\alpha + \frac{skz}{\rho r_0 L_f}\sin\alpha \qquad = \frac{sz}{L\rho} + \frac{skz}{r_0 L\rho}\tan\alpha, \tag{3.26}$$

$$B_z(s) = \frac{s}{\rho L_f\cos\alpha}\left[1+\frac{kx}{r_0}\right] \qquad = \frac{s}{\rho L}\left[1+\frac{kx}{r_0}\right], \tag{3.27}$$

for the domain $0 < s < L$. Applying the same thin-lens Lorentz force treatment as in Section 3.1.2, we integrate the fields above between $s = 0$ and $s = L$ to get the total magnetic fields in 3 dimensions seen by a particle traversing the fringe field, and apply a total kick for the length of the fringe field. In this manner, the following transfer matrix can be derived for the fringe field of an hFFA magnet:

$$\mathcal{M}_{\text{fringe}} = \begin{pmatrix} 1 & 0 & 0 & 0 \\ -\frac{1}{2}\frac{kL}{r_0\rho} & 1 & 0 & 0 \\ 0 & 0 & 1 & 0 \\ 0 & 0 & \frac{1}{2}\frac{kL}{r_0\rho} - \frac{1}{\rho}\tan\alpha & 1 \end{pmatrix} \tag{3.28}$$

One point of note is that the longitudinal B_y does not contribute to the transfer matrix derived above. This is because, via the Lorentz force (Eq. (1.1)), the momentum kick received from a longitudinal field is dependent on the transverse momenta. The longitudinal field described by Eq. (3.27) is a linear function of the transverse z-coordinate, so the change in momentum from the longitudinal field is consequently a second-order effect.

The effect of passing through the fringe field at an angle, in the short-L limit, can be seen to be a focussing effect in the vertical plane proportional to the tangent of the crossing angle α.

3.1.4 Properties of hFFA Lattices

A full model of an hFFA lattice can now be assembled using the transfer matrix results from the previous section (Eqs. (3.14), (3.19), and (3.28) alongside the drift space transfer matrix from Chapter 1, Eq. 1.45), using the parameters based on the geometry derived in Chapter 2. Transfer matrices corresponding to drifts of the appropriate length are also included.

Figure 3.2 shows the region of parameter space for which stable optics can be found as a function of the input values of θ_F and k in a sample FODO lattice (with parameters based on Table 2.2). Stability is evaluated in the analytic model by assembling a transfer matrix model based on the geometry determined from the input parameters and checking if the eigenvalues of the cell transfer matrix are all complex. Edge angles for the F and D-magnets are computed as

$$\begin{aligned} \alpha_F &= \theta_F - \beta_F \\ \alpha_D &= \theta_D + \beta_D, \end{aligned} \tag{3.29}$$

and the fringe lengths are not accounted for in the analytic model (i.e. a hard-edge approximation is assumed).

The predictions for tunes and stability of this analytic model are cross-checked against results from the numerical tracking code FIXFIELD, which evaluates tunes from a transfer matrix that is computed numerically by tracking particles with small deviations from the closed orbit.

The result in Fig. 3.2 shows that a fully analytic approach based on the transfer matrices derived above as well as the geometry derived in Chapter 2 can accurately predict the stability of a given lattice configuration when compared to simulated results, though agreement appears worse for higher values of θ_F.

We see this in more detail in Figure 3.3, which displays the variation of horizontal and vertical tune with input parameters, showing that the vertical tune increases faster with θ_F in the analytic model, though the overall numerical agreement is close. The discrepancy for increasing theta can be explained because the finite length of the magnet fringe transition simulated in the numerical model reduces the effective focussing from the edge angle in the vertical plane, compared to the hard-edge approximation of the analytic model. This effect reduces the gradient of the slope of the vertical tune as a function of θ_F for the numerical model, and hence explains why the upper bound of the stability region is reached slower in the numerical model than in the analytic case.

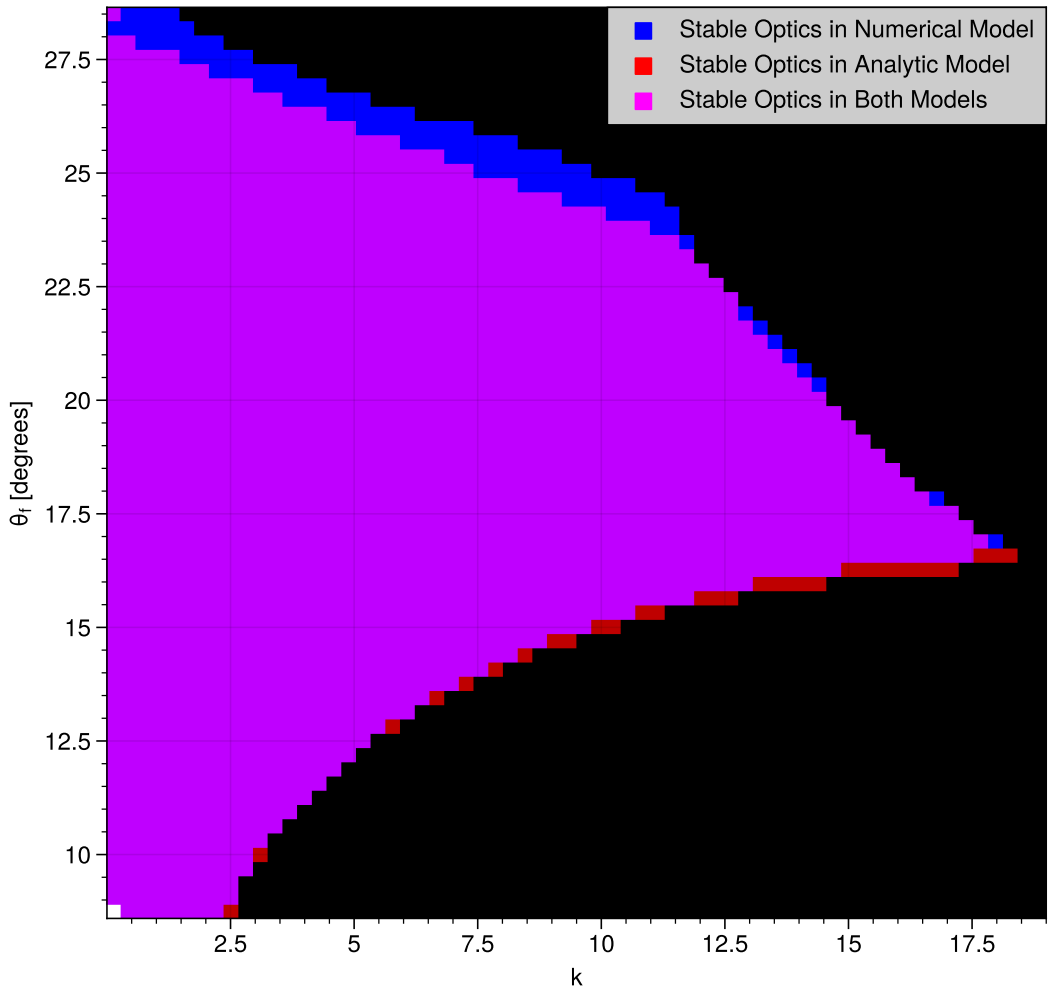

Figure 3.2: Necktie diagram for a scaling hFFA FODO lattice in which θ_F and k are varied whilst all other parameters are kept at the nominal values described in Table 2.2.

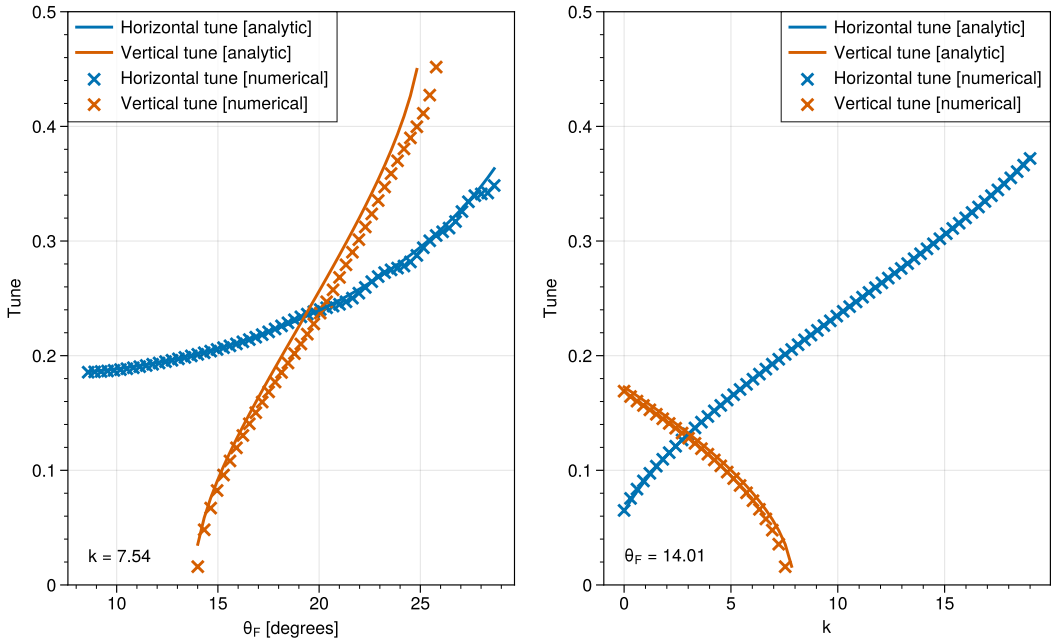

Figure 3.3: Dependence of tune on θ_F and k when all other parameters are kept fixed.

For the modelling of FFAs, the need to determine a closed orbit based on the geometry of the fields, and the dependence of optical properties on the closed orbit renders achieving equivalent result across different models a challenge even between comparable numerical codes. Agreement between these codes and the results of real experiments is a further difficulty [63]; in this context, the close agreement of the analytic model with the FIXFIELD evaluation across the parameter space demonstrates the utility of the analytic approach to the design and modelling of FFA machines.

3.2 Linear Optics in vFFAs

3.2.1 vFFA magnet body

Beginning with the fields outlined in Eq. (2.18), a vector potential $\mathbf{A}$ that satisfies the definition $\nabla \times \mathbf{A} = \mathbf{B}$ is as follows:

$$\begin{aligned} A_X &= 0, \\ A_Y &= \frac{B_0}{m} e^{mZ} \sin mX, \\ A_Z &= 0, \end{aligned} \tag{3.30}$$

in which a gauge choice is made such that the transverse components of $\mathbf{A}$ are zero.

The next step is to substitute this potential into a Frenet-Serret Hamiltonian (Eq. (1.37)). One important subtlety is that usually, when transforming to Frenet-Serret coordinates, the transverse coordinates of the Hamiltonian are defined as equivalent to the normal and bi-normal coordinates of the Frenet-Serret system. In a Frenet-Serret coordinate system, the local radius of curvature is collinear with the normal vector; in the torsionless planar system considered elsewhere in accelerator physics (e.g. employed in textbooks such as [5, 7]), the unit normal vector can be considered equivalent to the horizontal normal vector $\mathbf{x}$. However, in the case of the vFFA (even under the assumption that the fields are independent of position along the trajectory, which implies zero torsion), the plane of curvature exists at an angle γ with respect to the horizontal. Here, a choice is made to transform the Hamiltonian such that the horizontal unit vector x remains horizontal whilst the Frenet-Serret normal vector and the radius of curvature are at an angle with respect to x. This gives the modified Frenet-Serret Hamiltonian for transverse dynamics

$$\begin{aligned} \tilde{H} = \left(1 + \frac{x\cos\gamma + z\sin\gamma}{\rho}\right) \sqrt{1 + (\tilde{p_x} - \frac{q}{P_0}A_x)^2 + (\tilde{p_z} - \frac{q}{P_0}A_z)^2} \\ - \frac{q}{P_0}\left(1 + \frac{x\cos\gamma + z\sin\gamma}{\rho}\right) A_s. \end{aligned} \tag{3.31}$$

A further coordinate transformation is made to account for the horizontal offset of the closed orbit from the magnet midplane x_0, and the resulting Hamiltonian is written in terms

of transverse coordinates $x = X - x_0, z = Z$ and inclination angle $\gamma = mx_0$ (see Section 2.3.1.1) as follows:

$$\mathcal{H} = \left(1 + \frac{1}{\rho}[x\cos\gamma + z\sin\gamma]\right)\sqrt{1 + \tilde{p_x}^2 + \tilde{p_z}^2} - \left(1 + \frac{1}{\rho}[x\cos\gamma + z\sin\gamma]\right)\frac{B_0 q}{mP_0}e^{mz}\sin m\,(x + x_0), \quad (3.32)$$

which can be expressed via trigonometric addition formulae in the form

$$\mathcal{H} = \left(1 + \frac{1}{\rho}[x\cos\gamma + z\sin\gamma]\right)\sqrt{1 + \tilde{p_x}^2 + \tilde{p_z}^2} - \left(1 + \frac{1}{\rho}[x\cos\gamma + z\sin\gamma]\right)\frac{B_0 q}{mP_0}e^{mz}\left(\cos\gamma\sin mx + \cos mx\sin\gamma\right). \quad (3.33)$$

Expanding around $x = z = \tilde{p_x} = \tilde{p_z} = 0$ to second order and dropping constant terms (as these have no effect on the dynamics) leaves

$$\mathcal{H} \simeq \frac{\tilde{p_x}^2}{2} + \frac{\tilde{p_z}^2}{2} + \left[\frac{1}{\rho} - \frac{B_0 q}{P_0}\left(1 + \frac{\sin\gamma}{m\rho}\right)\right](x\cos\gamma + z\sin\gamma) - \frac{B_0 q}{P_0}\cos\gamma\left(m + \frac{2\sin\gamma}{\rho}\right)xz + \frac{B_0 q}{2P_0}m\left(x^2 - z^2\right)\sin\gamma - \frac{B_0 q}{P_0\rho}x^2\cos^2\gamma - \frac{B_0 q}{P_0\rho}z^2\sin^2\gamma. \quad (3.34)$$

Once again, first order terms must be removed from the Hamiltonian to make a linear map when Hamilton's equations are applied. This requires the choice that

$$\begin{aligned}\rho &= \frac{P_0}{B_0 q} - \frac{\sin\gamma}{m},\\ \frac{1}{\rho + \frac{\sin\gamma}{m}} &= \frac{B_0 q}{P_0}.\end{aligned} \quad (3.35)$$

Noting that B_0 is defined on the magnet midplane, at which point $\gamma = 0$, the additional $\frac{\sin\gamma}{m}$ term can be thought of as an adjustment factor to compensate for the horizontal offset of the closed orbit from the midplane. From here, the Hamiltonian can be written as follows:

$$\mathcal{H} \simeq \frac{\tilde{p_x}^2}{2} + \frac{\tilde{p_z}^2}{2} - \frac{1}{\rho + \frac{\sin\gamma}{m}} \left[\cos\gamma \left(m + \frac{2\sin\gamma}{\rho} \right) xz - \frac{1}{2} m \left(x^2 - z^2 \right) \sin\gamma \right] - \frac{1}{\rho \left(\rho + \frac{\sin\gamma}{m} \right)} \left(x^2 \cos^2\gamma + z^2 \sin^2\gamma \right). \quad (3.36)$$

The focussing terms can be considered as a skew quadrupole-like xz term (which dominates on the midplane) and a quadrupole-like $x^2 - z^2$ term that increases in magnitude away from the midplane - effectively rotating the focussing planes as γ increases - as well as geometric focussing quadratic terms acting in the plane of curvature. In the case that $\gamma = 90°$, the system acts as a combined function quadrupole plus skew dipole magnet, equivalent to a 90-degree rotation of a straight hFFA magnet [60] - together with the result from Section 2.3.1.1, this shows that a straight vFFA with $\gamma = 90°$ is completely equivalent to a straight scaling hFFA.

Equations of motion for the vFFA magnet body can now be derived by following Hamilton's equations to give

$$\begin{aligned}
\frac{\partial x}{\partial s} &= \tilde{p_x}, \\
\frac{\partial \tilde{p_x}}{\partial s} &= \frac{1}{\rho + \frac{\sin\gamma}{m}} \left[\left(\cos\gamma \left(m + \frac{2\sin\gamma}{\rho} \right) \right) z + \left(\frac{2\cos^2\gamma}{\rho} - m\sin\gamma \right) x \right] \\
\frac{\partial z}{\partial s} &= \tilde{p_z}, \\
\frac{\partial \tilde{p_z}}{\partial s} &= \frac{1}{\rho + \frac{\sin\gamma}{m}} \left[\left(\cos\gamma \left(m + \frac{2\sin\gamma}{\rho} \right) \right) x + \left(\frac{2\sin^2\gamma}{\rho} + m\sin\gamma \right) z \right].
\end{aligned} \quad (3.37)$$

We solve the system of differential equations to obtain a general solution; hence, an exact solution is found by imposing the boundary condition that at $s = 0$, $x\,(s = 0) = x_0$, $\tilde{p_x}\,(s = 0) = \tilde{p}_{x0}$, $z\,(s = 0) = z_0$, and $\tilde{p_z}\,(s = 0) = \tilde{p}_{z0}$ (analogous to the process used for the hFFA magnet body equations of motion in Section 3.1.1, though both planes of motion must be considered simultaneously for the vFFA case). The solutions then lead to a thick

lens transfer matrix for the vFFA magnet body:

$$\mathcal{M}_{\text{v-body}} = \begin{pmatrix} M_{11} & M_{12} & M_{13} & M_{14} \\ M_{21} & M_{22} & M_{23} & M_{24} \\ M_{31} & M_{32} & M_{33} & M_{34} \\ M_{41} & M_{42} & M_{43} & M_{44} \end{pmatrix}, .$$

$$M_{11} = M_{22} = \frac{(A+C+\psi)\cosh(s\omega_1) - (A+C-\psi)\cosh(s\omega_2)}{2\psi},$$

$$M_{12} = \frac{1}{2\psi}\left(\frac{(A+C+\psi)\sinh(s\omega_1)}{\omega_1} - \frac{(A+C-\psi)\sinh(s\omega_2)}{\omega_2}\right),$$

$$M_{13} = M_{24} = M_{31} = M_{42} = \frac{B(\cosh(s\omega_2) - \cosh(s\omega_1))}{\psi},$$

$$M_{14} = M_{32} = \frac{B}{\psi}\left(\frac{\sinh(s\omega_2)}{\omega_2} - \frac{\sinh(s\omega_1)}{\omega_1}\right),$$

$$M_{21} = \frac{1}{2\psi}\left(\frac{\sinh(s\omega_2)\,(A(A+C-\psi)+2B^2)}{\omega_2} - \frac{\sinh(s\omega_1)\,(A(A+C+\psi)+2B^2)}{\omega_1}\right),$$

$$M_{23} = M_{41} = \frac{B(\omega_2\sinh(s\omega_2) - \omega_1\sinh(s\omega_1))}{\psi},$$

$$M_{33} = M_{44} = \frac{(A+C+\psi)\cosh(s\omega_2) - (A+C-\psi)\cosh(s\omega_1)}{2\psi},$$

$$M_{34} = \frac{1}{2\psi}\left(\frac{(A+C+\psi)\sinh(s\omega_2)}{\omega_2} - \frac{(A+C-\psi)\sinh(s\omega_1)}{\omega_1}\right),$$

$$M_{43} = \frac{1}{2\psi}\left(\frac{\sinh(s\omega_2)\,(C(A+C+\psi)+2B^2)}{\omega_2} - \frac{\sinh(s\omega_1)\,(C(A+C-\psi)+2B^2)}{\omega_1}\right),$$

$$\psi = \sqrt{(A+C)^2+4B^2},$$

$$\omega_1^2 = \frac{-A+C-\psi}{2},$$

$$\omega_2^2 = \frac{-A+C+\psi}{2},$$

$$A = \frac{m\,(m\rho\sin(\gamma) - 2\cos^2(\gamma))}{\rho(\sin(\gamma)+m\rho)},$$

$$B = \frac{m\cos(\gamma)(2\sin(\gamma)+m\rho)}{\rho(\sin(\gamma)+m\rho)},$$

$$C = \frac{m\sin(\gamma)(2\sin(\gamma)+m\rho)}{\rho(\sin(\gamma)+m\rho)}.$$

(3.38)

The motion is apparent as a system with two distinct frequencies of oscillation, ω_1 and ω_2. These correspond to the normal modes of the coupled system. A transfer matrix for the

thin lens limit can be derived directly from the equations of motion (Eq. (3.37)) as follows:

$$\mathcal{M}_{\text{v-body}} \simeq \begin{pmatrix} 1 & 0 & 0 & 0 \\ \frac{L}{\rho+\frac{\sin\gamma}{m}}\left(\frac{2\cos^2\gamma}{\rho} - m\sin\gamma\right) & 1 & \frac{L}{\rho+\frac{\sin\gamma}{m}}\left(\cos\gamma\left(m+\frac{2\sin\gamma}{\rho}\right)\right) & 0 \\ 0 & 0 & 1 & 0 \\ \frac{L}{\rho+\frac{\sin\gamma}{m}}\left(\cos\gamma\left(m+\frac{2\sin\gamma}{\rho}\right)\right) & 0 & \frac{L}{\rho+\frac{\sin\gamma}{m}}(\left(\frac{2\sin^2\gamma}{\rho} - m\sin\gamma\right) & 1 \end{pmatrix}. \tag{3.39}$$

This result can be further simplified for large ρ, in which case terms proportional to $1/\rho^2$ (i.e. the geometric focussing terms) can be ignored, giving the matrix

$$\mathcal{M}_{\text{v-body}} \simeq \begin{pmatrix} 1 & 0 & 0 & 0 \\ -\frac{mL}{\rho+\frac{\sin\gamma}{m}}\sin\gamma & 1 & \frac{mL}{\rho+\frac{\sin\gamma}{m}}\cos\gamma & 0 \\ 0 & 0 & 1 & 0 \\ \frac{mL}{\rho+\frac{\sin\gamma}{m}}\cos\gamma & 0 & -\frac{mL}{\rho+\frac{\sin\gamma}{m}}\sin\gamma & 1 \end{pmatrix}. \tag{3.40}$$

This can be intuitively recognised as superimposed thin lens quadrupole and skew quadrupole matrices of strengths $m\sin\gamma/\left(\rho+\frac{\sin\gamma}{m}\right)$ and $m\cos\gamma/\left(\rho+\frac{\sin\gamma}{m}\right)$ respectively.

3.2.2 vFFA edge focussing

As for the hFFA edge focussing effect detailed in Section 3.1.2, when the beam crosses the edge of a magnet at an angle, a particle with a nonzero transverse displacement from the reference trajectory will travel an extra length within the magnet, proportional to the particle's displacement. However, for the vFFA, the reference trajectory will not necessarily be horizontal at the point it crosses the end plane of the magnet. As such, the edge effects must be characterised in terms of two angles: α, the angle about the vertical axis between the orbit and the normal vector of the magnet end plane, and γ, the angle through which the orbit is rotated about the magnet end plane normal (Fig. 3.4) with respect to the horizontal. Note that these coordinates are defined with respect to the magnet end plane, so for sector magnets or magnets with tilted end planes, the γ angle used here may not be equal to the γ used in the magnet body.

The extra length travelled within the magnet can then be expressed as

$$\Delta L = x\tan\alpha\cos\gamma + y\tan\alpha\sin\gamma. \tag{3.41}$$

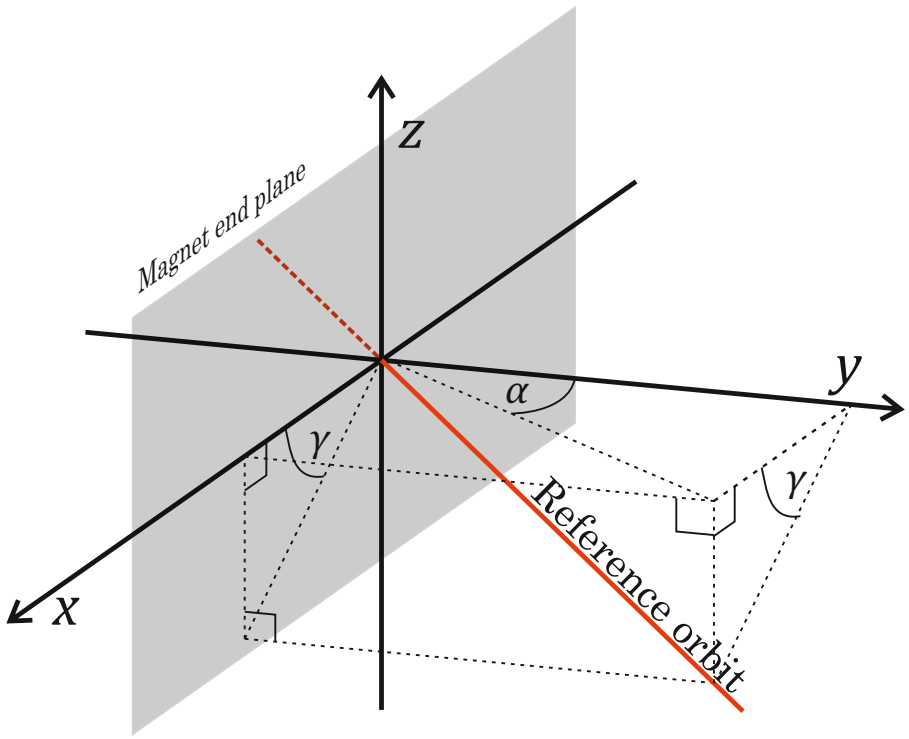

Figure 3.4: Illustration of reference orbit (red) crossing vFFA magnet boundary. The angle between the magnet end plane normal y and the reference orbit is denoted α, whilst the bank angle between the horizontal plane and the plane in which α lies is labelled γ.

Expanded to first order around x_0 (where, as previously, x_0 represents the horizontal offset from the magnet midplane) the magnetic fields can be written as

$$\begin{aligned} B_x &= -B_0(1+mz)\left(mx\cos mx_0 + \sin mx_0\right), \\ B_y &= 0, \\ B_z &= B_0(1+mz)\left(\cos mx_0 - mx\sin mx_0\right). \end{aligned} \tag{3.42}$$

The same Lorentz force treatment employed in Section 3.1.2 can be once again utilised to find the change in momenta as a consequence of a thin lens kick:

$$\begin{aligned} \delta x &= 0, \\ \delta\tilde{p_x} &= \delta L B_z \frac{q}{P_0} = \left(x\cos\gamma + y\sin\gamma\right) B_z \tan\alpha, \\ \delta z &= 0, \\ \delta\tilde{p_z} &= -\delta L B_x \frac{q}{P_0} = -\left(x\cos\gamma + y\sin\gamma\right) B_x \tan\alpha. \end{aligned} \tag{3.43}$$

Substituting in the fields, Eq. (3.42), and truncating the resulting expression at the first order leaves

$$\begin{aligned} \delta x &= 0, \\ \delta\tilde{p_x} &= \left(x\cos\gamma + y\sin\gamma\right) \frac{qB_0}{P_0} \left(\cos mx_0\right) \tan\alpha, \\ \delta z &= 0, \\ \delta\tilde{p_z} &= \left(x\cos\gamma + y\sin\gamma\right) \frac{qB_0}{P_0} \left(\sin mx_0\right) \tan\alpha, \end{aligned} \tag{3.44}$$

which can be written in transfer matrix form as

$$\mathcal{M}_{\text{v-edge}} = \begin{pmatrix} 1 & 0 & 0 & 0 \\ \frac{qB_0}{P_0}\cos\gamma\tan\alpha\cos mx_0 & 1 & \frac{qB_0}{P_0}\sin\gamma\tan\alpha\cos mx_0 & 0 \\ 0 & 0 & 1 & 0 \\ \frac{qB_0}{P_0}\cos\gamma\tan\alpha\sin mx_0 & 0 & -\frac{qB_0}{P_0}\sin\gamma\tan\alpha\sin mx_0 & 1 \end{pmatrix}. \tag{3.45}$$

In the special case where the magnets are rectangular and the change in transverse position of the orbit with respect to the midplane is small, the γ used to characterise the edge angle effects is equal to the inclination angle γ in the magnet body, and hence the transfer matrix reduces to

$$\mathcal{M}_{\text{v-edge-rect}} = \begin{pmatrix} 1 & 0 & 0 & 0 \\ \frac{qB_0}{P_0}\cos^2\gamma\tan\alpha & 1 & \frac{qB_0}{P_0}\cos\gamma\sin\gamma\tan\alpha & 0 \\ 0 & 0 & 1 & 0 \\ \frac{qB_0}{P_0}\cos\gamma\sin\gamma\tan\alpha & 0 & -\frac{qB_0}{P_0}\sin^2\gamma\tan\alpha & 1 \end{pmatrix}. \tag{3.46}$$

3.2.3 vFFA fringe fields

Finally, the effect of the magnet fringe fields must be considered. At the edge of the magnet, the field must continuously vary over a finite length, such that it is zero far away from the magnet, and has the nominal strength in the magnet (see the treatment of this in the hFFA, Section 3.1.3). Once again, as a first approximation, we assume a linear falloff over a length L_f such that:

$$B_z = \begin{cases} 0 & Y \leq 0, \\ B_0 e^{mZ} F(X) Y / L_f & 0 < Y \leq L_f, \\ B_0 e^{mZ} & Y > L_f. \end{cases} \tag{3.47}$$

where F(X) is a function to be found. Examining the region $0 < Y \leq L_f$, the remaining components of the field are assumed to take the form

$$\begin{aligned} B_x &= B_0 e^{mZ} G(X) g(Y) \\ B_y &= B_0 e^{mZ} H(X) h(Y), \end{aligned} \tag{3.48}$$

in which $G(X), g(Y), H(X)$, and $h(Y)$ are all arbitrary functions to be determined. Applying Maxwell's equation $\nabla \times B = 0$ in this region, we find

$$\begin{aligned} (\nabla \times B)_X &= B_0 e^{mZ} \left(\frac{F(X)}{L_f} - m H(X) h(Y) \right) = 0, \\ (\nabla \times B)_Y &= B_0 e^{mZ} \left(m G(X) g(y) - \frac{Y F'(X)}{L_f} \right) = 0, \\ (\nabla \times B)_Z &= B_0 e^{mZ} \left(H'(X) h(y) - G(X) g'(Y) \right) = 0, \end{aligned} \tag{3.49}$$

all of which can be satisfied if $H(X) = F(X), h(Y) = \frac{1}{mL_f}, g(Y) = \frac{Y}{L_f}$, and $G(X) = \frac{F'(X)}{m}$. Finally, substituting all of this into Maxwell's equation $\nabla \cdot B = 0$ gives

$$B_0 e^{mZ} G'(X) g(Y) + B_0 e^{mZ} H(X) h'(Y) + m B_0 e^{mZ} F(X) Y / L_f = 0, \tag{3.50}$$

$$\frac{B_0 e^{mZ} F''(X) Y}{m L_f} + 0 + m B_0 e^{mZ} F(X) Y / L_f = 0. \tag{3.51}$$

Solving this differential equation in $F(X)$ with the same boundary conditions as in Section 2.3.1.1 leads to the following expression for the magnetic fields in the fringe region of a

vFFA magnet:

$$\begin{aligned} B_X &= -B_0 e^{mZ} \sin mX \frac{Y}{L_f}, \\ B_Y &= \frac{B_0}{mL_f} e^{mZ} \cos mX, \\ B_Z &= B_0 e^{mZ} \cos mX \frac{Y}{L_f}. \end{aligned} \tag{3.52}$$

To obtain a transfer matrix for the fringe field of a vFFA from these fields, we approximate the change in position and momentum coordinates as a thin lens Lorentz kick proportional to the integral of the fields over the fringe field length as seen by a given particle. In order to do this, we define a new local orthogonal coordinate system x, y, z, in which the y axis is aligned with the trajectory through the fringe. The transformation between the X, Y, Z coordinates and the new x, y, z coordinates is computed as a rotation through a roll angle γ about the Y-axis (which is not necessarily equal to the inclination γ of the magnet body, depending on the geometry of the magnet) followed by a rotation through a yaw angle α about the Z-axis; we also include a horizontal translation in this step to account for the offset of the beam centroid (X_0) with respect to the magnet midplane:

$$\begin{pmatrix} x \\ y \\ z \end{pmatrix} = \begin{pmatrix} \cos\alpha & -\sin\alpha & 0 \\ \sin\alpha & \cos\alpha & 0 \\ 0 & 0 & 1 \end{pmatrix} \begin{pmatrix} \cos\gamma & 0 & \sin\gamma \\ 0 & 1 & 0 \\ -\sin\gamma & 0 & \cos\gamma \end{pmatrix} \begin{pmatrix} X - X_0 \\ Y \\ Z \end{pmatrix} = R \begin{pmatrix} X - X_0 \\ Y \\ Z \end{pmatrix}. \tag{3.53}$$

As we are approximating the fringe field effect as a thin lens, we are able to neglect the change in transverse position over the length of the fringe (assuming also that α is small). This means that we can integrate the field based on the original coordinates from $Y = 0$ to $Y = L_f / \cos\alpha$, and then transform the integrals to the x, y, z frame. We then Taylor-expand in the dynamical variable, collect first order terms and normalise by the magnetic rigidity to obtain the elements of the linear map. Fields collinear with the reference trajectory only interact through the transverse momentum of the particle, so we keep the 0-th order component of B_y only.

This gives a thin lens transfer matrix for the vFFA fringe field as:

$$\mathcal{M}_{\text{v-fringe-}xyz} = \begin{pmatrix} 1 & 0 & 0 & 0 \\ K_{zx} & 1 & K_{zz} & -K_y \\ 0 & 0 & 1 & 0 \\ -K_{xx} & K_y & -K_{xz} & 1 \end{pmatrix} \tag{3.54}$$

$$\begin{aligned} K_{xx} &= -\frac{1}{2\rho}(-\cos(\alpha+\gamma-mX_0)+\cos(\alpha-\gamma+mX_0)+L_f m\cos(2\gamma-mX_0)), \\ K_{xz} &= -\frac{1}{2\rho}\sec(\alpha)(\sin(\alpha+\gamma-mX_0)+\sin(\alpha-\gamma+mX_0)-L_f m\sin(2\gamma-mX_0)), \\ K_y &= \frac{(2\cos(mX_0)+L_f m\tan(\alpha)\sec(\alpha)\sin(\gamma-mX_0))}{2m\rho}, \\ K_{zx} &= \frac{1}{2\rho}L_f m\sec(\alpha)\sin(2\gamma-mX_0), \\ K_{zz} &= \frac{1}{2\rho}L_f m\sec^2(\alpha)\cos(2\gamma-mX_0), \end{aligned} \tag{3.55}$$

in which we have used the definition of the magnetic rigidity. To transform back into the original Frenet-Serret coordinates, we apply a roll transformation to the 4D phase space to obtain our final transfer matrix as

$$\mathcal{M}_{\text{v-fringe}} = \mathcal{R}_4^T \mathcal{M}_{\text{v-fringe-}xyz}\mathcal{R}_4, \tag{3.56}$$

$$\mathcal{R}_4(\gamma) = \begin{pmatrix} \cos\gamma & 0 & \sin\gamma & 0 \\ 0 & \cos\gamma & 0 & \sin\gamma \\ -\sin\gamma & 0 & \cos\gamma & 0 \\ 0 & -\sin\gamma & 0 & \cos\gamma \end{pmatrix}. \tag{3.57}$$

One of the most immediate effects of the vFFA fringe fields can be seen in the inclusion of longitudinal fields (the K_y terms in the transfer matrix, Eq. (3.54)). We see that there exists a longitudinal field component that couples the $\tilde{p_x}$ and $\tilde{p_z}$ momenta, and that the strength of this component in the transfer matrix depends only on the m-value, being unaffected by the length of the fringe field. This component is additionally independent of the form of the fringe field falloff (assuming that the trajectory can be considered a straight line), as shown using an alternative derivation in Section 2.5. For rectangular magnets in a FODO configuration, where $\gamma = mX_0$ (i.e. the inclination in the magnet body is equal to the roll angle of the coordinate system through the fringe), we find additionally that the longitudinal fields vanish in the limiting case of a 90° inclination.

3.2.4 Properties of vFFA lattices

Using the transfer matrices derived in the previous section, and the closed orbit models from Chapter 2, complete optical models of vFFAs can be assembled. A transfer matrix for a cell, $\mathcal{M}$ is assembled by multiplying matrices corresponding to each element in the cell with parameters set based on the closed orbits. One important distinction between hFFA and vFFA optics is the presence of coupling between the transverse dimensions for the vFFA. In the case of the hFFA, the cell transfer matrix can be considered a block diagonal matrix (as matrices for all individual lattice components are also block diagonals), with the upper left 2×2 block fully characterising the horizontal motion, and the lower right block describing the vertical dynamics. The elements of off-diagonal blocks are all zero, and therefore there is no effect from the position in horizontal phase space on the motion in vertical phase space, and vice versa. This is not the case for the vFFA, where the magnet body and fringe field elements can have non-zero off-diagonal blocks. As a consequence of this, the cell transfer matrix for a vFFA cell will not necessarily be in block diagonal form, and the motion in horizontal and vertical phase spaces cannot be separated.

A number of linear decoupling procedures exist, with well-known examples being found in the work of Edwards and Teng [64], and Parzen [65]. These methods, when applied to a system with two degrees of freedom, block diagonalise the 4D coupled matrix describing the periodic motion such that it can be considered as two systems oscillating in two decoupled planes (usually denoted as u and v, leading to the nomenclature uv-space for the combined 4D phase space describing the decoupled motion). It can be shown that the eigenvalues of a matrix $\mathcal{M}$ that can be block diagonalised to the matrix $\mathcal{B}$ are equal to the eigenvalues of $\mathcal{B}$. If $\mathcal{P}$ is the decoupling transformation, we have

$$\mathcal{B} = \mathcal{P}^{-1}\mathcal{M}\mathcal{P}, \tag{3.58}$$

then if $\mathbf{v}$ is an eigenvalue of $\mathcal{M}$ with eigenvalue λ such that $\mathcal{M}\mathbf{v} = \lambda\mathbf{v}$, we can write

$$\mathcal{P}\mathcal{B}\mathcal{P}^{-1}\mathbf{v} = \lambda\mathbf{v}, \tag{3.59}$$

Parameter	Value
N	720
β_F	$0.085714°$
β_D	$0.085714°$
r_0	4010.651232m
θ_F	$0.875°$
γ_F	$-25°$
m	4m^{-1}
c_1	0.05m

Table 3.1: Default parameters of the test vFFA FODO lattice, used to benchmark the analytic model of the closed orbits and optics against numerical predictions. These parameters are loosely based on preliminary designs for a muon accelerator ring for the LHC tunnel [61].

$$\mathcal{B}\left(\mathcal{P}^{-1}\mathbf{v}\right) = \lambda\left(\mathcal{P}^{-1}\mathbf{v}\right), \tag{3.60}$$

showing that $\mathcal{P}^{-1}\mathbf{v}$ is indeed an eigenvalue of $\mathcal{B}$ with the same eigenvalue λ. Therefore, if the decoupled tunes in uv-space are given by the argument of the eigenvalues of each block of the matrix $\mathcal{B}$ normalised by 2π, these same tunes can be computed directly from the eigenvalues of $\mathcal{M}$. Decoupled tunes for vFFA lattices are computed in this manner for the purposes of the following analyses.

The predictions of the analytic model are once again benchmarked against tune calculations from FIXFIELD, which computes decoupled $u-$ and $v-$ tunes using the Parzen decoupling routine. A test lattice with parameters listed in Table 3.1 is constructed in the analytic model, and the closed orbit calculations are used to assemble an equivalent FIXFIELD model. This lattice is chosen as it has a small dipole ratio, so the closed orbit is expected to be determined mostly by the magnet body behaviour rather than the fringe fields. The length of fringe fields is small when compared to the magnet lengths, and therefore the thin lens approximations used in deriving the fringe field transfer matrices are expected to hold well. In fact, comparing the cumulative integrals of magnetic fields throughout the cell (Fig. 3.5), it is reasonable to expect that the optics of this system should be dominated by the magnet body behaviour.

The model is able to accurately predict the range of stable θ_F values for this large-ring

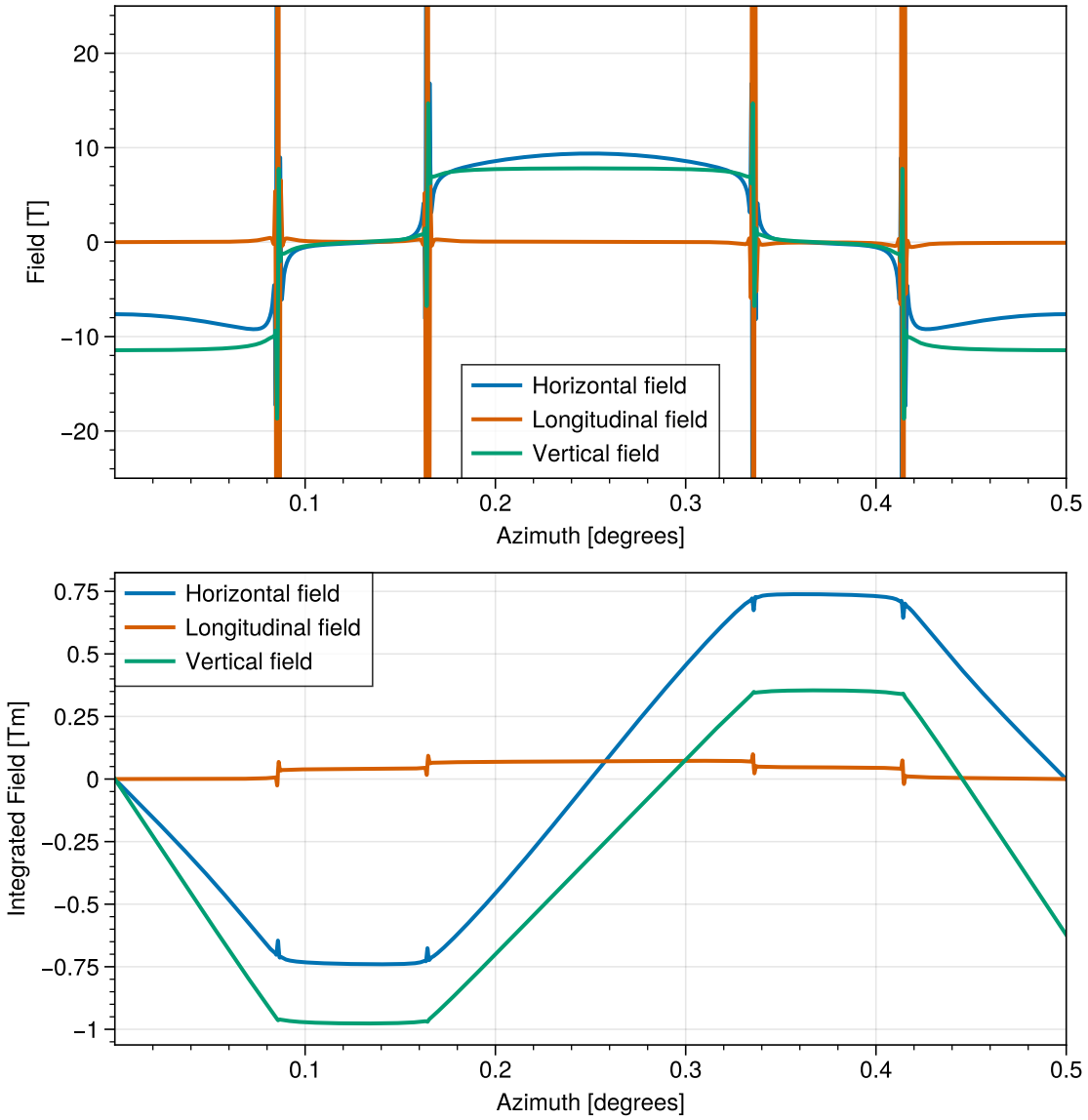

Figure 3.5: a). Fields through one cell of the test lattice, with parameters listed in Table 3.1.
b). Cumulative integral of the transverse and longitudinal fields along the closed orbits.

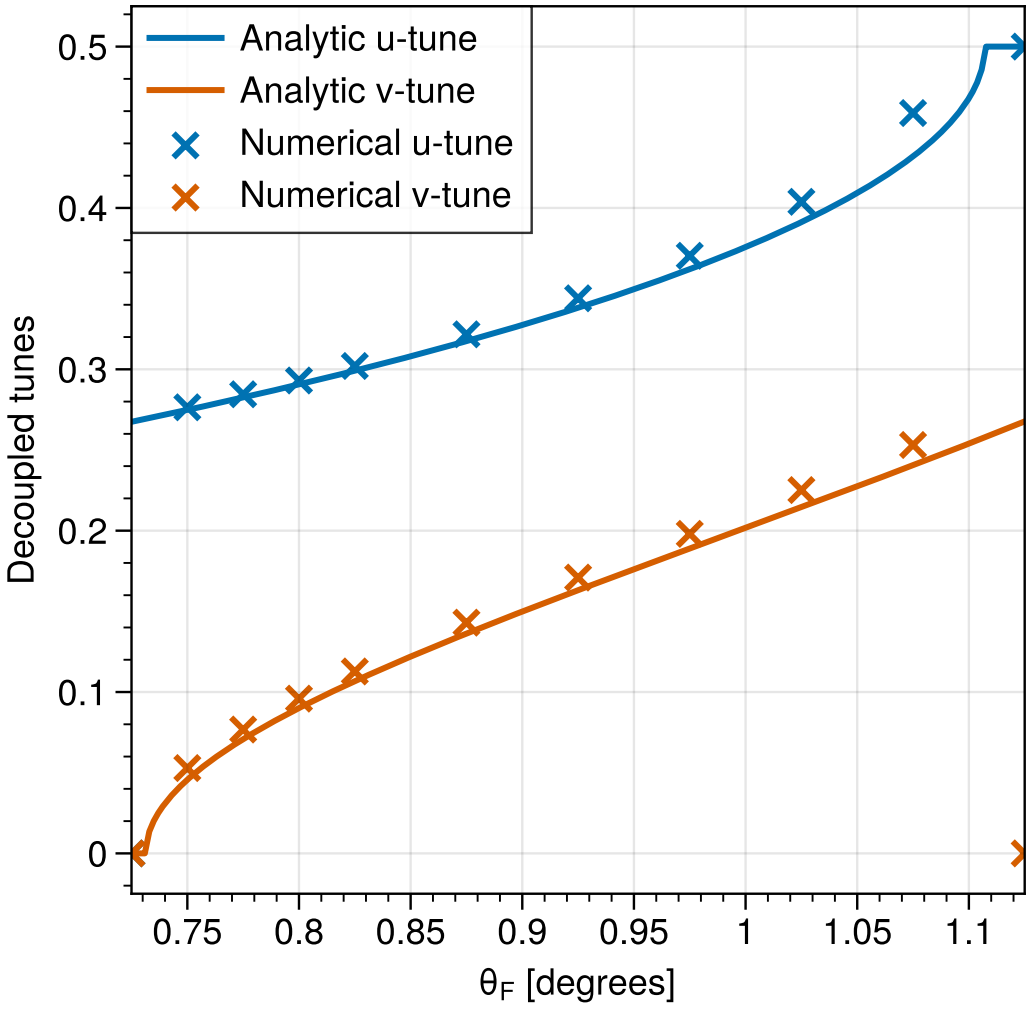

Figure 3.6: Decoupled u and v-tunes as a function of the input θ_F in the test vFFA lattice.

FODO lattice, when compared with numerical simulation, as demonstrated in Figure 3.6. The figure shows the behaviour of the two decoupled tunes as a function of the bending angle in the F-magnet. The tune dependence of the analytic model matches the behaviour of the numerical model, and the largest discrepancy in tune for the points evaluated is of order 10%.

Similarly, the prediction of the decoupled tunes as a function of the m-value shows good agreement for values of m greater than approximately $3/\mathrm{m}$: Figure 3.7 shows the dependence of the tunes on the chosen m-value. However, below this point, the analytic and numerical predictions diverge for the v-tune, with the numerical simulation tune decreasing more gradually compared to the analytic tune before a rapid decline towards 0. Whilst the result shown here implies good agreement for larger values of m, and the difference in the predicted minimum stable values of m is small (approximately $2.24/\mathrm{m}$ in the numerical model compared to 2.62 for the analytic), the behaviour of the tune for lower m implies the existence of an effect not accounted for by the analytic model.

The missing effect is likely to be a consequence of a fringe field effect: we know that the integrated longitudinal field effect is proportional to $1m^{-1}$, so this will be strongest at low m values. Section 2.5 discussed the influence of fringe fields on the closed orbit, and how the predicted closed orbit of the analytic model diverges from the numerically simulated closed orbit. On top of this, the thin-lens fringe field model derived above is unable to include the effect of Larmor rotation [66], an effective rotation of the optical planes that occurs in regions with longitudinal fields. Moreover, the modelling above assumed a linear fringe field function, which implied that the longitudinal field value must change instantaneously from zero to a constant value at the beginning of the fringe and back again at the end. This means that the fields are discontinuous, and are not technically Maxwellian. If the axial field distribution is defined by some smoothly varying continuous function $B(y)$, then there exists a radial component of the magnetic field as

$$B_r = -\frac{|\mathbf{r}|}{2}\frac{dB(z)}{dy}, \tag{3.61}$$

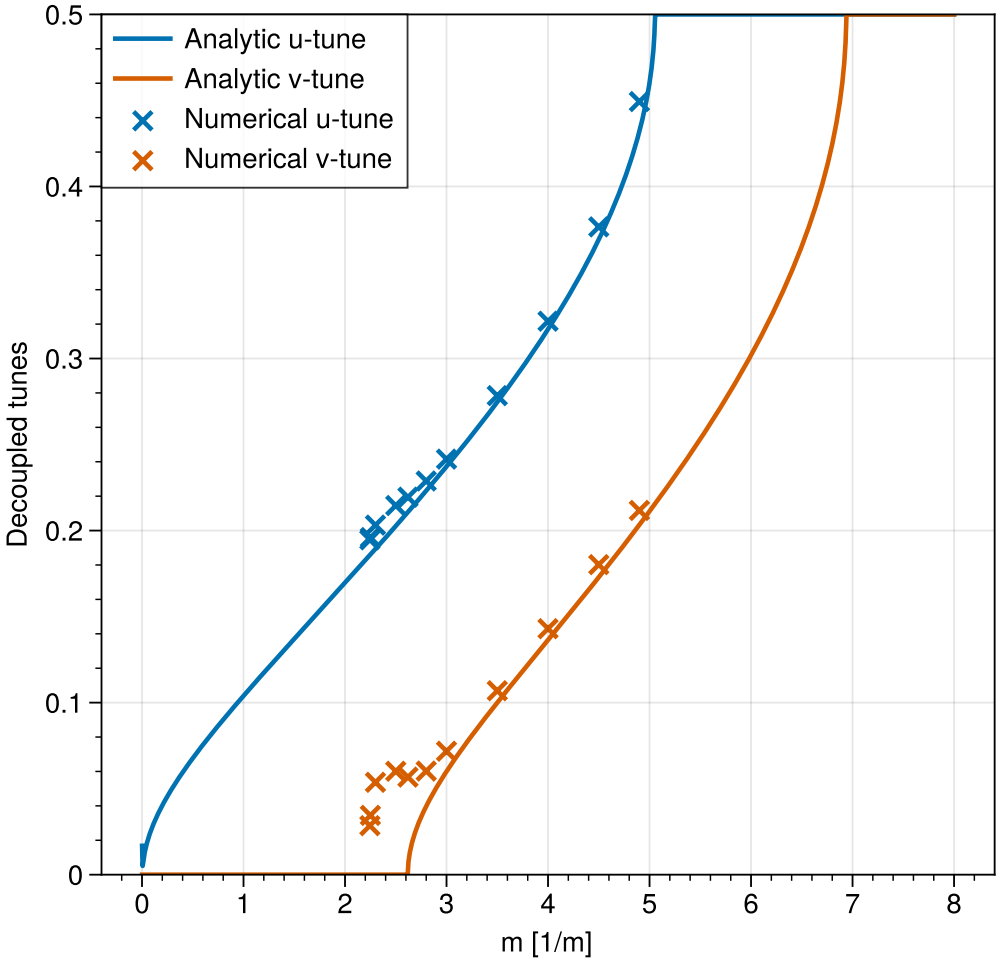

Figure 3.7: Decoupled u and v-tunes as a function of the input m-value in the test vFFA lattice.

in which $\mathbf{r}$ denotes a transverse radial coordinate $\mathbf{r} = \mathbf{x} + \mathbf{z}$ [66].

The effects of radial field components cannot be accounted for in a single thin lens transfer matrix. The elements of the matrix corresponding to the radial field would be given by the integral of the longitudinal field over the length of the fringe; as we know that the longitudinal field is zero before the fringe region and zero afterwards, the integral of its longitudinal derivative over this length must always be zero. As a consequence, a single thin lens would not be able to account for the radial field effects in the fringe field of a magnet.

These problems are exacerbated at low m-values: because the longitudinal field is proportional to $1m^{-1}$, its derivatives, and thereby the radial field strengths, must also be proportional to $1m^{-1}$, whilst the quadrupole-like and skew-quadrupole-like focussing terms in the magnet body Hamiltonian are proportional to m. This implies that as the m-value decreases the relative effect of the magnet body decreases, whilst the effects of the fringes increase. Therefore, at low m-values, we expect that the approximations made to derive the optical model begin to weaken, and alternative methods of analysis must be developed.

3.2.5 vFFA harmonic analysis

The model of the optics developed above has a number of limitations. Firstly, as discussed in Section 2.5, when the dipole ratio becomes large, the analytic model is no longer accurately able to predict the closed orbit. Moreover, when the length of the fringe field becomes similar to the length of the magnets, the thin lens approximation used for the fringe fields is no longer applicable. To understand the focussing structures of these lattices, and to characterise their behaviour, a numerical technique based on multipole decomposition is introduced. We term this technique harmonic analysis. This analysis uses a step-by-step process as follows:

1. Identify closed orbit via tracking (as in Section 2.1.2).

2. Record position and momentum at each integration step along the closed orbit.

3. Generate a unit vector $\hat{\mathbf{a}}$ perpendicular to the vertical unit vector $\hat{\mathbf{z}}$ and the unit vector tangential to the closed orbit $\hat{\mathbf{u}}$ at a point on closed orbit.

4. Generate a second unit vector $\hat{\mathbf{b}}$ perpendicular to both $\hat{\mathbf{a}}$ and $\hat{\mathbf{u}}$. $\hat{\mathbf{a}}$ and $\hat{\mathbf{b}}$ then form a basis orthogonal to the closed orbit.

5. Draw a circle at radius dr in the $\hat{\mathbf{a}}, \hat{\mathbf{b}}$ plane.

6. Record Cartesian magnetic fields at N points along the circumference of this circle. These points are defined in terms of an angle θ, which is an integer multiple of $2\pi/N$. θ characterises the angle between a radius vector $\mathbf{r}$ of length dr and the basis vector $\hat{\mathbf{a}}$.

7. Re-express Cartesian fields in terms of the radial field component perpendicular to the circumference of the circle, i.e.

$$B_r(\theta) = \mathbf{B} \cdot \mathbf{r} = \mathbf{drB} \cdot \left(\hat{\mathbf{a}} \cos\theta + \hat{\mathbf{b}} \sin\theta \right). \tag{3.62}$$

8. Take the Fast Fourier Transform (FFT) [67] of $B_r(\theta)$. The resulting complex Fourier Series gives the field on the circle as a series of circular harmonics.

9. Map the Fourier Series coefficients to the coefficients of an arbitrary-order magnetic multipole. By comparing the Fourier Series to the standard form of the multipole expansion in polar coordinates [7]

$$B_a + iB_b = B_{\text{ref}} \sum_{n=1}^{\infty} (b_n + ia_n) \left(\frac{re^{i\theta}}{R_{\text{ref}}} \right)^{n-1} \tag{3.63}$$

we can see that the normal and skew multipole coefficients b_n and a_n are equal to the real and imaginary coefficients of this Fourier series normalised by dividing by dr^{n-1} (note: the Fourier series starts at $n = 0$, whilst the multipole expansion is valid from $n = 1$). This means that the $n = 1$ element of the Fourier series measured about a point on the closed orbit describes the dipole field at that point, the $n = 2$ element

describes the quadrupole and skew quadrupole coefficients, and so on. The $n = 0$ entry of the Fourier series describes the zero-frequency (i.e. constant) component of the field. For this particular case, this means that the zeroth component of the Fourier series describes the local 2D monopole radial component of the field. Note that as this is a 2D projection of a 3D field, this radial field can be nonzero, and is in fact proportional to $\frac{dB_y}{dy}$ [66]. It is also important to measure the local longitudinal magnetic field (i.e. the field immediately parallel to the closed orbit) and to record this.

10. Iterate process for each integration step along the closed orbit, giving a multipole decomposition along the closed orbit.

11. Reconstruct the optics of the system by applying a series of thin lens multipole kicks at each integration step using the measured coefficients followed by a drift of length ds corresponding to the distance travelled over a single integration step.

By applying this procedure, the optics of a system can be understood in terms of multipole components at each step along the closed orbit, enabling us to analyse the contribution of different regions of the lattice and different orders of the multipole contributions.

The reconstruction process involves deriving thin lens kicks corresponding to each field component. These are listed in the following paragraphs (note that the effect of thin lens kicks is independent of the order in which they are applied).

We first apply kicks corresponding to the zeroth order components - i.e. the effects of longitudinal and radial fields. The effect of longitudinal field can generally be understood in terms of the concept of Larmor rotation [66], where the coupling between transverse planes can be removed by transforming to a reference frame that rotates at a Larmor frequency determined by the strength of the field and the magnetic rigidity. By transforming to this frame, we see that the longitudinal field acts to rotate the optical system.

A thin lens kick corresponding to a longitudinal field of normalised strength $k_{\text{sol}} = \frac{qB_y}{P_0}$ can be written as

$$\mathcal{M}_{\text{sol}} = \begin{pmatrix} 1 & 0 & 0 & 0 \\ 0 & 1 & 0 & k_{\text{sol}}ds \\ 0 & 0 & 1 & 0 \\ 0 & -k_{\text{sol}}ds & 0 & 1 \end{pmatrix}. \tag{3.64}$$

Similarly, the effects of a monopole radial field with normalised radial field gradient $k_{\text{rad}} = \frac{qB_r}{P_0 dr}$ can be expressed using the following transfer matrix

$$\mathcal{M}_{\text{sol}} = \begin{pmatrix} 1 & 0 & 0 & 0 \\ 0 & 1 & -k_{\text{rad}}ds & 0 \\ 0 & 0 & 1 & 0 \\ k_{\text{rad}}ds & 0 & 0 & 1 \end{pmatrix}, \tag{3.65}$$

i.e. angular momentum is imparted to the beam, proportional to the off-axis radial displacement of a particle.

To account for the curvature of the system, a further focussing kick corresponding to the curvature term in the Frenet-Serret Hamiltonian must be included. This focussing kick strength is proportional to the overall dipole field measured from the multipole decomposition, i.e $k_{\text{dipole}} = \sqrt{B_x^2 + B_z^2}$, and it acts in a plane at angle $\gamma_{\text{dipole}} = \arctan\left(B_z/B_x\right)$. The corresponding thin lens kick transfer matrix is then given by

$$\mathcal{M}_{\text{dipole}} = \mathcal{R}_4(\gamma_{\text{dipole}}) \begin{pmatrix} 1 & 0 & 0 & 0 \\ -k_{\text{dipole}}^2 Ds & 1 & 0 & 0 \\ 0 & 0 & 1 & 0 \\ 0 & 0 & 0 & 1 \end{pmatrix} \mathcal{R}_4^T(\gamma_{\text{dipole}}), \tag{3.66}$$

in which $\mathcal{R}_4$ denotes the rotation matrix given in Eq. (3.57).

The final contribution at linear-order comes from the normal and skew quadrupole terms of the harmonic decomposition. In terms of the multipole expansion, these are the coefficients b_2 and a_2 respectively. We normalise these conventionally as $k_{1n} = \frac{q}{P_0}\frac{B_{\text{ref}}}{R_{\text{ref}}}b_2$ and $k_{1s} = \frac{q}{P_0}\frac{B_{\text{ref}}}{R_{\text{ref}}}a_2$, giving the transfer matrix

$$\mathcal{M}_{\text{quad}} = \begin{pmatrix} 1 & 0 & 0 & 0 \\ -k_{1n}ds & 1 & 0 & k_{1s}ds \\ 0 & 0 & 1 & 0 \\ k_{1s}ds & 0 & k_{1n}ds & 1. \end{pmatrix} \tag{3.67}$$

The transfer matrices corresponding to each measured contribution are multiplied before a drift matrix of length ds is applied.

By constructing a cell matrix from the series of drifts and transfer matrix kicks measured from the numerical integration, the properties of the lattice can be reconstructed.

3.2.5.1 Harmonic Analysis in Large-Ring vFFA Regimes

Table 3.2 shows an example of the FIXFIELD tune compared to the harmonic analysis reconstructed tune for the $m = 4/\text{m}$ lattice and the $m = 2.25/\text{m}$ lattices plotted on Fig. 3.7. Notably, the latter case was one in which the analytic model was not able to predict the stability of the lattice; the harmonic analysis method is able to match the simulated tune to 2 decimal places, enabling an analysis of the focussing structure. Figure 3.8 shows a comparison of the closed orbits for these lattices, showing that the differences of closed orbit behaviour between the analytic model, the $m = 4/\text{m}$ simulation, and the $m = 2.25/\text{m}$ simulation are all small; Figure 3.9 shows the multipole decomposition along the cell for the two different m-values, showing that there appear large spikes of each field component at the end of the magnets for the low-m lattice. Returning to Table 3.2, we see the results of disabling certain elements in the optical reconstruction.

Critically, the low-m lattice is unstable when either longitudinal fields or radial fields are disabled. This explains the disparity between the stability of the analytic model and the numerical simulation at low values of m, showing that a simple thin lens fringe field model cannot replicate the focussing behaviour for these cases. The study performed here demonstrates the utility of the harmonic analysis approach in regions of parameter space where the assumptions necessary to construct the analytic model cannot be applied.

	FIXFIELD	Reconstruction	Longitudinal Fields Off	Radial Fields Off
$m = 4.0/\mathrm{m}$				
q_u	0.3217	0.3214	0.3213	0.3214
q_v	0.1429	0.1430	0.1432	0.1431
$m = 2.25/\mathrm{m}$				
q_u	0.1960	0.1959	0.1919	0.1930
q_v	0.0344	0.0349	N/A	N/A

Table 3.2: Cell tunes for the test vFFA FODO lattice when the optics are reconstructed using the harmonic analysis technique. The "Longitudinal Fields Off" and "Radial Fields Off" columns correspond to the calculated tunes when either longitudinal or radial field contributions are excluded from the transfer matrix reconstruction. N/A is written to denote an unstable plane of motion.

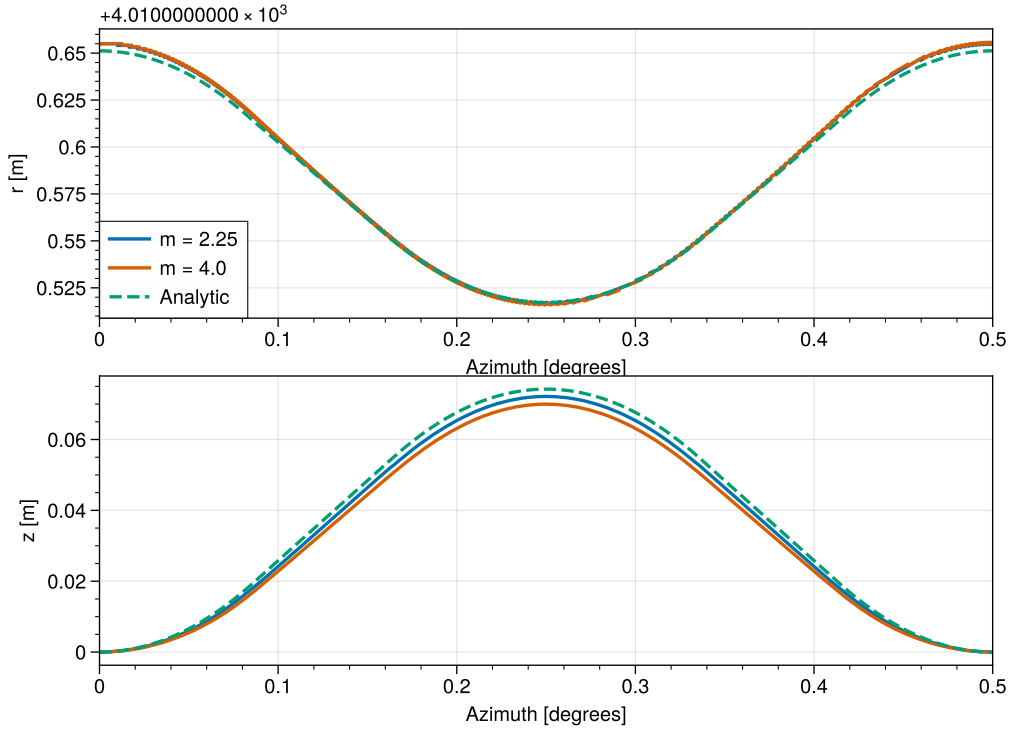

Figure 3.8: A comparison of closed orbits in a vFFA test lattice at different m-values, along with the analytic prediction. The closed orbit does not vary with m in the analytic model.

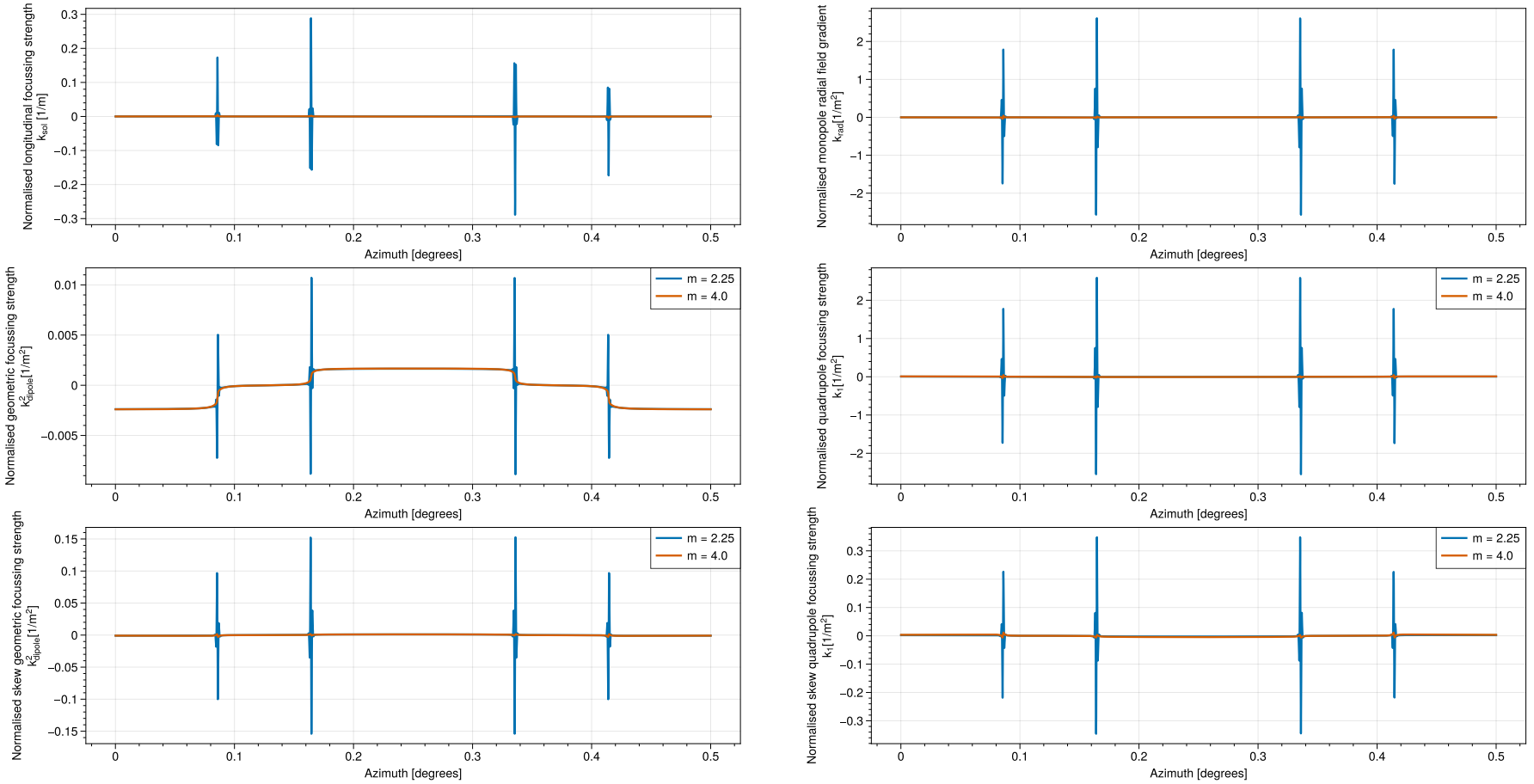

Figure 3.9: Multipole components along the closed orbit in the test vFFA FODO lattice at $m = 2.25$ and $m = 4$. All coefficients are given in terms of the respective transfer matrix elements to form a basis for understanding their comparative contributions to the focussing behaviour of the cell.

Parameter	Value
Cell Length	2.8m
L_F	0.5m
L_D	0.5m
B_{0F}	-1T
B_{0D}	2T
ΔY	0.04m
m	4.0m^{-1}
c_1	0.15m
Integration step size	0.001m

Table 3.3: Default parameters of a straight-line vFFA triplet, based on [32]. ΔY represents the horizontal displacement between F and D-magnet midplanes.

3.2.5.2 Harmonic Analysis in Small-Ring vFFA Regimes

The same harmonic analysis approach can be used to analyse small-ring vFFA lattices where the closed orbits are more strongly affected by the fringe fields, and the magnet lengths are similar to the fringe lengths. To verify the validity of the harmonic analysis multipole decomposition approach for a small-ring lattice, and to demonstrate the robustness of the method across parameter space, a comparison was generated between the tune as computed from this optical reconstruction procedure and the tune computed from the full FIXFIELD numerical simulation, for a version of the baseline FDF triplet FETS-vFFA lattice [32] (parameters displayed in table 3.3) modified to have zero net bending angle per cell. The results of this comparison are displayed in Fig. 3.10. It can be seen that the tune agrees across the full range of m-values tested.

With the effectiveness of this procedure demonstrated, it becomes possible to use the multipole decomposition to evaluate the focussing structures of the cell. Figure 3.11 displays the multipole coefficients plotted throughout the cell, along with the closed orbit. It can be seen that all components have peaks of similar magnitude, and contribute at similar orders to the optics of the cell: table 3.4 shows the tune when contributions from each element are 'switched on' in the matrix reconstruction. The results displayed in this table show how critical the effects of each aspect are to understanding the optics of the system –

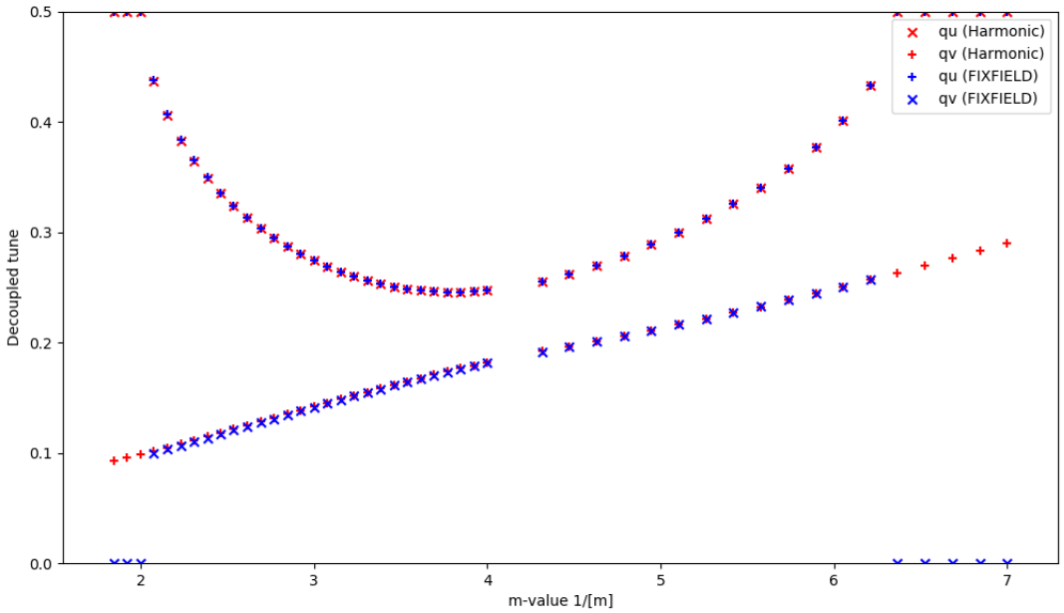

Figure 3.10: Tune dependence on m-value in a sample vFFA triplet lattice, with parameters listed in Table 3.3, showing the accuracy of the harmonic analysis method when compared with the full numerical tracking approach.

particularly the effects of longitudinal and radial fields, which contribute very little to the tune in most accelerators.

In order to characterise the significance of each focussing contribution across the parameter space, the strength of each coefficient is perturbed by a small amount (in this case 10% and the change in tune with respect to the unperturbed case is recorded. This procedure is repeated for a number of different test lattices with different m-values, and the results are shown in Fig. 3.12. We can see from this that the quadrupole-type effects dominate in both planes for high m-values ($m > 4.5/\mathrm{m}$), but the v-tune is predominantly determined by longitudinal effects below this point. Likewise, the u-tune is affected more by the longitudinal field effects below an m-value of approximately 3 per metre. Though Table 3.4 shows that each multipole element is necessary to model the cell tunes correctly, the result shown in Fig. 3.12 indicates that across the range tested the individual u and v-tunes are not sensitive to small changes in the radial fields.

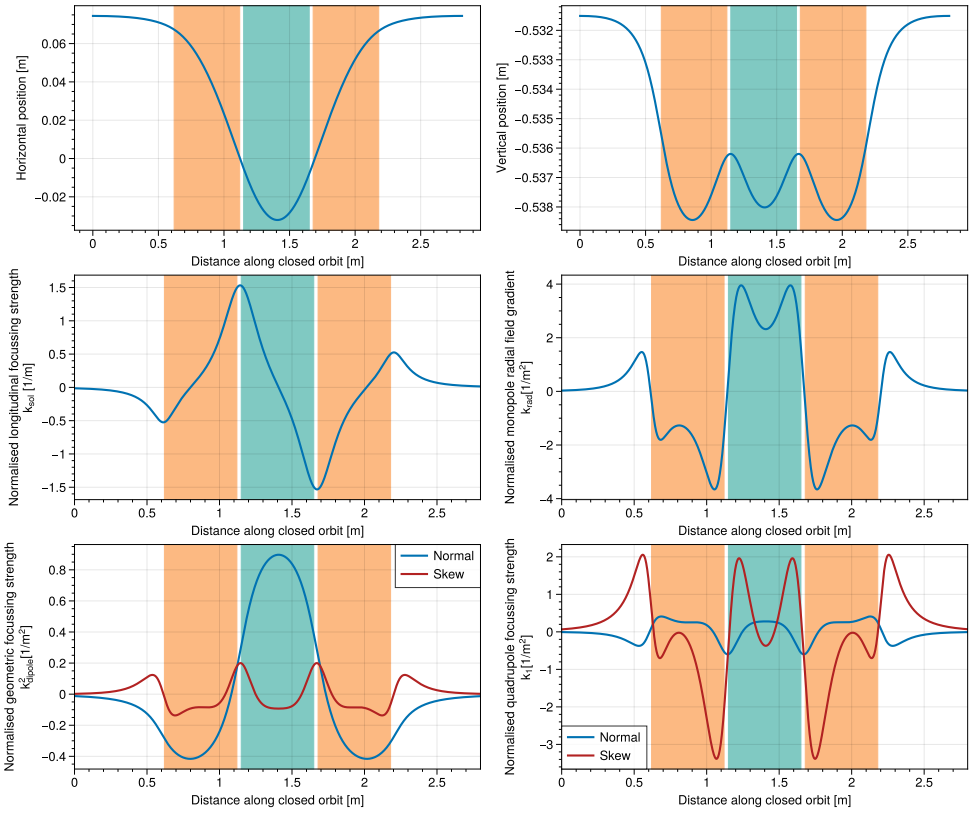

Figure 3.11: Multipole focussing coefficients throughout a sample vFFA triplet cell (Table 3.3). All coefficients are given in terms of the respective transfer matrix elements to form a basis for understanding their comparative contributions to the focussing behaviour of the cell.

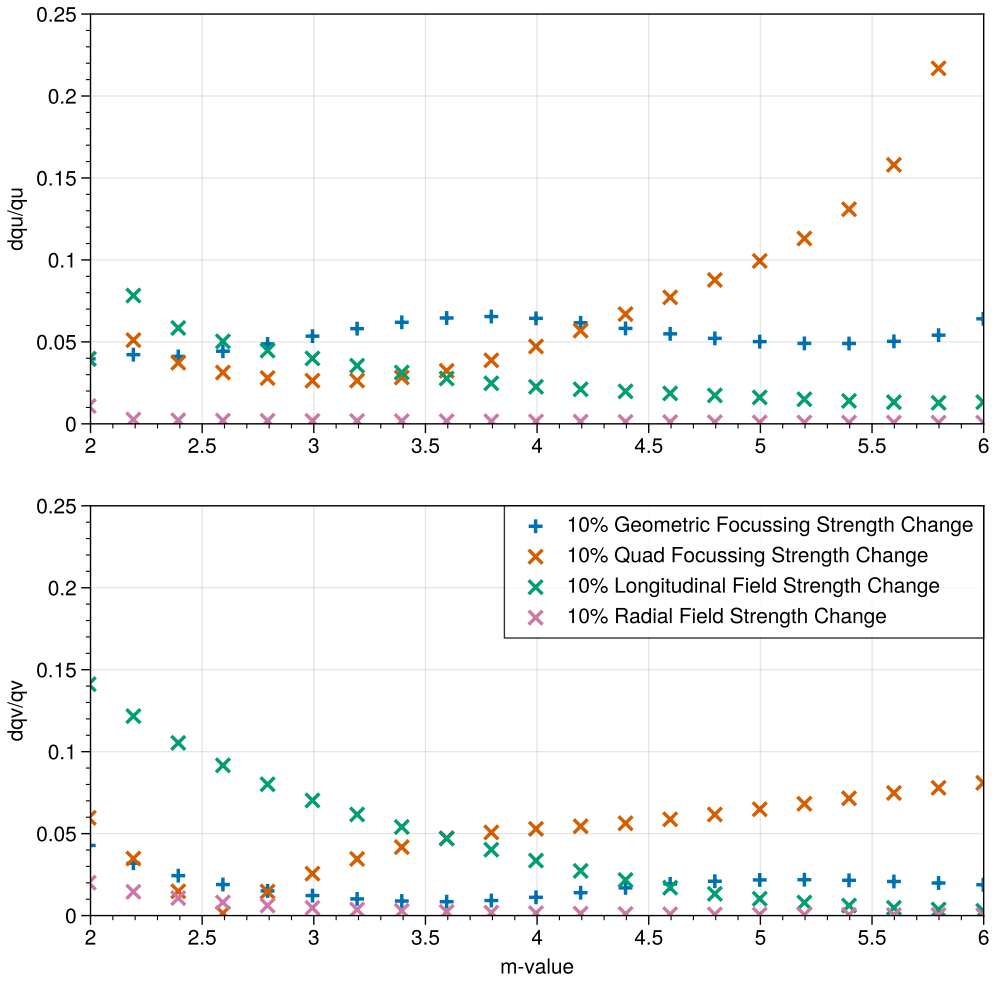

Figure 3.12: Change in tune for a small change in strength of multipole components at different m-values.

Combination	q_u	q_v
Quadrupole term only	0.137	0.124
Geometric term only	0.173	0.026
Longitudinal term only	N/A	N/A
Radial term only	0.006	0.006
Quadrupole + geometric	0.229	0.129
Quadrupole + longitudinal	0.095	0.156
Quadrupole + radial	0.079	0.079
Geometric + longitudinal	0.172	0.018
Geometric + radial	0.137	N/A
Longitudinal + radial	0.102	0.102
Quadrupole + geometric + longitudinal	0.211	0.154
Quadrupole + geometric + radial	0.196	0.079
Quadrupole + longitudinal + radial	0.141	0.192
Geometric + longitudinal + radial	0.203	0.104
Quadrupole + geometric + longitudinal + radial	0.247	0.182
Full numerical tracking	0.247	0.182

Table 3.4: Cell tunes of a straight-line vFFA triplet when the optics are reconstructed using the multipole kick decomposition. The combination column lists which focussing contributions that have been included in the optical reconstruction, and the q_u and q_v columns show the corresponding decoupled tunes.

3.3 Chapter Summary

In this chapter, modelling techniques for the linear optics of scaling hFFAs were reviewed. A Hamiltonian dynamics approach was used to derive transfer matrices for optical elements in an hFFA, and the transfer matrices were combined with the closed orbit modelling from Section 2 to assemble fully integrated models of hFFA lattices. The prediction of the cell tune as a function of input parameters was then benchmarked against a FIXFIELD simulation, and the analytic and simulated stability footprints were compared. We found close agreement for the stability region in the θ_F, k parameter space, with tunes diverging slightly for large values of θ_F due to fringe field effects.

Knowledge of these techniques was then applied in developing an equivalent approach for the vFFA, deriving for the first time a thick lens vFFA magnet body transfer matrix from the Frenet-Serret Hamiltonian, as well as thin lens edge focussing and fringe-field

matrices. These were then integrated together with the closed orbit models derived in Section 2 to obtain a full model of a vFFA, which was tested in a large-ring regime where the approximations of the modelling approach were expected to hold well. The results were found to agree with simulation, predicting accurate tunes as a function of θ_F and m, though the model was found to be limited at low m-values. A method based on multipole decomposition was then derived for study of the focussing structures in areas where the assumptions of the analytic model break down. Using this, we found that radial field effects were required for stability of the large-ring lattice at low m-values, though otherwise the tunes are well-predicted by the quadrupole and skew-quadrupole-like behaviour modelled by the magnet body transfer matrices.

In contrast, the multipole decomposition study identified that in a short-magnet regime (studied using a test lattice based on the FETS-vFFA triplet lattice), all focussing elements contributed much more significantly across the range of m-values tested, with full inclusion of all elements required to retrieve a tune accurate to within 2 decimal places. Whilst at high m-values the quadrupole and skew quadrupole elements became the predominant determining factor in the tune for these lattices, longitudinal fields were dominant for m-values below 4 per metre.

The successful development of an analytic model for the optics of a vFFA enables the study of the design and optics of novel vFFA lattices in regimes where the approximations used to derive the model hold, rendering possible the effective design of new vFFA rings for practical purposes. Meanwhile, the creation of a numerical tool for optical reconstruction lends itself to the analysis of optical properties where complete analytic models are unable to describe systems.

Chapter 4

Non-linear Dynamics of Fixed Field Accelerators

Whilst a first-order understanding of beam dynamics for a given lattice can be obtained from the analysis of linear effects (i.e. analyses in which we have applied linear approximations to the equations of motion to allow for exact solutions), higher-order terms in the equations of motion lead to additional nonlinear effects that have important consequences for machine design and operation. An example of such an effect is amplitude-dependent tune shift, which is a change in the tune for an individual particle as a function of the amplitudes of its motion in phase space.

Amplitude-dependent tune shift can place an effective limit on dynamic aperture (DA) by restricting the maximum amplitude of particles in stable motion; whilst an accelerator may be designed such that the nominal tune is away from resonance, the presence of a tune shift with amplitude means that particles oscillating with a large amplitude may encounter resonances, causing beam loss. Ensuring a large dynamic aperture is critical when it comes to minimising losses in a machine, and therefore is an especially salient consideration when it comes to the design of high-power accelerators (where beam losses reduce the potential maximum current, as well as carrying the risks of incurring damage to and irradiating machine components). Understanding of the tune shift becomes, as a result, a key element of machine design and is essential to the selection of nominal transverse tunes in such machines.

Scaling FFAs contain intrinsic higher order multipoles that cannot be eliminated, as can be seen from performing Taylor expansions of the scaling laws (as done in, for example, Eq. (3.1)). This means that all scaling FFAs have unavoidable nonlinear terms in the equations of motion, leading to higher-order effects including amplitude-dependent tune shift that ultimately limit the DA of a given ring. However, understanding of the nonlinear properties of FFAs is complicated by the dependence of closed orbits on input parameters and the presence of edge-angle effects (exploited by design in many FFA lattice configurations, especially in spiral-sector designs such as the FD spiral design chosen for the FETS-hFFA prototype ring).

This chapter begins with the theoretical background of amplitude-dependent tune shift, before detailing the first experimental measurements of amplitude-dependent tune shift in a scaling FFA, and demonstrating the validity of simulation-based studies of this property. Following this, we introduce numerical studies of the amplitude-dependent tune shift based on the harmonic analysis methodology outlined in Section 3.2.5, with an aim to understanding the sources of amplitude-dependent tune shift in hFFAs, and thereby enable the development of design strategies that may be employed to mitigate tune shift and maximise DA in fixed field machines. We give an example of the application of this method to the design of a spiral-sector FFA, and show the utility of the harmonic analysis as a quick method of estimating amplitude dependent tune shift coefficients for a given lattice, thereby giving a surrogate metric for dynamic aperture that is computationally cheaper to evaluate and may be able to be employed in future lattice optimisation routines.

4.1 Amplitude-Dependent Tune Shift

For an accelerator comprised of purely linear focussing elements, a particle with any displacement from the closed orbit will experience a transverse kick that is directly proportional to its displacement; this means that the focussing, and therefore the tune, is independent of the amplitude of the motion. However, when nonlinear elements are introduced,

this situation becomes more complicated. Consider a system with one degree of freedom described by the Hamiltonian [68]

$$H(x, \tilde{p_x}, s) = \frac{1}{2}\tilde{p_x}^2 + \frac{1}{2}K(s)x^2 - \int_0^x f(x', s)dx' \tag{4.1}$$

in which x and $\tilde{p_x}$ are the transverse position and conjugate momentum, $K(s)$ a linear focussing term, and $f(x, s)$ some nonlinear perturbation. x' is a dummy variable of the integration. This Hamiltonian has the equation of motion

$$\frac{d^2x}{ds^2} + K(s)x = f(x, s). \tag{4.2}$$

If $f(x, s) = 0$, this is simply Hill's equation [69]. The term $\int_0^x f(x', s)dx'$ in the Hamiltonian can be recognised as simply a potential

$$V(x, s) = -\int_0^x f(x', s)dx'. \tag{4.3}$$

H can then be written as

$$H(x, \tilde{p_x}, s) = \frac{1}{2}\tilde{p_x}^2 + \frac{1}{2}K(s)x^2 + V(x, s). \tag{4.4}$$

Via a canonical transformation, the Hamiltonian can be rewritten in terms of the action-angle variables J and ϕ that parametrise the solutions to Eq. (4.2) in the absence of a perturbation:

$$\begin{aligned} x &= \sqrt{2J_x\beta_x}\cos\phi, \\ \tilde{p_x} &= \sqrt{\frac{2J_x}{\beta_x}}\cos\phi, \end{aligned} \tag{4.5}$$

$$H(\phi, J, \theta) = qJ + V(J, \phi, \theta), \tag{4.6}$$

in which a new independent variable θ is defined as $\theta = \frac{1}{q}\int_0^s \frac{ds'}{\beta(s)}$ (q being the unperturbed tune of the system, and $\beta(s)$ being the unperturbed beta function). Taking the derivative of the Hamiltonian with respect to J we find

$$\frac{d\phi}{d\theta} = q + \frac{dV}{dJ}. \tag{4.7}$$

$\frac{d\phi}{d\theta}$ can be considered as the effective tune of the perturbed system; without a perturbation, we once again retrieve q, but for an amplitude-dependent perturbation the value of $\frac{d\phi}{d\theta}$ must change. For a perturbation with a linear dependence on the amplitude (e.g. a quadrupole perturbation), this manifests simply as a fixed change in the tune. However, perturbations that are a nonlinear function of J will have J-dependent terms in their derivatives, giving rise to an amplitude-dependent tune shift.

This tells us that for any machine that is not perfectly linear, particles with greater amplitudes will have tunes that are increasingly distant from the design tune. The ultimate consequence of this is that particles with sufficient amplitudes will begin to encounter resonances and be lost, even if the design tune is chosen far away from resonances. This limits the dynamic aperture of the accelerator, as the change in tune puts an effective maximum on the phase space displacement of particles that will survive for a large number of turns. This determines the acceptance of the machine – i.e. the range of transverse positions and momenta that can safely be injected. Furthermore, the presence of space-charge effects introduces additional sources of tune shift, with strength proportional to the beam's intensity. For example, the 2d potential induced by self-field forces at the longitudinal centre of a Gaussian bunched beam is given by [70]

$$V_{sc}(J_x, J_z) = \frac{r_0 N_b}{\beta^2\gamma^3\sqrt{2\pi}\sigma_s}\int_0^\infty \frac{-1 + e^{-\frac{2J_x\beta_x}{(2\sigma_x^2+t)}\frac{2J_z\beta_z}{(2\sigma_z^2+t)}}}{\sqrt{(2\sigma_x^2+t)(2\sigma_z^2+t)}}dt, \tag{4.8}$$

where r_0 is the classical particle radius, N_b the intensity of the bunch, β and γ are the relativistic factors, and $\sigma_{s,x,z}$ are the longitudinal, horizontal, and vertical beam sizes respectively. β_x and β_z denote the transverse beta functions. Tune shifts induced by space charge reduce the safe margins away from resonances for high-intensity machines, making amplitude-dependent tune shift an especially significant consideration (more complete discussions of space-charge effects and mitigation may be found in other works such as [71, 25].

Accordingly, understanding of the nature of amplitude-dependent tune shift is of critical

importance; not only from the perspective of minimising its presence, but also as knowledge of the magnitude and direction of amplitude-dependent tune shift must inform the choice of a machine's operational tune to optimise its dynamic aperture.

4.1.1 Sources of Amplitude-Dependent Tune Shift

Starting from the Hamiltonian of a system with a perturbation potential, Eq. (4.6), under the assumption of a weak perturbation away from resonances, we assume that J and $\frac{d\phi}{d\theta}$ are approximate constants of the motion as they vary slowly compared to the angular variables ϕ and θ. This enables the use of the so-called smooth approximation, where the Hamiltonian may be averaged over ϕ and θ to give an effective Hamiltonian that describes the perturbed behaviour of the system.

$$H(\phi, J, \theta) \simeq qJ + \frac{1}{4\pi^2}\int_0^{2\pi} d\phi' \int_0^{2\pi} V d\theta. \tag{4.9}$$

The change in tune then becomes

$$\delta q = \frac{1}{4\pi^2}\int_0^{2\pi} d\phi' \int_0^{2\pi} \frac{\partial V}{\partial J} d\theta. \tag{4.10}$$

The lowest order tune shift under this approximation comes from the octupole term of the system. Considering an octupole perturbation of strength $k_3(\theta)$ in one dimension with the corresponding potential

$$V_{\text{oct}}(\theta) = \frac{k_3(\theta)}{4}x^4 = J^2 k_3(\theta)\beta^2(\theta)\cos^4\phi. \tag{4.11}$$

The tune shift caused by this potential is thus

$$\Delta q = J\frac{3}{8\pi}\int_0^{2\pi} \beta^2(\theta)k_3(\theta)d\theta. \tag{4.12}$$

Sextupoles do not contribute to amplitude-dependent tune shifts under the smooth approximation, as integrating an odd power of $\cos\phi$ over a full period evaluates to zero. The tune shift for a sextupole perturbation of strength $k_2(s)$ in decoupled motion, defined by the Hamiltonian

$$H(x, \tilde{p_x}, s) = \frac{1}{2}\tilde{p_x}^2 + \frac{1}{2}K(s)x^2 + \frac{k_2(s)}{6}x^3, \tag{4.13}$$

is a second order effect, and can be derived from 1D canonical perturbation theory, as in [72]:

$$\Delta q = -\frac{J}{64\pi}\int_0^C \left[\beta(s)^{3/2}k_2(s)\int_s^{s+C}\beta(s')^{3/2}k_2(s')A(q,s,s')ds'\right]ds \tag{4.14}$$

where C is the length of one periodic cell. A is defined as follows:

$$A(q,s,s') = \frac{3\cos\left(\phi(s')-\phi(s)-\pi q\right)}{\sin\left(\pi q\right)} + \frac{\cos\left(3(\phi(s')-\phi(s)-\pi q)\right)s}{\sin\left(3\pi q\right)}, \tag{4.15}$$

where $\phi(s) = \int_0^s \frac{ds'}{\beta(s')}$.

We see that in the case that $3q$ is close to an integer, the second term in A grows asymptotically. This implies that when the tune is close to the third-integer resonance, sextupole components in the lattice will become the dominant source of amplitude-dependent tune shift.

4.2 Experimental observation of Amplitude-Dependent Tune Shift

4.2.1 Principle of Tune Measurement

In order to measure the transverse tunes of an accelerator, a coherent transverse oscillation must be excited in the desired plane. The frequency of this transverse oscillation in a co-moving Frenet-Serret system is the transverse tune of the beam. The excitation process must be short in time, such that it does not induce a persistent focussing effect that would affect the tune of the accelerator. Transverse oscillations must then be measured over time using beam position monitors (BPMs). By transforming this data from the time domain to the frequency domain using a method such as the Fast Fourier Transform (FFT), the frequency of transverse oscillations in the plane measured by the BPM can be extracted [73]. The transverse oscillations are apparent in the frequency spectrum as sidebands around harmonics of the revolution frequency f_{rev}, with frequencies corresponding to

$$\frac{(f_{\text{sideband}} - nf_{\text{rev}})}{nf_{\text{rev}}} = q/n \tag{4.16}$$

where $n \geq 1$ is the order of the harmonic and q is the fractional tune.

4.2.2 The KURNS FFA

Experimental studies of the amplitude-dependent tune shift in scaling hFFAs were carried out at the Kyoto University institute for integrated Radiation and Nuclear Science (KURNS) facility, which houses a 150 MeV FFA ring [39].

The accelerator complex at this site was designed to deliver proton beams for the Kyoto University Critical Assembly (KUCA) [38], a proof-of-principle nuclear reactor based on the Accelerator-Driven Subcritical Reactor (ADSR) concept [37], and commenced operation in 2009. Originally, beams were accelerated through two FFA rings (called ION-BETA and the BOOSTER ring) before being injected into the main ring, a 150 MeV FFA whose extracted beam goes directly to the reactor. The original injector system has since been replaced by an 11MeV H- linac that feeds directly into the main ring, a setup depicted in Fig. 4.1. The main ring itself is a DFD triplet design, with a periodicity of 12 and an injection radius of 4.8 m; an image of the ring is displayed in Fig. 4.2, and its nominal design parameters are listed in Table 4.1. Scaling is achieved in the magnets through shaping of the pole gap to produce the desired on-midplane dipole fields. The magnets of the triplet are constructed using the 'return-yoke-free' magnet design [74], in which the D-magnet acts as an effective return yoke for the flux from the main normal-bend F-magnet. This enables the F-magnet to be built with an open-gap configuration, such that the gap between the upper and lower poles of the magnet is accessible from the inner and outer edges of the magnet (this can be seen in Fig. 4.2). This construction allows injection and extraction to be routed directly through the azimuthal centre of the F-magnet (as illustrated in Fig. 4.1 for the injection line, whilst the extraction line is again visible in Figure 4.2).

Injection from the 11 MeV linac is performed using charge-exchange injection, where the beam of H- ions hits a thin carbon foil after being bent by the F-magnet field, losing electrons and generating a proton beam that can be circulated through the ring and accel-

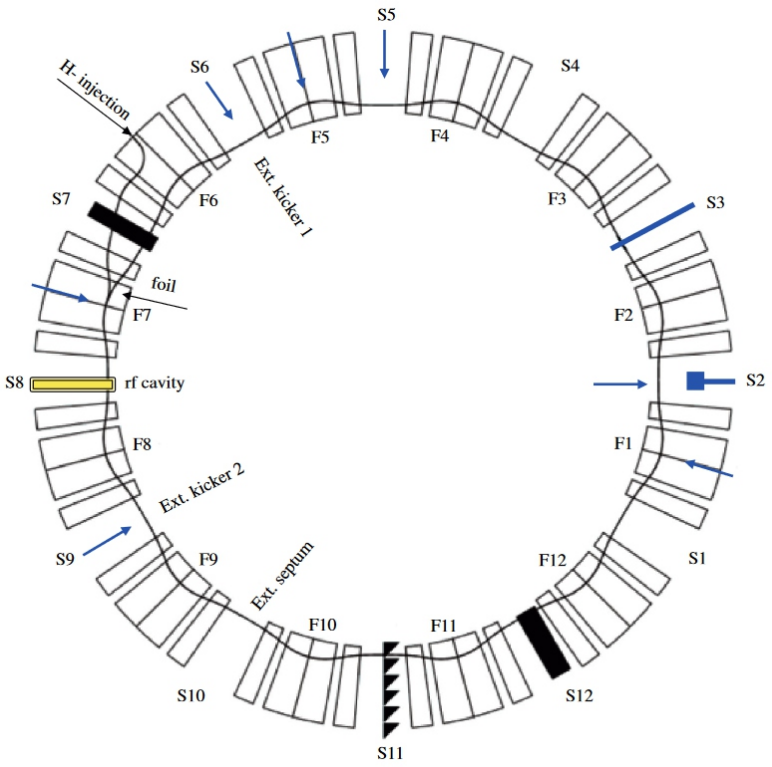

Figure 4.1: Plan view of the KURNS main ring accelerator, taken from [75], showing the positions of the magnets, RF cavity, and extraction kickers. The horizontal beam position monitor (BPM) is positioned at the location marked S11.

Parameter	Value
Reference radius r_0 [m]	5.4
k	7.6
B_{0F} [T]	-1.6
B_{0D} [T]	1.168
Number of cells	12
Angular separation between F-magnet and D-magnet centres [Degrees]	8.535
Opening angle of half F-magnet β_F [Degrees]	5.12
Opening angle of D-magnet β_D [Degrees]	3.43

Table 4.1: Nominal parameters of the KURNS main ring FFA

Figure 4.2: Photograph of the KURNS main ring FFA [76]. This displays the return-yoke-free magnet design, where the gap of the F-magnet can be seen and accessed from the outer and inner sides of the magnets. The extraction line is visible towards the left-hand side of the picture, where it can be seen exiting the azimuthal centre of one of the F-magnets. The central smaller ring is the BOOSTER ring, which was originally used as part of the injection system, but is no longer operated.

erated to top energy. Conventionally, the KURNS main ring uses a combined kicker and septum system for extraction, where the beam is shifted from its circulating orbit to the far side of a septum by the use of a fast-firing kicker magnet; however, the beam is not extracted for the experiment series described here.

The tune of the accelerator over the acceleration cycle is displayed in Fig. 4.3, taken from measurements completed in 2016 [75]. The horizontal tune varies by approximately 0.2 over the acceleration cycle, and the vertical tune by 0.1; this means that the KURNS main ring is not able to be considered an ideal scaling FFA. The tune variation must be accounted for when modelling the machine; its nature and sources are discussed in detail in [77]. It was found that within the F-magnet there was a variation of the measured k-value between 7.44 and 7.76 across the acceleration cycle. The variation in the k-value observed in the D magnet was shown to be more significant, decreasing from 10.49 to 7.49 as a function of the radius. The main sources of these scaling imperfections were measured to originate from the interaction region between the F- and D-magnets, and were most significant towards the inner radius of the D-magnet.

4.2.3 Experimental Procedure

The aim of the experiment was to induce oscillations of varying amplitudes in circulating beams, measuring the frequency of the corresponding horizontal oscillations picked up on a beam position monitor (BPM). In order to do this, the beam was accelerated to a fixed energy below the extraction energy of the typical operation cycle, and kept circulating at this energy by reducing the synchronous phase of the RF system to zero. This left a circulating bunched beam with a constant energy. This process of accelerating a beam to a fixed energy (or, in terms of the revolution frequency and the RF cycle, a fixed frequency), is referred to as a flat-top acceleration cycle. The extraction kicker magnet (shown in Fig. 4.4) was positioned radially to be in line with the flat-top orbit selected for the experiment. This setup enabled the beam to be kicked horizontally, with an amplitude dependent on the

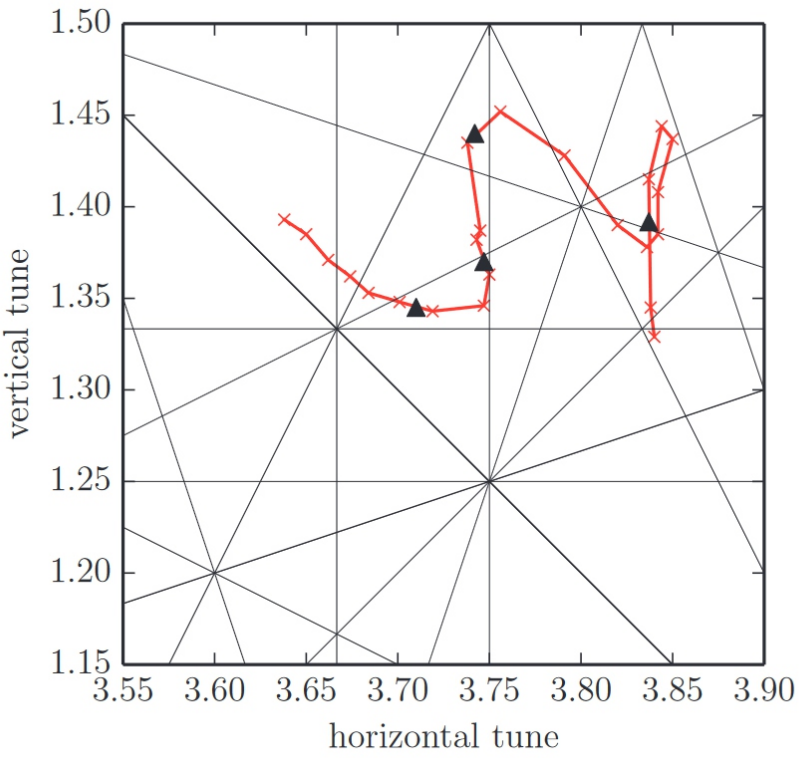

Figure 4.3: Transverse tunes of the KURNS main ring over acceleration from 11MeV to 150MeV, and nearby resonance lines, taken from the 2016 study [75]. The triangle markers show the approximate timings of beam loss identified in the study.

voltage applied across the kicker coil. Reducing the experimental energy to an energy below the nominal extraction energy of the machine was done to decrease the orbit radius. As the orbit radius at the lower energy is much smaller than the radius of the beam pipe, large amplitude horizontal kicks could be applied non-destructively (i.e. most of the circulating beam would be preserved) – as opposed to performing the experiment at the extraction energy, where horizontal kicks would cause the beam to collide with the outer walls of the beam pipe.

Horizontal oscillations were then recorded by recording data from the triangle BPM. This BPM, of which a plan view is shown in Fig. 4.5, consists of pairs of parallel plate electrodes placed above and below the beam position. A charge distribution in proximity to a conductive plate induces an image charge on the plate [1], which can be measured as a voltage. Considering a plate of finite length, and a line distribution of charge, the amount of charge seen by the plate is proportional to the length of the plate, and therefore the induced charge on the plate is also proportional to its length. Analogously, then, the charge induced in a triangular plate (such as those displayed in Fig. 4.5) by a line distribution of charge is proportional to the length of this line exposed to the plate, and therefore the induced charge is dependent on the radial position of the beam.

4.2.3.1 Preliminaries

A preliminary investigation was performed to optimise the choice of flat-top frequency and the choice of kicker position. For the preliminary, voltage on the electrodes of the horizontal BPM was recorded over time. Fast Fourier Transforms (FFTs) were computed from this data with a rolling window (i.e. taking data from time intervals of fixed length but advancing the start time of the window through the dataset) to obtain the frequency spectra of the system as a function of the time since injection. During the preliminary experiment, the beam was accelerated using the RF programme for normal operation, which ramps the energy and frequency of the beam continuously from injection to the nominal extraction

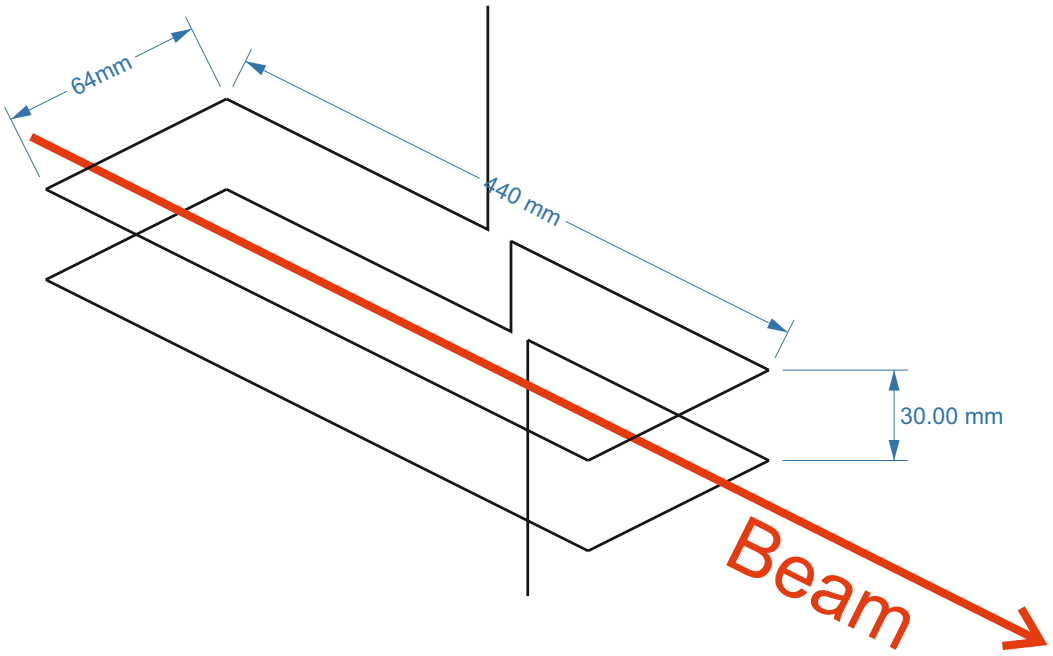

Figure 4.4: Schematic of the extraction kicker magnet for the KURNS main ring. The black lines show the path of the copper coils.

energy. The kicker was then activated once per acceleration cycle with an input voltage of 50 kV. The kicker timing was adjusted to maximise the magnitude of oscillation sidebands around the revolution frequency. When beam loss was observed (apparent as a large decrease in the amplitude of the revolution frequency peak following the activation of the kicker magnet), the kicker was repositioned at a smaller radius. The experiment was repeated until a kicker activation that caused distinct sidebands to be present in the signal was achieved with minimal reduction in height of the revolution frequency peak (comparing before and after the kicker activation). The timing of the kicker activation that produced this result was then correlated to the frequency ramp script to select the flat-top frequency of the radiofrequency programme to be used for the main series of experiments.

An RF programme was developed to capture the beam, accelerate it with a constant synchronous phase, and linearly ramp this synchronous phase to zero such that the final

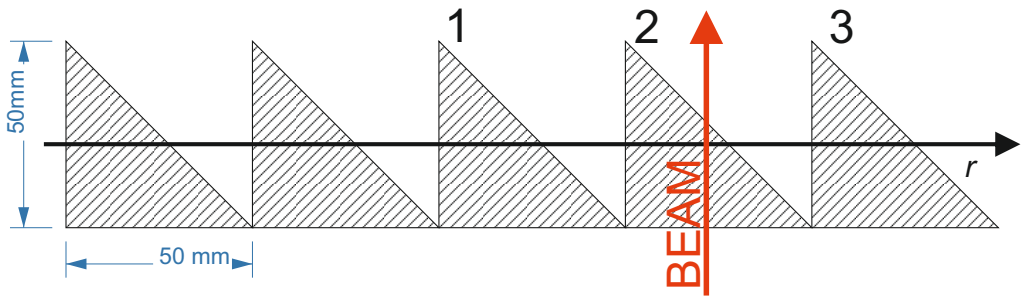

Figure 4.5: Plan view of the triangle BPM used to measure the horizontal tune. The five hatched triangles are the identical metal electrodes of the BPM. The numbered electrodes denote the three electrodes from which data was recorded in the experiment.

revolution frequency of the beam was 3.846 MHz, the frequency as selected from the results of the preliminary investigation. This frequency corresponds to a kinetic energy E_{kin} of approximately 103.4 MeV. This was computed from the relation

$$f = \frac{pc/(E_{\text{total}})}{2\pi r_{\text{ref}}(p/P_{\text{ref}})^{1/(k+1)}}, \tag{4.17}$$

in which momentum can be substituted as $p = \sqrt{E_{\text{total}}^2 - m^2}$, and E_{total} is the kinetic energy of the particle plus its rest energy. The frequency relation derives from computing the average radius of an orbit from the scaling law, Eq. (1.67), given a reference momentum P_{ref} and a reference radius r_{ref}. In this case, the reference momentum is calculated from the extraction energy of 150 MeV, and the reference radius is the extraction radius, 5.37 m. For the purposes of this calculation, the k-value for the ring is taken to be 7.6, as in Table 4.1.

With the new RF programme in place, the frequency spectrum behaviour of the voltages recorded on the BPM electrodes was measured whilst the kicker was operated, but with no circulating beam. This was necessary to enable interference effects to be distinguished from the true behaviour of the beam. Figure 4.6 shows the voltage profile of the kicker at a 40 kV activation alongside the recorded voltages from the BPM electrodes. The frequency spectra of the kicker current (measured using a current transformer (CT)) and BPM signals are also shown. We can see that, even without a circulating beam, a peak at approximately 400 kHz was present in the frequency spectrum of the BPM signals. This peak represents

ringing effects from the firing of the kicker magnet. This frequency is an order lower than the revolution frequency of the beam, meaning that interference from the kicker can easily be distinguished from transverse oscillations of the beam if analysis is done around the first harmonic of the revolution frequency.

The data additionally shows some low-amplitude broad-spectrum noise around 3.85MHz. 3.846MHz is the frequency at which the RF cavities were operated during the flat-top part of the cycle, so this can be attributed to interference from the RF cavity. Higher harmonics of the RF frequency can additionally be seen as defined peaks in the frequency spectrum (in particular, the second harmonic peak is apparent in Fig. 4.6 at 7.7MHz). The amplitude of these peaks is approximately a factor of 10 lower than those in the equivalent spectra when beam is present (Fig. 4.7), and no sidebands or other features can be distinguished in the spectrum of the beam-off dataset. The same observations were made across all tested kicker voltages, showing that additional structures in the frequency spectra measured with a circulating beam must be caused by real beam effects, rather than interference from other elements of the setup. The decay time of the kicker CT signal was measured from this data (3μs), so that the start time of the frequency analysis window could be selected such that any field in the kicker would be negligible.

4.2.3.2 Measurements

With this baseline measurement series complete, the beam was switched on again and the accelerator was operated whilst the kicker was fired at a range of input voltages from 0 to 55kV in 5kV increments. Voltage data was recorded from 3 adjacent electrodes of the triangle BPM (labelled 1, 2, and 3 in Fig. 4.5) to ensure the entirety of large-amplitude oscillations would be detected (in the case that the change in radial position of the beam during such oscillations caused it to cross over the boundary between two BPM electrodes). The FFT of the voltage signals was then taken for each set of recorded data over a 26μs window beginning 3μs after the kicker activation. The length of this window corresponds

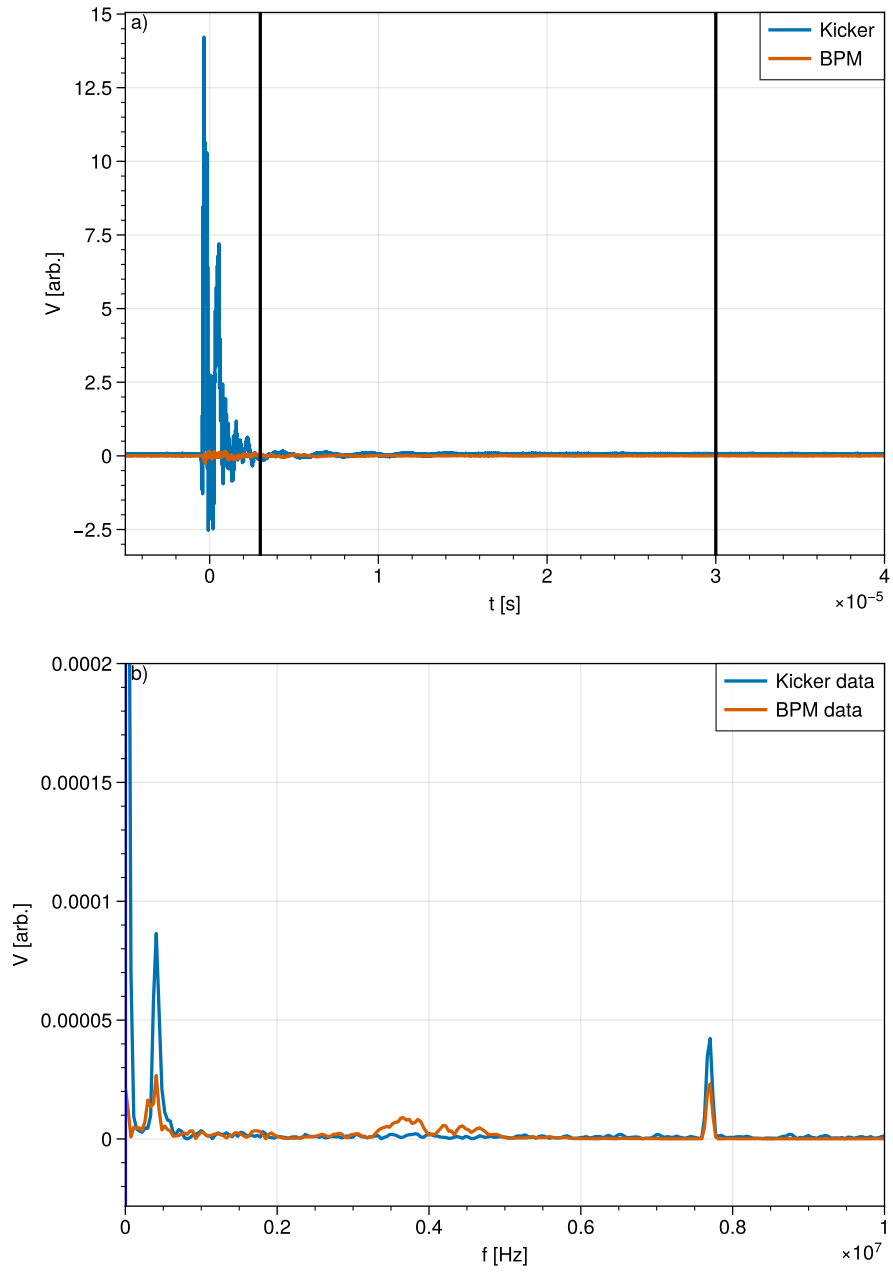

Figure 4.6: a) Voltage profile of the kicker CT and BPM electrode response during kicker activation at 40kV nominal voltage, with no circulating beam. Vertical black lines denote the beginning and end of the window used to compute the FFT. The BPM data is recorded from electrode 2 (according to the labelling scheme in Fig. 4.5). b) Frequency spectrum of the voltage data from the kicker CT and the BPM.

to 100 revolutions of the beam.

A preliminary analysis was done using a 55 kV kicker activation (the maximum voltage possible) to see which signals contained frequency data corresponding to transverse oscillations of the beam (which would manifest as a peak at the revolution frequency with sidebands at an interval corresponding to the transverse fractional tune multiplied by the revolution frequency peak); such signals were observed in the spectra of the outer two electrodes (electrodes 2 and 3), but not the inner one (electrode 1), implying that the beam when circulating at the selected 3.846MHz frequency was positioned towards the outside of electrode 2, and, at the maximum kicker amplitude, oscillations were large enough to cross the boundary between this electrode and electrode 3 – but did not bridge the full width of the central electrode. This means that the data from the outer electrodes can be combined, and we find that taking the difference of the two voltages produces the most well-defined structure in the frequency spectra (of which an example can be seen in Fig. 4.7). For small-amplitude kicks, the expected frequency components corresponding to transverse oscillations of the beam were present only in the data recorded from electrode 2.

4.2.4 Results and Analysis

Figure 4.8 shows the amplitude of the sideband peak in the frequency spectrum as a function of time by computing the FFT with a rolling window after a 40 kV kicker activation; this shows the rapid decay of the signal due to decoherence of the transverse oscillations of the beam. A consequence of this decay is that the length of the window from which to take data should be minimised, so that the coherent response of the beam to the kick with a defined amplitude can be accurately measured. However, the theoretical maximum frequency resolution of the FFT is given by the sampling frequency over the number of samples taken [78]. This places a fixed uncertainty α_f on any measured frequency f. If the tune is calculated from the first harmonic of the revolution frequency f_{rev} and a corresponding sideband at frequency f_1 using Eq. (4.16), the uncertainty in the calculated tune

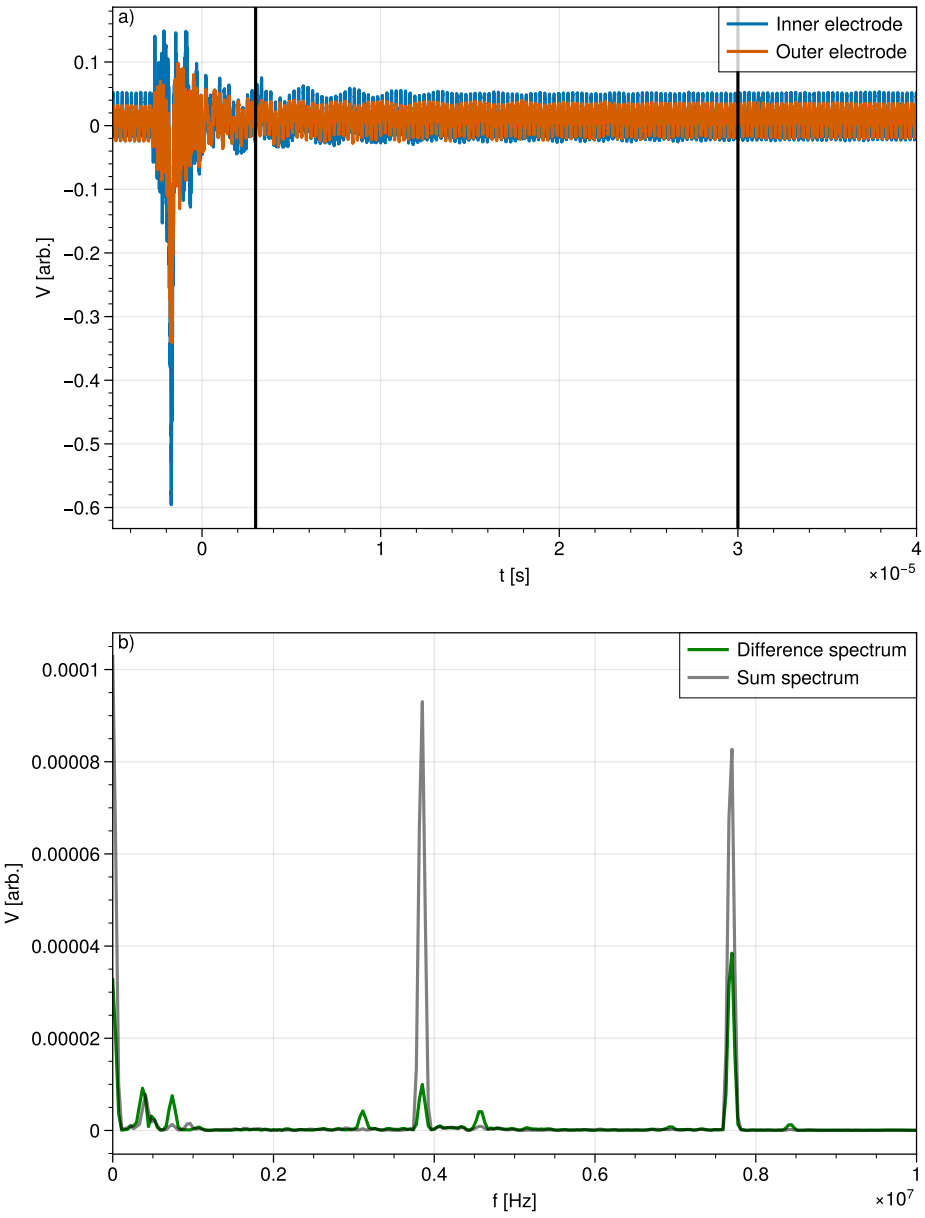

Figure 4.7: a) Voltage profile of the central and outer BPM electrodes response (referred to in terms of the radial position of the three electrodes from which data was recorded) during kicker firing at a 40kV nominal voltage, with a circulating beam at 3.846MHz. Vertical black lines denote the beginning and end of the window used to compute the FFT. b) Frequency spectrum of the voltage data from the two BPM electrodes, showing a comparison of the signal from the sum of the voltages from each electrode to the signal measured when the difference is taken.

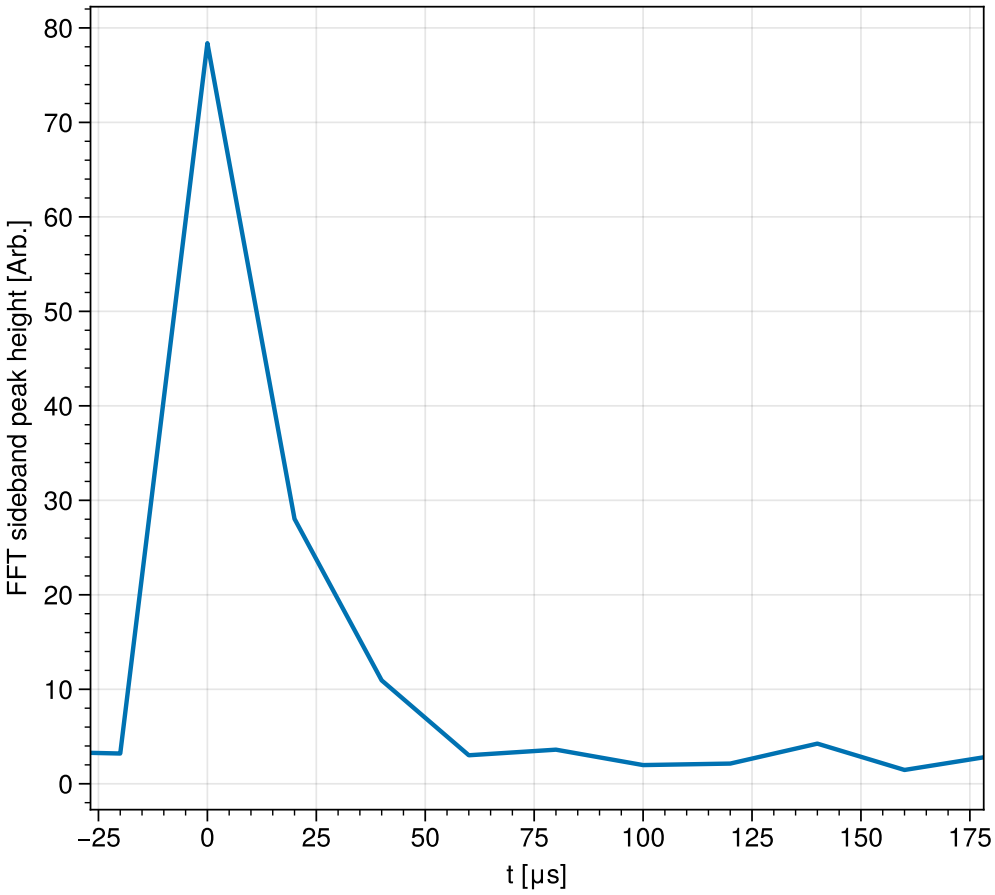

Figure 4.8: Height of the sideband peak in the frequency spectrum of the BPM data over time during a 40kV kicker activation, calculated using a rolling 100-turn FFT window.

from this is then given by

$$\alpha_q = q\sqrt{\left(\frac{\alpha_{f_1}^2 + \alpha_{f_{\text{rev}}}^2}{(f_1 - f_{\text{rev}})^2}\right) + \left(\frac{\alpha_{f_{\text{rev}}}}{f_{\text{rev}}}\right)^2}, \tag{4.18}$$

having applied error propagation techniques as found in [79].

For a 100-turn FFT window (i.e. the length of time used to take the data is 100 times the revolution frequency) the uncertainty in the measured tune from the first sideband for the 40kV kick is ± 0.03. This is insufficient to perceive the difference in tune between a number of the different amplitudes tested, and drawing conclusions with this high amount of uncertainty would be challenging. However, increasing the length of the FFT window will introduce effects from the decoherence of the transverse oscillations.

For high-resolution estimation of the frequency of periodic components in time-domain data, the Numerical Analysis of Fundamental Frequencies (NAFF) method [80] may be used. For a real signal $z(t)$ that can be written as a combination of an infinite number of orthonormal functions, in the form,

$$z(t) = \int_{-\infty}^{\infty} \phi(f) e^{2\pi i f t} df \tag{4.19}$$

its Fourier transform $\phi(f)$ is then written as

$$\phi(f) = \frac{1}{T}\int_0^T z(t) e^{-2\pi i f t} dt. \tag{4.20}$$

The main frequency of $z(t)$ is the value of f at which $\phi(f)$ is maximised. For discretely-sampled data, the function $z(t)$ is defined only where t is a multiple of the sampling period (i.e. $t = n/f_s$ for integer n and sampling frequency f_s). In this case the integrals in Eqs. (4.19) and (4.20) are replaced with finite sums, leading to the following expression for the Fourier transform of the discretely-sampled signal [81]:

$$\phi(f) = \frac{1}{N}\sum_{n=0}^{N} z(n/f_s) e^{-2\pi i f n/f_s}, \tag{4.21}$$

where $N = T/f_s$ is the number of samples. The value of f that maximises $\phi(f)$ is then found numerically using a root-finding method such as the Newton-Raphson method [82].

As f is a continuous variable, the NAFF technique allows for a greater precision in determining the main frequency of the signal than the FFT, for which frequencies are divided into discrete bins of finite width. However, the NAFF method is affected by noise [83]; a method for estimating its uncertainty in the presence of noise is outlined in Appendix B.

For data with many unwanted frequency components, including large-amplitude unwanted frequency components (for instance, when measuring sideband frequencies, we are uninterested in the harmonics of the revolution frequency), such as the data taken for this experiment, the efficiency of the NAFF method may be improved by applying a band-pass filter around the frequency of the peak that we want to measure. The width of the band-pass filter should be chosen as wide as possible, to avoid any bias of the frequency measurement caused by the shape of the band-pass filter. Figure 4.9 shows FFT spectra for the 40kV kicker activation before and after band-pass filters with a width of 200kHz are applied around the revolution frequency peak and one of the two sideband peaks. It is apparent from this data that the shape of the peak in the FFT spectrum is unchanged by the application of the band-pass filter, implying that the frequency selected by the NAFF algorithm should be unaffected by the imposition of the band-pass filter.

A method of estimating the uncertainty in a frequency measurement from the NAFF algorithm in the presence of noise is found in Appendix B. This analysis is performed for all measured frequencies to obtain an estimate for the error in each frequency measurement. These uncertainties can then be converted into the uncertainty of a measured tune using Eq. (4.18).

As a measure of the amplitude of the beam oscillations, we calculate the expected kick induced by the kicker magnet. The current in the kicker magnet coils is given by the input voltage divided by the impedance of the transmission line (25Ω). From here, we approximate the kicker magnet as two planar rectangular coils with dimensions as illustrated in Fig. 4.4, and apply the Biot-Savart law [1] to compute the on-beam field at the centre of the magnet. The total kick seen by the beam is then approximated as the estimated central

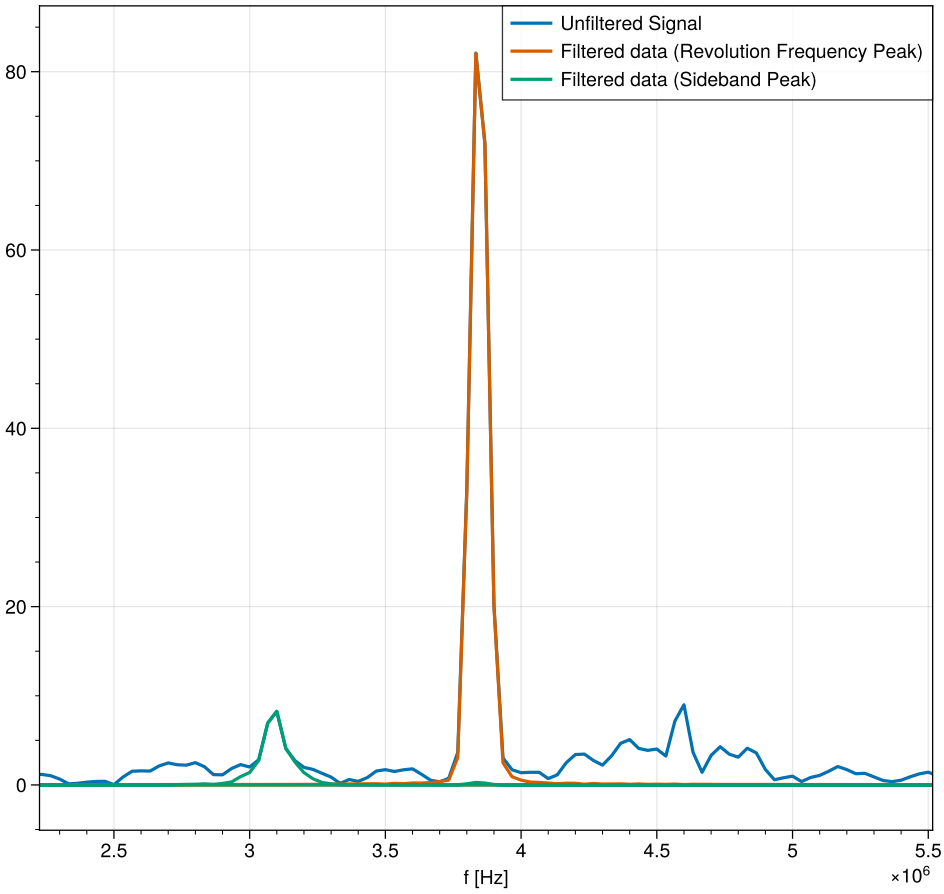

Figure 4.9: FFT spectra before and after the application of bandpass filters of width 200kHz centred alternately on the revolution frequency peak and the lower-frequency sideband peak.

B-field of the kicker magnet multiplied by the length of the magnet. This can be interpreted as a transverse kick (i.e. an instantaneous change in the momentum coordinate) by dividing this by the magnetic rigidity of the beam at the selected energy. The value of magnetic rigidity used is 1.510 Tm, computed from the estimated energy of 104.3 MeV.

Comparing the magnitude of the horizontal kick to the definition of the action-angle coodinates, Eq. (4.5) we find that the action J can be correlated to the value of this kick through the equation

$$\frac{\beta_x \tilde{p_x}^2}{2} = J_x, \tag{4.22}$$

in which β_X is the value of the horizontal β-function at the position of the kick, and we have used the fact that α_x = 0 at the centre of the drift (where the kicker is positioned). The local β-function is computed based on a FIXFIELD simulation, and evaluated at $\beta_x = 0.828$m. Table 4.2 shows the computed field strengths and kick amplitudes for the different kicker amplitudes, alongside the corresponding tunes and their uncertainties as computed using Eq. (4.18) and the uncertainties in the frequencies given by the method of Appendix B.

The tune uncertainties are smaller at larger kick amplitudes as larger kicks increase the amplitude of the sideband peaks, and the uncertainty of the NAFF method is dependent on the signal-to-noise ratio (Appendix B). Variation in the uncertainties aside from this is caused by fluctuations in beam intensity.

4.2.5 Comparison with simulation

A lattice was generated in the FIXFIELD simulation code to match the geometry of the KURNS lattice (given in Table 4.1). To account for the tune variation over the acceleration cycle (Fig. 4.3) and the field imperfections noted in [77], the parameters of the lattice were modified to match the measured tune at the operating point of the experiment. To estimate the zero-amplitude tune of the lattice, a weighted least-squares fit (with weights according to the reciprocal of the tune uncertainty) was made for the experimental data. The intercept

V [kV]	I [A]	B [T]	$\delta\tilde{p_x}$	Amplitude [m]	Q_x
5	200	0.0024	1.374E-03	1.106E-06	3.804 ± 0.013
10	400	0.0047	2.749E-03	4.424E-06	3.8054 ± 0.0055
15	600	0.0071	4.123E-03	9.953E-06	3.8051 ± 0.0055
20	800	0.0094	5.497E-03	1.769E-05	3.8067 ± 0.0035
25	1000	0.0118	6.872E-03	2.765E-05	3.809 ± 0.023
30	1200	0.0141	8.246E-03	3.981E-05	3.8073 ± 0.0019
35	1400	0.0165	9.621E-03	5.419E-05	3.8083 ± 0.0014
40	1600	0.0189	1.099E-02	7.078E-05	3.8085 ± 0.0019
45	1800	0.0212	1.237E-02	8.958E-05	3.8105 ± 0.0007
50	2000	0.0236	1.374E-02	1.106E-04	3.8115 ± 0.0012
55	2200	0.0259	1.512E-02	1.338E-04	3.8129 ± 0.0012

Table 4.2: Kicker input voltages, calculated amplitudes, and measured tunes at 103.4MeV in the KURNS main ring FFA.

with the vertical axis of the least-squares fit is taken as 3.8051. The point with the horizontal tune of 3.8051 is identified on the tune diagram (Fig. 4.3) and the corresponding vertical tune of this point is taken (approximately 1.41). A numerical optimisation routine is then used to adjust the k-value, B_{0F}, and B_{0D} of the lattice to match this tune, keeping the geometric parameters at their nominal values - thereby effectively computing an average field index k for the orbit radius used in the experiment. The adjusted k-value after tune optimisation was 7.711, and the B_0 field values for the F and D-magnets respectively were -1.632T and 1.176T.

Once a lattice with the desired horizontal and vertical tunes has been found, a closed orbit is identified. Particles are then initialised at coordinates perturbed from the closed orbit at chosen amplitudes (varying the amplitude J and displacing the particles according to Eq. (4.5). Tracking data is then saved over several turns, corresponding to the particles' positions at each integration step. The displacement between the closed orbit and the perturbed particle is measured using this saved data, which is then passed to a frequency analysis routine. Where the frequency components and amplitudes remain unchanged over a large number of turns, it is appropriate to use the Fast Fourier Transform (FFT); however, the symplectic condition is not fully satisfied in the RK4 integrator [84] and the amplitudes

of oscillations can change over the course of the large number of turns needed to measure tune using the FFT method (hence affecting measurements of amplitude-dependent tune). This effect (the severity of which is dependent on the step size of the simulation) was noted in preliminary simulations of amplitude-dependent tune shift in the ring. To avoid a computationally-expensive simulation of a large number of terms using a small integration step size, the NAFF method can once again be employed to reduce the number of turns required to determine the frequencies to a given precision.

Figure 4.10 shows a comparison between the tunes calculated using this method and those measured experimentally. The simulation tunes do not pass through all the error bars of the experimental data, when using the zero-amplitude tune computed from the least-squares fit. However, a zero-amplitude tune of 3.806 (an increase of 0.026% over the value computed from the least-squares fit) is still within the range of possible zero-amplitude tunes supported by the experimental data, and a modified simulation optimised for this tune produces results in complete agreement with the experimental data.

The close agreement for the data shows the validity of the numerical modelling in the FIXFIELD simulation, and the application of the FIXFIELD modelling to making predictions about the behaviour of scaling FFA rings, even in the presence of field imperfections (as long as these are accounted for by making small adjustments to the model). This demonstrates additionally that tune shift and nonlinear effects are still governed by the scaling law for this machine, despite the presence of field imperfections.

4.2.6 Sources of tune shift in the KURNS Main Ring

The Harmonic Analysis methodology employed to analyse the focussing structure of vFFAs in Section 3.2.5 can be expanded to include multipole decompositions up to arbitrary order. Closed orbits are found for individual lattices using the combination of numerical integration and root-finding methods, and the multipole decomposition about this orbit is then evaluated according to the procedure detailed in Section 3.2.5.

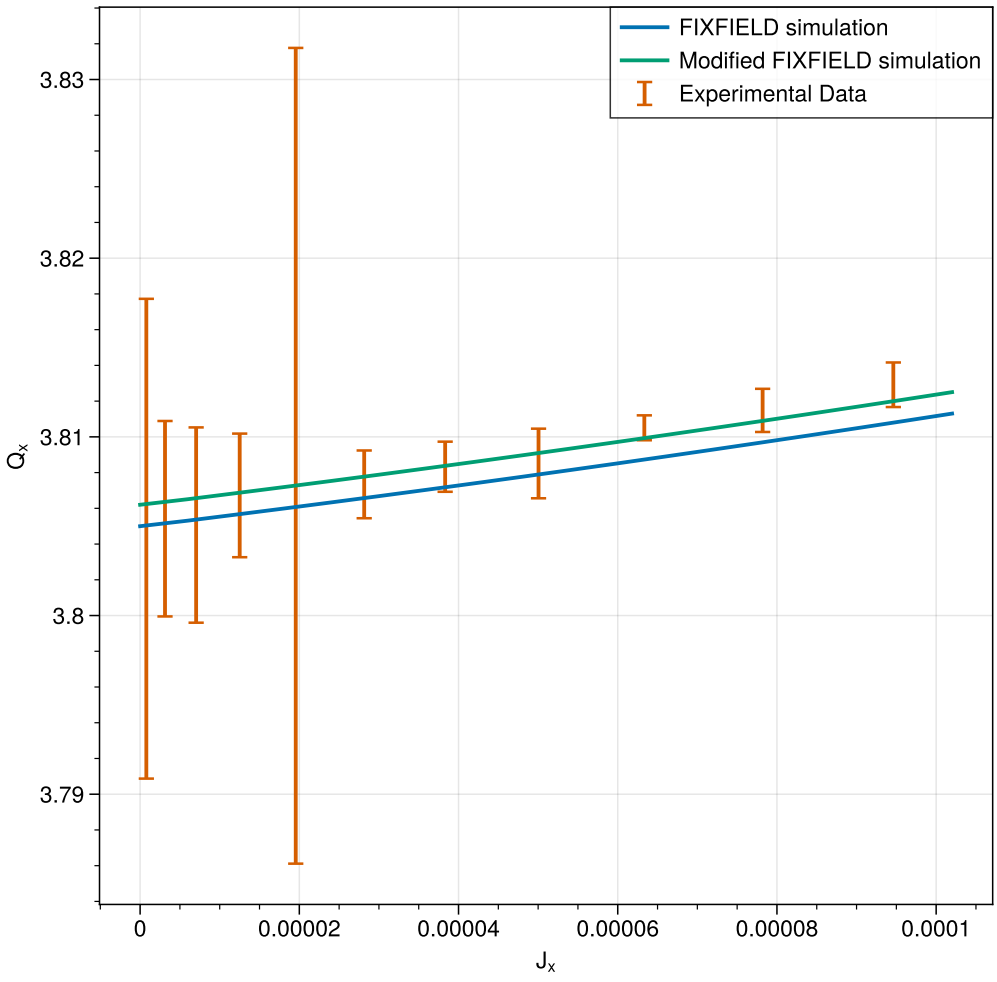

Figure 4.10: Measured and simulated tune in the KURNS main ring as a function of amplitude for a beam circulating at 3.846MHz.

Eqs. (4.12) and (4.14) shows the tune shift with amplitude as a function of the local multipole coefficients along the closed orbit, and the Courant-Snyder parameters at each position. β-functions are evaluated by deriving a cell matrix using the infinitesimal linear transfer matrices corresponding to the linear part of the multipole decomposition (as in Section 3.2.5); this is done for each integration step in the cell by iterating through one-cell transport matrices derived from cyclic permutations of the list of infinitesimal transfer matrices and computing Courant-Snyder parameters for each one. These, along with sextupole and octupole coefficents measured from the multipole decomposition, are then substituted in to Eqs. (4.12) and (4.14) to evaluate tune shifts.

The sextupole and octupole distributions throughout a cell for the model of the KURNS ring assembled in Section 4.2.5 are displayed in Fig. 4.11. From these, we compute the expected tune shift due to the sextupole and octupole contributions as $dQ_{x,\text{sext}}/dJ_x = 62.93/\text{m}$, $dQ_{x,\text{oct}}/dJ_x = 1.460/\text{m}$. This compares to a total tune shift with amplitude coefficient measured from the full simulation (by computing a linear fit using the method of least squares minimisation) of $65.19/\text{m}$. The result confirms that the dominant source of amplitude-dependent tune shift for the KURNS main ring is indeed the sextupole component (as the cell tune for KURNS is 0.317, which is close to the third-integer resonance at $0.33\dot{3}$).

4.3 Amplitude-dependent tune shift in FD Spiral Scaling hFFA rings

The spiral-sector hFFA design was originally proposed in 1960 [26] as a concept wherein stability in the vertical plane would be provided entirely by edge focussing effects; this removed the need for reverse-bend magnets, leading to a more compact ring. This concept was realised in a low-energy electron ring, with an extraction energy on the order of 100s of keV. However, when we scale the FFA concept to higher energies, the number of cells in the ring has to increase to maintain magnets with achievable field strengths and realistic

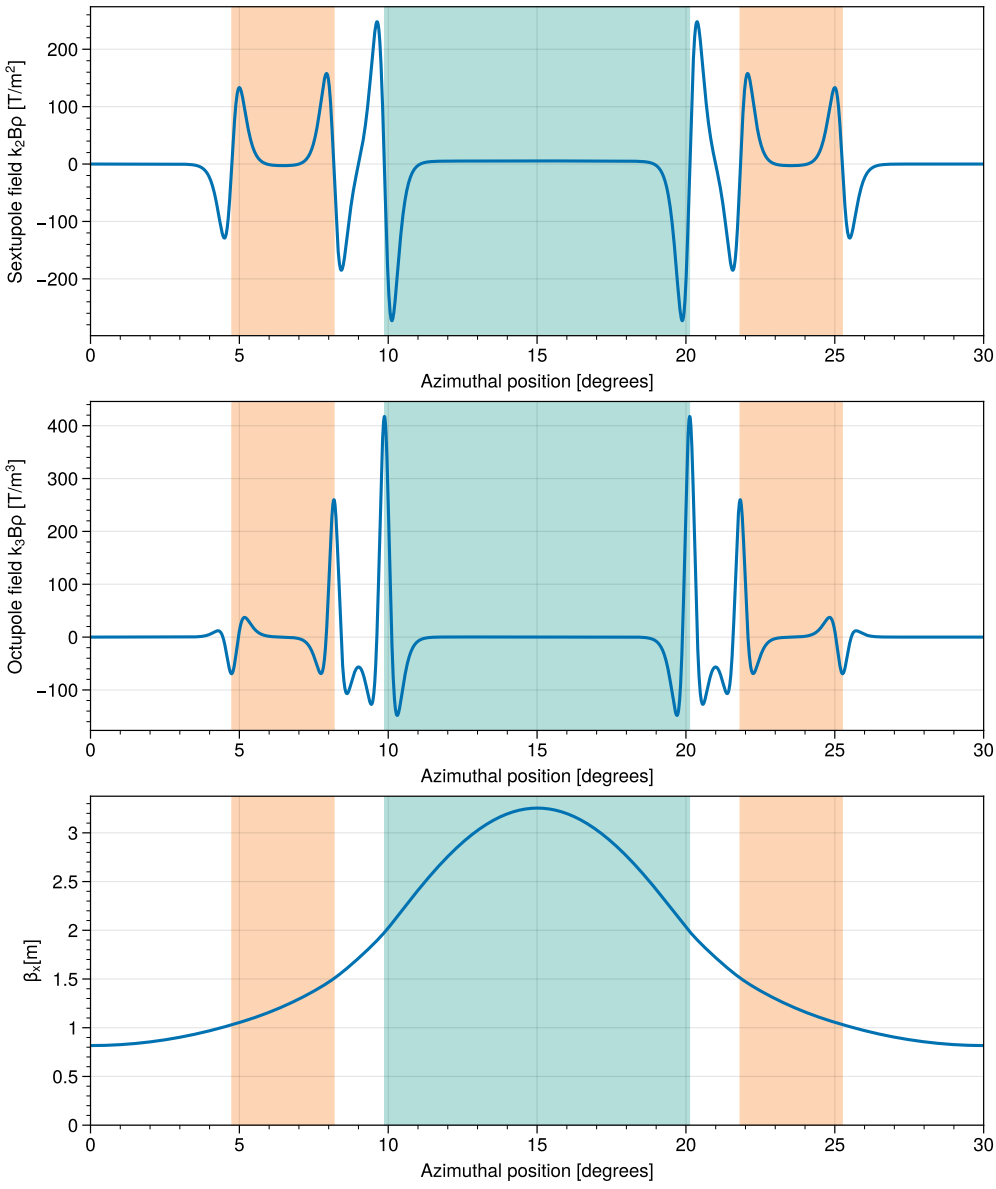

Figure 4.11: Calculated sextupole coefficient, octupole coefficient, and beta function for one cell of the KURNS lattice as simulated in FIXFIELD. The positions of the D- and F-magnets are indicated with the orange and teal shaded areas respectively.

lengths. The overall bending angle of the cell then becomes smaller, leading to a decrease in the edge focussing (if spiral angle is kept constant). This must be compensated for by increasing the edge focussing added to the ring by the spiral angle. Increasing the spiral angle of the magnets increases their engineering complexity, and, moreover, the introduction of extreme edge angles in the presence of the nonlinear fields leads to increased fringe-field multipole components [85].

With an aim to mitigate these factors, the FD-spiral concept has since been devised, in which a ring is constructed with a combination of normal and reverse-bend spiral magnets [27]. By including an element of vertical focussing from a reverse bend magnet, the requirement for an extreme spiral angle may be reduced, mitigating the engineering complexity of the machine and increasing its dynamic aperture (by reducing the edge angles and therefore the magnitude of fringe-field multipole components). In recent years, spiral-sector FFAs (including FD-spiral machines) have been proposed for a number of applications [48, 86, 87].

In such a design, the choice of spiral angle becomes an essential optimisation parameter; increasing the spiral angle decreases the need for reverse bend, minimising the size of the ring, but at the same time increasing the magnitude of multipolar components in the fringe field - in turn leading to adverse effects on dynamic aperture. The negative effects of spiral angle were identified in [27]; we now present a study of an FD-spiral lattice and an analysis of the sources of tune shift in this lattice, and an outline of how these factors can be used to select an optimised ring design in the context of the FETS-FFA design study [58].

4.3.1 Harmonic Analysis of FD Spiral FFAs

To examine the tune shifts of spiral-sector FFAs, and thereby begin to understand the limiting factors on their dynamic apertures, a 16-cell FD-spiral FFA lattice was simulated according to the parameters listed in Table 2.2. Figure 4.12 shows the horizontal and ver-

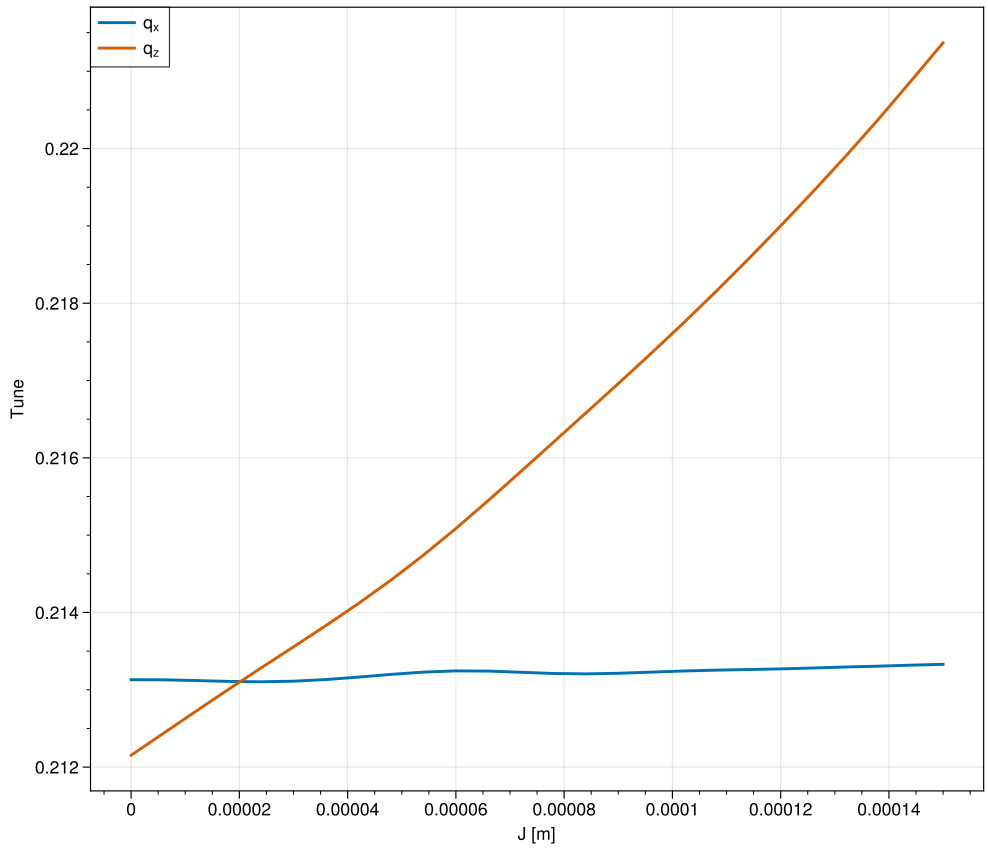

Figure 4.12: Horizontal and vertical cell tunes in the example FD-spiral ring as a function of transverse amplitudes J_x and J_z respectively.

	$\partial q_x/\partial J_x$ [1/m]	$\partial q_z/\partial J_z$ [1/m]
FIXFIELD	1.40	60.12
Harmonic analysis		
Octupole (first-order)	-13.88	61.19
Sextupole (second-order)	5.48	5.53
Total	-8.40	66.72

Table 4.3: A comparison of tune shift coefficients as computed from a linear least-squares fit to the FIXFIELD data, and as calculated using the combination of harmonic analysis and perturbation theory.

tical cell tune as a function of horizontal and vertical amplitude respectively in this lattice (computed using the method outlined in Section 4.2.5). Using the same closed orbit, we apply the harmonic analysis approach to compute the tune shift coefficient from the octupole, and compare this to the measured tune shift coefficient from the simulation (which includes all orders of nonlinearities). A comparison of the tune shift coefficients between the two approaches is shown in Table 4.3.

This result confirms that the vertical tune shift is dominated by the octupole components in the lattice. The total vertical tune shift coefficient calculated from the harmonic analysis method is approximately 10% higher than the FIXFIELD calculation, which indicates that the perturbation theory at first order (octupole effects) and second order (sextupole effects) does not give a complete description of the system (though a cross-check of this result with other simulation codes would be a priority of further study). The tune shift for the horizontal plane is much smaller than that for the vertical plane in both the full simulation and the harmonic analysis, demonstrating that the predominant source of tune shift (and therefore the expected limiting factor on the dynamic aperture) comes from the vertical tune plane. However, the magnitude and direction of the horizontal tune shift is different in the full FIXFIELD simulation to the predictions from harmonic analysis, indicating that the combined first-order and second-order tune shifts developed from the perturbation theories discussed in this chapter are insufficient to completely describe the system.

To understand how the tune shift factors into the choice of spiral angle, the harmonic

analysis study is repeated across a range of spiral angles ζ. In each case, the value of the reverse bend field and the k-value are adjusted to keep the same horizontal and vertical tunes. Figure 4.13a shows the variation in B_{0D} and k lattice parameters as a function of the spiral angle when the horizontal and vertical tunes are kept constant. Figure 4.14a shows the octupole component along the ring for the different values of ζ, whilst Fig. 4.14b and c show the horizontal and vertical beta functions respectively for each lattice.

Considering the positive values of ζ we find that the magnitude of the octupole components in the F-magnet increases with spiral angle, with this effect being most apparent at the entrance and exit. This is a consequence of the increased edge angles. The behaviour in the D-magnet is similar, with octupole components increasing in magnitude with spiral angle until spiral angle exceeds 45°, at which point the decrease in B_{0D} outweighs the effect of increasing edge angle. Whilst both the magnitudes of positive and negative octupole components increase with spiral angle in the F-magnet, we see that the magnitude of the positive peak is greater at all positive spiral angles, leading to a net positive vertical tune shift that increases with spiral angle. The effect of this on the ultimate tune shift is further exacerbated by the growth in β-function at the position of the positive octupole coefficient peak.

At negative spiral angles, the overall effect is similar, though the position of the positive and negative peaks of the octupole function are exchanged. Nonetheless, we still see octupole coefficients that increase with $|\zeta|$, and an increasing beta function at the position of the maximum of the octupole coefficients.

By applying Eq. (4.12), the octupole tune shifts for each case can be computed; the result is shown in Fig. 4.13b.

From Fig. 4.13 we can see that a spiral angle of 45 degrees is sufficient to reduce the required field strength of the D-magnet to 59% of that required for the $\zeta = 0°$ radial sector lattice. However, when the spiral angle is increased beyond $45°$, the amplitude-dependent tune shift rises sharply as a consequence of the coincidentally increased octupole and beta

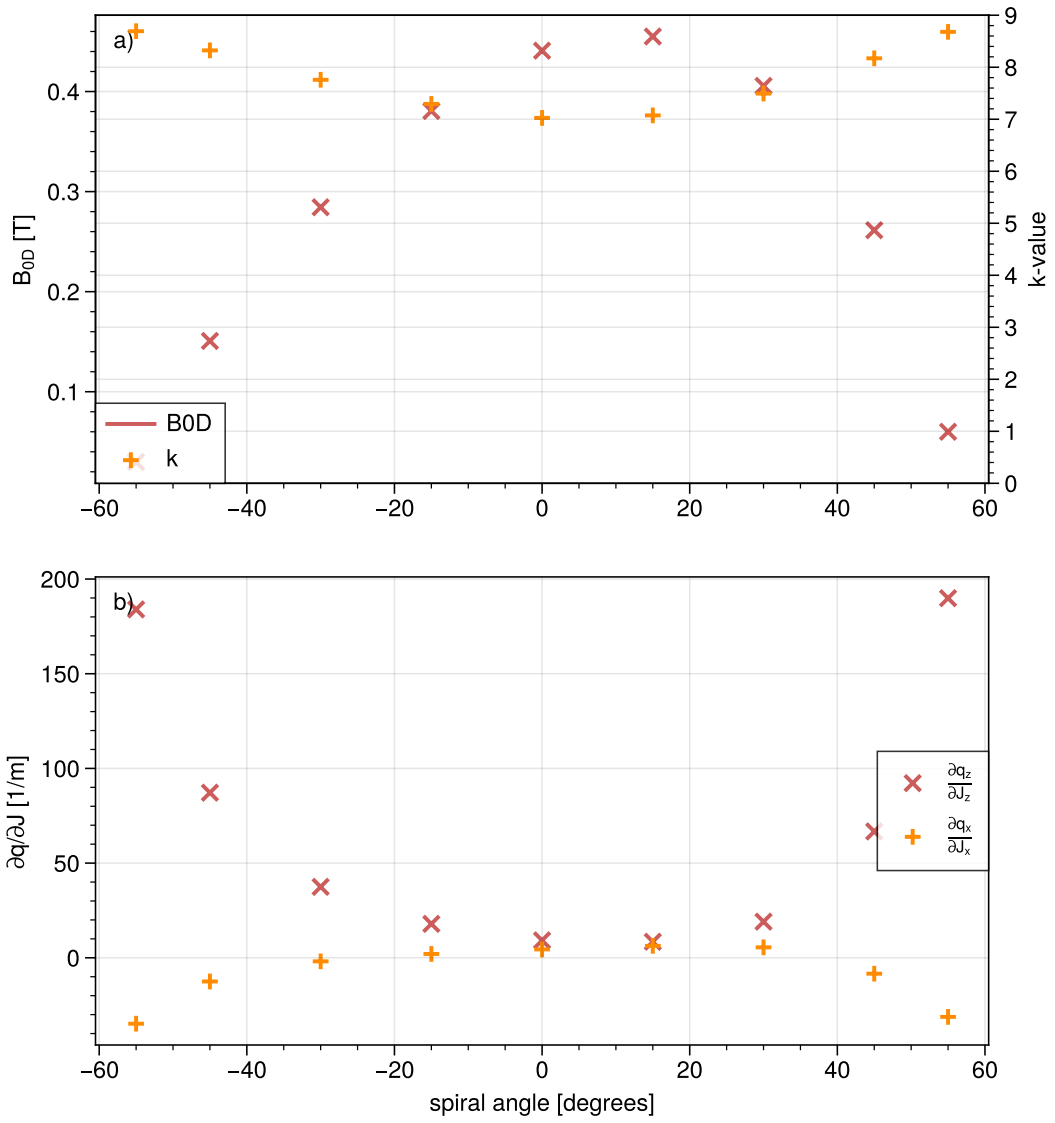

Figure 4.13: a). Dependence of lattice k-value (unitless) and reference B-field (units T) in the D-magnet on spiral angle.
b). Horizontal and vertical amplitude-dependent tune shifts in the FETS-FFA lattice as a function of the spiral angle.

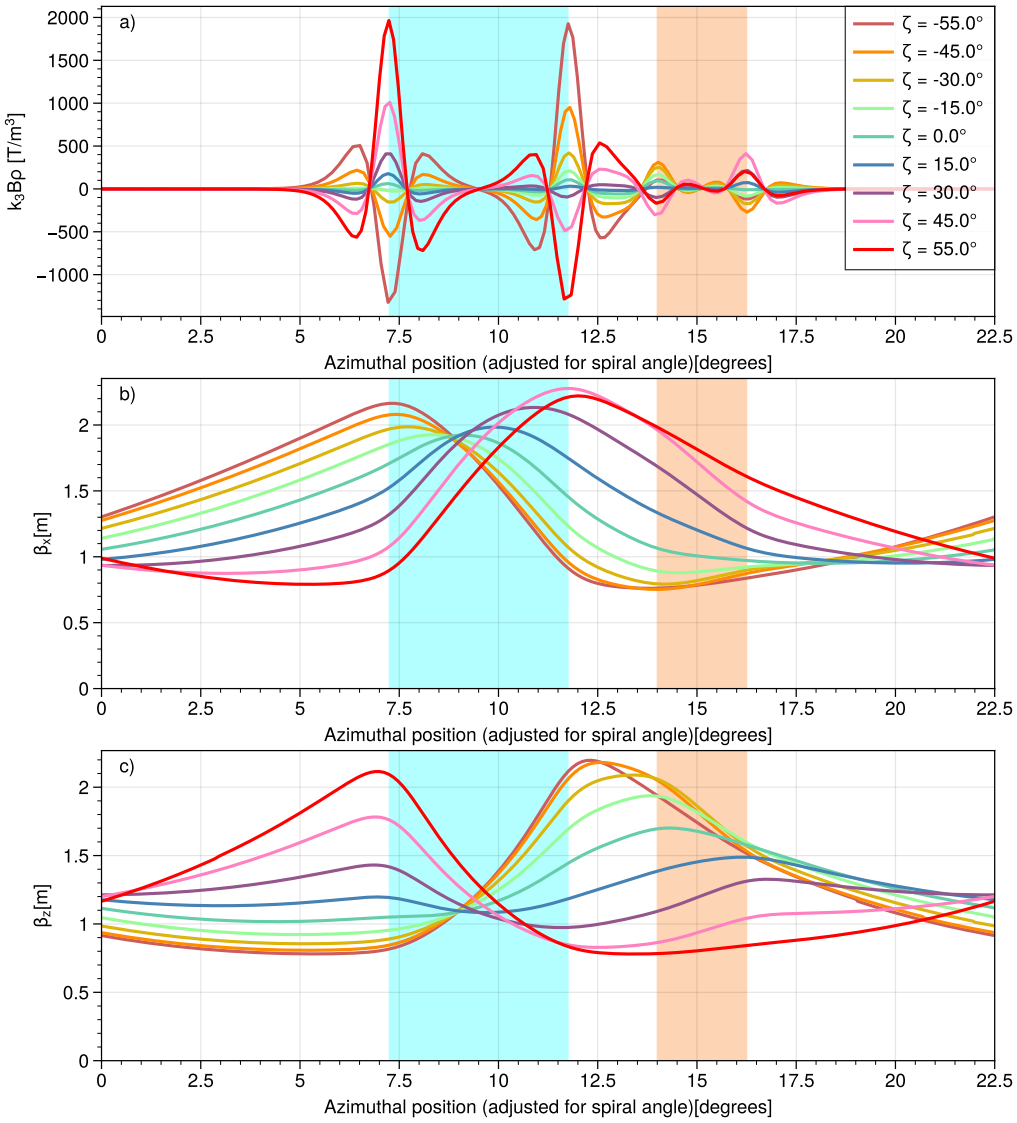

Figure 4.14: a). Octupole field components along the closed orbit for different spiral angles.
b). Horizontal beta function along closed orbit at different spiral angles.
c). Vertical beta function along closed orbit at different spiral angles.

function at the entrance of the F-magnet (Fig. 4.14). This is a contributing factor to the reduction in dynamic aperture for large spiral angle as observed in tracking studies for the FETS ring [88]. Comparing positive to negative spiral angles, we find that at $\zeta = -45^\circ$ the required D-magnet strength is reduced further to 34% of the value from the radial sector lattice; however, the vertical tune shift in this lattice is approximately 31% larger than the $\zeta = 45^\circ$ equivalent.

The horizontal tune shift, by contrast, appears more stable as a function of the spiral angle across both positive and negative values. An explanation for this can be seen when we compare the beta function for the horizontal plane (Fig. 4.14b) to the previous plot of the octupole coefficient (Fig. 4.14a). As spiral angle is increased to 45 degrees, the horizontal beta function becomes larger at the position of the negative octupole component at the right-hand side of the F-magnet as it is drawn in the figure. When the beta function and the octupole coefficients are multiplied, the negative octupole at the right-hand side of the F-magnet is able to cancel the positive tune shift that would otherwise be induced by the positive octupole component at the F-magnet's left-hand side. As the spiral angle is increased beyond 30 degrees, the drop in beta function at the location of the positive octupole causes the negative tune shift to become dominant, and hence the total horizontal amplitude-dependent tune shift becomes negative for large spiral angles.

4.4 Conclusion

We presented the first measurements of amplitude-dependent tune shift in a scaling hFFA, and used this result to benchmark the use of numerical simulation codes to study amplitude-dependent tune shift. The same simulation was then applied to the study of a novel FFA accelerator to measure the expected amplitude dependent tune shift. We developed a technique based on multipole decomposition to identify the principal sources of amplitude-dependent tune shift in FFA rings, and used it to show that the sources of the tune shift are different depending on the optics of the machine; in the KURNS machine, the primary

source of the tune shift was identified as the second-order effect from the sextupole components in the horizontal plane, due to the proximity of the horizontal tune to the third-integer resonance. Conversely, at the working point of the proposed FETS-FFA FD spiral lattice, the dominant source of tune shift was found to be the first-order effects from the octupole in the vertical plane. We then explored how input parameters of the FETS-FFA lattice affected the octupole components, β-functions, and the resulting tune shifts to find the dependence of tune shift on spiral angle. This showed how the harmonic analysis methodology might be employed in the optimisation of new designs; implementation of this form of analysis into future study and optimisation procedures could enable an increased understanding of a machine and a more efficient design procedure. For example, the octupole and beta function product integral employed here can be used for a quick computation of the expected amplitude-dependent tune shift. This could be used to choose an optimal working point for the ring to avoid resonances, or to give a rapid estimate of DA for a given tune (by computing the maximum allowed amplitudes before problematic resonances would be encountered), which could be inserted into a numerical optimisation procedure and used to identify the best set of lattice parameters to maximise DA. In this application, this metric would be able to replace computationally intense particle survival simulations, enabling more streamlined optimisation processes and aiding in the design and study of future machines.

Chapter 5

Design of vFFA Lattices

This chapter outlines the context for one possible application of a vFFA as part of a high-energy muon collider complex. Here, the vFFA offers the potential for quasi-isochronous zero-chromatic acceleration without the ramp time constraints associated with rapid cycling synchrotron alternatives.

We introduce first the concept of the muon collider in terms of its advantages over alternative collider proposals for the energy frontier, and discuss the engineering challenges associated with fast acceleration within the lifetime of the muon. We discuss the current baseline design for the acceleration phase of the muon collider complex, which is based on the novel 'hybrid RCS' concept, and how the difficulties with muon acceleration and the drawbacks of the baseline design might be addressed with a vFFA. With this basis established, we present new designs for muon acceleration based on the vFFA concept, comparing these to the existing baselines developed by the muon collider collaboration. We show how the analytic formalism may be applied to an existing vFFA design for the purpose of optimisation, and develop further proof-of-concept muon accelerator designs to prove its viability as an alternative candidate to the hybrid RCS for muon acceleration stages.

5.1 Muon Accelerators

5.1.1 Background

The search for new high energy physics in the post-LHC era will require the construction of new multi-TeV colliders. A number of proposals to this end have already been made, including the FCC-hh [89] concept based on a large-ring synchrotron design, as well as linear collider schemes such as CLIC [90] and the ILC [91]; however, each of these is faced with a number of limiting factors. A novel alternative for a new energy-frontier collider is present in the muon collider concept, which offers ways of mitigating these limiting factors - though in itself raising a number of new challenges in accelerator physics.

The challenges faced by new energy-frontier machines stem from a number of different factors.

The top energy of a linear collider scheme is ultimately determined by the gradient of the cavities, the available space for the tunnel, and the power budget available to the facility. An example proposal is given by the CLIC collaboration [90], which in its ultimate form suggests construction of a machine with cavity gradients on the order of 100 MV/m [92] and a length of 50.1 km to achieve a maximum collision energy of 3 TeV, with an expected input power to the cavities alone of 130 MW.

In circular (and other recirculating) machines, some of these limitations may be overcome through multi-pass operation; by using each cavity many times over the acceleration cycle, a higher energy may in principle be achieved for the same number of cavities and the same accelerating gradient. This enhances not only the power efficiency of a machine, but also renders it more compact and theoretically less expensive to construct. A further advantage of a recirculating machine is that beams intersect at each interaction point many times over the course of a run, meaning that requirements on the final focus system can be relaxed to achieve the same luminosity as a linear collider at the same energy.

These factors would, taken in isolation, seem to imply that a circular, multi-pass ma-

chine is the obvious choice for an energy-frontier collider. However, circular machines are not without their own drawbacks when scaled to higher centre-of-mass energies. A charged particle undergoing an acceleration perpendicular to its velocity emits synchrotron radiation, a phenomenon first observed visually in an accelerator at the General Electric 70MeV synchrotron [93]. The instantaneous power lost to this radiation for a particle in circular motion is given by the formula [44]

$$P = \frac{2}{3}\frac{q^2}{4\pi\epsilon_0}\frac{\beta^4\gamma^4}{\rho^2}, \tag{5.1}$$

In which ϵ_0 is the permittivity of free space, β is the ratio of the particle's velocity to the speed of light (v/c), γ is the Lorentz factor, q is charge, and ρ is the local radius of curvature. Notably, power lost to synchrotron radiation scales with the 4th power of the beam energy (as $E = \gamma E_0$ for a particle with rest energy E_0), and therefore increases dramatically as we try to increase the energy of the collider. This ultimately places an upper bound on the energy of a collider, when the power lost due to synchrotron radiation per turn exceeds that which can be given to the beam with accelerating cavities. For the LEP, the power lost at its top energy of 100GeV was 18 MW [94] at a total beam intensity of 6mA – more than 10% of the entire power budget of 120 MW for the entire ring [95].

It can be seen from Eq. (5.1) that the power loss to synchrotron radiation is inversely proportional to the bending radius, so one means of achieving a higher maximum energy in an electron collider is to increase the radius of the ring; however, as the energy loss is proportional to the 4th power of the beam energy the required increase in radius to mitigate the increased radiated power at higher energies becomes very large. As such, modern proposals for circular electron machines limit themselves to relatively modest top energies: the proposed FCC-ee concept, a 100 km-circumference electron-positron collider, has a planned top centre-of-mass energy of 185.5 GeV, and is designed instead to produce results on the precision frontier (as opposed to the energy frontier). The operation parameters

for this machine were selected based on a chosen limit of synchrotron radiation power of 100 MW [95].

An alternative method of circumventing synchrotron power losses is found in increasing the mass of the accelerated particles. Equation (5.1) implies that, for a given energy $E = \gamma E_0$, the radiated power will be inversely proportional to the 4th power of the particle rest energy E_0. This solution has been used in previous high-energy machines such as the Large Hadron Collider [96] and the Tevatron [97], which accelerated protons (alongside, in the latter case, antiprotons). With protons having approximately 2000 times the mass of the electron, this choice results in a 10^{13} reduction in radiative losses for the same beam energy compared to an equivalent electron beam. The reduced synchrotron losses enable the practical construction of energy-frontier hadron colliders on scales where electron machines would be untenable. However, hadrons are composite particles, meaning that each colliding parton only carries a fraction of the nominal collision energy – reducing the effective centre-of-mass energy for each collision and introducing uncertainties into collisions due to the momentum distribution of the parton structure (in contrast to the 'clean' collisions provided by point-like lepton-lepton interactions).

The concept of a muon collider is to take a best-of-both-worlds approach; providing point-like leptonic collisions, whilst keeping synchrotron losses small enough to reach multi-TeV energies on a practical scale. Muons have a greater mass than electrons by a factor of 200, reducing the radiated synchrotron power by order 10^9 compared to an equivalent electron beam and enabling operation at energy scales comparable to hadron machines whilst maintaining a more compact footprint. As leptons, muons are still fundamental particles, and do not suffer from the issues caused by the composite nature of hadrons – most interactions will occur at the full collision energy. This means that a muon collider with a given centre-of-mass energy can access an equivalent physics potential to a proton-proton collider at ten times the centre-of-mass energy [98].

A number of additional challenges must be overcome to realise a muon collider with

the required luminosity for a large-scale high-energy physics experiment. Foremost among these are the difficulties associated with producing a low-emittance muon beam, and ensuring the survival of muons throughout their acceleration cycle, due to the short lifetime of the muon ($\tau = 2.2\mu s$ in the rest frame of the muon). Recent breakthroughs have begun to address the former point, with the MICE collaboration demonstrating the world-first 4-dimensional cooling of a muon beam [99] using the ionisation cooling technique. The decay of the muon beam is a critical consideration in the design of any muon accelerator complex: the muon population will decay rapidly at rest, but time dilation at higher energies increases the muon lifetime as measured in the lab frame. Consequently, for a linearly increasing energy acceleration cycle of duration t_{ramp}, the survival rate of a muon beam is given by [100]

$$\frac{N_{ext}}{N_{inj}} = exp[-\int_0^{t_{ramp}} \frac{dt}{\gamma(t)\tau_\mu}] = \left(\frac{\gamma_{ext}}{\gamma_{inj}}\right)^{\frac{t_{ramp}}{(\gamma_{inj}-\gamma_{ext})\tau_\mu}}, \tag{5.2}$$

in which N_{ext} and N_{inj} denote the numbers of muons at extraction and injection respectively, with γ_{inj} and γ_{ext} the corresponding Lorentz factors at those points. For a muon survival rate of $\frac{N_{ext}}{N_{inj}} > 50\%$ from 63 GeV up to 5 TeV, this means that the acceleration cycle must be completed in a maximum time of millisecond order.

This represents a significant engineering challenge for a conventional Rapid-Cycling Synchrotron (RCS). The current fastest-accelerating RCS is the ISIS proton synchrotron, which ramps from 70MeV to 800MeV over the course of approximately 20ms [101] using normal-conducting (NC) magnet technology. The maximum field that can be achieved with NC magnets is approximately 2 T [102]. The minimum circumference of a 5 TeV muon ring with a peak field of 2 T would be 52 km, without accounting for the space needed for focussing structures, drift lengths, RF cavities, and any other insertions. In the context of rapid acceleration, large amounts of high-gradient RF would need to be distributed around this large ring. As such, it is desirable to minimise the ring footprint as much as possible to maximise the number of times each cavity is used over the accelerating cycle. The 2 T

magnetic field limit associated with NC magnets limit is overcome in existing synchrotrons through the use of superconducting (SC) magnets; these are, however, limited to extremely slow ramp rates when compared to normal-conducting counterparts.

The combination of the limited ramp rate of SC magnets and the limited field strength achievable with NC magnets places limits on the applications of conventional RCS schemes to rapid muon acceleration. One proposal, considered as the baseline for the acceleration stage by the International Muon Collider Collaboration [103], circumvents these limits via the construction of an RCS chain, using a conventional RCS for the initial acceleration stage, but switching to a novel 'hybrid' RCS design for later acceleration stages (which uses interleaved ramped NC magnets and fixed-field SC magnets). This concept is discussed in more detail below.

The issue of ramp rate could also be avoided in a fixed-field machine, which would entirely remove this constraint on the speed of acceleration – in which case the only limit on acceleration rate would be the amount and gradient of the RF cavities that could be incorporated into the ring. A number of additional advantages may also be gained in switching to a fixed-field machine (in particular, a vertical-excursion design), which are further explored in the following sections.

5.1.2 RCS Chain Baseline

The baseline parameters for the RCS chain studied by the muon collider collaboration [104] are displayed in Table 5.1. The first accelerator is specified as a conventional RCS based on normal-conducting magnets, taking the beam from an injection energy of 63 GeV to a 300 GeV extraction energy, whilst the later stages (up to 5 TeV) are designed as so-called hybrid RCS machines.

In a hybrid RCS, cells consist of a single ramped NC dipole sandwiched between two strong fixed superconducting dipoles. The ramped magnet goes between a 1.8 T reverse bend field at injection to a 1.8 T normal bend field at extraction to ensure the correct net

Parameter	Symbol	Unit	RCS1	RCS2	RCS3	RCS4
Hybrid RCS	-	-	No	Yes	Yes	Yes
Repetition rate	f_{rep}	Hz	5	5	5	5
Circumference	C	m	5990	5990	10700	35000
Injection energy	E_{inj}	GeV	63	314	750	1500
Extraction energy	E_{ext}	GeV	314	750	1500	5000
Energy ratio	$E_{\text{ext}}/E_{\text{inj}}$	-	4.98	2.39	2	3.33
Assumed survival rate	$N_{\text{ext}}/N_{\text{inj}}$	-	0.9	0.9	0.9	0.9
Acceleration time	τ_{acc}	ms	0.343	1.097	2.37	6.37
Revolution period	T_{rev}	μs	20	20	36	117
Number of turns	n_{turn}	-	17	55	66	55
Required energy gain per turn	ΔE	GeV	14.8	7.9	11.4	63.6
Average accel. Gradient	G_{avg}	MV/m	2.44	1.33	1.06	1.83
Number of bunches/species	-	-	1	1	1	1
Bunch population at injection	N_{inj}	10^{12}	2.7	2.4	2.2	2
Bunch population at extraction	N_{ext}	10^{12}	2.4	2.2	2	1.8
Max. NC dipole field	B_{NC}	T	1.8	1.8	1.8	1.8
Max. SC dipole field	B_{SC}	T	-	10	10	16
Ramp rate	B	T/s	4200	3282	1519	565
Main RF frequency	f_{RF}	MHz	1300	1300	1300	1300
Max RF voltage	V_{RF}	GV	20.9	11.2	16.1	90

Table 5.1: Baseline parameters of the RCS chain developed for the muon collider study, retrieved from [104]

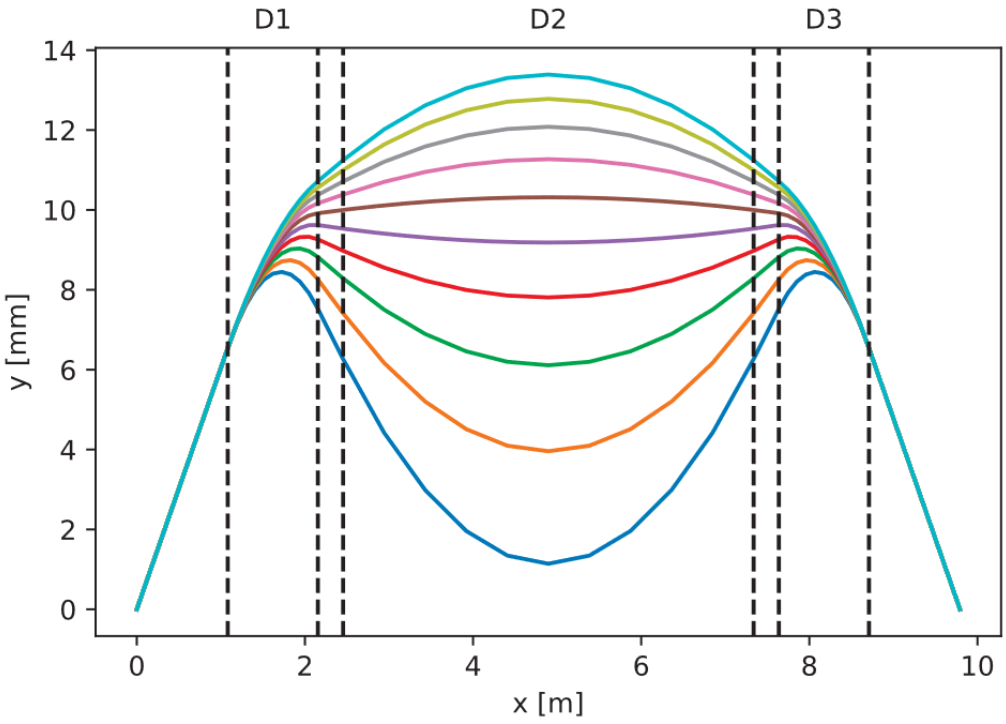

Figure 5.1: Closed orbits at different energies through one cell of the hybrid RCS2 design, retrieved from [105]. Note that x and y here represent cartesian coordinates in the horizontal plane, which differs from the convention used throughout this thesis.

bending for each beam energy (see Figure 5.1).

A consequence of this is a changing path length with energy, giving a variation in time-of-flight over the acceleration cycle. RCS2, with the parameters given in [105], has a 9.1 mm path length difference over its acceleration. The consequence of this is that the hybrid RCS cannot be operated at a fixed RF frequency, requiring a change in revolution frequency of approximately 2 kHz over the acceleration cycle. This is further complicated by the profile of the path length variation over time, displayed in Fig. 5.2, which shows that the minimum and maximum path length (and therefore minimum and maximum required RF frequencies) are only approximately 0.4 ms apart [106]. This results in a required frequency tuning speed on the order of 10 MHz/s, which will require the development of novel tuning systems for this purpose [107].

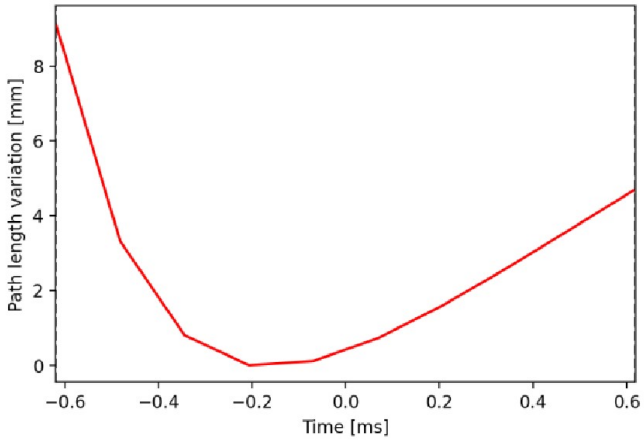

Figure 5.2: Path length variation as a function of time over the acceleration cycle of the RCS2 design [106].

5.1.3 vFFAs for Muon Acceleration

A fixed-field accelerator would be able to circumvent many of the issues associated with the RCS and hybrid RCS designs. Firstly, the removal of the requirement for ramped magnets removes the associated constraints on the acceleration rate of the machine. Secondly, the whole ring may be constructed with fixed-field superconducting magnets, reducing power consumption: not only from the lack of resistance in SC magnets reducing ohmic losses but also considering eddy current losses through the ramp cycle – which are likely to be significant. The gains in power efficiency are anticipated to be an increasingly major advantage, when the rising costs of energy and the need for sustainability in the face of climate adversity are considered.

When compared to the hybrid RCS, the quasi-isochronous nature of the vFFA becomes a particularly salient advantage. Isochronicity enables the use of on-crest acceleration (i.e. the choice of ϕ_s such that particles encounter the maximum of the sine waves). This is not possible in a synchrotron, where ϕ_s must be chosen away from the voltage peak to maintain phase stability. This means that a vFFA-based accelerator would be able to access increased accelerating voltage for an equivalent cavity design, an advantage that could be used to increase muon survival rates for the acceleration cycle by decreasing the overall time taken,

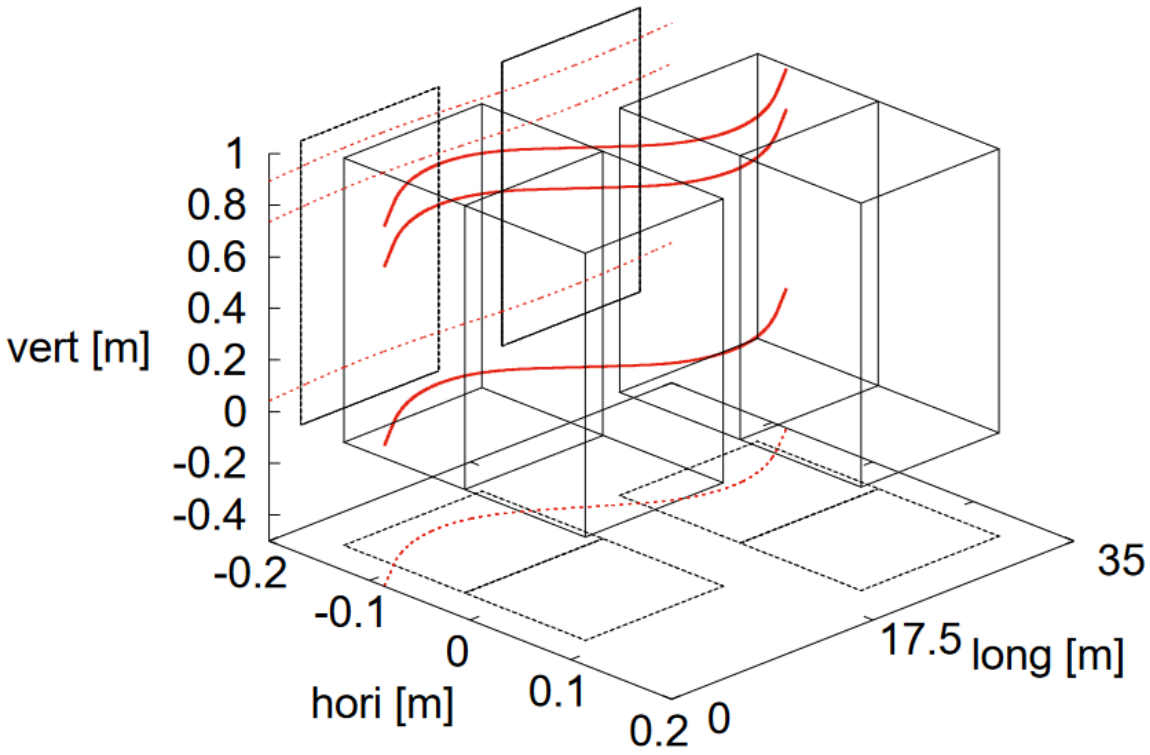

Figure 5.3: Diagram of the initial FODO lattice for muon acceleration taken from [108]. Here, the left block represents the reverse bend D-magnet, whilst the right block is the normal bend F-magnet. The solid red lines are the 3D paths corresponding to orbits at different momenta; the 2D projection of these on the horizontal and vertical planes are shown with dashed red lines.

or alternatively to relax demands on the RF voltage if the survival rate were kept fixed instead. Moreover, the hybrid RCS designs have a nonzero path length difference between injection and extraction, and a corresponding change in revolution frequency, requiring fast tunable RF. This would not be required for a vFFA, relaxing the need for development of new RF tuner technology.

5.2 vFFA Optimisation

An initial design based on a FODO lattice structure (according to the geometry depicted in Figure 5.3) was developed in 2019 [61, 108] to accelerate muons from 50 GeV to 1.5 TeV – with parameters listed in Table 5.2. This showed the feasibility of the vFFA concept for

	2019 Lattice	Optimisation
Circumference [m]	28350	25200
Number of Cells	810	720
Injection Energy [TeV]	0.05	0.05
Extraction Energy [TeV]	1.5	1.5
F-magnet length [m]	12.00	14.14
D-magnet length [m]	12.00	9.25
Drift length [m]	5.5	5.8
Peak Dipole Field [T]	8.7	7.7
m-value [1/m]	6.8	7.00
Excursion [m]	0.50	0.49
Tune	(0.40,0.086)	(0.44, 0.098)

Table 5.2: vFFA muon accelerator lattice parameters from an initial 2019 design exercise [61], and an optimisation of the same design using the analytic formula to reduce the peak B-fields, the excursion, and the circumference whilst maintaining the same drift lengths.

muon acceleration, though a number of optimisation targets were identified: firstly, the ring circumference is 28 km, larger than the LHC tunnel, and secondly the peak field on-beam is 8.7 T, a challenge from a magnet engineering perspective. The overall excursion is also large (0.5 m), which would require large-aperture magnets and RF systems to be developed for the machine; though it should be noted that this preliminary design had an energy factor of 30, having been designed as a single ring to occupy the same roles as RCS stages 1, 2, and 3. The design of this vFFA was derived from an approach based solely on manual trial-and-error optimisation of numerical simulations.

The parameters listed in Table 5.2 are given in terms of the magnet positions, and relative strengths of the magnets specified as the FD ratio – the ratio between the midplane dipole field of the F-magnet to the midplane dipole field of the D-magnet. The optimum magnet positioning and selection of the appropriate FD ratio is not immediately intuitive from this approach. Consequently, optimisation of this design proved challenging due to the multidimensional parameter space and the sensitivity of the closed orbit to changes in the inputs. For instance, a change in the FD ratio while keeping the horizontal offset of the magnets constant requires changes not only the horizontal bending of the closed orbit but also the bending in the vertical plane. Similarly, changing the m-value and keeping all

other parameters constant would cause changes to both the horizontal position and vertical profile of the closed orbit, unless the FD ratio was chosen such that the inclination in each magnet was zero.

In order to gain insight into the system, the analytic model derived in Chapters 2 and 3 was applied. The preliminary design was replicated in the analytic formalism by using a curve-fitting approach to select appropriate values of γ_F and θ_F that could be used as input in Eqs. (2.27-2.34) to produce a closed-orbit that matched the simulated closed orbit of the original lattice. These new input parameters were then used as a starting point from which knowledge of the analytic model could be employed to achieve the optimisation targets, whilst maintaining constraints from the original lattice (e.g. keeping the minimum allowed length of the drift the same to maximise space for cryostatic components, diagnostics, RF cavities, and other ancillaries). Transfer matrices for lattices were computed from input parameters by evaluating Eqs. (2.27 - 2.34) and substituting the results for the magnet parameters and drift lengths into the element transfer matrices (Eqs. (1.45), (3.38), (3.45), and (3.56)). The tunes were calculated by computing the arguments of the eigenvalues for the transfer matrices.

Reducing θ_F (as long as $\theta_F > \pi/N$) reduces the amount of excess bending in the cell, and correspondingly acts to reduce θ_D; minimising the bending reduces the dipole field requirements and helps to reduce the demands on magnet strength. The relationship between the magnetic field in the F-magnet of a given lattice and its input parameters can be computed by substituting ρ_F in Eq. (2.30) for the definition of magnetic rigidity, Eq. (1.4), and rearranging the result to obtain

$$\frac{P_0}{q}\frac{\sin\theta_F + (1-\cos\theta_F)\cos\gamma_F\tan\beta_F}{r_0\tan\beta_F} = B_F. \tag{5.3}$$

The same can be done for Eq. (2.33) to obtain B_D, substituting in Eqs. (2.27-2.32) beforehand. Figure 5.4 shows the relationship between θ_F in this lattice and the required dipole fields (as seen by a particle on the closed orbit).

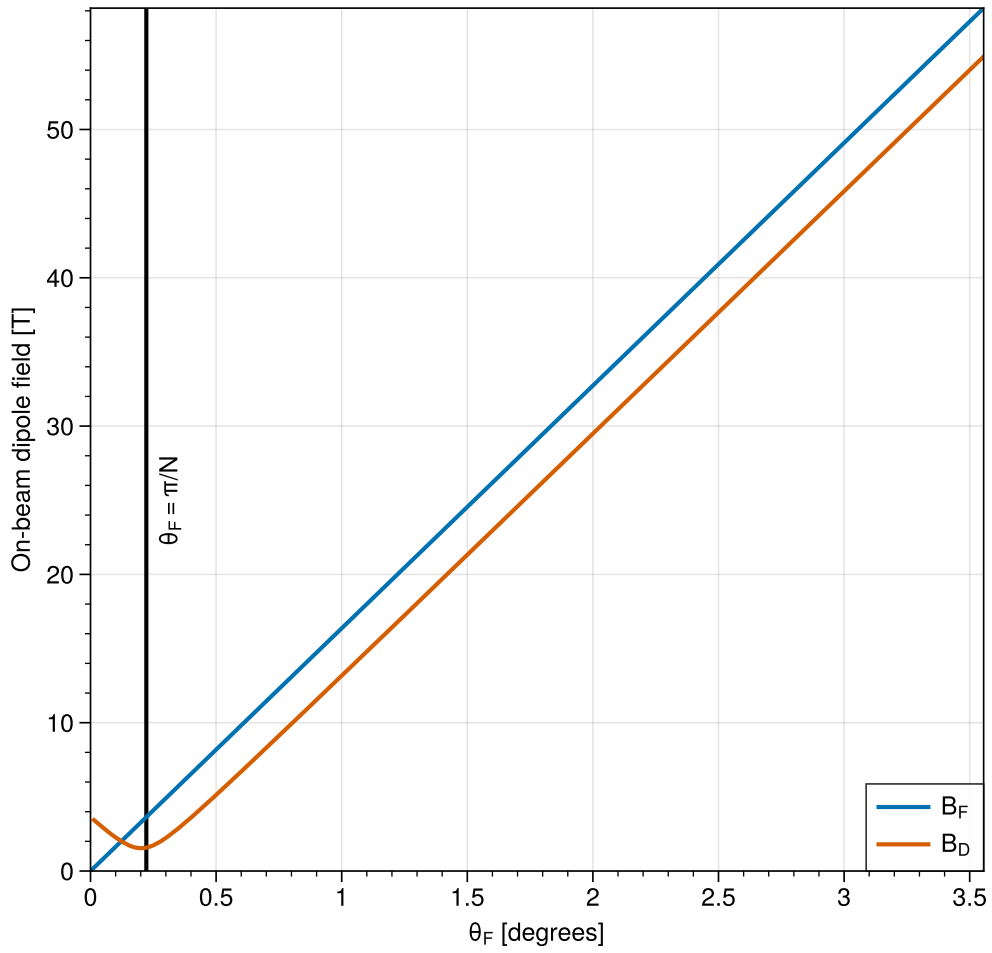

Figure 5.4: The dipole field experienced by a particle on the closed orbit as a function of the bending angle of the F-magnet (when all other parameters are kept fixed).

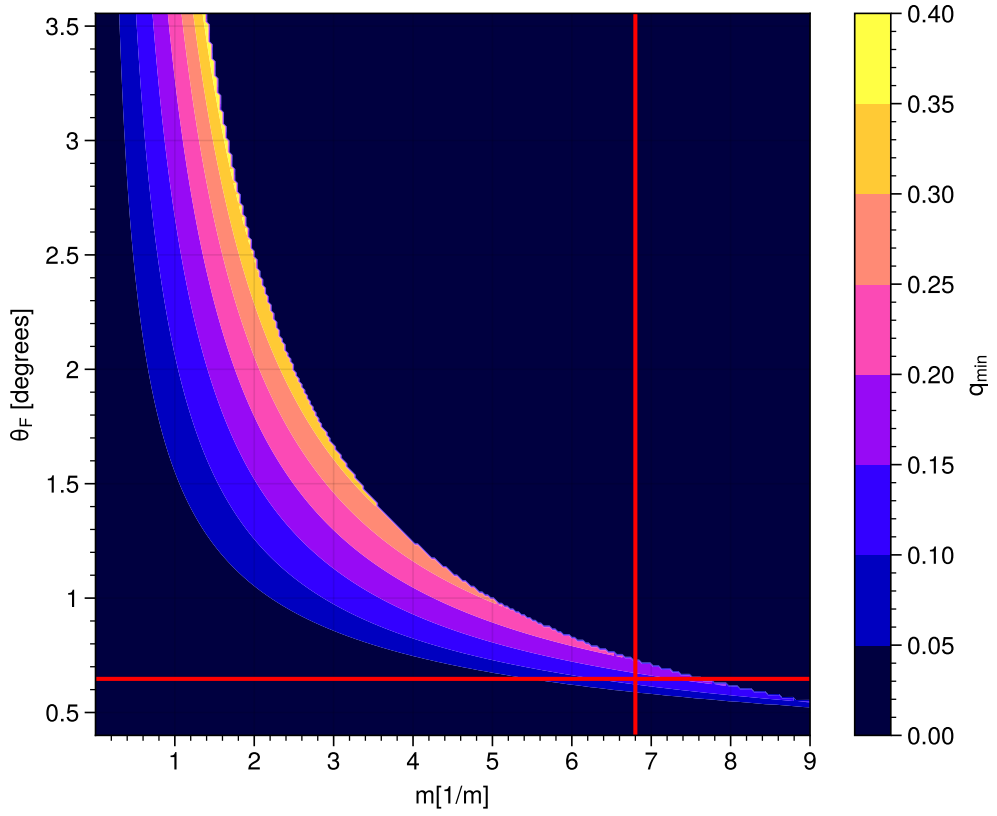

Figure 5.5: Stability region as a function of θ_F and m-value. The colour denotes the lower of the two decoupled tunes in cases where both planes are stable. The intersection of the red line shows the parameters of the preliminary lattice.

Figure 5.5 shows the effect of choosing different values of θ_F and m-value in the original 810-cell design. Reducing θ_F, while beneficial in terms of the dipole fields required for the magnets, acts to decrease the focussing strength in both planes: writing Eq. (2.30) in terms of a small angle approximation in θ_F we find that ρ_F is inversely proportional to θ_F;

$$\rho_F \simeq \frac{r_0 \tan \beta_F}{\theta_F}. \tag{5.4}$$

Equation (2.27) shows that decreasing θ_F (where $\theta_F > \pi/N$) also decreases θ_D, meaning that according to Eq. (2.33) ρ_D also decreases. Assuming r_2 is approximately constant as a function of θ_F, which is valid in the case that $r_0 >> \rho_{F,D}$, we find that Eq. (2.33) can be once again approximated as an inverse relationship between θ_D and ρ_D according to

$$\rho_D \simeq \frac{r_2 \sin \beta_D}{\sin \theta_D}. \tag{5.5}$$

If we examine the Hamiltonian of the vFFA magnet body, Eq. (3.36), we find that the quadrupole-like focussing terms are inversely proportional to the radius of curvature associated with the dipole component of the magnet. This means that a reduction in the magnitude of θ_F leads in turn to a decrease in focussing strength in both planes, affecting the tunes and stability of the lattice. The effect can be compensated by increasing the m-value to increase the strength of quadrupole components in the magnet bodies, indicated once again in Eq. (3.36).

This analysis serves to illustrate how the analytic model is able to explain the underlying physics of the system; it now becomes possible to apply these insights to the design of the machine by taking parameters from the analytic model and using these to position magnets and set their strengths. Figure 5.5 shows that the θ_F of the preliminary lattice is not at the minimum possible value for stability, and could be decreased further if the m-value were allowed to increase. This demonstrates that there is room to optimise this lattice.

To apply this knowledge to the 2019 vFFA lattice, the following procedure was used. First, the number of cells was reduced whilst maintaining the same cell length to achieve a machine circumference of 25.2 km. This value was chosen based on the circumference of

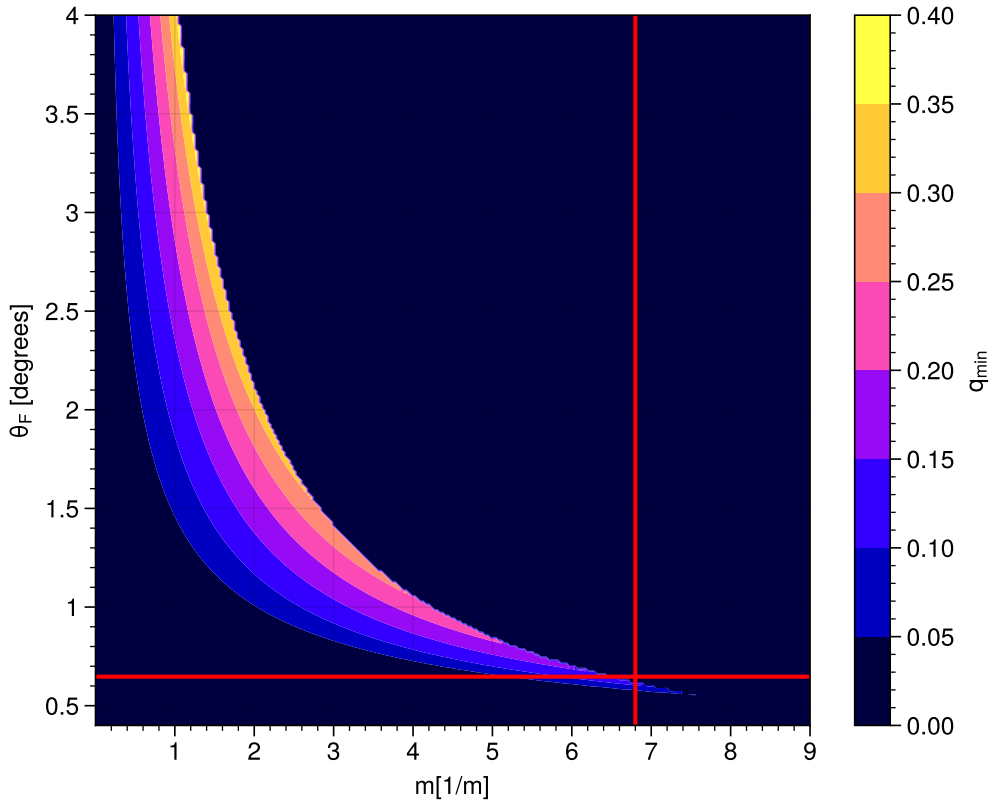

Figure 5.6: Stability region as a function of θ_F and m-value in the reduced-circumference lattice. The colour denotes the lower of the two decoupled tunes in cases where both planes are stable. The intersection of the red line shows the parameters of the preliminary lattice.

the LHC ring (26.7 km) with an allowance of 1.5 km for extra components to be inserted (e.g. straights for injection or extraction). A 2D slice of the new parameter space for this ring size is shown in Figure 5.6. This adjustment meant that the original choices of θ_F and m-value no longer produced stable optics. From here, θ_F and m-value were then reduced to restore lattice stability with both tunes satisfying $0.05 < q < 0.45$. Further optimisation was then achieved by increasing the lengths of the F- and D-magnets, reducing the dipole fields required to achieve the same overall bending; however, this also acts on the tune and decreases the space available for the drift. Figure 5.7 shows the dependence of the maximum required dipole field on the opening angles β_F and β_D of the F- and D- magnets, whilst the effect on the minimum of the two tunes is displayed in Figure 5.8.

The combination of these dependencies shows that for an optimal lattice it is necessary to reduce θ_F as much as possible whilst increasing the opening angles of magnets, and increasing the m-value until the drift is at its minimum viable length and the lattice is at the upper limit for m-value in terms of its stability.

Optimising by tweaking these parameters with the constraint of keeping a 5.5 m drift length through an iterative multi-dimensional gradient descent approach led to the set of parameters shown in the right column of Table 5.2. This represents a nearly 3 km decrease in the circumference of the machine – which is critical, as it would then fit in the LHC tunnel whilst leaving space for straight sections to use for injection, extraction, or high-gradient RF – concurrent with a reduction in the peak field of 1.0 T. At the same time, the drift length is increased by 30 cm, and the m-value is slightly increased, reducing the excursion by a small factor. The tunes of this lattice were verified numerically using the FIXFIELD tracking software to create a new equivalent lattice based on the input parameters of the analytic model: the numerically computed tunes were evaluated at $(0.41, 0.094)$, which is within 10% of the quoted value from the analytic model.

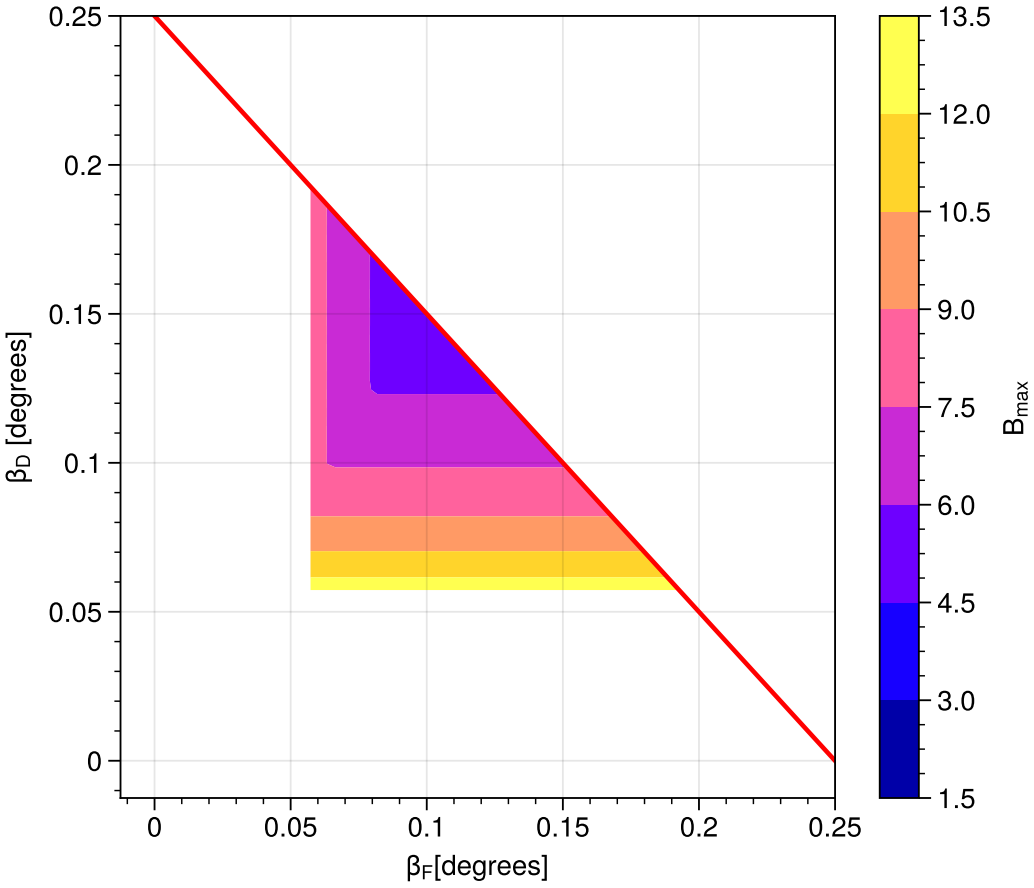

Figure 5.7: Maximum required dipole field as a function of β_F and β_D when other parameters are fixed. Points where $\beta_F + \beta_D > \pi/N$ are discarded as this would imply a negative drift length. Additionally, the fields for small values of $\beta_{F,D}$ are not displayed for visualisation reasons, as the asymptotic tendency of the required B-fields at low $\beta_{F,D}$ values would cause detail in the central region to be lost; however the scale is kept the same for consistency with Figure 5.8.

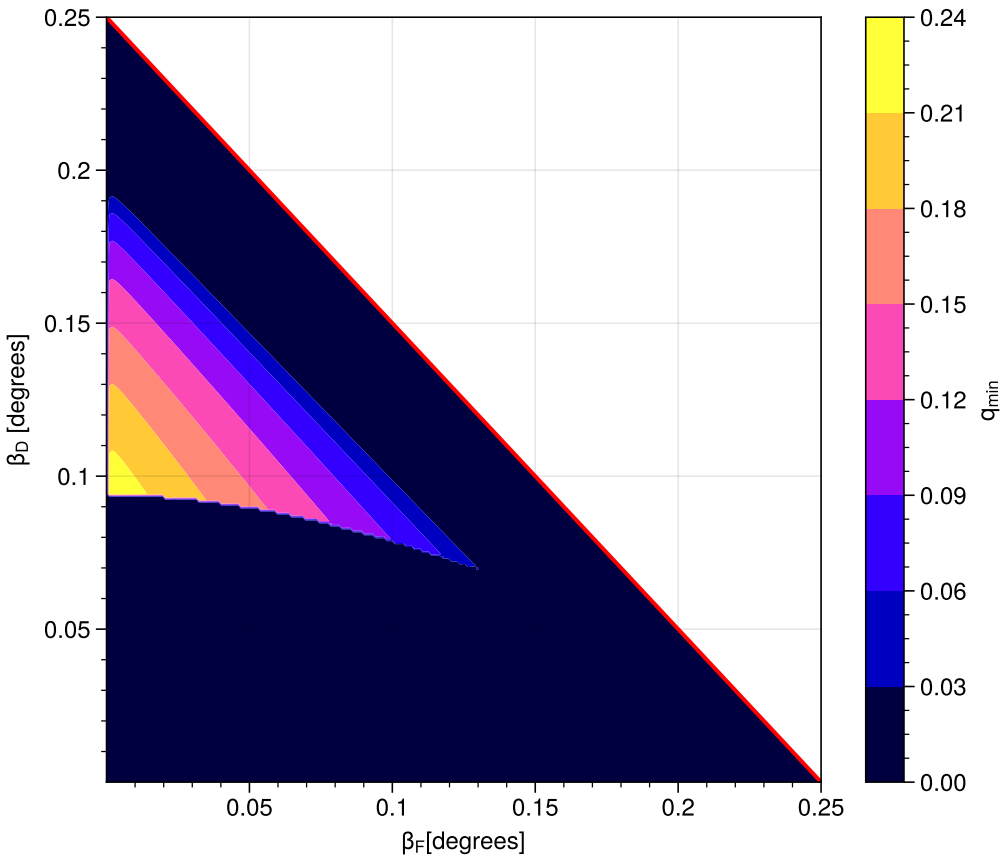

Figure 5.8: Minimum tune as a function of β_F and β_D when all other lattice parameters are fixed. Points where $\beta_F + \beta_D > \pi/N$ are discarded as this would imply a negative drift length.

	Stage 1 vFFA	Stage 4 vFFA
Circumference [m]	5990	35000
Number of Cells	810	1000
Injection Energy [TeV]	0.06	1.5
Extraction Energy [TeV]	0.3	5
F-magnet length [m]	6.36	18.76
D-magnet length [m]	4.24	13.12
Drift length [m]	1.05	1.56
Peak Dipole Field [T]	7.14	14.8
m-value [1/m]	30	10.44
Excursion [m]	0.048	0.12
Tune	(0.39, 0.13)	(0.41, 0.070)

Table 5.3: vFFA designs for equivalent ring sizes and energy ranges to the stage 1 and stage 4 RCS concepts

5.3 vFFA Design

Whilst the lattice above demonstrates a possible option for construction of a muon acceleration stage, it is not immediately comparable to the RCS designs (having been developed to a different specification, with a top energy equivalent to RCS3 but an injection energy equivalent to RCS1, and being designed with a larger circumference). In order to provide a more accurate basis for comparison, to demonstrate the capability of the vFFA to match the performance associated with RCS designs at similar input parameters, we propose two additional proof-of-concept vFFA muon accelerator lattices, designed to match the specifications of RCS1 and RCS4. With the efficacy of the analytic model proven in this regime of operation (large radii of curvature, comparatively short fringe fields), the design process for these rings is able to begin purely from the analytic model. The design targets selected are to match the circumferences of the RCS designs, whilst minimizing the maximum B-fields required, and keeping the excursion from injection to extraction at a minimum. Simultaneously, reasonable drift lengths ($> 1m$) must be maintained to accommodate diagnostics and magnet components. Table 5.3 shows the parameters of these designs.

This demonstrates not only the use of the analytic model to design new rings to different specifications, but also the viability of the vFFA as an alternative to an RCS for muon

acceleration. These do not represent finalised accelerator designs, however: a detailed parameter study could find room for further optimisation by adjusting the energy ranges of the accelerator stages from the values selected for the RCS project to values specifically tailored to exploit the vFFA's advantages.

A principal question in the development of this concept into a full facility design would concern the distribution of the accelerating cavities around the ring. The act of adding energy to the beam can be considered to cause an effective vertical shift of the equilibrium orbit. This means that if the accelerating cavities are not distributed around the ring, the beam will gain a large amount of energy at once with no change in transverse position, resulting in the beam being at a large displacement from the equilibrium orbit for the new energy. The vertical dispersion D in a vFFA is given by the relation

$$D = \frac{1}{m\Delta P/P_0} \ln\left(\frac{P_0 + \Delta P}{P_0}\right), \tag{5.6}$$

in which ΔP is the difference in the particle's momentum from the reference momentum P_0. This effect of nonzero dispersion combined with momentum gain at cavities would induce coherent oscillations, or for sufficiently large amplitudes, beam loss due to exceeding the dynamic aperture of the machine. By distributing the RF cavities into a number n_{RF} of cavities around the ring, the value of ΔE and therefore the magnitude of any individual kick can be made smaller. However, increasing the number of RF stations increases the requirements for distributed power, the number of required cryomodules, and the cost of the ring. It would be necessary to consider whether sufficient RF could be placed in the drifts of the FODO structures, or whether the acceleration requirements would be better served by RF included in potential straight sections (possibly with dispersion suppressors included in these straights to reduce the transverse oscillations caused by energy gain). The requirement for distributed RF is not however unique to the vFFA; for example, [109] discusses the need for distributed RF in the RCS due to synchrotron tune effects. Studies would also need to consider the design of the cavities themselves to achieve high-gradient, large-aperture cavities.

Lastly, design for a muon collider would need an in-depth study of magnet design to realise high-field superconducting magnets with a large vertical aperture. This would need to include an assessment of the effects of the neutrino flux from decaying muons on these magnets, and ensure their resilience in this high radiation environment. The radiated neutrino flux outside of the accelerator would also need to be studied for an assessment of the radiobiological impact of the machine's construction; as the vFFA design includes reverse bend and up-and-down vertical bending elements, the neutrino flux would be dissipated over a larger area than in RCS designs, which would reduce its peak intensity on the surface.

5.4 Conclusion

The analytic formalism for the vFFA was deployed to optimise an existing design, demonstrating its utility in application to accelerator parameter choices. It was then used to derive two novel designs to show the competitiveness of the vFFA concept for muon acceleration for similar parameter ranges to RCS baseline designs. This shows the use of the analytic model both in the context of existing designs, as well as for deriving new ones. The feasibility of vFFAs for muon acceleration is also displayed, with vFFA lattices designed to the specifications of the RCS chain baseline able to achieve the same energy ranges in the same footprint without exceeding dipole field constraints.

Chapter 6

Conclusions and Further Work

Scaling Fixed-Field Accelerators are a compelling option for future accelerator facilities, granting many of the advantages associated with synchrotron machines (multi-pass acceleration with a fixed tune and alternating gradient focussing) whilst providing the ability for flexible pulse structures, high repetition rates, and high-efficiency operation. The latter point, stemming from the use of time-independent fields (minimising eddy current losses in magnets and facilitating more widespread use of superconducting technologies), is becoming increasingly significant as a consideration in the design of new accelerators due to the rising costs of energy and the need for sustainability. A novel variation on the Fixed Field Accelerator, the vertical-excursion Fixed Field Accelerator (vFFA) was also recently proposed, wherein successive higher-energy orbits would be stacked vertically on top of lower-energy orbits. This adds the advantage of a fixed path length, which is not possible in a horizontal-excursion scaling FFA.

Both horizontal and vertical excursion FFAs have complexities in their modelling; each must support a continuum of closed orbits determined by geometric constraints, and each has a scaling law that mandates the existence of high-order multipoles throughout the lattice. The vFFA is additionally complicated by the presence of midplane longitudinal fields and skew-quadrupole components that introduce unavoidable coupling behaviour. Tracking studies also identified the non-planar nature of the closed orbits in many vFFA lattice designs.

This thesis reviewed methods of analytically determining closed orbits for FFAs, deriving new analytic models of closed orbits in three different classes of vFFA lattice (straight-cell FODO lattices, FODO ring cells, and DFD/FDF triplet ring cells). Performance of analytic models for closed orbits was benchmarked against the FIXFIELD integration code, and the predictions were found to agree closely. However, analytic models of the vFFA closed orbits based on the assumptions made in Chapter 2 are not able to account for fringe field components affecting closed orbits; this was found to be a significant factor in the closed orbit geometry found in tracking studies for low m-values at larger bending angles.

A model of linear optics for hFFAs was then derived using a Hamiltonian approach and shown to be able to predict the tunes and stability of hFFA lattices, when integrated with the closed orbit modelling from the previous chapter. The same techniques were also employed to model the linear optics of vFFA lattices, combining the Hamiltonian approach with the geometrical models of closed orbits to obtain a full analytic model of the vFFA. The predictions of this model were shown to agree well with simulation when the bending angle per cell is small (on the order of 1 degree or smaller) which is the case for a large ring such as those proposed for muon acceleration. The agreement became worse, however, for lower m-values.

A multipole decomposition technique was developed and then employed to identify the source of this discrepancy, which was significantly affected by the presence of monopole radial fields in the fringes of the magnets. This was an element that could not be accounted for in the analytic model using a single thin lens element to approximate a fringe field. The same multipole decomposition technique was then used to analyse the behaviour of small-ring lattices (i.e. of the order of tens of degrees bending angle per cell), where the approximations used to derive the analytic model become weak. This showed that, for the triplet lattice studied as part of the FETS-FFA design study for ISIS-2, modelling of quadrupole and skew quadrupole-type focussing alone was not sufficient to understand the optical behaviour of the lattice, and to understand its properties it was necessary to consider

additionally the effects of radial fields, geometric focussing, and Larmor rotation. Longitudinal fields were shown to become increasingly dominant at low m-values, having much greater effect on the tune than quadrupole components for these lattices. These present significant steps towards the understanding of the vertical FFA, which will be crucial to its development as a realistic option for new accelerators.

Designing FFAs for practical applications requires knowledge of their nonlinear properties; the presence of multipole components gives rise to effects such as amplitude-dependent tune shifts, which cause particles at large amplitudes to encounter resonances and therefore be lost. This ultimately limits the dynamic aperture of the machine, which is undesirable in high-power machines where the reduction of beam loss is a primary concern. Understanding nonlinear effects can be particularly challenging in FFAs, due to the distributed nature of multipole components, the reliance on edge-angle focussing, and the complicated nature of closed orbits.

We studied the effect of amplitude-dependent tune shift in the horizontal plane for hFFAs with an experiment at the KURNS main ring, comparing experimental results to predictions based on simulation. The simulation was shown to be able to predict the real tune shifts of the ring, given an adjustment of input parameters to match the same zero-amplitude tune observed from experimental data. With the simulation effectively benchmarked against experimental studies, the multipole decomposition technique used for analysis of the linear optics in vFFAs was deployed for the study of sources of tune shift in hFFA rings, and we were able to positively identify the primary source of tune shift in the KURNS ring as the second-order effect of the sextupole components. We then applied simulation-based techniques to study amplitude-dependent tune shifts in the context of optimising the dynamic aperture of an FD-spiral hFFA lattice, identifying the octupolar component of the fringe field as the primary source of amplitude-dependent tune shift in these lattices. These studies demonstrated that the optimal spiral angle for the 16-cell lattice tested was 45 degrees (which minimised reverse bending without a large increase in

the amplitude-dependent tune shift coefficient).

Finally, the analytic model of the vFFA was employed to study the prospect of a vFFA ring for muon acceleration. An initial FODO design based on a 2019 design study was taken and replicated in the analytic model, and the insights of the analytic model were used to reduce the peak B-fields as well as the ring's circumference whilst maintaining the same drift lengths. This study resulted in a reduction of ring circumference of 3.15 kilometres (from 28.35 km to 25.20 km) whilst simultaneously reducing the peak dipole fields required by 1.0T (down to 7.7 T from 8.7 T). Designs were also presented based purely on the analytic model to show the feasibility of the vFFA concept as an alternative option for rapid muon acceleration; it was shown that vFFA rings could be designed with equivalent footprints and peak dipole strengths to the RCS baseline designs for the same energy ranges. This demonstrates the possibility of fixed-field isochronous muon acceleration for a high-efficiency high-energy future collider.

6.1 Further Work

The work outlined in Chapters 2 and 3 laid the foundations for analytic study of the vFFA and benchmarked analytic predictions against simulations from the tracking code FIXFIELD; future studies would develop this research with further benchmarking against other tracking codes, and would develop numerical studies to test its predictions against other variations on the vFFA design. In particular, all results were benchmarked against simulations of rectangular magnet designs. Constructing a ring with sector magnets, as proposed in [110], would mitigate the effects of longitudinal fields on the closed orbits by decreasing the dipole contribution ratio discussed in Section 2.5. This fact could decrease the limits on the domain of applicability for the analytic model for sector magnet machines. Developing a simulation of a sector magnet vFFA would enable the testing of this concept. Furthermore, the work of Brooks [31] proposed the construction of a 'tilted' vFFA, where the end planes of vFFA magnets would be skewed to provide additional edge focussing effects

(and thereby enable the reduction of reverse-bending requirements - an effective equivalent to the spiral sector magnet of the hFFA). Testing the analytic model's ability to approximate the effects of this would be a worthwhile investigation, as it would introduce another parameter that could be optimised to achieve desired machine properties for a given application, and study of the tilted vFFA concept may enable the construction of more compact vFFA rings.

The fringe field modelling approach for the vFFA as outlined in Chapter 3 was additionally found to be lacking at smaller values of m due to the effects of radial and longitudinal fields. The effect of monopole radial fields in the fringe field of a magnet could not be approximated using a single thin-lens transfer matrix; a future investigation could test the possibility of developing an analytic model of a vFFA fringe consisting of multiple elements (for instance, a radial field transfer matrix at the entrance of a fringe, a combined Larmor rotation and drift matrix of the length of the fringe field, and a second thin lens radial field transfer matrix with the opposite sign to the original), or a full thick-lens model based on a chosen axial field distribution function $F(Y)$ (such that $B(Y) = B_0 e^{mz} F(Y)$.

In study of the nonlinear properties of FFAs, the harmonic analysis approach was applied only to the study of the hFFA. The same arbitrary-order multipole decomposition could be applied to the vFFA; however, understanding the effects of multipoles on the properties of the beam is substantially complicated by the presence of coupling. Multipole coefficients are easily understood in terms of their impacts on the x and z transverse planes in which they act, but understanding of the action of an individual multipole component on the decoupled u and v planes becomes substantially harder. Such a study would require an advanced implementation of linear decoupling techniques, but could go a long way towards advancing knowledge of vFFA properties. Numerical studies [34, 111] have begun to test the dynamic aperture of the vFFA and to identify regions of parameter space that maximise vFFA dynamic aperture, but understanding of the reasons for favourable properties in these areas of parameter space is as yet limited. Reparametrising the lattices identified by these

studies in terms of the geometry of the closed orbit modelling instead of the properties of the magnets used to generate them may also grant some degree of insight (analogous to how, when designing the vFFA muon accelerator ring, optimisation of the ratio of strengths of the magnets was unintuitive, but once the lattices were expressed in terms of the bending angles of the closed orbit, optimisation became much more trivial).

Finally, an integrated design of a muon accelerator facility containing one or more vFFA rings would be necessary to truly prove the viability of the vFFA as a candidate for muon acceleration. The parameters shown in Section 5.3 were based on those selected for the rapid cycling synchrotron chain; as the vFFA has differing strengths and weaknesses to the RCS and hybrid RCS counterparts, choosing different energy ranges and geometries for vFFA rings could optimise a facility design further. For instance, adjusting a vFFA to have a smaller energy range (thereby reducing its excursion) but a faster rate of acceleration (as it would not be limited by the ramp rate of magnets as in an equivalent RCS design) could achieve a higher muon survival rate for delivery to the next accelerator.

Detailed design of acceleration, injection, and extraction systems would also be a vital part of vFFA design. Section 5.3 outlined some considerations for this, as to whether RF would be included in dispersive drifts throughout the ring or whether acceleration would be best served by a smaller number of RF cavities contained in dedicated straights (potentially in dispersion-suppressed regions). A future study of a muon accelerator vFFA would combine all of these elements to propose a full facility design.

Furthermore, detailed study of the longitudinal motion in FFAs is necessary for the full understanding of the 6D behaviour of the systems. In particular, study of longitudinal dynamics of a vFFA will be of vital importance to the realisation of the vFFA concept and to designing effective acceleration schemes for these machines - both for applications in muon acceleration and in other fields. Future studies will investigate the longitudinal dynamics of vFFAs both at sub-relativistic momenta and in the relativistic quasi-isochronous regimes.

Appendix A

The FIXFIELD Tracking Code

Throughout this work, numerical results are provided by simulations carried out using the FIXFIELD code [53]. FIXFIELD is a particle tracking code tailored specifically for simulation of scaling FFAs (though other types of magnets are also included).

The FIXFIELD tracking code, developed in C, is based on an implementation of a 4th-order Runge-Kutta integrator [56] in a Frenet-Serret coordinate system. Particles are tracked cell-by-cell via integration of the equations of motion through the magnetic fields associated with the magnets in the lattice.

Once a cell is established in the FIXFIELD simulation, closed orbits are found by tracking a test particle with given starting coordinates, and computing the displacement between its initial transverse coordinates on the cell boundary and its final transverse coordinates on the opposing cell boundary; this displacement is minimised using an iterative search of 4D initial coordinates (with the option of employing a number of different minimisation algorithms, such as the Nelder-Mead simplex algorithm [57], or more brute-force 4D scans). Transfer matrices and Courant-Snyder functions are computed by tracking particles with small deviations from the reference orbit, and tunes may either been computed directly from these transfer matrices or by frequency analysis methods such as the FFT [67].

Early studies using FIXFIELD included the simulation of a straight scaling FFA cell, and the performance of its tracking in this case was later confirmed with experimental results [60]. Further to this, FIXFIELD was used in the development of the NUSTORM

FFAG concept [112], in which study the results of the FIXFIELD tracking were checked against simulations based on the Zgoubi tracking code [113].

At the point at which research for this thesis began in 2019, FIXFIELD was one of the very few codes that contained an implementation of vFFA magnetic fields, and hence presented an obvious choice for the study of vFFA beam dynamics. Other vFFA implementations at the time known to the author included the FORTRAN-based SCODE [114], and the MUON1 code [115], the latter of which is not publicly distributed. FIXFIELD was chosen over SCODE as the primary simulation tool in this thesis due to the author's familiarity with C and relative lack of FORTRAN experience. Since 2019, implementations of vFFAs have now been added to numerous other codes, including OPAL [116] and Zgoubi [117].

The agreement of these simulations has since been cross-checked, and an example benchmarking of vFFA simulation results from FIXFIELD, SCODE, and OPAL can be found in [32] (Appendix A). Agreement is close across all three codes, differing by a maximum of 1% in the calculated tunes. This benchmarking was later extended to include a result from Zgoubi [117], which shows a convergence of the Zgoubi simulation on a tune value in both planes close to that computed by the FIXFIELD simulation.

This gives a high degree of confidence in the validity of FIXFIELD simulations for making predictions about the behaviour of scaling FFAs, and in the utility of FIXFIELD simulation as a crosscheck for theoretical modelling.

Appendix B

Uncertainty Estimation for the Numerical Analysis of Fundamental Frequencies

The uncertainty in a frequency measurement as obtained using the Numerical Analysis of Fundamental Frequencies [80] (NAFF) is often quoted as being proportional to $1/N^2$ for a number of samples N. A derivation of the uncertainty for a NAFF measurement is found in Appendix C of [81] for a simplified signal $z(t)$ of the form

$$z(t) = e^{2\pi i f_a t} + b_0 e^{2\pi i f_b t}, \tag{B.1}$$

comprised of a sinusoidal component of unit amplitude at the desired frequency f_a with a superimposed sinusoidal perturbation at a different frequency f_b and an amplitude $|b_0| \ll 1$. This signal is then discretely sampled N times at regular intervals of $1/f_s$.

The Fourier transform of the sampled signal is then given by

$$\phi(f) = \phi_a(f) + \phi_b(f) = \frac{\sin\left[\pi(f_a - f)N\right]}{\pi(f_a - f)N} + b_0 \frac{\sin\left[\pi(f_b - f)N\right]}{\pi(f_b - f)N}. \tag{B.2}$$

The maximum of this function would be the measured frequency from the NAFF method. By taking the derivative and setting equal to zero, we are able to derive an expression for the maximum of the Fourier transform for the combined signal:

$$\frac{d\phi}{df}(f) = 0 = \phi_b'(f_a) + (f - f_a)(\phi_a''(f_a) + \phi_b''(f_b)) + O(f - f_a)^2. \tag{B.3}$$

The resulting measured frequency estimate f_M is then

$$f_{\mathrm{M}} = f_a - f_s \frac{\phi_b'(f_a)}{\phi_a''(f_a) + \phi_b''(f_a)} = f_a - f_s \frac{\phi_b'(f_a)}{\pi^2 N^2/3 - \phi''(f_a)}. \tag{B.4}$$

Expanding in powers of N^{-1} gives an estimate for the uncertainty as

$$\alpha_{f_M} = f_s \left(\frac{3b_0}{\pi^2 N^2} \frac{\sin(\pi(f_b - f_a)N) + \pi N(f_a - f_b)\cos\left(\pi(f_b - f_a)N\right)}{\pi(f_b - f_a)^2 N} \right). \tag{B.5}$$

This result for the uncertainty confirms the $1/N^2$ dependence. However, computing the absolute uncertainty in the measured frequency f_M using this relation requires knowledge of the relative amplitude of the perturbation b_0 and its frequency f_b. Additionally, the validity of approximating the signal observed in the experimental data taken for Chapter 4 as a superposition of two sine waves is not guaranteed.

Further to this, results such as [83] indicate that the uncertainty of the NAFF method is sensitive to the presence of more broad-spectrum noise, with the uncertainty in the tune measurement being measured in this paper as proportional to $1/N^{1.5}$ for a waveform with Gaussian noise at 5% of the amplitude of the signal. In order to estimate uncertainties for the NAFF frequency measurements of the experiment described in Chapter 4 of this thesis, the performance of a NAFF algorithm was tested on artificially-generated noisy data.

Firstly, a set of 2^6 signals were generated consisting of sinusoidal oscillations with superimposed Gaussian noise.

$$z(t) = A\sin(2\pi f_{\text{test}} t) + B * \text{Noise} \tag{B.6}$$

The amplitude of the sinusoidal oscillation A was chosen to match the measured amplitude of the sideband peak in the FFT spectrum for a given data series from the experiment. The amplitude B of the added Gaussian noise was chosen such that, when the FFT of the artificial signal was taken, the mean FFT amplitude measured across a large number of frequency bins (away from spectral peaks) as the same as an equivalent measurement performed on the real dataset. The frequencies of the artificial signals were then normally

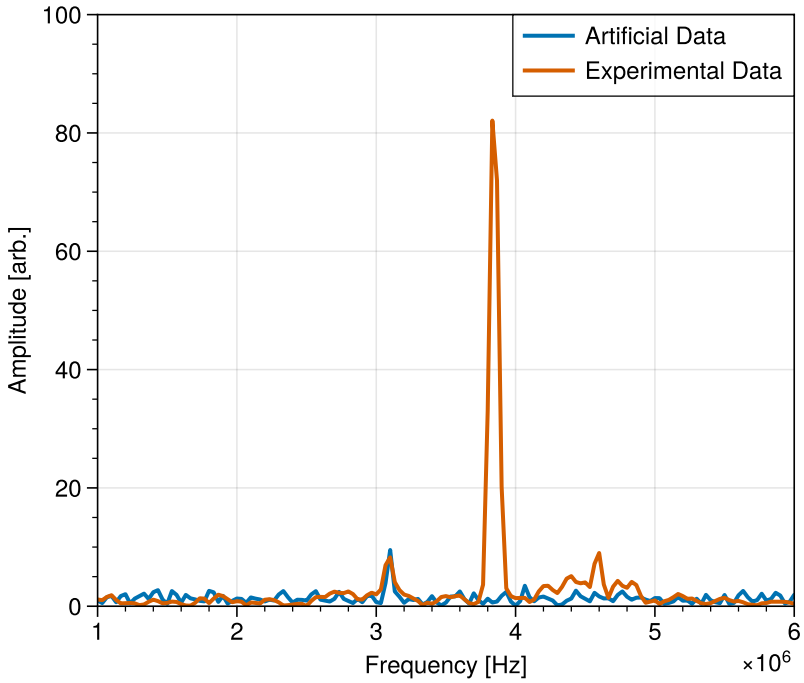

Figure B.1: Comparison of artificially generated test data to experimental data for a 5kV kicker activation.

distributed about the measured sideband frequency from the experimental data with a standard deviation of 300kHz. An example of an artificially generated signal compared to its equivalent from the experimental data is displayed in Figure B.1 for the 5 kV kicker activation (in this case the frequency is selected to be equal to the frequency of the sideband).

The NAFF algorithm was then used to compute frequencies from the artificial data. The frequencies measured using the NAFF f_{NAFF} were then compared to the input frequencies f_{test}, and the standard deviation of the measured frequency minus the input frequency $f_{\mathrm{test}} - f_{\mathrm{NAFF}}$ was taken as an estimate of the error in the presence of random noise.

This process was repeated for all kick amplitudes to measure the standard deviation of the NAFF frequency measurement at different signal-to-noise ratios. The same routine was also used to estimate the frequency uncertainty in the for the revolution frequency peaks. Whilst the revolution frequency peak should in principle be the same for all kick amplitudes, fluctuations in beam intensity cause variations in the height of the revolution

frequency peak, and as a result the uncertainties in the position of the revolution frequency peak are individual to each measurement.

The method outlined here for estimating the uncertainty in the frequency is limited in that it only considers the effect of random noise on the frequency measurement; the presence of other periodic signals could introduce more uncertainty. A future experiment would be able to carry out a large number of repeat measurements at each kick amplitude and thereby estimate uncertainties directly from the standard deviation of measured data.

Bibliography

[1] A. Zangwill, Modern Electrodynamics. Cambridge: Cambridge University Press, 2013.

[2] S. Y. Lee, Accelerator Physics. World Scientific, 3rd ed., 2011.

[3] B. Taylor, Methodus incrementorum directa & inversa. (Taylor's Version). Londini: Typis Pearsonianis prostant apud Gul. Innys ad Insignia Principis in Coemeterio Paulino, 1715.

[4] H. Goldstein, J. Safko, and C. Poole, Classical Mechanics: Pearson New International Edition. Pearson Education, 2014.

[5] E. Wilson, An Introduction to Particle Accelerators. Oxford University Press, 2001.

[6] A. Seville, D. Adams, D. Bayley, R. Bendall, I. Gardner, M. Glover, A. Morris, J. Thomason, and C. Warsop, "First Results from the use of Dual Harmonic Acceleration on the ISIS Synchrotron," in Proceedings of the 2005 Particle Accelerator Conference, pp. 1871–1873, 2005.

[7] A. Wolski, Beam Dynamics in High Energy Particle Accelerators. Imperial College Press, 2014.

[8] E. O. Lawrence, "Method and apparatus for the acceleration of ions," U.S. Patent 1,948,384, 1934.

[9] J. K. G. et. al., "The energy efficiency of high intensity proton driver concepts," in Proceedings of of the 8th International Particle Accelerator Conference (IPAC2017), Copenhagen, Denmark, p. 4842, 2017.

[10] H. A. Bethe and M. E. Rose, "The maximum energy obtainable from the cyclotron," Phys. Rev., vol. 52, pp. 1254–1255, Dec 1937.

[11] L. H. Thomas, "The paths of ions in the cyclotron i. orbits in the magnetic field," Phys. Rev., vol. 54, pp. 580–588, Oct 1938.

[12] M. K. Craddock, "AG Focusing in the Thomas Cyclotron of 1938," in Particle Accelerator Conference (PAC 09), p. FR5REP113, 2010.

[13] R. Baartman and T. Planche, Cyclotrons. A textbook introduction to cyclotron dynamics, unpublished.

[14] M. Seidel and P. Schmelzbach, "Upgrade of the PSI cyclotron facility to 1.8 MW," Proc. Cycl. and their Appl, 2007.

[15] I. Bylinskii and M. Craddock, "The TRIUMF 500 MeV cyclotron: the driver accelerator," Hyperfine Interactions, vol. 225, pp. 9–16, 2014.

[16] E. McMillan, "Synchro-cyclotron," US Patent 2 615 129, Oct. 1952.

[17] E. Courant, M. Livingston, and H. Snyder, "The strong-focusing synchroton, - a new high energy accelerator," Physical Review, vol. 88, p. 1190, 1952.

[18] R. P. Walker, "Synchrotron radiation," CERN Accelerator School, 1994.

[19] K. R. Symon, D. W. Kerst, L. W. Jones, L. J. Laslett, and K. M. Terwilliger, "Fixed-Field Alternating-Gradient Particle Accelerators," Phys. Rev., vol. 103, p. 1837, 1956.

[20] T. Ohkawa in Proc. Annual meeting of JPS, 1953.

[21] A. A. Kolomensky and A. N. Lebedev, Theory of Cyclic Accelerators. North-Holland, Amsterdam, 1966.

[22] J. Thomason, "The ISIS Spallation Neutron and Muon Source—The first thirty-three years," Nuclear Instruments and Methods in Physics Research Section A: Accelerators, Spectrometers, Detectors and Associated Equipment, vol. 917, pp. 61–67, 2019.

[23] K. R. Symon and A. M. Sessler, "Methods Of Radio Frequency Acceleration In Fixed Field Accelerators With Applications To High Current And Intersecting Beam Accelerators," Conf. Proc. C, vol. 560611, pp. 44–58, 1956.

[24] T. Uesugi, Y. Ishi, Y. Kuriyama, Y. Mori, C. Jolly, D. Kelliher, J.-B. Lagrange, A. Letchford, S. Machida, M. Topp-Mugglestone, D. Posthuma de Boer, C. Rogers, and E. Yamakawa, "Beam stacking experiment at a Fixed Field Alternating Gradient Accelerator." Forthcoming, 2024.

[25] J. Flowerdew, Investigating Nonlinear Integrable Optics with a Paul Trap. PhD thesis, University of Oxford, 2023.

[26] D. W. K. others., "Electron model of a spiral sector accelerator," Rev. Sci. Instrum., vol. 31, pp. 1076–1106, 1960.

[27] S. Machida, "Scaling Fixed-Field Alternating-Gradient Accelerators with Reverse Bend and Spiral Edge Angle," Phys. Rev. Lett., vol. 119, p. 064802, Aug 2017.

[28] T. Ohkawa Phys. Rev., vol. 100, p. 1247, 1955.

[29] G. Leleux, J. Proy, and M. Salvat, "F.F.A.G. helicoïdal etude de la stabilite betatron," tech. rep., Papport O. C. 70 (Service de Physique Appliquee, Section D'Optique Corpusculaire)., 1959.

[30] J. Teichmann Sov. J. At. Energ., vol. 12, p. 507, 1963.

[31] S. Brooks, "Vertical orbit excursion fixed field alternating gradient accelerators," Physical Review Special Topics - Accelerators and Beams, vol. 16, 08 2013.

[32] S. Machida, D. J. Kelliher, J.-B. Lagrange, and C. T. Rogers, "Optics design of vertical excursion fixed-field alternating gradient accelerators," Phys. Rev. Accel. Beams, vol. 24, p. 021601, 2021.

[33] M. Vanwelde, Characterization of advanced vertical orbit excursion fixed-field accelerators. PhD thesis, Université libre de Bruxelles, Ecole polytechnique de Bruxelles, 2023.

[34] A. Oeftiger, A. Santamaría García, J.-B. Lagrange, and S. Hirlander, "Active deep learning for nonlinear optics design of a vertical FFA accelerator," in Proc. 14th International Particle Accelerator Conference (IPAC2023), 2023.

[35] T. P. Wangler, RF Linear Accelerators. John Wiley & Sons Ltd., 2008.

[36] Y. Yonemura, A. Takagi, M. Yoshii, Y. Mori, M. Aiba, K. Okabe, and N. Ikeda, "Development of RF acceleration system for 150MeV FFAG accelerator," Nuclear Instruments and Methods in Physics Research Section A: Accelerators, Spectrometers, Detectors and Associated Equipment, vol. 576, no. 2, pp. 294–300, 2007.

[37] Y. Kawase, "Neutron Factory Project at KURRI," in Proc. 1st Asian Particle Accelerator Conference, Tsukuba, Japan, p. 104, 1998.

[38] C. H. Pyeon, Accelerator-Driven System at Kyoto University Critical Assembly. Springer Singapore, 2021.

[39] M. Tanigaki, Y. Mori, M. Inoue, K. Mishima, S. Shiroya, Y. Ishi, and S. Fukumoto, "Present status of the FFAG accelerators in KURRI for ADS study," 2006.

[40] J.-B. Lagrange, D. J. Adams, C. Brown, H. V. Cavanagh, I. S. K. Gardner, P. Griffin-Hicks, B. Jones, D. J. Kelliher, A. P. Letchford, S. Machida, B. G. Pine, C. R. Prior, C. T. Rogers, J. W. G. Thomason, C. M. Warsop, R. E. Williamson, J. Pasternak, J. K. Pozimski, and G. H. Rees, "Progress on Design Studies for the ISIS II Upgrade," in Proc. 10th International Particle Accelerator Conference (IPAC'19), Melbourne, Australia, 19-24 May 2019, (Geneva, Switzerland), pp. 2075–2078, JACoW Publishing, Jun. 2019.

[41] D. J. S. Findlay, "ISIS: Pulsed neutron and muon source," Conf. Proc. C, vol. 070625, p. 695, 2007.

[42] M. Kinsho, "Status of the J-PARC 3 GeV RCS," Proc. IPAC2015, THPF044, 2015.

[43] T. G. Trippe, A. Barbaro-Galtieri, R. L. Kelly, A. Rittenberg, A. H. Rosenfeld, G. P. Yost, N. Barash-Schmidt, C. Bricman, R. J. Hemingway, M. J. Losty, M. Roos, V. Chaloupka, and B. Armstrong, "Review of particle properties," Rev. Mod. Phys., vol. 48, pp. S1–S245, Apr 1976.

[44] K. Hübner, "Synchrotron radiation," tech. rep., CERN, Geneva, 1984.

[45] K. D. Held, H. Kawamura, T. Kaminuma, A. E. S. Paz, Y. Yoshida, Q. Liu, H. Willers, and A. Takahashi, "Effects of charged particles on human tumor cells," Frontiers in Oncology, vol. 6, 2016.

[46] X. Zhang and S. Sheehy, "Current and future synchrotron designs for carbon ion therapy," AIP Conference Proceedings, vol. 2346, p. 050005, 03 2021.

[47] J. Yap, A. De Franco, and S. Sheehy, "Future developments in charged particle therapy: Improving beam delivery for efficiency and efficacy," Frontiers in Oncology, vol. 11, 2021.

[48] F. Meot, "RACCAM: An example of spiral sector scaling FFA technology," tech. rep., Brookhaven National Laboratory, 2019.

[49] K. J. Peach, J. H. Cobb, S. L. Sheehy, H. Witte, T. Yokoi, M. Aslaninejad, M. Easton, J. Pasternak, R. Barlow, H. L. Owen, S. Tygier, C. Beard, P. McIntosh, S. Pattalwar, S. Smith, S. Tzenov, N. Bliss, T. Jones, J. Strachan, R. Edgecock, J. Pozimski, R. Fenning, A. Khan, I. Gardner, D. Kelliher, S. Machida, M. Hill, C. Johnstone, B. Jones, B. Vojnovic, and R. Seviour, "Pamela : overview and status," in Proceedings of the 1st International Particle Accelerator Conference IPAC 2010, pp. 112–114, Kyoto, Japan: JACoW, May 2010.

[50] V. Favaudon, L. Caplier, V. Monceau, F. Pouzoulet, M. Sayarath, C. Fouillade, M.-F. Poupon, I. Brito, P. Hupé, J. Bourhis, J. Hall, J.-J. Fontaine, and M.-C. Vozenin, "Ultrahigh dose-rate flash irradiation increases the differential response between normal and tumor tissue in mice," Science Translational Medicine, vol. 6, no. 245, pp. 245ra93–245ra93, 2014.

[51] E. Courant and H. Snyder, "Theory of the Alternating-Gradient Synchrotron," Annals of Physics, vol. 281, no. 1, pp. 360–408, 2000.

[52] S. Machida, "Design and particle tracking of FFAG," Nuclear Instruments and Methods in Physics Research Section A: Accelerators, Spectrometers, Detectors and Associated Equipment, vol. 503, no. 1, pp. 322–327, 2003. Proceedings of the 3rd International Workshop on Neutrino Factories based on Muon Storage Rings.

[53] J.-B. Lagrange, "The Particle Tracking Code Fixfield," in 12th International Particle Accelerator Conference , 8 2021.

[54] C. Runge, "Ueber die numerische Auflösung von Differentialgleichungen," 1895.

[55] W. Kutta, Beitrag zur näherungsweisen Integration totaler Differentialgleichungen, Inaugural-Dissertation ... von Wilhelm Kutta ... Druck von B.G. Teubner, 1901.

[56] P. L. DeVries, A First Course in Computational Physics. USA: John Wiley & Sons, Inc., 1st ed., 1993.

[57] J. A. Nelder and R. Mead, "A Simplex Method for Function Minimization," The Computer Journal, vol. 7, no. 4, pp. 308–313, 1965.

[58] S. Machida, J.-B. Lagrange, A. Letchford, C. Jolly, D. Kelliher, C. Rogers, E. Yamakawa, and J. Pasternak, "FFA Design Study for a High Intensity Proton Driver," JACoW, vol. IPAC2023, 2023.

[59] H. Enge, "Deflecting Magnets, in "Focusing of Charged. Particles", edited by A. Septier," 1967.

[60] J.-B. H. R. Lagrange, Study of zero-chromaticity in FFAG accelerators. PhD thesis, Kyoto U., 2012.

[61] S. Machida, "Bandwidth of FFAGs," in CERN Muon Collider Workshop, Oct. 2019.

[62] J.-B. Lagrange, "VFFA magnet prototype," (Kyoto, Japan), International Workshop on Fixed Field alternating gradient Accelerators, FFA'21, 2021.

[63] S. Sheehy, D. J. Kelliher, S. Machida, C. R. Prior, C. Rogers, M. Haj Tahar, F. Meot, Y. Ishi, T. Uesugi, Y. Kuriyama, M. Sakamoto, Y. Mori, and A. Adelmann, "Progress on Simulation of Fixed Field Alternating Gradient Accelerators," in Proc. 6th International Particle Accelerator Conference (IPAC2015), p. MOPJE077, 2015.

[64] D. A. Edwards and L. C. Teng, "Parametrization of linear coupled motion in periodic systems," IEEE Transactions on Nuclear Science, vol. 20, no. 3, pp. 885–888, 1973.

[65] G. Parzen, "The linear parameters and the decoupling matrix for linearly coupled motion in 6 dimensional phase space," in Proceedings of the 1997 Particle Accelerator Conference (Cat. No.97CH36167), vol. 2, pp. 1430–1432, 1997.

[66] P. H. Royer, "Solenoidal Optics," tech. rep., CERN, Geneva, 1999.

[67] J. W. Cooley and J. W. Tukey, "An algorithm for the machine calculation of complex Fourier series," Mathematics of computation, vol. 19, no. 90, pp. 297–301, 1965.

[68] A. W. Chao, Special Topics in Accelerator Physics. World Scientific, 4 2022.

[69] G. W. Hill, "On the part of the motion of the lunar perigee which is a function of the mean motions of the sun and moon," Acta Mathematica, vol. 8, pp. 1 – 36, 1900.

[70] F. Asvesta, H. Bartosik, S. Gilardoni, A. Huschauer, S. Machida, Y. Papaphilippou, and R. Wasef, "Identification and characterization of high order incoherent space charge driven structure resonances in the CERN Proton Synchrotron," Phys. Rev. Accel. Beams, vol. 23, p. 091001, Sep 2020.

[71] L. Martin, Experimental investigation of accelerator beam dynamics with a linear Paul trap. PhD thesis, University of Oxford, 2020.

[72] R. D. Ruth, "Single-particle dynamics in circular accelerators," AIP Conf. Proc., vol. 153, pp. 150–235, 1987.

[73] H. Koziol and K. H. Reich, "Beam Diagnostics at the CERN PS Booster," IEEE Transactions on Nuclear Science, vol. 18, no. 3, pp. 347–351, 1971.

[74] T. Adachi, M. Aiba, K. Koba, S. Machida, Y. Mori, A. Mutoh, J. Nakano, C. Ohmori, I. Sakai, Y. Sato, M. Sugaya, A. Takagi, R. Ueno, T. Uesugi, T. Yokoi, M. Yoshii, M. Yoshimoto, and Y. Yuasa, "A 150 MeV FFAG synchrotron with Return-Yoke Free magnet," in Proceedings of the 2001 Particle Accelerator Conference (PAC2001), vol. 5, pp. 3254 – 3256 vol.5, 02 2001.

[75] S. L. Sheehy, D. J. Kelliher, S. Machida, C. Rogers, C. R. Prior, L. Volat, M. Haj Tahar, Y. Ishi, Y. Kuriyama, M. Sakamoto, T. Uesugi, and Y. Mori, "Characterization techniques for fixed-field alternating gradient accelerators and beam studies using the KURRI 150 MeV proton FFAG," Progress of Theoretical and Experimental Physics, p. 073G01, 07 2016.

[76] C. Jolly, "Photograph of the KURNS main ring," 2023.

[77] M. Haj Tahar, High power ring methods and accelerator driven subcritical reactor application. PhD thesis, Université Grenoble Alpes, Jan. 2017.

[78] R. Bartolini, A. Bazzani, M. Giovannozzi, E. Todesco, and W. Scandale, "Algorithms for a Precise Determination of the Betatron Tune," 1996.

[79] I. Hughes and T. Hase, Measurements and Their Uncertainties: A Practical Guide to Modern Error Analysis. OUP Oxford, 2010.

[80] J. Laskar, C. Froeschlé, and A. Celletti, "The measure of chaos by the numerical analysis of the fundamental frequencies. Application to the standard mapping," Physica D: Nonlinear Phenomena, vol. 56, no. 2, pp. 253–269, 1992.

[81] R. Bartolini, A. Bazzani, M. Giovannozzi, W. Scandale, and E. Todesco, "Tune evaluation in simulations and experiments," Part. Accel., vol. 52, no. 3-4, pp. 147–177, 1996.

[82] K. Atkinson, An Introduction to Numerical Analysis, 2nd Ed. Wiley India Pvt. Limited, 2008.

[83] N. Biancacci and R. Tomás, "Using ac dipoles to localize sources of beam coupling impedance," Phys. Rev. Accel. Beams, vol. 19, p. 054001, May 2016.

[84] Étienne Forest, "Geometric integration for particle accelerators," Journal of Physics A: Mathematical and General, vol. 39, p. 5321, apr 2006.

[85] M. Aiba, S. Machida, Y. Mori, A. Mutoh, J. Nakano, C. Ohmori, I. Sakai, Y. Sato, M. Sugaya, A. Takagi, R. Ueno, T. Uesugi, A. Yamazaki, T. Yokoi, Y. Yonemura, M. Yoshii, M. Yoshimoto, Y. Yuasa, and K. Koba, "Study of Acceptance of FFAG Accelerator," 2002.

[86] S. Machida, "FFA Options for ISIS Upgrade and the Feasibility Study," in 3rd J-PARC Symposium (J-PARC2019), p. 011005, Jan. 2021.

[87] G. Aymar, T. Becker, S. Boogert, M. Borghesi, R. Bingham, C. Brenner, P. N. Burrows, O. C. Ettlinger, T. Dascalu, S. Gibson, T. Greenshaw, S. Gruber, D. Gujral, C. Hardiman, J. Hughes, W. G. Jones, K. Kirkby, A. Kurup, J.-B. Lagrange, K. Long, W. Luk, J. Matheson, P. McKenna, R. McLauchlan, Z. Najmudin, H. T. Lau, J. L. Parsons, J. Pasternak, J. Pozimski, K. Prise, M. Puchalska, P. Ratoff, G. Schettino, W. Shields, S. Smith, J. Thomason, S. Towe, P. Weightman, C. Whyte, and R. Xiao, "LhARA: The Laser-hybrid Accelerator for Radiobiological Applications," Frontiers in Physics, vol. 8, 2020.

[88] S. Machida, "FFA study for ISIS-II and FETS-FFA," Workshop on Fixed Field Accelerators, 2022.

[89] M. Benedikt, A. Chance, B. Dalena, D. Denisov, M. Giovannozzi, J. Gutleber, R. Losito, M. Mangano, T. Raubenheimer, W. Riegler, V. Shiltsev, D. Schulte, D. Tommasini, and F. Zimmermann, "Future circular hadron collider fcc-hh: Overview and status," 2022.

[90] CERN, "CERN Yellow Reports: Monographs, Vol 2 (2018): The Compact Linear e+e- Collider (CLIC) : 2018 Summary Report," 2018.

[91] A. Aryshev et al., "The International Linear Collider: Report to Snowmass 2021," Snowmass 2021, 2022.

[92] C. Achard, H. H. Braun, S. Döbert, I. V. Syratchev, M. Taborelli, I. H. Wilson, and W. Wuensch, "A Demonstration of High-Gradient Acceleration," 2003.

[93] J. P. Blewett, "Synchrotron radiation — 1873 to 1947," Nuclear Instruments and Methods in Physics Research Section A: Accelerators, Spectrometers, Detectors and Associated Equipment, vol. 266, no. 1, pp. 1–9, 1988.

[94] R. Bailey, B. Balhan, C. Bovet, B. Goddard, N. Hilleret, J. M. Jiménez, R. Jung, M. Placidi, M. Tavlet, and G. Von Holtey, "Synchrotron Radiation Effects at LEP," 1998.

[95] S. Aull, M. Benedikt, D. Bozzini, O. Brunner, J.-P. Burnet, A. Butterworth, R. Calaga, E. Jensen, V. Mertens, A. Milanese, M. Nonis, K. Oide, N. Schwerg, L. Tavian, J. Wenninger, F. Zimmermann, L. Rinolfi, A. Blondel, M. Koratzinos, and S. Gorgi Zadeh, "Electrical Power Budget for FCC-ee," tech. rep., CERN, 2016.

[96] Physics at the high-energy frontier - the Large Hadron Collider project, (London), Royal Society Publishing, 2012.

[97] "Design Report Tevatron 1 project," tech. rep., Fermilab, 1984.

[98] D. Neuffer and V. Shiltsev, "On the feasibility of a pulsed 14 TeV c.m.e. muon collider in the LHC tunnel," Journal of Instrumentation, vol. 13, p. T10003–T10003, Oct. 2018.

[99] MICE Collaboration, "Demonstration of cooling by the Muon Ionization Cooling Experiment," Nature, vol. 578, 02 2020.

[100] T. Dascalau, J. Flowerdew, P. Griffin-Hicks, A. Hughes, C. A. Mussolini, C. Pakuza, M. Topp-Mugglestone, W.-T. Wang, and L. Wroe, "A Design for a 3 TeV Rapid Cycling Synchrotron for Muon Acceleration in the SPS Tunnel," tech. rep., 2020.

Student design project as part of the John Adams Institute Graduate Accelerator Physics Programme.

[101] B. Boardman, "Rutherford Laboratory Report RL-82-006," tech. rep., 1982.

[102] F. Bordry, L. Bottura, A. Milanese, D. Tommasini, E. Jensen, P. Lebrun, L. Tavian, J. P. Burnet, M. C. Bastos, V. Baglin, J. M. Jimenez, R. Jones, T. Lefevre, H. Schmickler, M. J. Barnes, J. Borburgh, V. Mertens, R. W. Aβmann, S. Redaelli, and D. Missiaen, Accelerator Engineering and Technology: Accelerator Technology, pp. 337–517. Cham: Springer International Publishing, 2020.

[103] D. Schulte, "The International Muon Collider Collaboration," in Proceedings of the 12th International Particle Accelerator Conference (IPAC2021), International Particle Accelerator Conference, pp. 3792–3795, JACoW Publishing, Geneva, Switzerland.

[104] International Muon Collider Collaboration, "Tentative parameter list for the international muon collider collaboration," tech. rep., 2023.

[105] A. Chance, A. David, F. Batsch, F. Boattini, L. Bottura, C. Carli, H. Damerau, A. Grudiev, I. Karpov, E. Métral, D. Schulte, and K. Skoufaris, "Parameter ranges for a chain of rapid cycling synchrotrons for a muon collider complex," in Proceedings of the 14th International Particle Accelerator Conference (IPAC2023), p. MOPL162, 2023.

[106] A. Chance, "From top level to RCS parameters," in IMCC Annual Meeting, 2023.

[107] F. Batsch, R. Calaga, H. Damerau, and I. Karpov, "Overview of requirements for the SRF system of RCS chain," in IMCC Annual Meeting, 2023.

[108] S. Machida, J.-B. Lagrange, and M. Topp-Mugglestone, "Application of the FFA Concept to a Muon Collider Complex," in Proc. IPAC'21, no. 12 in International Par-

ticle Accelerator Conference, pp. 4006–4008, JACoW Publishing, Geneva, Switzerland, 08 2021. https://doi.org/10.18429/JACoW-IPAC2021-THPAB124.

[109] F. Batsch, D. Amorim, C. Carli, H. Damerau, A. Grudiev, I. Karpov, E. Métral, D. Schulte, and A. Chance, "Longitudinal beam dynamics and RF requirements for a chain of muon RCSs," in Proceedings of the 14th International Particle Accelerator Conference (IPAC2023), p. TUPA040, 2023.

[110] K. Adachi, "An electron model of vertical FFA accelerator for Harmonytron," JACoW, vol. IPAC2023, p. TUPA043, 2023.

[111] M. Vanwelde, C. Hernalsteens, and N. Pauly, "Linear and nonlinear beam dynamics of vertical fixed-field accelerators," Phys. Rev. Accel. Beams, vol. 27, p. 024003, Feb 2024.

[112] J.-B. Lagrange, R. Appleby, J. Garland, J. Pasternak, and S. Tygier, "Racetrack FFAG muon decay ring for nuSTORM with triplet focusing," Journal of Instrumentation, vol. 13, no. 09, p. P09013, 2018. (n.b. in this early paper, the FIXFIELD code is referred to as JBT).

[113] F. Méot, "The ray-tracing code zgoubi," Nuclear Instruments and Methods in Physics Research Section A: Accelerators, Spectrometers, Detectors and Associated Equipment, vol. 427, no. 1, pp. 353–356, 1999.

[114] S. Machida, "Modeling of a nonscaling FFAG and findings with the new code," in ICFA Beam Dynamics Newsletter, Issue 43, 2007.

[115] S. Brooks, Muon capture schemes for the neutrino factory. PhD thesis, University of Oxford, 2010.

[116] A. Adelmann, P. Calvo, M. Frey, A. Gsell, U. Locans, C. Metzger-Kraus, N. Neveu, C. Rogers, S. Russell, S. Sheehy, J. Snuverink, and D. Winklehner, "OPAL a versatile tool for charged particle accelerator simulations," 2019.

[117] M. Vanwelde, C. Hernalsteens, F. Méot, N. Pauly, and R. Tesse, "Modeling and implementation of vertical excursion FFA in the Zgoubi ray-tracing code," Nucl. Instrum. Methods Phys. Res., A, vol. 1047, p. 167829, 2023.